Study on the Unloading Shear Behavior of Granular Materials with Different Particle Shapes

粒子形状の異なる粒状体の除荷せん断挙動に関する研究

by

Li Zhuang

PH.D Thesis Presented to

Department of Civil and Environmental Engineering

Yamaguchi University, Ube

November 2013

Abstract

This study aims on unloading shear behavior of cohesionless granular materials. The unloading is often seen in underground engineering such as tunneling, open cutting, slop cutting. It is known that unexpected deformation often happened during these constructions. For purpose of understanding the basic mechanical behavior of unloading shear behavior, a series of experiments and numerical simulation were performed with influence of particle shape, relative density being discussed. Moreover, small-scale retaining wall model tests were performed to investigate the unloading shear behavior by change of boundary conditions.

First, plane strain compression experiments were performed. Four types of granular material including two sands and two glass beads with different particle shape and particle size were selected. For the two sands, one has angular particle shape while another has sub-angular particle shape. Unloading shear experiments were performed considering confining pressure and relative density. The unloading shear was implemented by plane strain compression tests under decreasing confining pressure (shorted for PSCD), where the vertical axial stress is kept constant and the confining pressure is reduced until failure occurs. A well-known general plane strain compression test (shorted for PSC) was also performed to make a comparison. The PSC test The main different point between the two tests is the mean stress on the test specimen decreases in the PSCD test while it increases in the PSC test. In other word, the PSCD reflects unloading while the PSC reflects loading from physical viewpoint. Photographs of specimens during shear process were taken and local deformations of specimens were analyzed by digital image analysis method. Stress-strain relationship and local deformation analysis results obtained from the experiments were shown as below.

In general, sands showed different shear behavior from glass beads. Under the same test condition, the sand with angular particle shape showed the highest shear strength and dilatancy. Shear behavior in both sands and glass beads is influenced by stress path, however the influence was found different. For the shear behavior of sands, the maximum principle stress ratio and initial stiffness of stress ratio ~ deviatoric strain were found generally higher in the PSCD test than those in the PSC test.

The differences are more significant in dense specimens than those in loose specimens. Moreover, shear bands appeared earlier in the PSCD tests for sands. The sands were strongly influenced by stress path and stress level compared to glass beads. Development of shear bands, final inclination angle and width of shear bands were observed by image analysis. Generally, the onset of shear bands occurs prior to the specimen reaching its maximum principal stress ratio for both dense and loose specimens. Between the peak in shear strength and the end of strain softening, the local maximum shear strain grew approximately linearly with the global axial strain. For the same material, the growth rate of the local maximum shear strain became smaller with wider shear band. The shear band width became smaller when the particle shape of materials with similar mean particle size gets more angular, and it decreased with increase of confining pressure regardless of particle shape. Moreover, the measured shear band inclination angles were compared with prediction values by Coulomb and Roscoe equations having been often used in past study. It is found that the shear band inclination angles in sands matched well with those estimated by Coulomb's formula, while Roscoe's formula predicted shear band inclination angles relatively close to the corresponding measured values in dense glass beads.

Next, based on the analysis of elemental experiment results, discrete element method (DEM) was used to investigate underlying mechanism from micro viewpoints. Biaxial compression (loading) and decompression (unloading) tests were performed. Two types of particle model, round disk model and angular clump model were used in the simulation. The simulation results generally reflected the influence of particle shape, relative density and stress path in the elemental experiments. Through micro behavior analysis including coordination number, contact distribution, fabric inside specimens, the reason of different contact variations in specimens that resulted in different macro shear behavior was found. Moreover, strain energy variations at particle contacts were analyzed in detail. Strain energy variation with the mean stress was compared for the two types of shear test and isotropic consolidation test. It is found that strain energy variation rate is the highest in unloading shear test. Under the same test condition, the variation rate is higher in the loose specimens than in the dense specimens, and is also higher in disk specimen than in clump specimen. The behavior was considered to be influenced by the interlocking among particles. The interlocking is stronger in angular particles than that in round particles, and also stronger in dense specimens than that in loose specimens. When particles are interlocked, the relative displacements between particles shall become difficult and thus strain energy varies little. As a result, the stiffness of specimens behaves strong. In the loading shear test with mean stress increased, the interlocking developed until the peak strength and then failed. Instead, for the shear test with decreasing confining pressure, variation of interlocking gets smaller from the beginning. Thereby, the particle shape effect is different on the different stress path and the difference is more significant in dense specimens.

Finally, unloading retaining wall model tests were performed to investigate particle shape effect and boundary effect on unloading shear behavior. The same two sands and one glass beads were used again. Investigation was focused on the failure mode behind the wall and transition process to the active state. It is found that the particle shape has influence on the resultant force of retaining wall. The more angular particle shape of sand, the resultant force was smaller and the displacement of wall until the final active state was smaller. Shear band inclination angle and width were influenced by particle shape and relative density, while the progress shear band pattern is dependent on the wall movement mode regardless of particle shape. Within a limited range of wall speed in this study, shear band became wider and local deformation became larger with increase of wall speed.

In summary, a series of experiments and numerical analysis were performed in this study to investigate the fundamental unloading behavior of granular materials with different particle shapes. Based on the study, particle shape effect on the macro mechanical behavior was presented and further investigations were made on micro mechanical behavior and its relevance to the macro behavior. Particularly, unloading shear behavior was found to be clearly different from the general loading shear behavior and influence of particle shape and relative density on the difference between the behaviors was revealed. The influence was considered rooting in the interlocking effect, which was qualitatively discussed from micro viewpoint.

Table of contents

Chapter1 Introduction

Chapter2 Unloading behavior of granular materials with different particle shapes in plane strain compression tests

Chapter 3 Unloading shear behavior of granular materials in biaxial DEM simulation

Chapter 4 Unloading shear behavior of granular materials with different particle shapes in retaining wall model tests

References

Appendixes Main DEM codes for the simulation

Chapter 1 Introduction

1.1 Background

There are many kinds of unloading projects in the field of civil engineering, such as excavation for retaining wall, slope cutting, tunneling, and preloading and unloading in subgrades of railway or highway, as shown in Fig. 1.1. Here, “unloading” is an engineering concept and it is different from the mechanical meaning in “loading-unloading” of a cyclic elemental test. Such excavation or removal of soil (load) will generate a new boundary and the soil around the new boundary will undergo different stress paths accompanied by stress release. Taking the construction of a retaining wall as an example, soil at the bottom of the excavation pit is subjected to extension as the overburden is removed, and soil behind the retaining wall in active state is subjected to shear compression by the progressive decrease of the lateral pressure while the vertical stress remains constant (Head 1992). The stability of new boundaries is very important, and unloading behavior of soils especially deformation development deserves much attention to help selecting construction method or support (Nicolini and Nova 2000, Ng and Lee 2002).

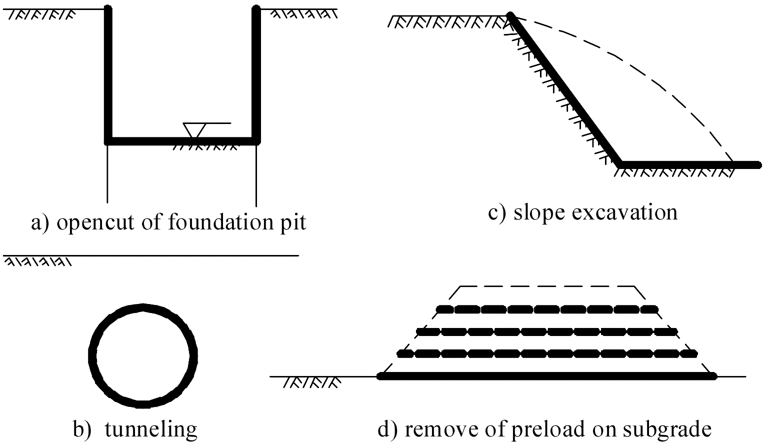

(a) sketch

(b) in-situ photos

Figure 1.1 Different unloading cases in civil engineering

Currently, excavation problems are mainly solved as a boundary and constitutive model problem based on continuum theory. However, soil properties are abstracted as mechanical or mathematic parameters and selecting their values is very challenging. From author's opinion, there are still several problems that haven't been solved very well in excavation calculation. These including:

(1) Soil rebound. Compared with some in-situ measurements, such as at the base of foundation pit, and in subgrade after removing the preload, soil rebound is often overestimated by elastic modulus of soil. The main reason is that soil is not elastic, even during unloading. Resilient modulus may be much larger than compressive modulus.

(2) Stress release. How much stress released around the new boundary? This is usually estimated by empirical values, in addition, it is related with excavation method, supporting as well as soil properties (Zhou 2005).

(3) Residual stress. This topic relates to stress release. Are there residual stresses in soils? This is still a controversial problem.

Figure 1.2 presents the time history of vertical stresses at different locations during loading and unloading on sand (Zhuang 2009). The vertical stresses at different depths almost increased linearly with external load during staged loading. However, the stress release behavior was highly nonlinear and the amount of released stress is different in each stage of unloading. The stress release was much smaller at the beginning of unloading, but increased significantly when unloading continues, particularly when the external pressure was unloaded to very low levels. After the applied load was completely removed, residual stresses were measured in sand. However, some researches insisted that measured stresses by soil cell can't represent real stresses in soil but they are only contact stresses between soil cell and soil (Talenick et al. 2008).

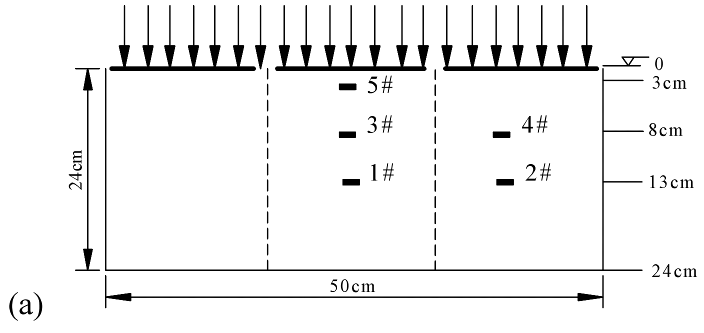

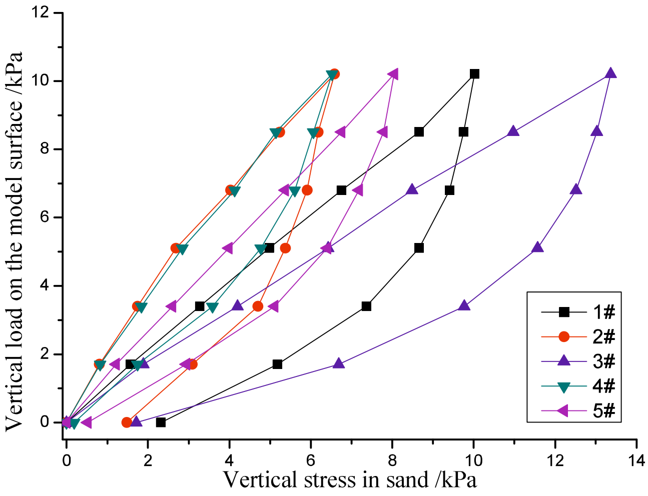

(b)

Figure 1.2 Static loading and unloading behavior of sand and residual stress: (a) locations of soil stress cells in test box, (b) Vertical stress variations in sand with applied external load (after Zhuang 2009)

Nevertheless, photoelastic study showed that there may have some residual contact forces in particles when the previously applied load was removed, as shown in Fig. 1.3.

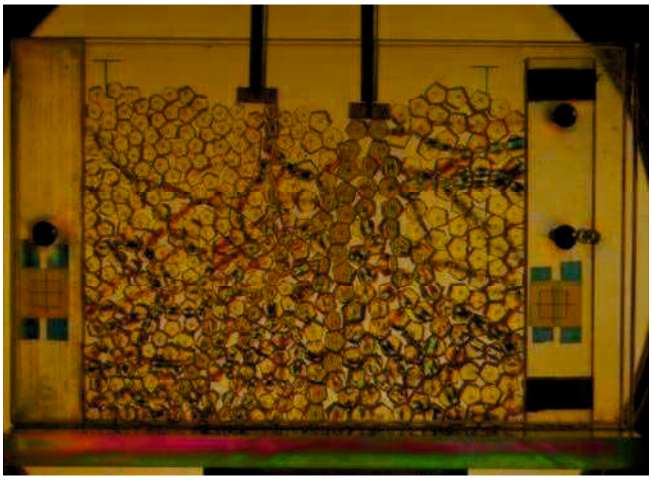

Figure 1.3 Force chains in granular material by photoelastic technology

(4) Progressive and sudden failure. Soil failure and resulted collapse often happened in practical engineering. Although they maybe attributed to different reasons including soil properties and boundary conditions,

progressive deformation of soils is still not clear and needs more study (Asaoka et al. 1997). Shearing failure by local deformation was and is still a hot topic. It is still a hard issue that how to use the appropriate theory to explain or successfully predict the formation and development of the shear bands in granular matter (Bi et al. 2011).

With the above confusing problems, it is necessary to further investigate unloading behavior of soils, especially from micro viewpoints to reveal the underlying mechanism. On the other hand, as soils with and without cohesion behave much different, this study only focus on cohesionless soils such as sands.

1.2 Literature review

1.2.1 Past study on unloading behavior of granular materials

Unloading behavior has been known to be very complex. Progressive failure or sudden failure accidents happened a lot in practical engineering. The current calculation methods of analyzing unloading problems are mostly based on boundary conditions and constitutive models of soils (Nakai et al. 1997).

On the one hand, excavation load, a kind of counterforce of removed soils to new boundaries, attracted attentions for a long time. Three methods have been developed in the past to determine the excavation load on supporting structures induced by excavation, which are: (i) load-structure method, (ii) stiffness reduction method, and (iii) equivalent reverse nodal force method. The first method considers the arch effect in soil, and the excavation load is determined by Terzaghi's soil arch formula (1936) in European countries and Протодьяконову's formula (1907) in Russia and China, respectively. In the second method, excavation in soil was considered as an equivalent process of gradually decreasing the stiffness of the soil to be removed. The essence of the third method as discussed by Mana (1981) is to determine the nodal forces resulted from removed soil elements. The excavation is considered equivalent to a process of stress release under initial stress conditions accompanied by soil deformation, and the stress release is generally affected by excavation shape, soil properties and construction method (Gao 1999, Nicolini and Nova 2000, Ren 2005). For example, Zhou (2005) pointed out that piperoof could reinforce ground soil and diffuse overlying load; soil nailing system can reduce the magnitude of stress relief at the tunnel heading (Ng and Lee 2002). The remained problem in these past studies is that, some important parameters such as the height of arching and stress release coefficient are generally taken to be empirical values.

On the other hand, it is also very important to choose a suitable constitutive model to estimate excavation deformation or stability if using continuum method. Soil stress paths during excavation are very complex and are much influenced by excavation method and support etc. Taking triaxial test as an example, some typical stress paths are shown in Fig. 1.4. So far, most study had been focused on the common compression behavior (stress path ①). Some researchers compared the yielding behavior, steady state, viscous properties and stress-dilatancy of sands in both triaxial compression and extension tests (Yasufuku et al. 1991; Masuda et al. 1999, Kiyota and Tatsuoka 2006; Yoshimine and Kataoka 2007; Khan 2009; Chang and Yin 2010). Masuda et al. (1999) studied sand behavior under different stress paths including plane strain compression, extension and cyclic loading to investigate effects of preloading to struts in open cut excavations and the experimental results indicated influence of stress paths on unloading behavior of sand.

There are also a few studies on triaxial or plane strain extension tests where stress paths were close to path ③. Wolf et al. (2006) noted that, results of pre-tests as well as experimental results in the literature suggest that not only the density but also the applied stress path affects the stress–strain response of the material. They also presented that the stress path in direct shear test can be described most suitably by stress path ③. Röchter et al. (2010) observed shear banding and strain softening in plane strain extension test of sand and sand-clay mixtures.

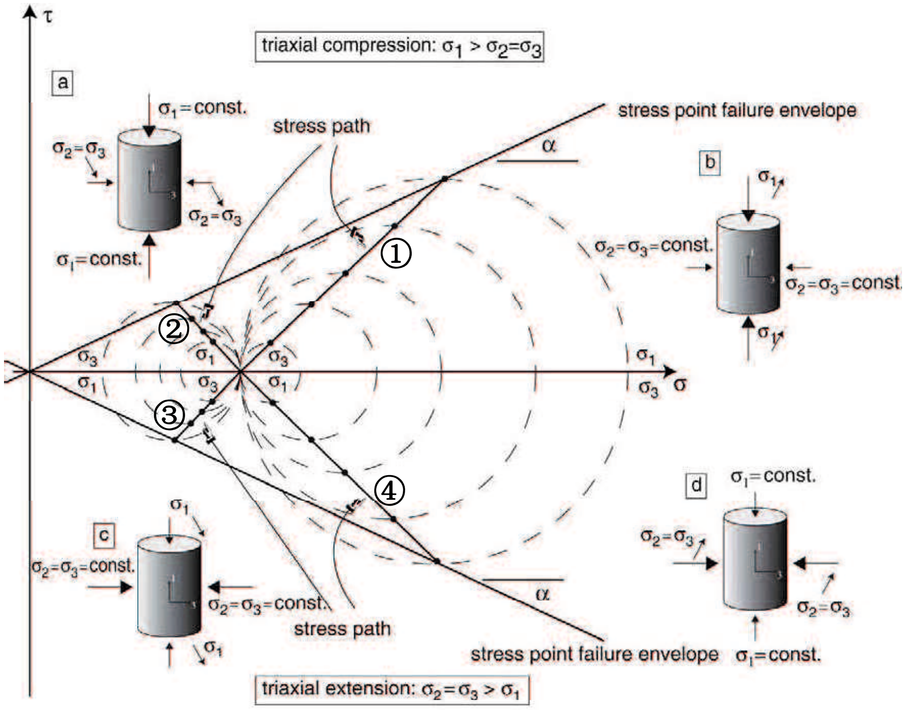

Figure 1.4 Different stress paths in a triaxial test (after Wolf et al. 2006)

Despite many past studies on various stress paths, it is still rare to see experimental or numerical study on soil behavior under stress path ② or ④ under either triaxial or plane strain condition, while stress path ② is very important for tunneling and open cut problems. Numerical simulations covering this topic include those study of Ng (2004), Thornton and Antony (1999). Moreover, soil behavior before failure was sometimes treated too simply like linear or nonlinear elastic in most constitutive models. Collins (2005) also stated that most existing models are based on yield loci, flow and hardening rules and failure lines while rarely have any firm physical basis. According to the critical state theory, compression or extension tests will arrive at the same critical state line even if experiencing different stress paths (without considering particle crush). However, mobilized strength and shear deformation show considerably different behaviors. This is very important for the calculation of unloading problems and deserves more attention.

1.2.2 Past study on local deformation in granular materials by elemental test

Soil is a typical kind of inhomogeneous material, and shows many complex types of discontinuous deformation. Therein the shear band or strain localization in various granular materials had been and is still being focused on by many researchers through triaxial test or plane strain test since a long time before (Vardoulakis 1981, Peters 1988, Lade et al. 1996, Finno et al. 1997, Alshibli et al. 2000, 2003, Desrues and Viggiani 2004, Hall et al. 2010, Rechenmacher et al. 2011, Borja et al. 2013)

Figure 1.5(a) shows an example of shear bands formed in sand specimen in plane strain compression test. The formation process of shear band during shearing and its two key factors including the inclination angle θ and thickness w are very important for understanding shear behavior of the test material. Also, soil pressure behind retaining wall is also related to the shear band properties.

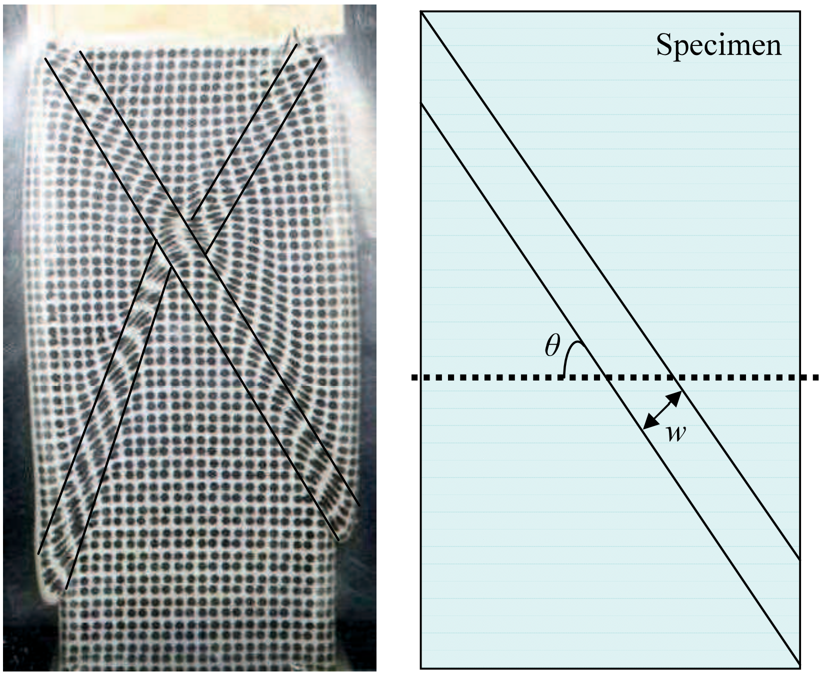

Figure 1.5 Shear bands in specimen of granular material

It is known that shear band is developed from the discontinuous deformation of materials, and much rotation happened within shear bands (Iwashita and Oda 1998, 2000, Powrie et al. 2005, Cheung and O'Sullivan 2008, Belheine et al. 2009, Jiang et al. 2009). Several equations for calculation of inclination angle of shear band had been suggested in the past study, as shown in Table 1.1. Here, Φ_m is mobilized friction angle at the maximum stress ratio, and ψ_f is the dilation angle. The thickness of shear band was summarized to be A* D_{50}, where A is a constant related to material properties and stress level etc., and was reported to be several times or several ten times in the past study.

Table 1.1 Main equations of inclination angle of shear band in the past study

Coulomb's solution	45°+ $\Phi_m/2$	$\Phi_m=\arcsin[(\sigma_1-\sigma_3)/(\sigma_1+\sigma_3)]_{max}$ $\psi_f=\arcsin(d\varepsilon^p_1+d\varepsilon^p_3)/\lvert(d\varepsilon^p_1-d\varepsilon^p_3)\rvert$
Roscoe's solution (1970)	45°+ $\Phi_f/2$	
Authur's solution (1977)	45°+($\Phi_m+\psi_f)/4$	

Note: σ_1, σ_3 are maximum and minimum principal stresses, and ε^p_1, ε^p_3 are maximum and minimum plastic principal strains.

Some other researchers also focused on the boundary effects on the shear band, such as by Desrues and Viggiani (2004), Xu (2005), Powrie et al. (2005). These studies show that formation process and resulting patterns of strain localization are much influenced by loading speed, relative friction and movement of boundaries.

Local stress-strain behavior was also discussed in a few studies, in order to explain progressive local deformation and sudden failure (Xu 2004). Related to this, bifurcations in granular materials were analyzed from both micro and macro viewpoints in past study (Darve and Laouafa 2000, Darve *et al.* 2007, Nicot and Darve 2007). "Bifurcation" is defined as "a sudden or discontinuous change or response (for example, deformation) under constant or small disturb loading". Shear band in soil is a kind of bifurcation, which means that softening will occur in material and failure (sometimes temporary hardening occur) will be accelerated. Another kind of bifurcation is diffuse failure, which was introduced in geomechanics in 1998 (Darve *et al*. 2007) to describe failure modes with no strain localization pattern in either shear bands or compaction/dilation bands.

Pradhan (1997) showed that the direction of shear band is highly influenced by the inherent anisotropy, confining pressure and particle size, and the direction of shear band changes from Coulomb's type to Authur's type (this means the inclination angle decreased) when the confining pressure is increased. There was also study on the PSC test which shown that thickness of the shear band decreases with the increase of confining pressure. Alshibli et al. (2000) showed that shear band inclination angle increased as the confining pressure increases for fine sand, but not for medium sand and coarse sand. Also, they pointed out that there is no definite conclusion about the influence of the confining pressure on the shear band orientation angle of sands in the past study, and the relationship between them was also related to the boundary condition and material properties including grain angularity, particle size distribution and packing state.

Until now, influence factors on shear band formation and shear band characteristics are still not completely clear. This is because there are too many influence factors, which can be generally classified into two types: (1) boundary condition such as confining pressure, stress path, loading or unloading speed, (2) material properties such as particle size distribution, particle shape, relative density etc. These influence factors are usually mixed together and therefore the problem becomes complex. One example is given here. Fig. 1.6 shows the effect of confining pressure on shear band inclination angle. It was found that the values are quite discrete for different materials and different study.

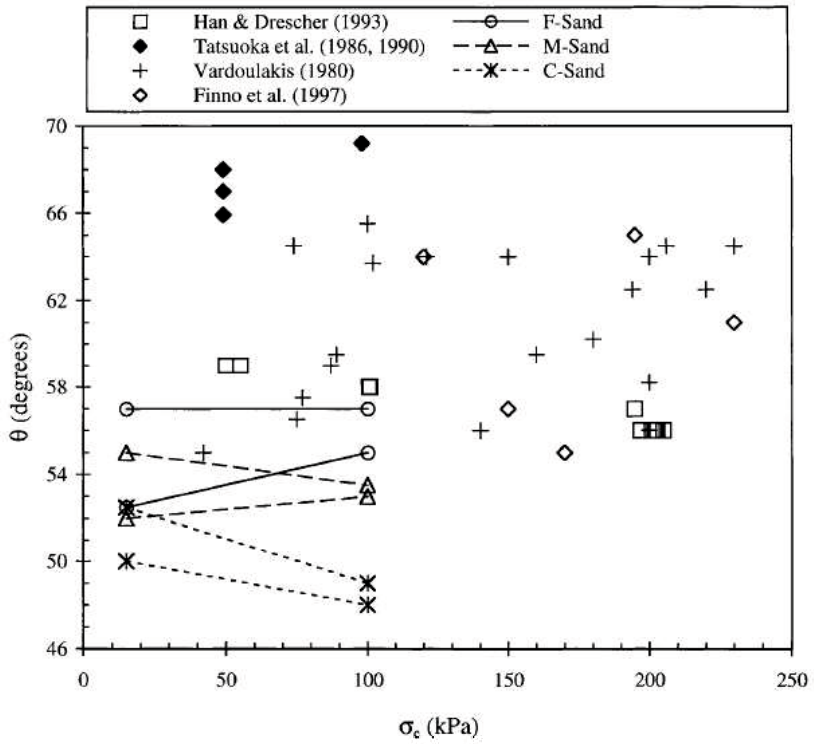

Figure 1.6 Effect of confining pressure on shear band inclination angle (after Alshibli and Sture 2000)

Although much study had been done on local deformations, it is rarely related to unloading process. Moreover, compared with the resulting patterns of shear bands, the beginning and development process and their influence factors are more important for the unloading problems.

1.2.3 Past study on effects of particle shape on shear behavior of granular materials

From the micro viewpoint, the key factors that determine the mechanical behavior of granular material are the particle shape, as well as size distribution and initial arrangement. The influence of particle shape on strength, shear flow of granules has been confirmed in past studies, such as the work by Shinohara (2000), Unland (2009), Lin (2005) and Cleary (2008). Cho et al. (2003) showed that the particle shape has a large effect on the packing density, small strain stiffness and the strength of sands; Maeda et al.(2010) showed that the macro critical state of granules is controlled by the micro critical state of coordination number and limit of anisotropy, which depend on grain shape effects; Cavarretta et al. (2010) noted that the granular material response is slightly dependent on the surface roughness and friction, while the influence of particle shape is much more significant; Zeghal (2001) showed that an assemblage with irregular particles has a higher resilient modulus than one with round regular particles. Despite such extensive research on the influence of particle shape, very little study has considered the effects of stress paths, especially the stress path during excavations.

It has been known for some time that particle shape has a great influence on the strength, deformation and crushability of granules (Unland and Al-Khasawneh 2009, Wang et al. 2011, Kato et al. 2002, Maeda et al. 2010, Cavarretta et al. 2010, Zeghal 2001, Matsushima and Chang 2011, Ferellec and McDowell 2007, Kock and Huhn 2007). Alshibli *et al.* (2000) noted that influence of confining pressure on strength and stability decreases as grain angularity decreases. Maeda et al. (2010) pointed out that the macro critical state of granules is controlled by the micro critical state of coordination number and limit of anisotropy, depending on grain shape effects. Cavarretta et al. (2010) noted that the granular material response is slightly dependent on the surface roughness and friction, while the influence of particle shape is very much more significant. Zeghal (2001) showed that sample with irregular particles has a higher resilient modulus than one with round regular particles. Matsushima and Chang (2011) qualitatively evaluated the effect of particle shape in sheared granular assemblies. Despite such extensive research of influence of particle shape, very little has been found that have considered effects of stress paths, especially the stress paths in excavations.

Because of the extremely irregular shapes of particles in most of soils and limitation of computation ability, very few studies had tried to describe the real complex shape of each particle in calculations (Ferellec and McDowell 2010). Particle shapes are simplified in most studies using DEM simulation, such as clump model or cluster model, which has been verified to be able to reflect the particle shape effects (Zeghal 2001, Matsushima and

Chang 2011, Ferellec and McDowell 2007, Kock and Huhn 2007, Katagiri et al. 2010). Besides various micro properties being able to be investigated in DEM simulations, one advantage is that it can trace energies and work both inside granular materials and at boundaries. Energy dissipation analysis has been shown to be very helpful for studies on granular flow problems, bifurcation and diffuse phenomena in granular materials (Asmar et al. 2003, Stegmann et al. 2011, Nicot and Darve 2007, Darve et al. 2007).

1.2.4 Application of DEM simulation and DIC method to local deformation analysis of granular materials

In order to investigate micro behavior of granular material especially local deformation and its underlying mechanism, Discrete Element Method (DEM) and image analysis are being used more and more since 1980s.

DEM is short for the "Discrete Element Method", and is being used more and more in study on granular materials since it was firstly proposed by Cundall in 1971 (Itasca 2008, Cundall and Strack 1979) to solve discontinuous problem in rocks. This method is much different from the FEM being often used in various fields, as compared in Fig. 1.6. It is much different from the FEM in that, material is not treated as continuum but as assembly of discrete particles, which can have different sizes and particle shapes. Take a simple tunneling problem shown in Fig. 1.7 as an example, in the FEM, soils are treated as elements controlled by constitutive model, while in the DEM, soils are treated as many particles whose behavior is controlled by contact model between particles and the Newton's second law. Therefore, equilibrium equations, physical equations and so on for continuum theory are not applied. Particles move and interact according to the Newton's second law and force-displacement law (contact model). Details will be introduced in Chapter 3.

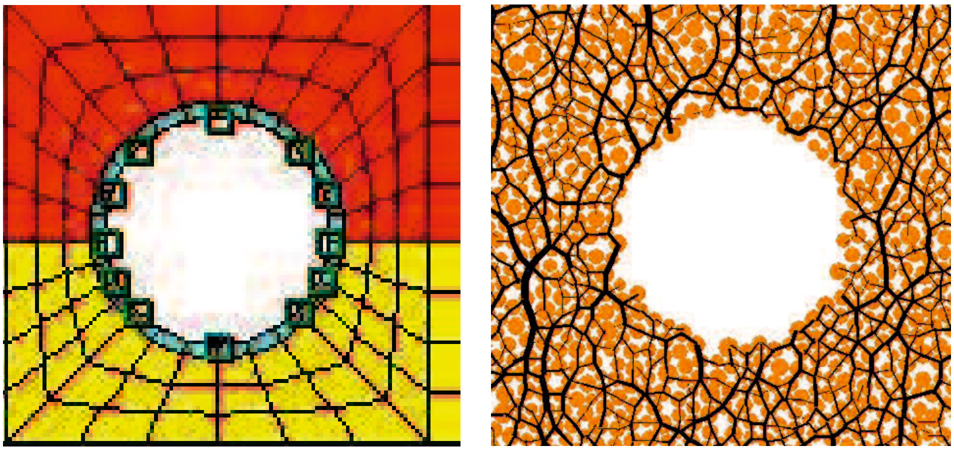

(a) FEM (b) DEM

Figure 1.7 Different elements used in FEM and DEM

DEM has been successfully to solve problems of particle flow, particle crushing, discontinuous deformations and so on. The main advantages of DEM are that it can directly simulate physical and geometric properties of granular materials, such as particle shape, size distribution and arrangement, and therefore can help to explore underlying mechanism of macro behavior. Some pioneer work in the field can refer to Cundall (1979), Ting et al. (1989), Anandarajah (1992), Thomas and Bray (1999), Iwashita et al. (1998, 2000), Thornton and Antony (2000).

PFC is one of commercial DEM code developed by Itasca and it has both 2D and 3D versions. Fig. 1.8 shows an example of elemental test simulation. In the figure, (a) shows a model composed of spheres to simulate ideal granular material, and (b) shows test result of stress-strain behavior and comparison of rigid and flexible lateral boundaries. DEM can also well simulate model test, such as in Fig. 1.9. A different EM code called YADE was used to simulate local deformation in retaining wall model test, and the simulation results were shown to be well agreed with image analysis results by DIC method (introduced as below).

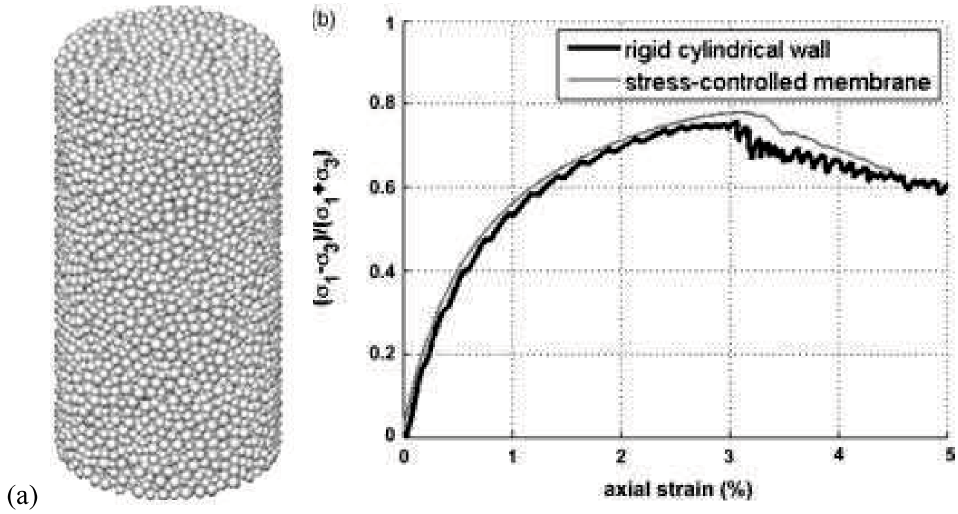

Figure 1.8 Three-dimension DEM simulation on trixial test (After Cheung and O'Sullivan 2008)

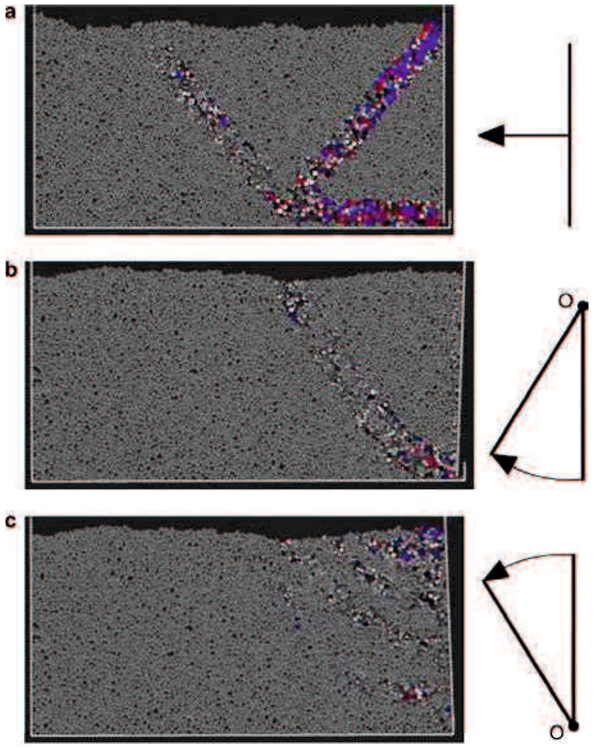

Figure 1.9 Two-dimension DEM simulation on retaining wall model test on initially dense sand: (a) translating wall, (b) wall rotating around top, (c) wall rotating around toe (after Widuliński 2011)

DIC is short for “Digital Image Correlation” and is a kind of image analysis (http://en.wikipedia.org/wiki/Digital_image_correlation). Its basic idea is to solve deformation (especially inside the object) according to the variations of gray levels, see the Fig. 1.10. The gray levels of image patches of observed object at different time are matched, assuming that they present some similarity. This method is based on the PIV (Particle Image Velocity), and the cross-correlation method is used. Some detail introductions and applications of the DIC in soil mechanics especially for the local soil deformation had been done by Bruck et al. (1989), Rechenmacher et al. (2002, 2004), White et al. (2003), Sadek et al. (2003), Slominski et al. (2007), and recently by Hall et al. (2010). These studies had shown that DIC has high accuracy and is very helpful for soil analysis. Fig. 1.11 shows DIC analysis results of model tests on sands. It is found that the local deformation in test photos that is invisible to the naked eyes can be well reflected by DIC analysis.

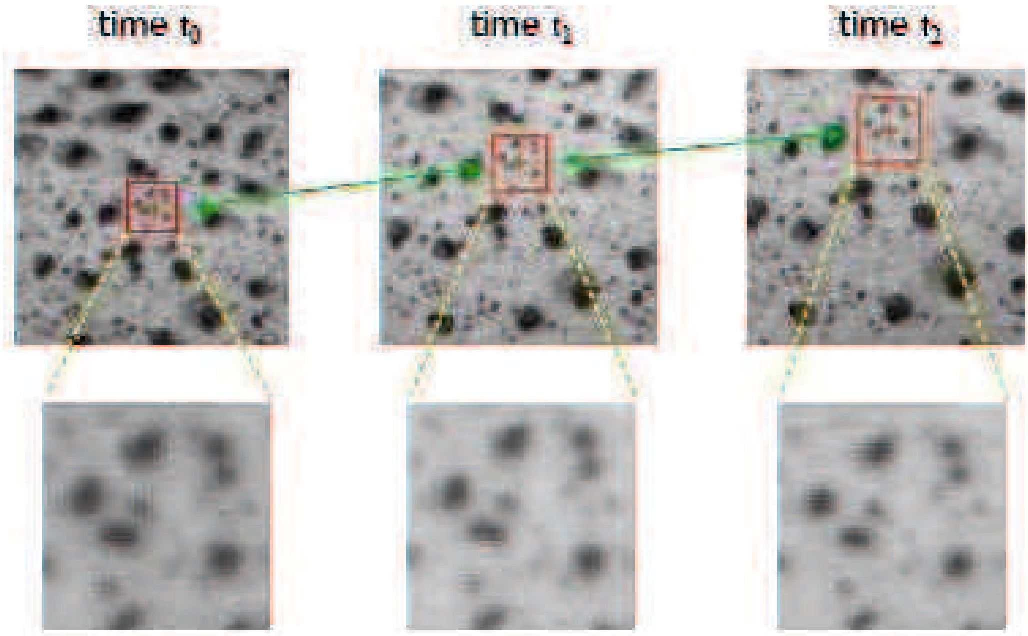

Figure 1.10 Image matching in the DIC method

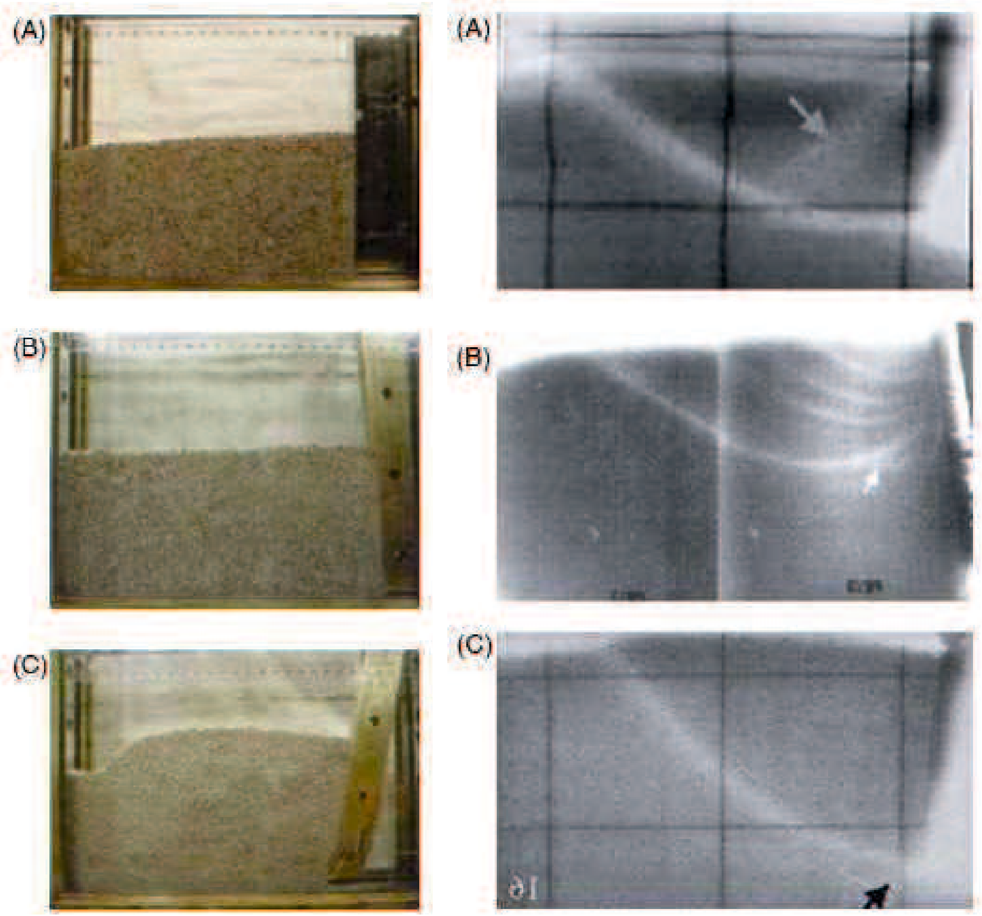

Figure 1.11 PIV analysis results of retaining wall model test (after Niedostatkiewicz et al. 2010)

1.3 Research objective and main contents

This study aims on unloading shear behavior of granular materials. Details of the objective including:

(1) Macro unloading shear behavior of granular materials during and its influence factors especially particle shape, relative density;

(2) Micro unloading behavior of granular materials and the underlying mechanism corresponding to the macro behavior;

(3) Progressive local deformation during unloading and its influence

factors including material properties and boundary conditions;

(4) Shear band characteristics in granular materials during unloading.

With the above objectives, this study mainly focused on unloading shear behavior of non-cohesive granular materials including sands and glass beads. Unloading shear behavior is investigated from both macro and micro viewpoints. Elemental experiments, 2D DEM simulation and retaining wall model tests were performed. Photographs of specimens in both elemental experiments and model tests were taken and image analysis on local deformations was done. This dissertation is composed of five chapters.

Chapter 1, Introduction

Chapter 2, Unloading shear behavior of granular materials with different particle shapes in plane strain compression tests

Chapter 3, Unloading shear behavior of granular materials in biaxial DEM simulation

Chapter 4, Unloading shear behavior of granular materials with different particle shapes in retaining wall model tests

Chapter 5, Summary and conclusions

In chapter 1, background and purpose of this study were mainly introduced. Past study about unloading behavior and existing problems were reviewed. Local deformation in granular materials, particle shape effect, DEM simulation and image analysis method were particularly reviewed.

In chapter 2, plane strain compression tests under two different stress paths were performed on two sands and two glass beads with angular, sub-angular and round particle shape. The unloading shear behavior of granular materials under decreasing confining pressure was mainly analyzed and compared to that in common loading shear test under constant confining pressure. Influence of particle shape and relative density was especially analyzed.

In chapter 3, based on the experimental test results in chapter 2, 2D (biaxial) DEM simulations under the two different stress paths were performed. Disk and clump models were used to investigate particle shape effects. Both macro and micro behaviors were analyzed, and underlying mechanism of the different shear behavior presented in chapter 2 was explained from micro viewpoint.

In chapter 4, retaining wall model tests were performed on the two sands and one glass bead used in Chapter 2. Local deformation of granular materials in active state behind the retaining wall and particle shape effect were mainly studied. Influence of the boundary condition including wall movement mode and speed on the formation process of local deformation during unloading was discussed.

In chapter 5, main conclusions obtained in each chapter are summarized. Questions not solved yet and to be continued in future are presented.

Main contents and structure of this draft dissertation are shown in the flowchart in the next page.

1.4 Innovation of this study

In this study, there are three points thought as research innovations:

(1) Plane strain compression tests under decreasing confining pressure were performed in this study to investigate unloading shear behavior. It was noted that the unloading shear behavior is different from that in common plane strain compression test. Particle shape and relative density were found to be very important influencing factors.

(2) Three materials with similar mean particle size but angular, sub-angular and round particle shapes were compared. The particle shape effect can therefore be separated from particle size effect. The angular particle shape was found to be a critical factor for shear behavior.

(3) Strain energy variation with mean stress in DEM simulation was analyzed. It was linked to macro shear behavior. Moreover, it is expected to serve as a bridge connecting particle interlocking and macro shear behavior.

Flowchart of this study

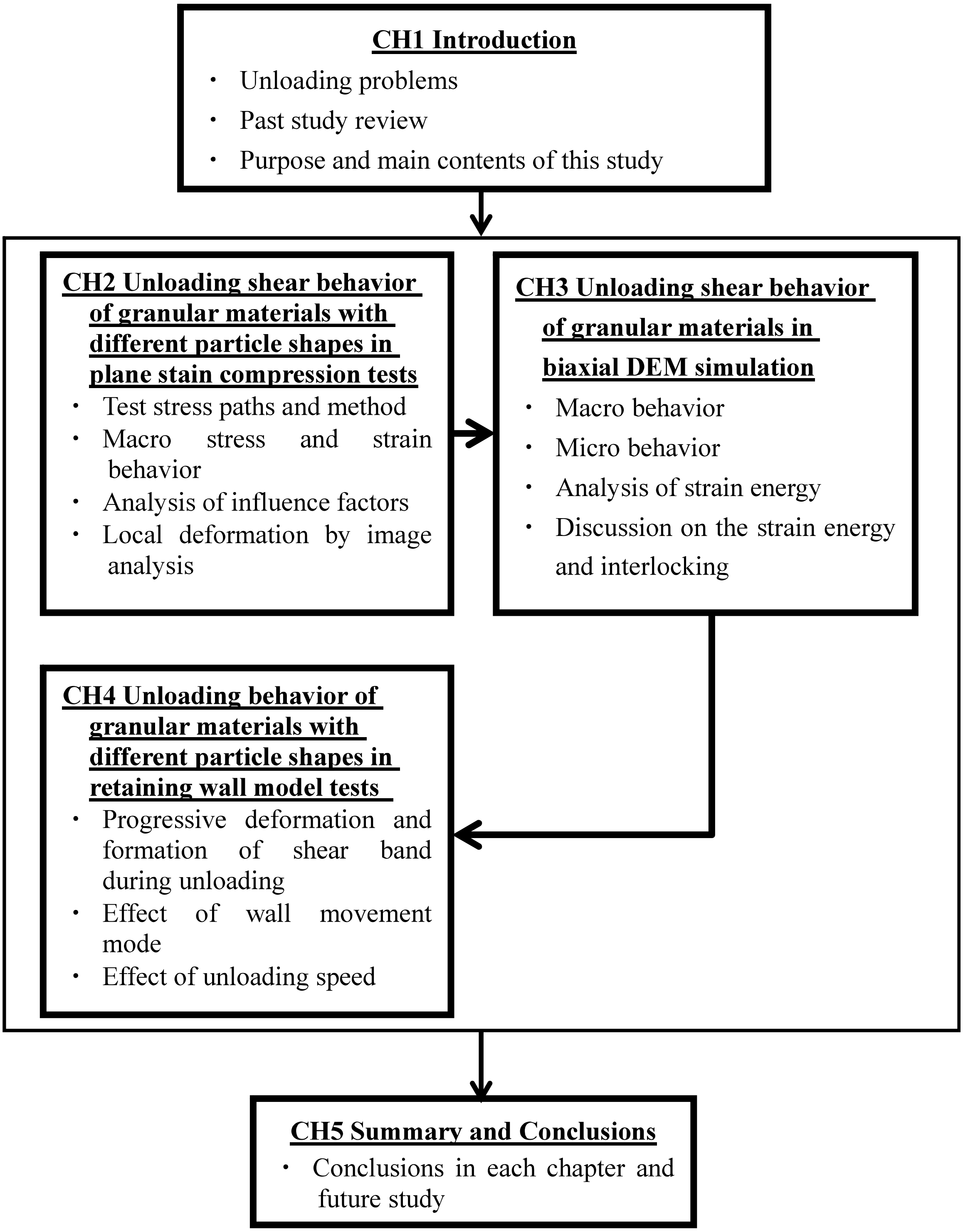

Chapter 2 Unloading shear behavior of granular materials with different particle shapes in plane strain compression tests

The natural ground is a semi-infinite stratum being composed of various soils and rocks. Therefore a plane strain condition is often considered when analyzing soil or rock problems. For practical unloading problems, soils may undergo different stress paths including shear compression and extension. In this study, only shear compression behavior was investigated. Experiments were mainly focused on plane strain compression under decreasing mean stress to explore unloading shear behavior. To investigate influence factors, four kinds of granular materials with different particle shape or particle size were selected. Moreover, influence of relative density of specimen, confining pressure is also studied in this chapter.

2.1 Two stress paths in plane strain compression test

As mentioned earlier in Fig. 1.4, there are two different simple stress paths for the triaxial compression test. This is the same for the plane strain compression test. In this study, plane strain compression tests under the two different stress paths were performed, and the corresponding stress paths are shown in Fig. 2.1. One test type is the conventional plane strain compression test (referred to as PSC test), where the specimen was sheared under a constant axial displacement rate (displacement-controlled test) and a constant effective confining stress (σ'_3). The other plane strain test type is the load-controlled test (referred to as PSCD test), which shears the specimen by decreasing the effective confining pressure σ'_3 under a constant effective axial stress (σ'_1). In the PSCD test, when a specimen reaches peak strength (the highest σ'_1/σ'_3), a decrease in the confining pressure stops and shearing is continued under a constant axial displacement loading rate. Practical field problems corresponding to the two different stress paths are illustrated in Fig. 2.1. The soil element below a long strip footing, which is continuous unlike an isolated footing, approximately follows the stress path of the PSC test, while those located at the lateral sides of excavation of tunnels or continuous foundation pits are close to the stress path of the PSCD test. A main difference between the PSCD test and the PSC test is that the mean stress on specimen decreased in the former while it increases in the later.

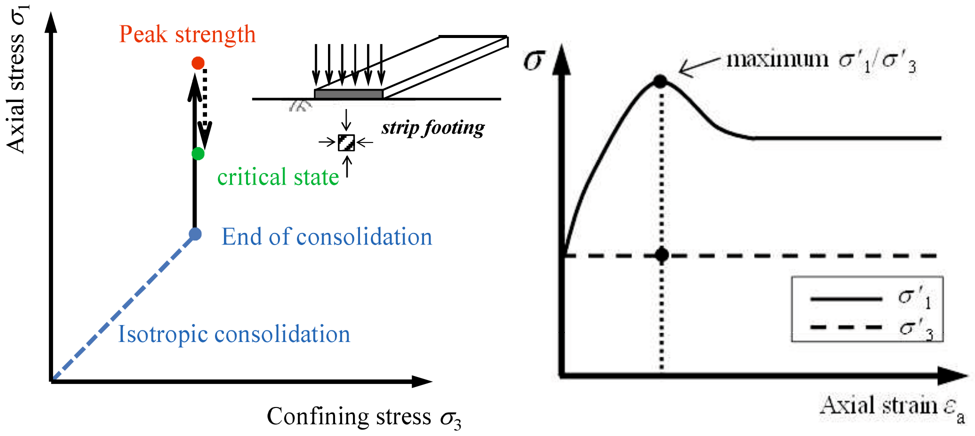

(a) PSC test

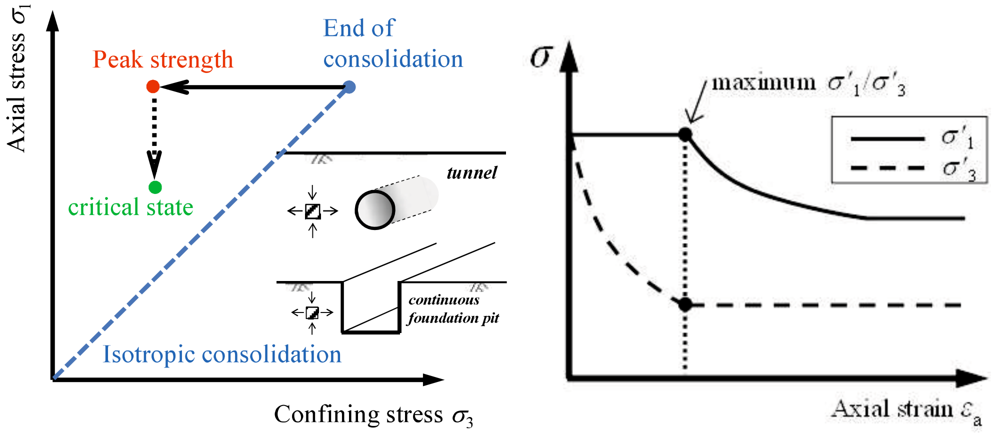

(b) PSCD test

Figure 2.1 Stress paths of the two compression tests

2.2 Experimental set-up

2.2.1 Test apparatus

The plane strain compression test apparatus used in this study is shown in Fig. 2.2. Each specimen has a width of 60 mm, a depth of 80 mm, and a height of 160 mm, approximately. An axial load was applied at the top of the specimen and grease was painted on the front and back planes of the specimen in the direction of zero strain to reduce friction. The intermediate principal stress cannot be measured in this study. Photos of the front plane of specimens were taken during the shearing process to observe local deformations of the specimens (Fig. 2.3). Some black points were pasted on the surface of membrane to enhance the accuracy of image analysis. The latex membrane used in the tests has a thickness of 0.3 mm and is quite smooth. Alshibli and Sture (2000) performed the triaxial tests using a comparable membrane under a low confining pressure of 15 kPa and concluded that the membrane influence on the test results is expected to be negligible. Therefore, a limited membrane effect on the material behavior is assumed in this study.

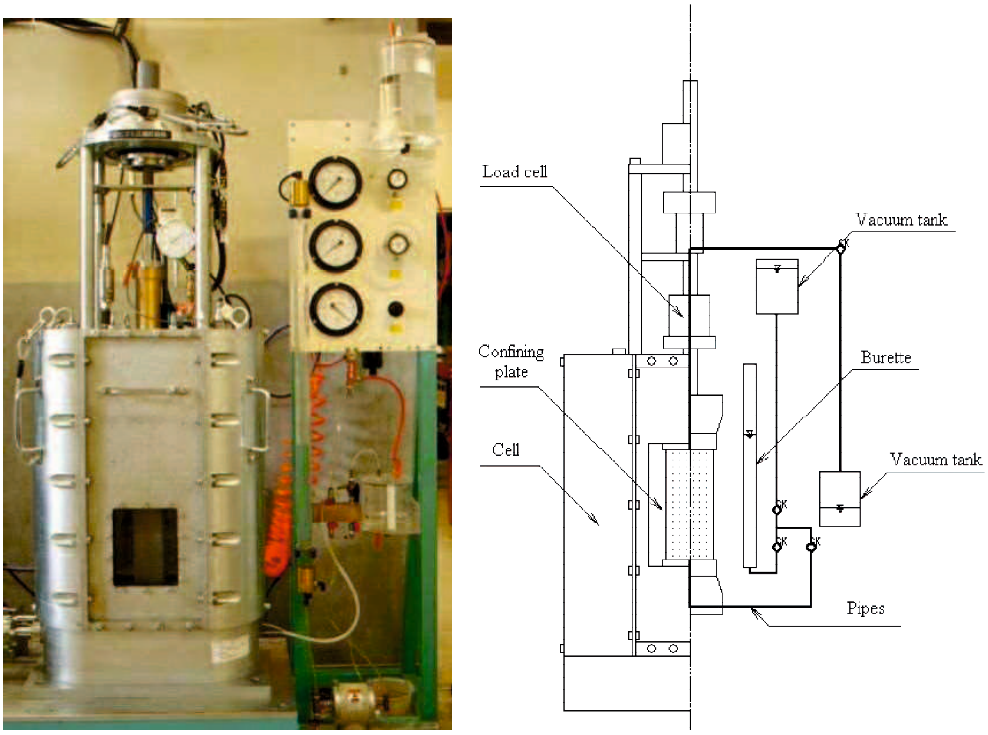

Figure 2.2 Plane strain compression test apparatus: (a) photograph; (b) sketch

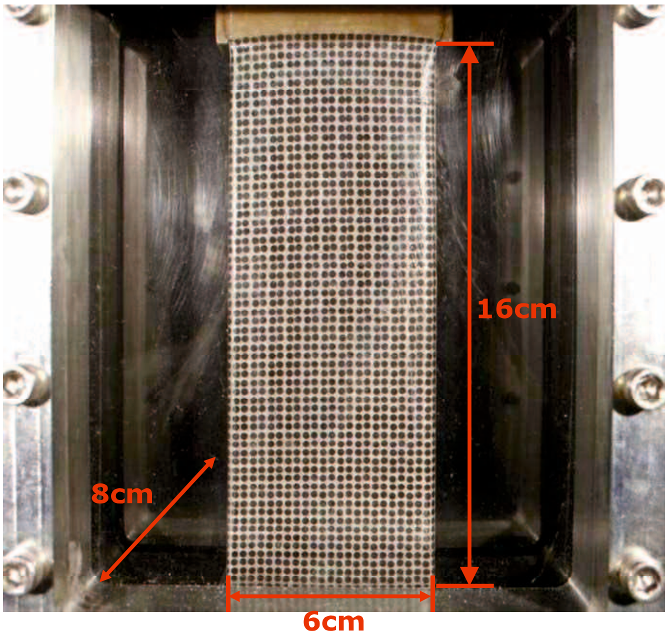

Figure 2.3 Installed specimen

2.2.2 Test materials and methods

Four types of materials consisting of two silica sands and two glass beads were used and these are referred to in this paper as Ube NO.6A sand, Toyoura sand, Glassbead1 and Glassbead2, respectively. The first three materials have similar mean particle sizes (D_{50}≈0.2 mm) with different uniformities, while Glassbead2 consists of quite uniform glass beads with much bigger particle sizes. Physical properties of the materials are summarized in Table 2.1. Ube No. 6A and Toyoura sands mainly consists of angular and subangular grains, respectively, and the particle shapes of the two glass beads are rounded, as shown in the photos (Figs. 2.5(a)−(d)) taken using scanning electron microscope (SEM). The aspect ratio (A_r: the ratio of length to width of a particle) and roundness (R_c: a measure of circularity of a particle; equation given in Table 2.1) were calculated for particles with its mean grain size (D_{50}) from the SEM images. Fig. 2.6 shows an example of how to measure the geometric size of particles. The aspect ratios is 1.3~2.3 for the Ube NO.6A sand with the mean value of about 1.8, and is 1.1~2.1 for the Toyoura sand with the mean value of about 1.5. For the two glass beads materials, the aspect ratio is exactly 1.0. The sands and glass beads are not reused in each test to avoid possible changes of particle surface characteristics, such as shapes or abrasion especially in beads.

Table 2.1 Physical properties of the four materials

Material	G_s	D_{50} (mm)	e_{max}	e_{min}	Aspect ratio $A_r = a/b$	Roundness $R_c = L^2/4\pi A$
Ube No.6A sand	2.60	0.215	1.044	0.623	1.1~2.44	1.2~2.0
Toyoura sand	2.65	0.205	0.976	0.635	1.16~2.27	1.09~1.84
Glassbead1	2.50	0.200	0.742	0.569	1.0	1.0
Glassbead2	2.50	1.072	0.689	0.571	1.0~1.04	1.01~1.05

Note: G_s is the specific gravity; D_{50} is the mean grain size; e_{max} and e_{min} are the maximum and minimum void raios; a and b are the length and width of a particle; and L and A are the perimeter and area of the projection of particles.

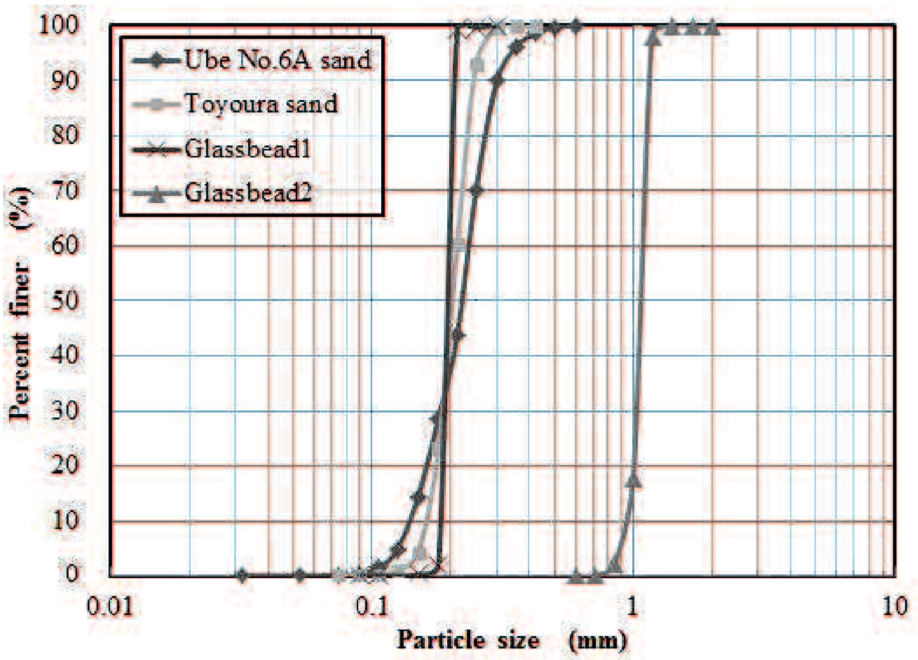

Figure 2.4 Particle size distributions of the four materials

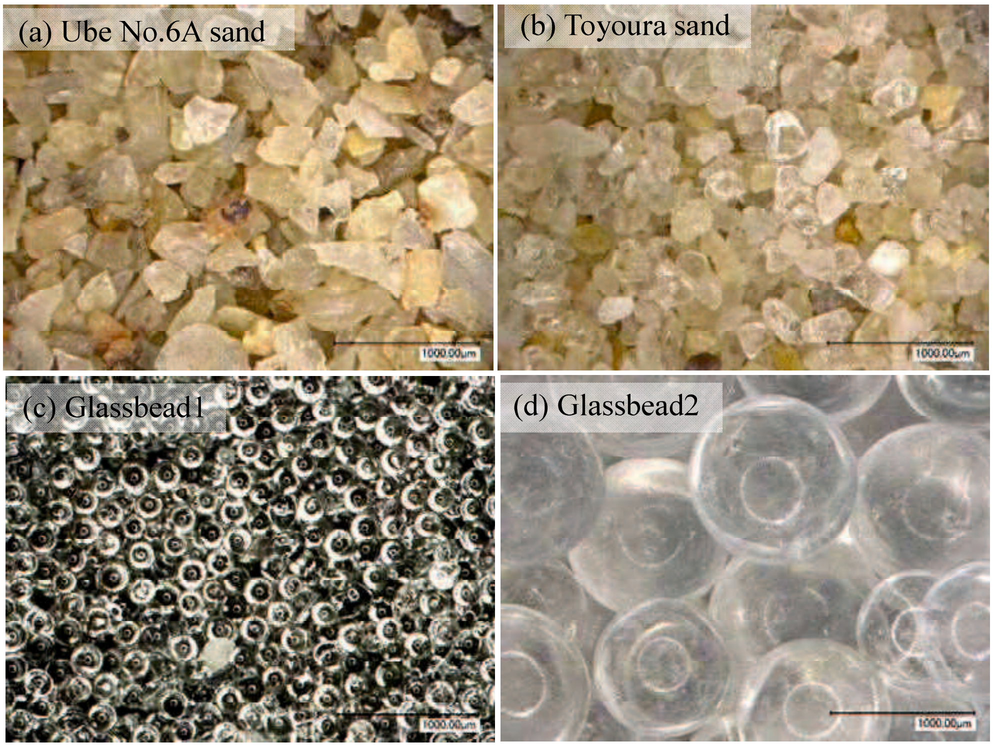

Figure 2.5 SEM photos of the four materials

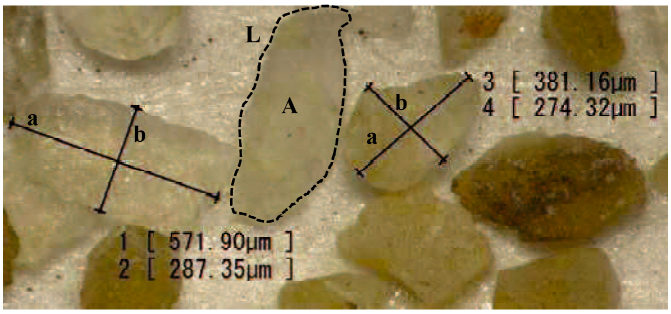

Figure 2.6 Measurement of geometry sizes of particles [the symbols (**a**, **b**, **L**, and **A**) in the figure are the same notations in Table 2.1]

Dense specimens were prepared by air pluviation method maintaining a constant falling height of 125 cm, while loose specimens were made using the same funnel but with almost zero falling height. The initial void ratio (e_0), void ratio after consolidation (e_c), and initial relative density (D_r) are listed in Table 2.2. For the four different materials, dense samples were prepared at their maximum possible relative densities by applying the maximum possible manageable falling distances. For the maximum possible falling heights, however, only Ube No.6A sand with the most angular particle shape produced a much lower relative density (around 52%) compared to those of the other three materials. Therefore, a little bit of compaction is done on the Ube No.6A sand specimen by hitting on the side platens (steel model) of specimen uniformly using a small rubber hammer to prepare denser specimens. However, the final obtained relative density of dense Ube No.6A sand was about 73%, which is approximately lower by 10% compared to those of the other materials.

To saturate the specimens, de-aired water was flushed through the specimens and then a back pressure of 50 kPa was applied. All the specimens were isotropically consolidated and were sheared under drained condition until a global axial strain of about 12%. The volumetric strain was obtained by measuring the water level in a burette with a differential pressure transducer.

For each kind of material, two PSC tests on dense and loose specimens were performed at a constant axial displacement rate of 0.1 mm/min and a constant confining pressure of 50 kPa. Three PSCD tests under initial consolidation pressures of 50 kPa, 100 kPa or 200 kPa were performed on dense specimens, and one PSCD test under confining pressure of 100 kPa was performed on loose specimens. In all the PSCD tests, the confining pressures were decreased at a loading rate within 1-3 kPa/min and smaller decrement of loading rate was taken near the failure. Specimen and test conditions are summarized in Table 2.2.

Table 2.2 Summary of specimen and test conditions

Material		Test type	Relative density D_r (%)	Initial void ratio e_0	Void ratio e_c	Effective consolidation pressure σ_{c0}' (kPa)
Ube No.6A sand	U-1	PSC	73.4	0.735	0.721	50
	U-2	PSCD	72.7	0.738	0.729	50
	U-3	PSCD	73.6	0.734	0.711	100
	U-4	PSCD	73.9	0.733	0.673	200
	U-5	PSC	22.8	0.948	0.943	50
	U-6	PSCD	21.6	0.953	0.917	100
Toyoura sand	T-1	PSC	85.6	0.684	0.681	50
	T-2	PSCD	75.1	0.72	0.701	50
	T-3	PSC	79.8	0.704	0.671	100
	T-4	PSCD	82.4	0.695	0.673	200
	T-5	PSC	24.9	0.891	0.881	50
	T-6	PSCD	24	0.894	0.885	100
Glassbead 1	G1-1	PSC	82.1	0.6	0.596	50
	G1-2	PSCD	82.1	0.6	0.596	50
	G1-3	PSC	78	0.607	0.599	100
	G1-4	PSCD	76.3	0.61	0.596	200
	G1-5	PSC	16.8	0.713	0.705	50
	G1-6	PSCD	28.3	0.693	0.648	100
Glassbead 2	G2-1	PSC	89.8	0.583	0.575	50
	G2-2	PSCD	78.8	0.596	0.569	50
	G2-3	PSCD	96.6	0.575	0.549	100
	G2-4	PSCD	97.5	0.574	0.543	200
	G2-5	PSC	11	0.676	0.671	50
	G2-6	PSCD	12.7	0.674	0.608	100

2.3 Test results and analysis

Test results including macro stress-strain relationship and volume changes were mainly analyzed in this section. PSCD test results were especially compared with PSC test results. Confining pressure and relative density influences were investigated.

2.3.1 Comparison of shear behavior of the four dense materials in the PSC test

Developments of the effective principal stress ratio and volume change with axial strain of the four materials at the same consolidation pressure of 50 kPa are compared in Fig. 2.7 for dense specimens. Here, the principal stress ratio R is defined as σ'_1/σ'_3, the ratio of effective vertical stress σ'_1 and effective confining stress σ'_3.

In Fig. 2.7, all the materials gave typical results of dense granular materials showing gradually increasing strength until the peak and then softening. R shows high to low values from Ube No.6A sand to Glassbead2. Dilation in Glassbead1 and Glassbead2 happened earlier than that in Toyoura sand, which is also earlier than that in Ube No.6A sand. Dilation angle measured around the peak strength is 20.5°, 19.2°, 19.2° and 16.2° in the four types of material, respectively. Here, the dilation angle is calculated by:

$$\Psi = \sin^{-1}[(d\varepsilon^p_1 + d\varepsilon^p_3) / |(d\varepsilon^p_1 - d\varepsilon^p_3)|] \qquad (2.1)$$

where ε^p_1 and ε^p_3 are the major and the minor plastic principal strains.

It is inferred that the most irregularity of particle shape of Ube No.6A sand contributes to the highest dilation angle, even if its relative density is the lowest in the four dense specimens. Alshibli et al. (2000) also reported that the dilatancy angles of sands are greater for more angular grains.

Moreover, compared with Glassbead1, Glassbead2 clearly shows later peak strength and the curve from the peak to the residual state is less steep.

This means the localization process is slower in Glassbead2 than that in Glassbead1. The difference resulted from particle size effect and this will be discussed in later section 2.4.

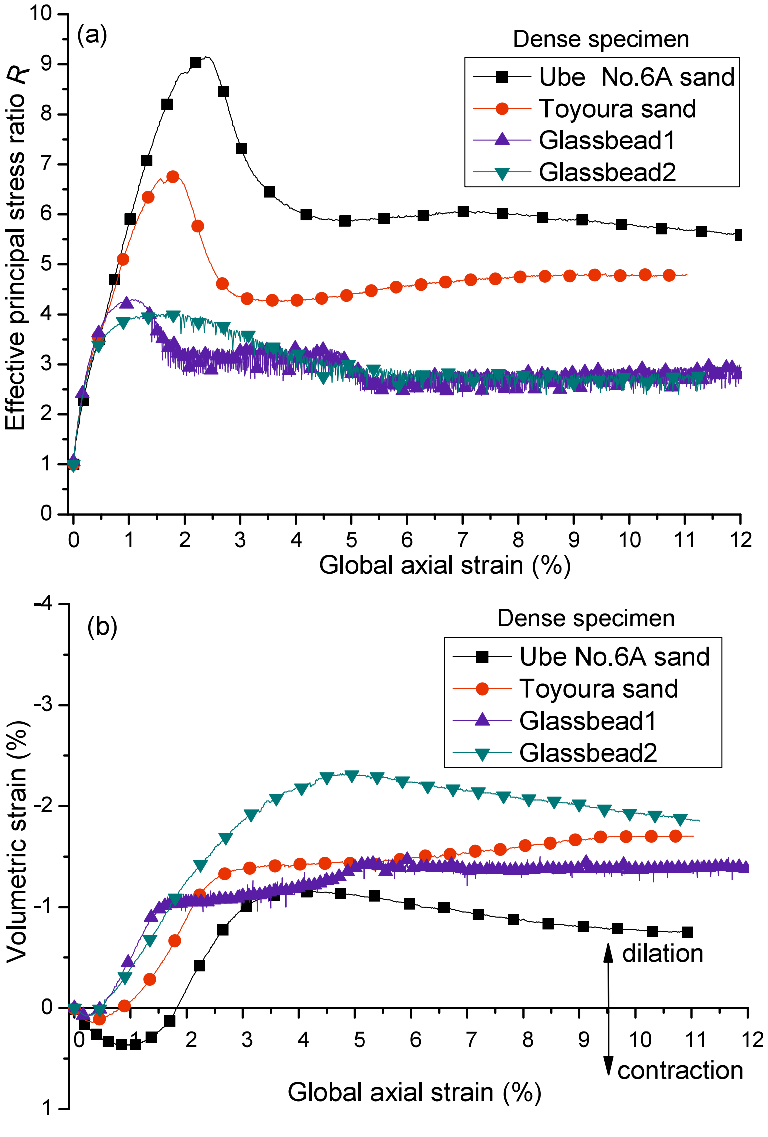

Figure 2.7 Comparison of shear stress, strain behavior of the four dense specimens in the PSC test: (a) principle stress ratio ~ global axial strain; (b) volumetric strain.

2.3.2 Comparison of shear behavior of dense specimens in PSC and PSCD tests

Figure 2.8 shows the effective principal stress ratio R verses the deviatoric strain relationships in both PSC and PSCD tests for each material. Here, the deviatoric strain ε_q is defined by:

$$\varepsilon_q = \sqrt{\frac{2}{9}[(\varepsilon_1 - \varepsilon_2)^2 + (\varepsilon_2 - \varepsilon_3)^2 + (\varepsilon_3 - \varepsilon_1)^2]} \qquad (2.2)$$

where ε_1 and ε_3 are approximated by the global vertical and lateral strain separately and ε_2=0.

The maximum effective principal stress ratio $R_{\max}$, peak frictional angle ϕ_p, peak dilation angle Ψ_p and secant modulus $E_{0.03}$ in each case, were listed and compared in Table 2.3. Ψ_p is calculated according to Eq. (2.1) using the parameters at the peak strength. ϕ_p and $E_{0.03}$ are calculated by:

$$\varphi_p = \sin^{-1}[(\sigma'_1-\sigma'_3)/(\sigma'_1+\sigma'_3)]_{\max} \qquad (2.3)$$

$$E_{0.03} = [(\sigma'_1-\sigma'_3)/\varepsilon_1]_{\varepsilon 1=0.03\%} \qquad (2.4)$$

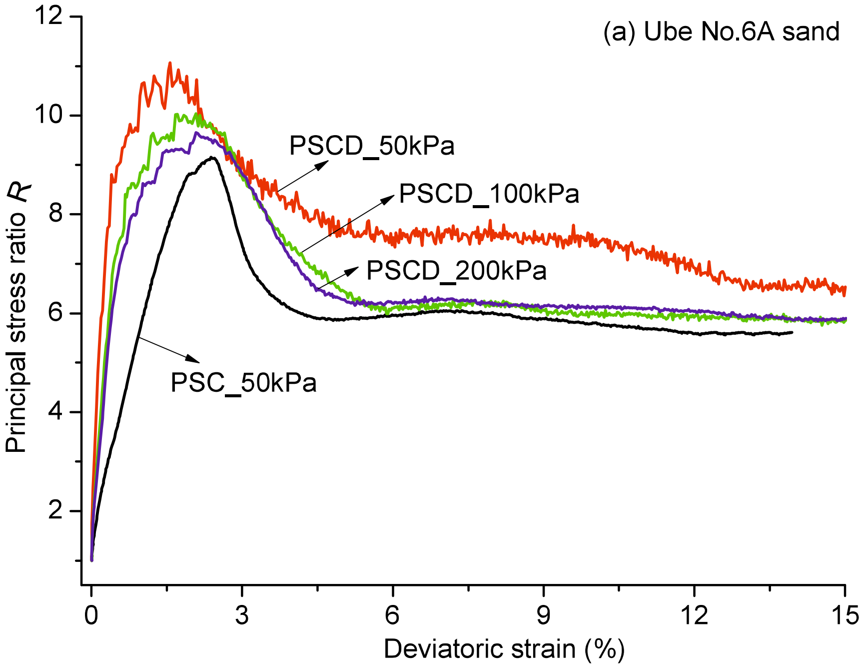
(a) Ube No.6A sand
Principal stress ratio R
Deviatoric strain (%)
0
3
6
9
12
15
2
4
6
8
10
12
PSCD_50kPa
PSCD_100kPa
PSCD_200kPa
PSC_50kPa

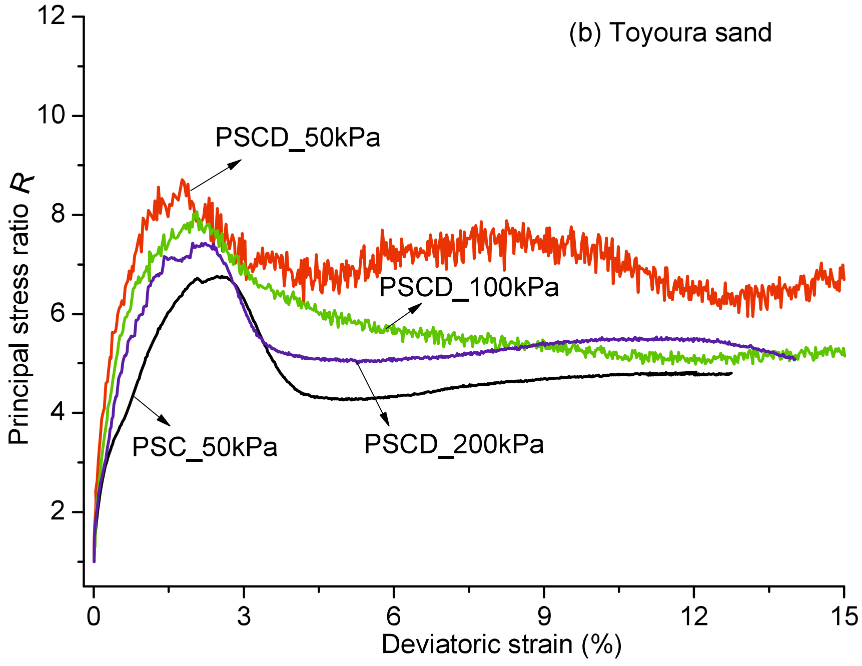
(b) Toyoura sand
Principal stress ratio R
Deviatoric strain (%)
0
3
6
9
12
15
2
4
6
8
10
12
PSCD_50kPa
PSCD_100kPa
PSCD_200kPa
PSC_50kPa

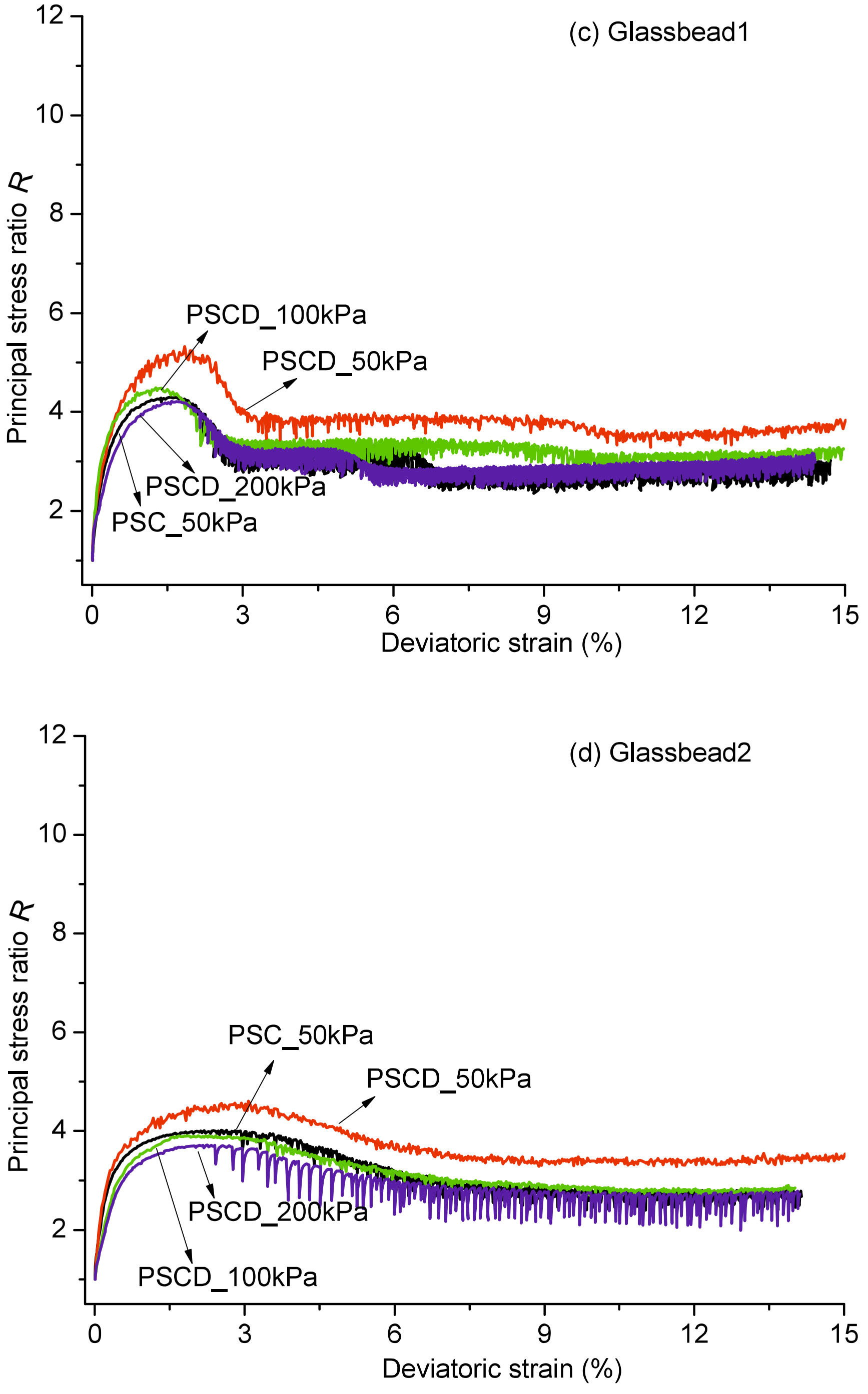

Figure 2.8 Principal stress ratio – deviatoric strain relationships in the four types of material

Table 2.3 Summary of test results

Material		Test type	Relative density D_r (%)	Maximum principal stress ratio R_{max}	Peak friction angle ϕ_p (°)	Peak dilation angle Ψ_p (°)	Secant modulus $E_{0.03}$ (MPa)
Ube No.6A sand	U-1	PSC	73.4	9.1	53.3	20.5	51.8
	U-2	PSCD	72.7	11.0	56.4	24.2	108.6
	U-3	PSCD	73.6	10.0	54.9	23.0	136.9
	U-4	PSCD	73.9	9.6	54.2	21.1	314.9
	U-5	PSC	22.8	5.0	41.8	0.0	20.8
	U-6	PSCD	21.6	6.0	45.6	5.7	84.0
Toyoura sand	T-1	PSC	85.6	6.8	48.0	19.2	65.4
	T-2	PSCD	75.1	8.7	52.5	18.1	81.0
	T-3	PSCD	79.8	8.0	51.1	17.7	111.1
	T-4	PSCD	82.4	7.4	49.6	17.7	252.5
	T-5	PSC	24.9	3.8	35.7	0.0	32.1
	T-6	PSCD	24	4.4	39.0	4.0	72.2
Glassbead1	G1-1	PSC	82.5	4.3	38.5	19.2	56.3
	G1-2	PSCD	82.1	5.2	42.6	18.3	62.4
	G1-3	PSCD	78.5	4.5	39.5	17.8	114.6
	G1-4	PSCD	76.3	4.2	38.0	16.8	241.6
	G1-5	PSC	16.8	2.9	29.2	4.0	54.6
	G1-6	PSCD	28.3	2.7	27.4	4.0	96.3
Glassbead2	G2-1	PSC	89.8	4.0	36.9	16.2	70.0
	G2-2	PSCD	78.8	4.5	39.5	15.1	73.4
	G2-3	PSCD	96.6	3.9	36.3	15.1	98.8
	G2-4	PSCD	97.5	3.7	35.1	15.1	195.1
	G2-5	PSC	11	2.7	27.4	2.2	51.1
	G2-6	PSCD	12.7	3.1	30.8	2.2	67.8

There are several findings from Fig. 2.8 and the listed values in Table 2.3. First, all the three specimens in the PSCD test showed clearly higher stiffness (R/ε_q) before the peak, and earlier peak stress ratio than those in the PSC test for both the two sands. However, this was not found for the two glass beads. The R - ε_q curves in the PSC test and in the two PSCD tests under σ'_{c0} = 100 kPa, 200 kPa almost overlapped in both the two glass beads. The relationships between deviator stress q (= σ'_1-σ'_3) and axial strain are shown in Fig. 2.9. The two sands especially Ube No.6A sand showed almost linear stress-strain behavior up to 1% axial strain in the PSC test, while they behaved nonlinearly in the PSCD test when 0.1% axial strain was exceeded. This means that stiffness degradation is quicker in the PSCD test than in the PSC test for sands. However, this is less noticeable for the two glass beads.

Second, variation of peak strength with confining pressure in the three PSCD tests is also different. In general, R_{max} decreased with increasing stress level in both sands and glass beads. However, variations of R_{max} are more significant in Ube No.6A sand (R_{max} = 11.1, 10.0, 9.1) than those in Toyoura sand (R_{max} = 8.7, 8.0, 7.4). R_{max} in glass beads is clearly higher under σ'_{c0} = 50 kPa while there is little variation when σ'_{c0} increased from 100 kPa to 200 kPa. It should also be noted that stick-slip of glass beads is more remarkable under higher stress level. Then, the peak appeared earlier with decreasing confining stress in the two sands but not in the glass beads.

Third, the after-peak stress-strain behavior in the two sands varied differently under different test conditions while it showed quite similar behavior in the two glass beads.

Fourth, according to values of secant modulus $E_{0.03}$ listed in the Table 2.3, it is known that $E_{0.03}$ is higher in the PSCD tests than that in the PSC test for both dense and loose specimens for each material. $E_{0.03}$ also increased with increase of confining pressure in the PSCD test.

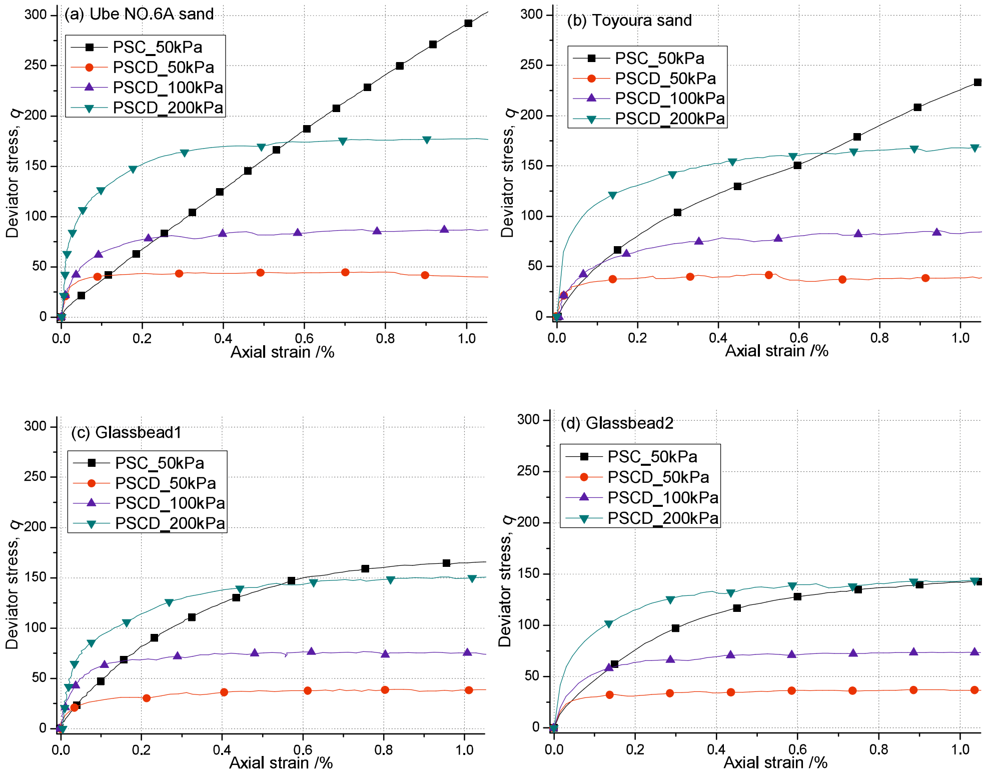

Figure 2.9 Deviator stress – global axial strain relationships within 1% axial strain in dense specimens under different test conditions

Figure 2.10 shows volumetric strain variations with deviatoric strain in dense specimens of the four types of material. It is found that volume response in the PSCD test is different from that in the PSC test at the beginning of shearing. Volume expansion happened instead of contraction due to stress release. Dilation developed gradually due to shearing and dilation angle reached the maximum value at the peak strength. It can also be known from Figs. 2.10(a), (b) that before the peak strength, at the same global axial strain, total volumetric strains of sand specimens in the three PSCD tests are higher than that in the PSC test. Under the plane strain condition, this means more lateral extension was generated in the PSCD test than that in the PSC test for the two sands.

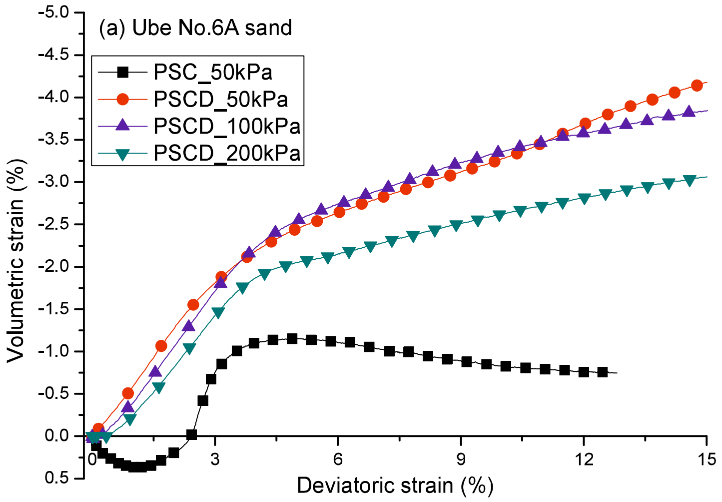
(a) Ube No.6A sand
PSC_50kPa
PSCD_50kPa
PSCD_100kPa
PSCD_200kPa
Volumetric strain (%)
-5.0
-4.5
-4.0
-3.5
-3.0
-2.5
-2.0
-1.5
-1.0
-0.5
0.0
0.5
0
3
6
9
12
15
Deviatoric strain (%)

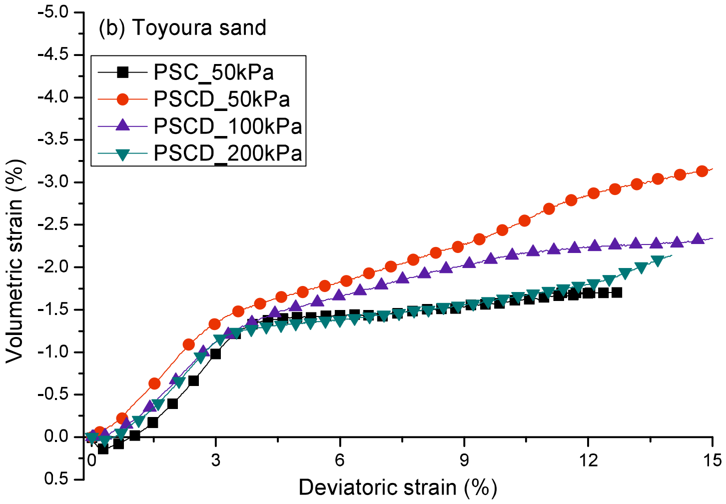
(b) Toyoura sand
PSC_50kPa
PSCD_50kPa
PSCD_100kPa
PSCD_200kPa
Volumetric strain (%)
-5.0
-4.5
-4.0
-3.5
-3.0
-2.5
-2.0
-1.5
-1.0
-0.5
0.0
0.5
0
3
6
9
12
15
Deviatoric strain (%)

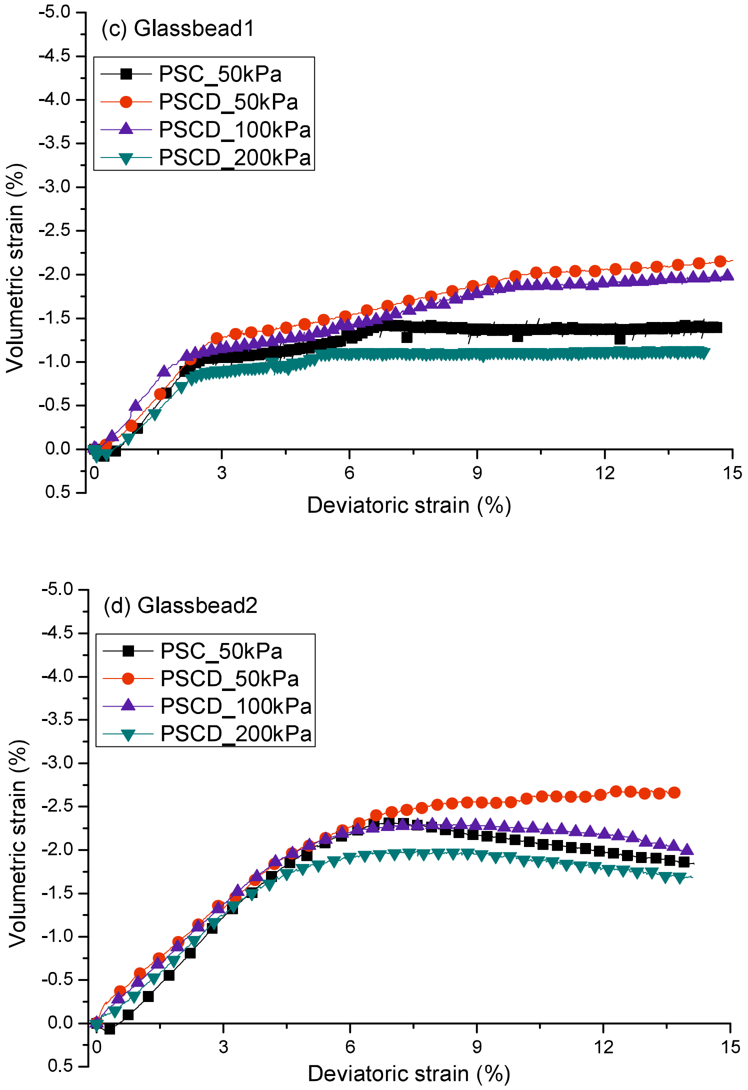

Figure 2.10 Volume responses in the four types of material

From the Table 2.3, it is known that the dilation angle is no more than 50% of mobilized frictional angle at the peak. The percentage is 38 - 43% for Ube No.6A sand, 34 - 40% for Toyoura sand, 43 - 50% for Glassbead1 and 38 - 44% for Glassbead2, respectively. It has been noted that the mobilized angle was composed of several contributors including internal particle friction, dilation, particle rearrangement and probably particle interlocking (Guo and Su 2007). Moreover, it is found that the peak dilation angle decreased with increasing consolidation pressure in the three PSCD tests, except that Glassbead2 showed the same value. The peak dilation angle decreased from 24.2° to 21.1° in Ube No.6A sand, while it only changed 0.4° in Toyoura sand and 1.5° in Glassbead1. This also indicates that the Ube No.6A sand with the most irregular particle shape is most vulnerable to stress level change.

The p'-q relationship in the PSC and PSCD tests were shown in Fig. 2.11. Here, $p' = (\sigma'_1+\sigma'_3)/2$. Two lines were drawn in each figure for different materials. The dashed line noted as "$q_{\max}$ line" connected the points at the peak deviator stress in each test, while the solid line noted as "critical line" connected the points at the residual stress. In general, for each material, the four curves under different test conditions arrived at the same $q_{\max}$ line or critical line approximately.

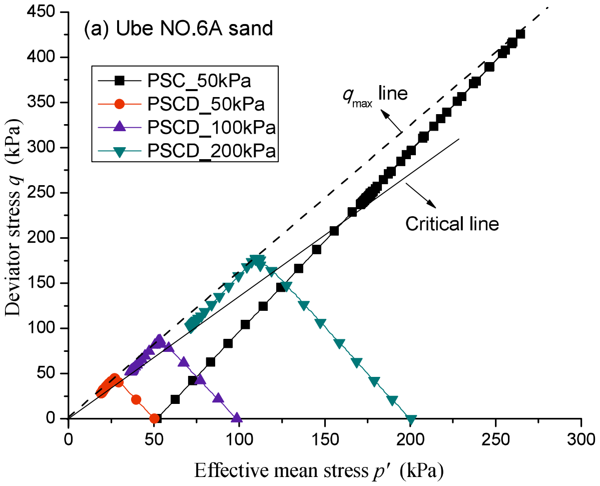

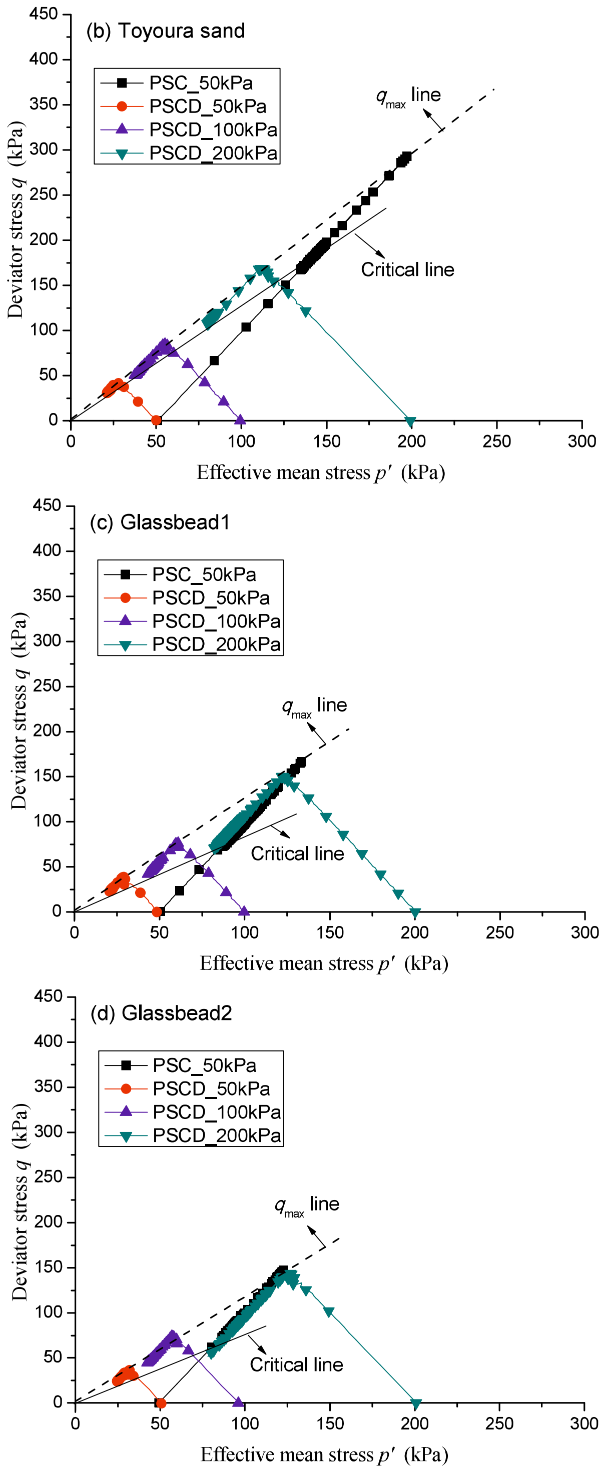

Figure 2.11 $q - p$' relationships in the four types of material

2.3.3 Comparison of shear behavior in PSC and PSCD tests between dense and loose specimens

Following the same way in section 2.3.2, test results on loose specimens were summarized and they were compared with the results of dense specimens, as shown in Fig. 2.12. In each subfigure, it is shown two PSC tests under σ'_{c0} = 50 kPa and two PSCD tests under σ'_{c0} = 100 kPa in dense and loose specimen, separately. In general, there is also difference between R-ε_q curves of PSC and PSCD tests in loose sand specimens. However, the difference was thought smaller than that in dense specimens. The overall R-ε_q curves and volumetric strain change produced from the PSC and PSCD tests for the two loose glass beads specimens were quite similar.

The volumetric responses were quite dependent on both the stress paths and the relative density, especially in sands. As seen from the PSC test results in Fig. 2.7, as typically known, a dense specimen slightly contracts initially due to an increase in mean effective stress, and then dilation becomes dominant until the specimen reaches the residual state; while a loose specimen mostly exhibits a contractive behavior during shearing. For a specimen of the PSCD test, a small amount of expansion occurs because of a decrease in confining stress and a subsequent decrease in mean effective stress. Therefore, in the current study, the dense specimens expanded instead of being contracted in the beginning of shearing. For the loose specimens, the expansion amount was less than the contraction amount at the beginning of shearing, and therefore loose specimens initially showed contractive behavior in the PSCD test as well as in the PSC test. The dilation angle of loose specimen is 0 in the PSC test, while it is 5.7 and 4.0 in the PSCD test for the two sands separately. This is because that the mean stress in the PSCD test is lower than that in the PSC test, and specimen dilates easier under a low stress condition.

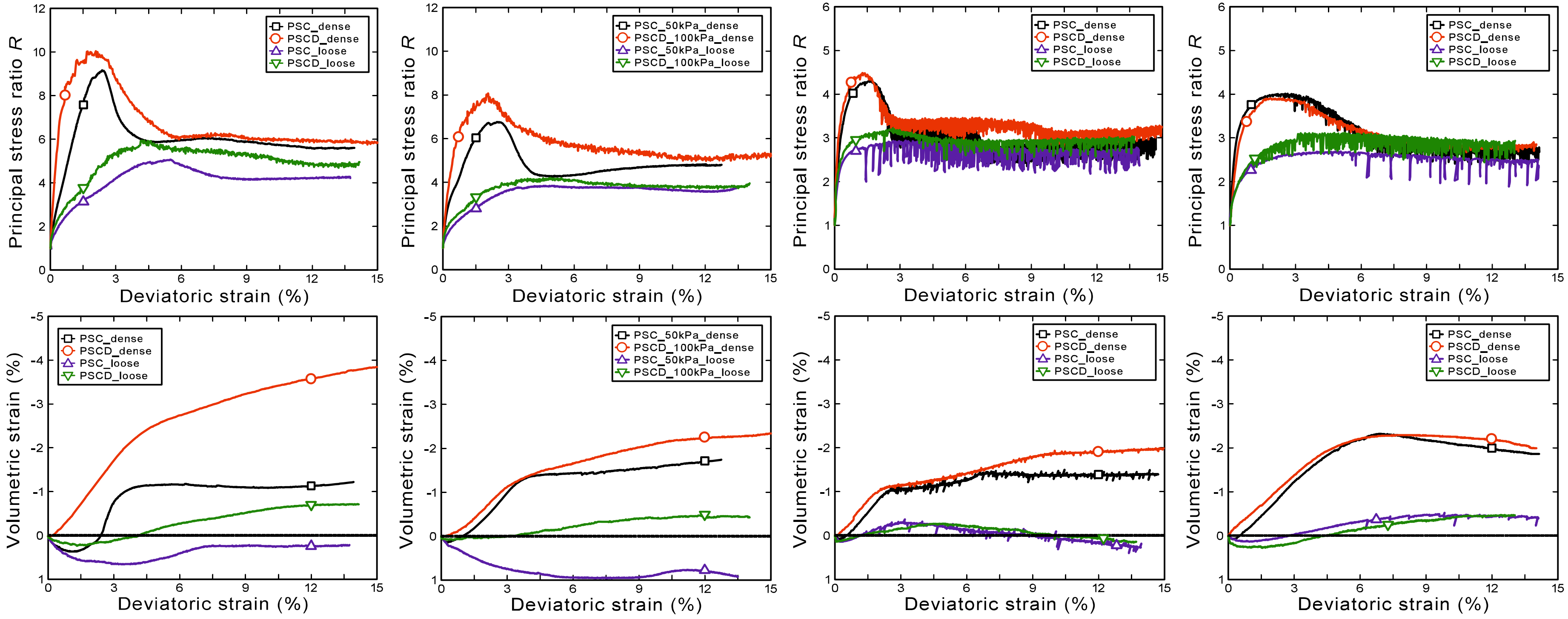

(a) (b) (c) (d)

Figure 2.12 Comparison of stress, strain behavior of dense and loose specimens: (a) Ube No.6A sand; (b) Toyoura sand; (c) Glassbead1; (d) Glassbead2

2.3.4 Summary of test results

From the above test results, it is clearly found that unloading shear behavior in PSCD test is different from that in PSC test, and the difference varies in different materials and also depends on relative density. It can be inferred that particle shape has a significant influence on the shear behavior, and the more angular particle shape makes the macro stress-strain behavior more sensitive to the stress level and stress path. In the subsequent sections, local deformation developments and shear band patterns in the specimens and particle shape effects are examined by image analysis.

2.4 Local deformation by digital image correlation analysis

To observe the developments of local deformations, photos of the specimens were taken during the shearing and were analyzed using the photogrammetry method.

2.4.1 Digital image correlation method

The photogrammetry method used in this study follows the technique introduced by White et al. (2003). This method is originated from the PIV (Particle Image Velocimetry) method, and a cross-correlation function is used to trace the deformation of the material based on the photos. Therefore, it is also called DIC (Digital Image Correlation) method. The DIC method has been proven to have a reasonable accuracy in measuring the soil (or particle) deformation and to be very useful to investigate shear band patterns (Desrues and Viggiani 2004, Hall et al. 2010, Rechenmacher 2006).

In order to illuminate the specimens, two 500-Watt LED lights were installed symmetrically in front of the observation window. Photos were taken using a digital camera with a 35 mm focal length. Geometric correction was implemented to reduce errors induced by lens distortion. The procedure of tracking specimen deformation is as follows: First, geometric correction is done by taking a photo of the grid of nodes with a fixed node spacing of 10 mm. In this study, approximately 300 nodes are included in the image used for the correction. The corrected photos have a scale of about 0.07-0.09 mm/pixel. The error between the artificial node locations and their corresponding locations analyzed by DIC is no more than 0.1 pixel. Then, node points of interest with a spacing of 20 pixel between each other are selected inside the first photo and their coordinates are specified. For a node of interest, a square standard pattern with its size of 20 pixels by 20 pixels is generated and its center located at the node. The mean gray scale of the standard pattern is calculated to keep track of the movement of the center point of the standard pattern. Third, since locations of selected points change in the next taken photo due to shear deformation, new positions of the points will be decided by searching new standard patterns having similar grey scale with previous ones. The photographic coordinates of the node points are computed at an accuracy of 0.1 pixel by applying the Gaussian distribution or the quadratic curve to the longitudinal and lateral distribution of the correlation coefficients in the pixels which have the maximum correlation coefficients in the regions recognized as the node points (Kikkawa *et al.* 2006). A cross correlation method is used, and the cross correlation coefficient is calculated by the following equation:

$$R_c = \frac{\sum_{j=0}^{N-1}\sum_{i=0}^{M-1}\left(f[i,j]-\overline{f}\right)\left(s[i,j]-\overline{s}\right)}{\sqrt{\sum_{j=0}^{N-1}\sum_{i=0}^{M-1}\left(f[i,j]-\overline{f}\right)^2}\sqrt{\sum_{j=0}^{N-1}\sum_{i=0}^{M-1}\left(s[i,j]-\overline{s}\right)^2}} \tag{2.5}$$

where $f\,[i,j]$ is the grey scale of a single pixel in the standard pattern, $\overline{f}$ is the mean grey scale of the standard pattern, $s[i,j]$ is the grey scale of a single pixel in the unknown pattern, $\overline{s}$ is the mean grey scale of the unknown pattern, M and N are the pixel sizes of the decided standard patterns in the vertical and horizontal directions.

When the new coordinates of the selected points are determined, total displacements of the selected points at each shearing stage can be calculated by comparing the new coordinates with the original corresponding coordinates of the initial image. Finally, four-noded isotropic elements are used to determine the strains of the specimen based on the finite element method. Comparing the observed total displacement of the top platen with the corresponding measured displacement predicted by the DIC analysis, it is found that the maximum error in the estimation of the top platen displacement is no more than 0.6 mm for which the total axial displacement was 20 mm. The error of 3% (0.6 mm divided by 20 mm) could be assumed reasonably small; therefore, the DIC method used in this study is considered a reasonable technique to measure local deformations of the specimens.

2.4.2 Local lateral deformation

Lateral strain distributions in the specimens are compared at the same global axial strain ε_a (near the peak strength) for each material, as shown in Figs. 2.13~2.16. Here, '+' represents compression and '-' represents extension. (a), (b), (c) and (d) represent test conditions of PSC test with σ'_{c0}=50 kPa and PSCD tests with σ'_{c0}=50 kPa, σ'_{c0}=100 kPa and σ'_{c0}=200 kPa respectively. Butterfly shaped distribution was found in both sands and glass beads. They are more symmetrical in the two glass beads compared to those in the two sands. For each specimen, local lateral deformation showed almost extension. For the Ube No.6A sand, local extension in the PSC test (Fig. 2.13(a)) is seen clearly less than those in the PSCD tests (Figs. 2.13(b)~(d)).

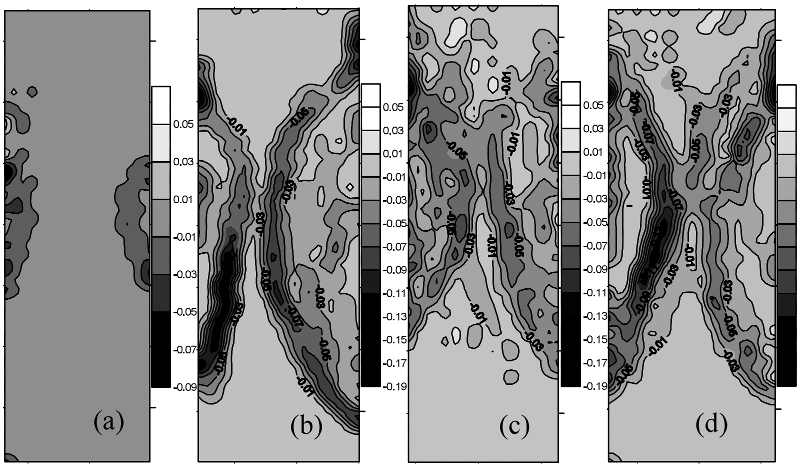

Figure 2.13 Local lateral strain distributions in Ube No.6A sand (ε_a=2%)

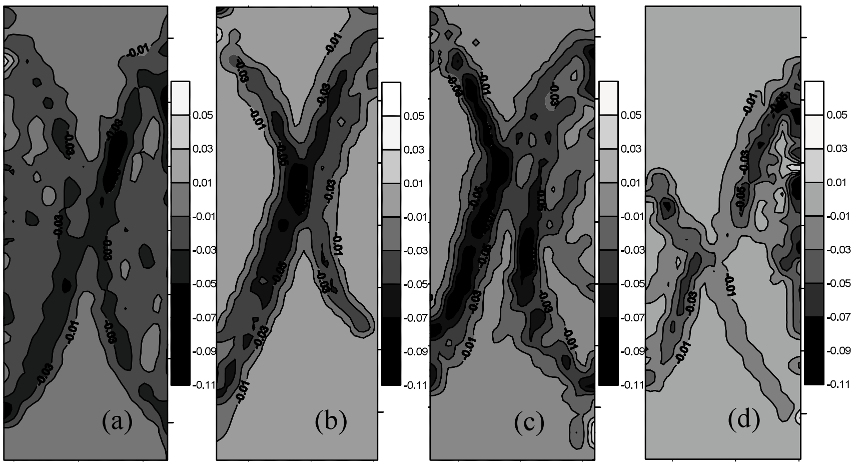

Figure 2.14 Local lateral strain distributions in Toyoura sand (ε_a=1.5%)

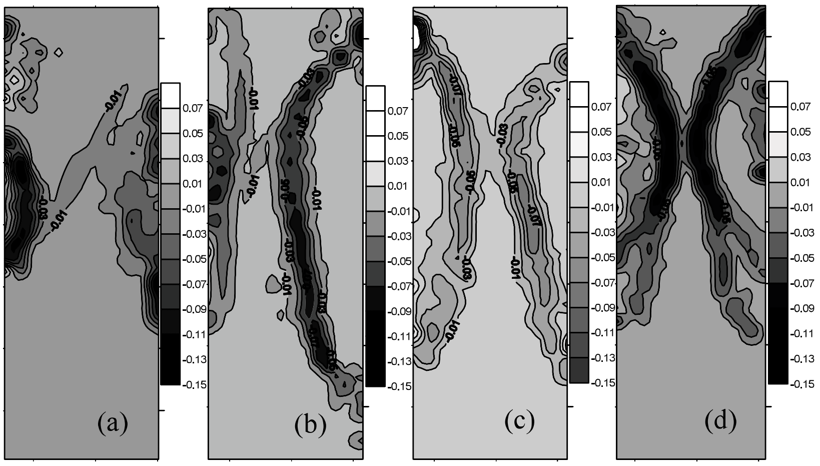

Figure 2.15 Local lateral strain distributions in Glassbead1 (ε_a=1.2%)

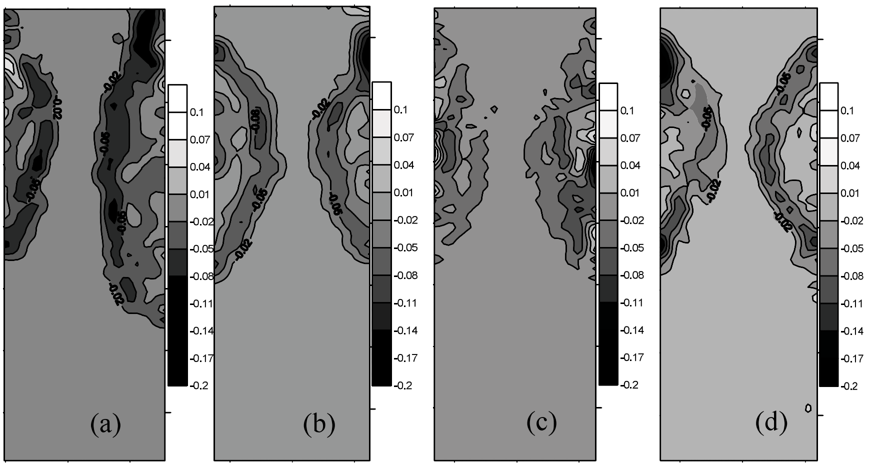

Figure 2.16 Local lateral strain distributions in Glassbead2 (ε_a=1.5%)

2.4.3 Shear band evolution and shear band thickness

In this study, shear bands were captured from the maximum shear strain distributions based on the image analysis. The maximum shear strain $\gamma_{\max}$ is calculated as:

$$\gamma_{\max} = \sqrt{\left(\varepsilon_x - \varepsilon_y\right)^2 + \gamma^2_{xy}} \tag{2.6}$$

where ε_x, ε_y, and γ_{xy} are the horizontal, vertical, and shear strains of a divided element in the observed plane, respectively.

According to the observations, double shear bands were finally generated in all the glass beads specimens, while both single and double shear bands were commonly found in sand specimens. For all the specimens under different test conditions, shear bands evolutions have similar but distinct ways. Shear bands developed with changing patterns during the whole shearing. The final shear bands are quite different from the initial ones, especially in sands. Fig. 2.17 shows a case of Toyoura sand in the PSCD test under σ'_{c0} = 100 kPa. Five stages were chosen including (a) at the peak, (b) - (d) typical stages and (e) at final state. It can be seen from Fig. 2.17(a) that several shear bands have been formed at the peak and they are quite nonuniform. Then, only the left-inclined band developed as shearing went on until 4.2% axial strain. After that the first shear band pattern had almost no change and a second shear band began to appear. The second one gradually evolved from discontinuous localized deformations and crossed with the first shear band. It grew wider and wider until the final state.

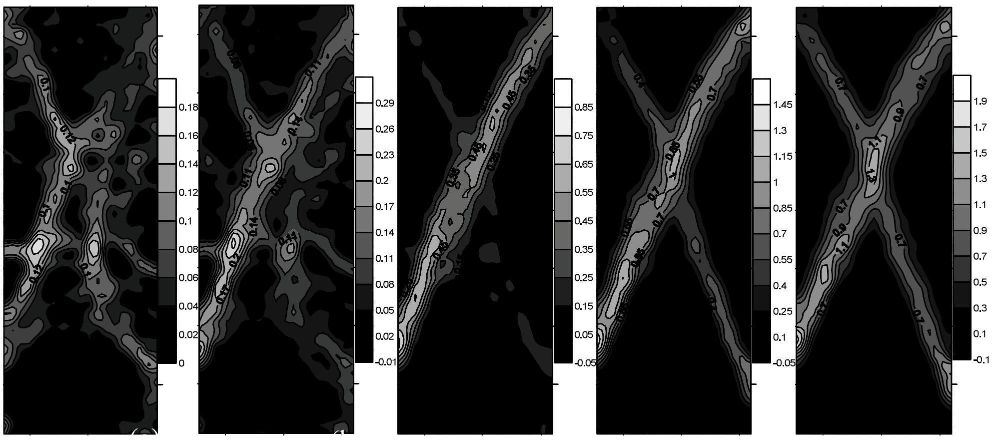

Figure 2.17 Shear band evolutions in the PSCD test of Toyoura sand, σ'_{c0} = 100 kPa: (a) ε_a = 1.5%; (b) ε_a = 2.0%; (c) ε_a = 4.2%; (d) ε_a = 8.2%; (e) ε_a = 12.0%

The above shear band evolutions are not limited to sands with irregular particle shapes. Similar case was also found in Glassbead1. Fig. 2.18 shows an example of the PSCD test under σ'_{c0} = 100 kPa. Symmetric shear bands have been formed at the peak with ε_a = 1.2%, however they changed immediately and only one shear band was clearly observed at ε_a = 1.6%. Then the shear band developed for a relatively long shearing period and a second shear band initiated at ε_a = 6.7%. After that development in the first shear band almost ceased and increased deformation was localized within the second one until the final state.

Although two shear bands were finally formed in all the four cases of Glassbead1, they were not developed at the same time. The second shear band appeared at the under part of specimens as shown in Fig. 2.18 in two of the four cases, and it appeared at a symmetric location of the first one in the other two cases (see Fig. 2.23(b) and (d)). Therefore, even for the Glassbead1 with very round particle shape and the relatively uniform narrow particle size distribution, shear bands are not always symmetric and they are hard to predict. However, for the Glassbead2 with almost five times of particle size of Glassbead1, symmetric and conjugate shear bands were always formed (see later Fig. 2.24).

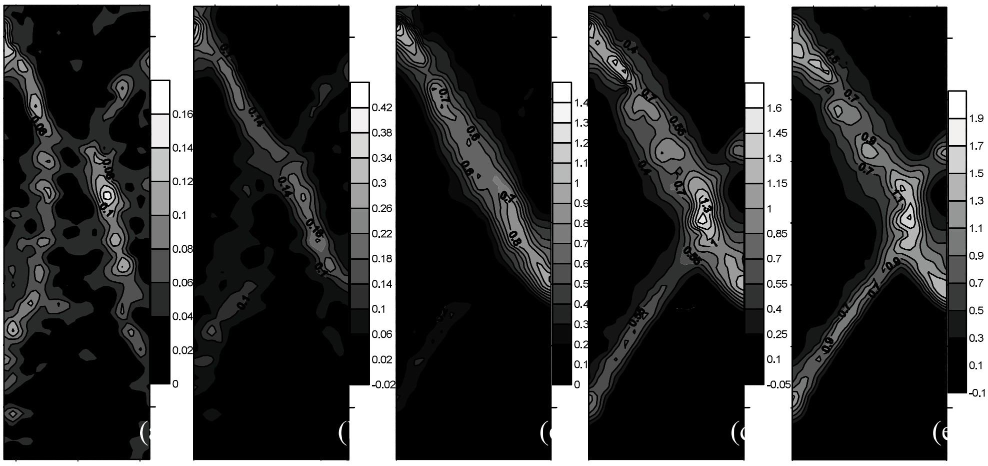

Figure 2.18 Shear band evolutions in the PSCD test of Glassbead1, $\sigma'_{c0} = 100$ kPa: (a) $\varepsilon_a = 1.2\%$; (b) $\varepsilon_a = 1.6\%$; (c) $\varepsilon_a = 6.7\%$; (d) $\varepsilon_a = 10.3\%$; (e) $\varepsilon_a = 12.0\%$

From Figs. 2.17 and 2.18, it can be seen that shear band is not perfectly uniform and its thickness changes at different places of specimen. To make comparison of shear band thickness of the four materials, the thicknesses were measured at the middle of the main shear bands or at slightly lower location from the intersection of two conjugate shear bands based on the maximum shear strain contours. Shear band thickness is measured according to the outermost contour lines of the main shear band based on the maximum shear strain contours. For the measurement purpose of the shear band thickness, the shear band is defined for which the local maximum shear strain γ_{max} exceeds 10%.

Figure 2.19 shows shear band thickness in dense specimens at about 12% axial strain for each material. Although the two sands and Glassbead1 have almost the same D_{50}, and Toyoura sand has very similar relative densities with Glassbead1, their shear band thicknesses are not always similar. Glassbead1 has larger shear band thickness than the two sands. This is because Glassbead1 has a very uniform size distribution and round particle shape compared with the two sands. When comparing the two glass beads with the similar uniform size distribution but different particle size, Glassbead2 shows clear higher thickness than Glassbead1. However, the shear band thickness is not proportional to the mean particle size. The D_{50} size of Glassbead2 is almost 5 times as that of Glassbead1 while the ratio of their shear band thicknesses is only about 1.1 - 1.4 times. The ratio of shear band thickness and the D_{50} size is not constant for different granular materials and it decreases significantly when grain size becomes very big. This was also reported by Desrues and Viggiani (2004). Moreover, it is clearly seen that shear band thickness decreases with the increase of confining pressure in the PSCD test for all the materials.

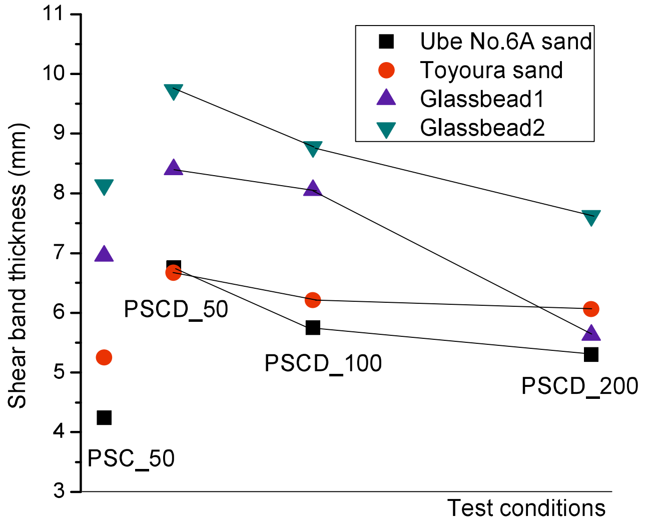

Figure 2.19 Comparison of shear band thickness in the PSC and PSCD tests

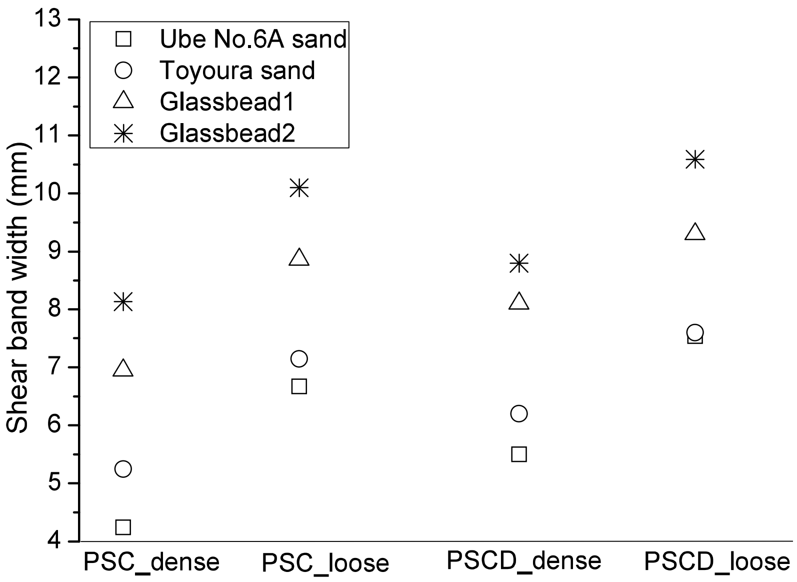

Figure 2.20 Comparison of shear band thickness in dense and loose specimens

Figure 2.20 shows comparison of measured shear band thicknesses between loose and dense specimens at about 12% axial strain. The PSCD test results were compared at $\sigma'_{c0} = 100$ kPa. Clearly, for each material, shear band thickness is much smaller in the dense specimen than that in the loose specimen for the same test condition.

The shear band thickness was introduced here also for the analysis of local deformation development in next sub-section.

2.4.4 Local deformation developments within shear band

Developments of local deformations in the specimens with detail values under different test conditions for the four materials were examined, as shown in Figs. 2.21-2.24. The maximum shear strain contours at the end of shearing (shearing ended around 12% of global axial strain) were produced in the same scale as in the figures to represent general images of shear band patterns.

As shown in Figs. 2.21-2.24, for the given five locations (marked by the circular points in the figures) along the shear band, development of the maximum shear strains within the shear band was plotted with respect to the global axial strain for each test condition. One or two shear bands were observed in both dense and loose specimens. When two shear bands appeared, the more apparent shear band is considered to be the main shear band. The five locations were determined in a way that the locations are approximately equally distributed along the main shear band. Lagrange method is used to trace the local maximum shear strain variations. From Figs. 2.21-2.24, maximum shear strains slowly developed at the beginning of shearing. As the global axial strain increased and reached to a certain value, the local maximum shear strains of the five locations almost simultaneously began to increase abruptly. Then, the start of abrupt change in gradient of the maximum shear strain curve is considered “the onset of shear band.” For each test condition, the global axial strain (ε_a^{sb}) corresponding to the onset of shear band is determined and listed in Table 2.4.

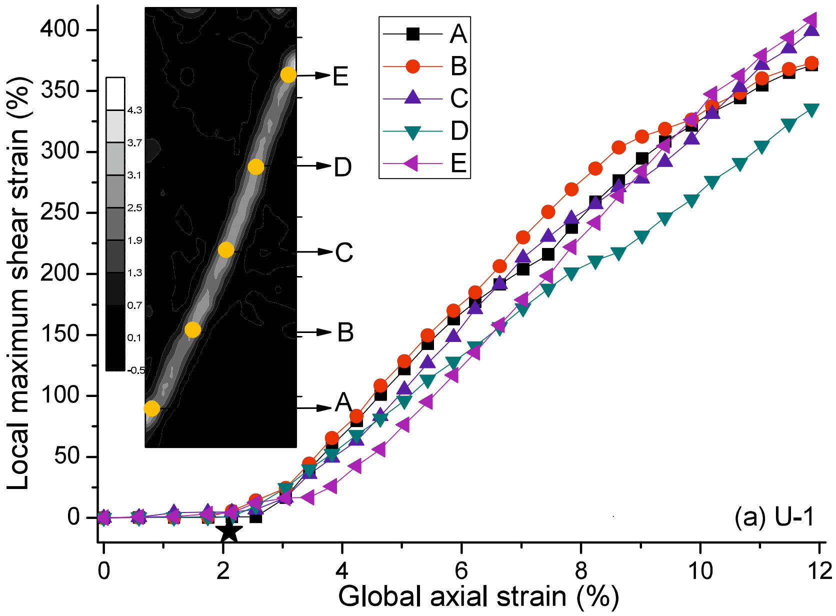

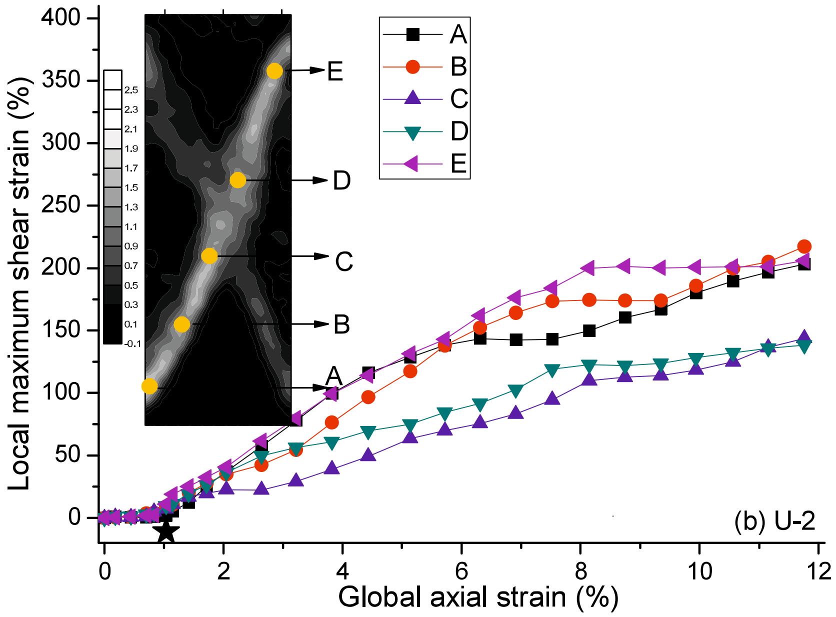
Local maximum shear strain (%)
400
350
300
250
200
150
100
50
0
Global axial strain (%)
0
2
4
6
8
10
12
2.5
2.3
2.1
1.9
1.7
1.5
1.3
1.1
0.9
0.7
0.5
0.3
0.1
-0.1
E
D
C
B
A
A
B
C
D
E
(b) U-2

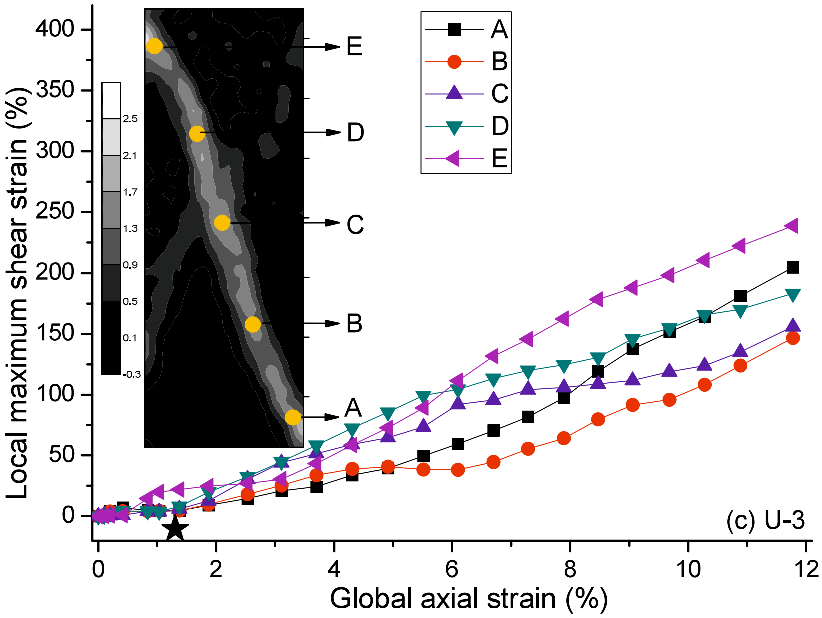
Local maximum shear strain (%)
400
350
300
250
200
150
100
50
0
Global axial strain (%)
0
2
4
6
8
10
12
2.5
2.1
1.7
1.3
0.9
0.5
0.1
-0.3
E
D
C
B
A
A
B
C
D
E
(c) U-3

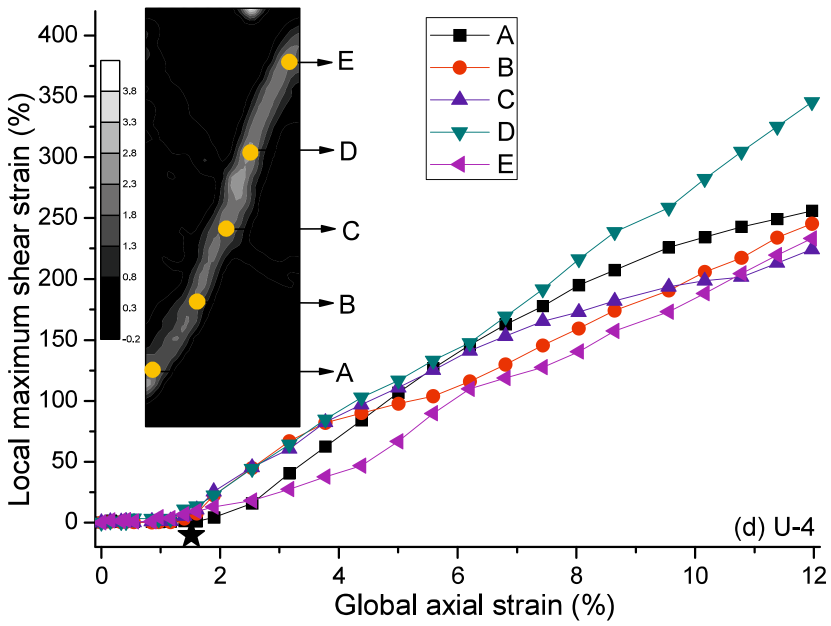
Local maximum shear strain (%)
400
350
300
250
200
150
100
50
0
0
2
4
6
8
10
12
Global axial strain (%)
3.8
3.3
2.8
2.3
1.8
1.3
0.8
0.3
-0.2
E
D
C
B
A
A
B
C
D
E
(d) U-4

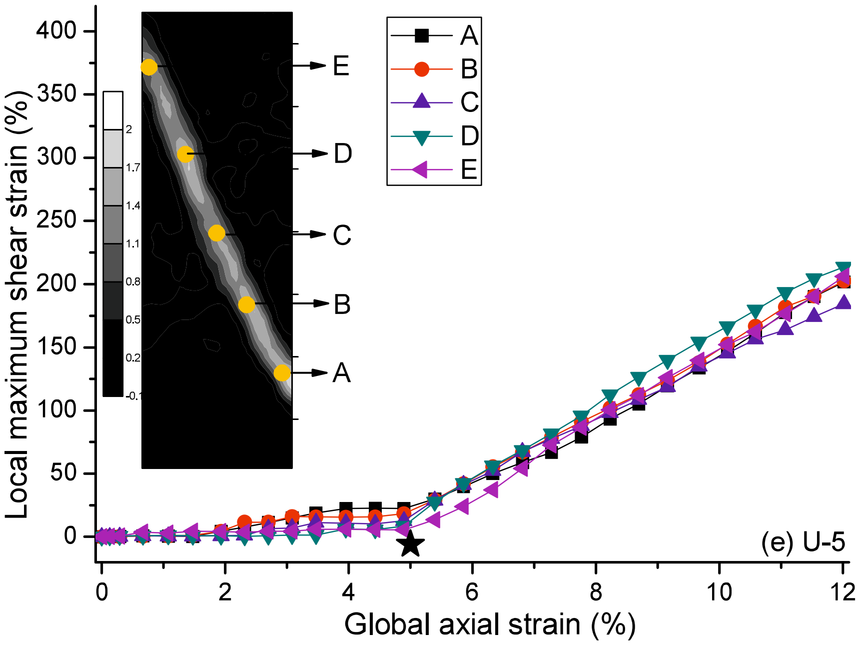
Local maximum shear strain (%)
400
350
300
250
200
150
100
50
0
0
2
4
6
8
10
12
Global axial strain (%)
2
1.7
1.4
1.1
0.8
0.5
0.2
-0.1
E
D
C
B
A
A
B
C
D
E
(e) U-5

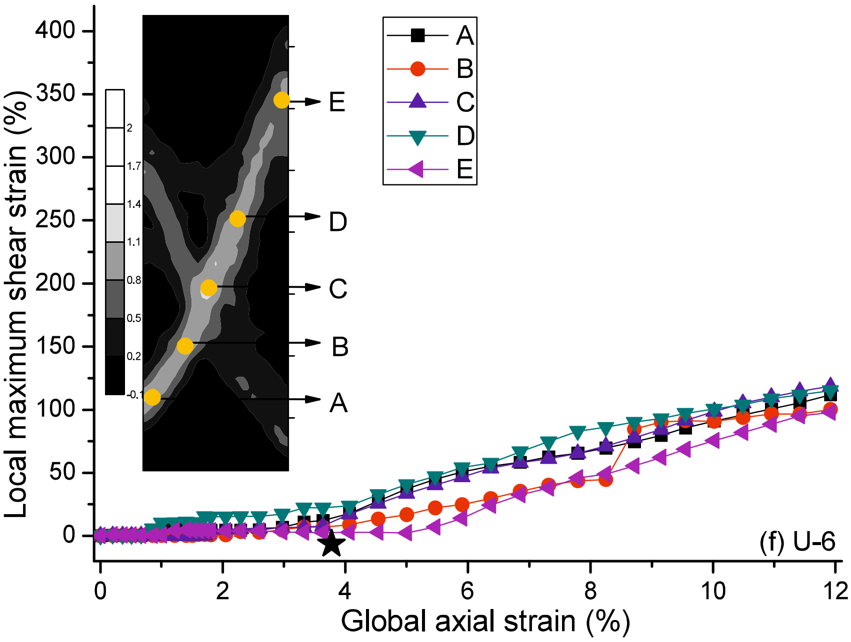

Figure 2.21 Local deformation developments within shear bands in Ube No.6A sand:
(a) dense, PSC, σ'_{c0} = 50 kPa; (b) dense, PSCD, σ'_{c0} = 50 kPa;
(c) dense, PSCD, σ'_{c0} = 100 kPa; (d) dense, PSCD, σ'_{c0} = 200 kPa;
(e) loose, PSC, σ'_{c0} = 50 kPa; (f) loose, PSCD, σ'_{c0} = 100 kPa

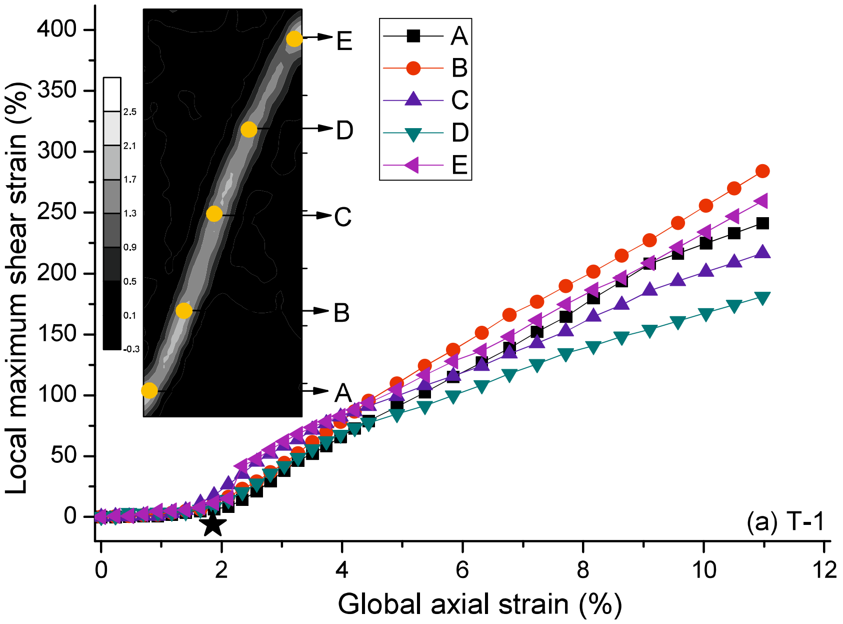

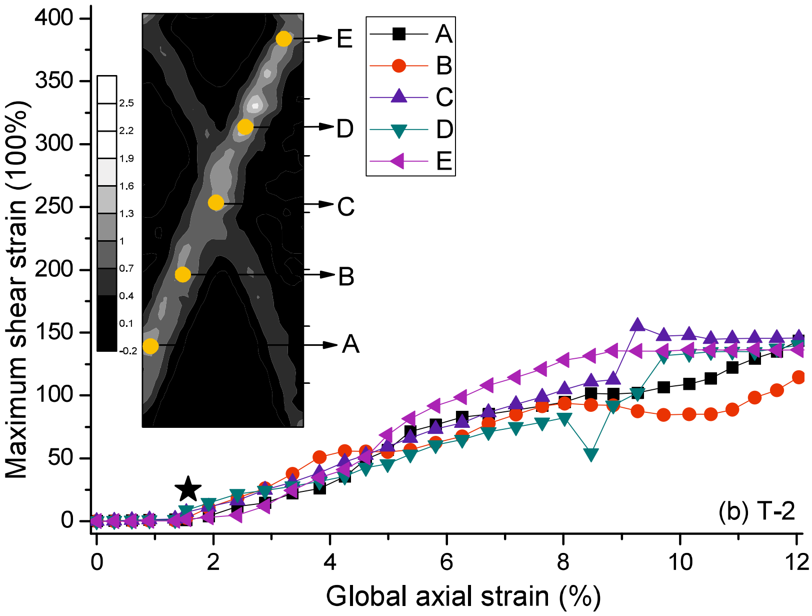
Maximum shear strain (100%)
400
350
300
250
200
150
100
50
0
Global axial strain (%)
0
2
4
6
8
10
12
2.5
2.2
1.9
1.6
1.3
1
0.7
0.4
0.1
-0.2
E
D
C
B
A
A
B
C
D
E
(b) T-2

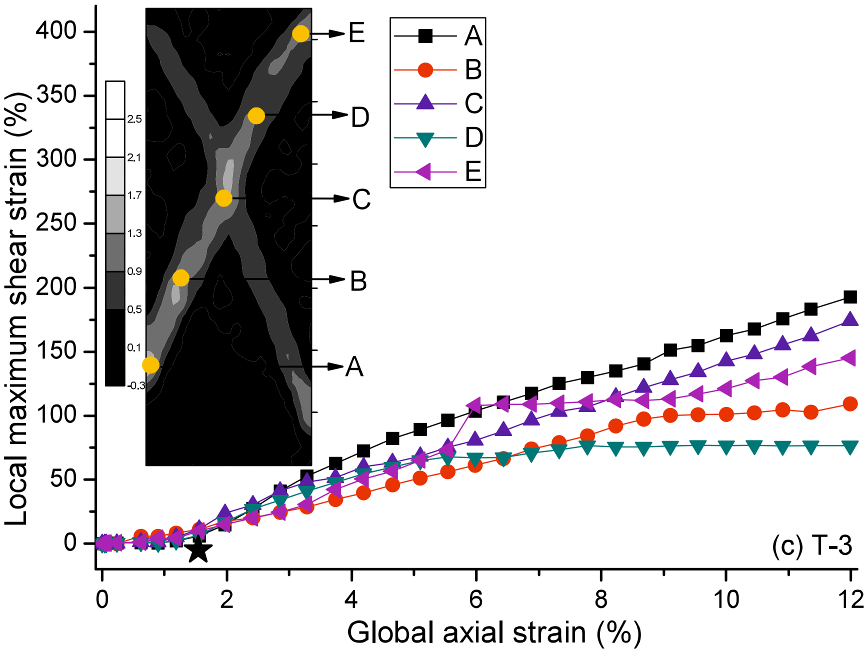
Local maximum shear strain (%)
400
350
300
250
200
150
100
50
0
Global axial strain (%)
0
2
4
6
8
10
12
2.5
2.1
1.7
1.3
0.9
0.5
0.1
-0.3
E
D
C
B
A
A
B
C
D
E
(c) T-3

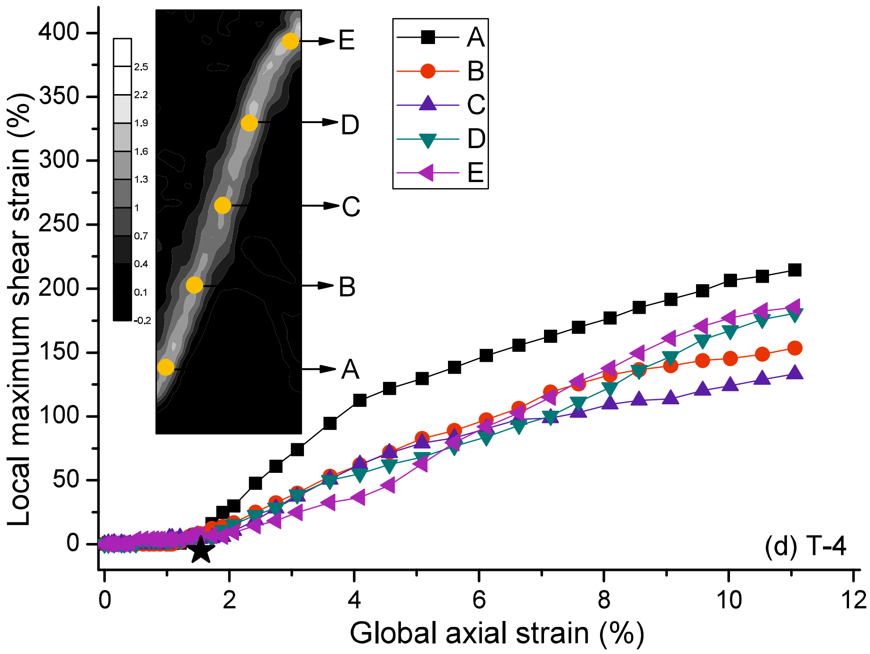
Local maximum shear strain (%)
Global axial strain (%)
0
50
100
150
200
250
300
350
400
0
2
4
6
8
10
12
2.5
2.2
1.9
1.6
1.3
1
0.7
0.4
0.1
-0.2
E
D
C
B
A
A
B
C
D
E
(d) T-4

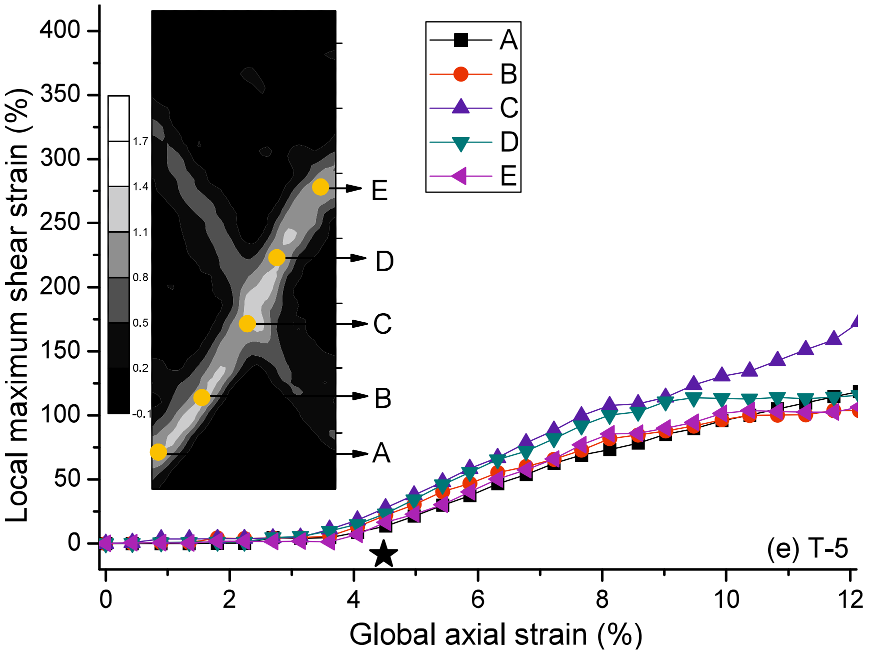
Local maximum shear strain (%)
Global axial strain (%)
0
50
100
150
200
250
300
350
400
0
2
4
6
8
10
12
1.7
1.4
1.1
0.8
0.5
0.2
-0.1
E
D
C
B
A
A
B
C
D
E
(e) T-5

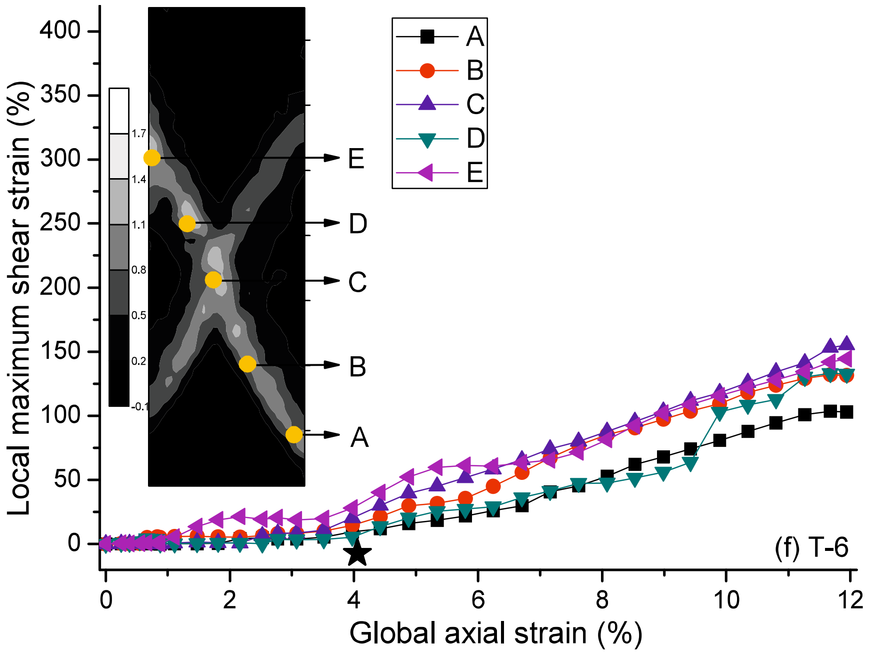

Figure 2.22 Local deformation developments within shear bands in Toyoura sand: (a) dense, PSC, σ'_{c0} = 50 kPa; (b) dense, PSCD, σ'_{c0} = 50 kPa; (c) dense, PSCD, σ'_{c0} = 100 kPa; (d) dense, PSCD, σ'_{c0} = 200 kPa; (e) loose, PSC, σ'_{c0} = 50 kPa; (f) loose, PSCD, σ'_{c0} = 100 kPa

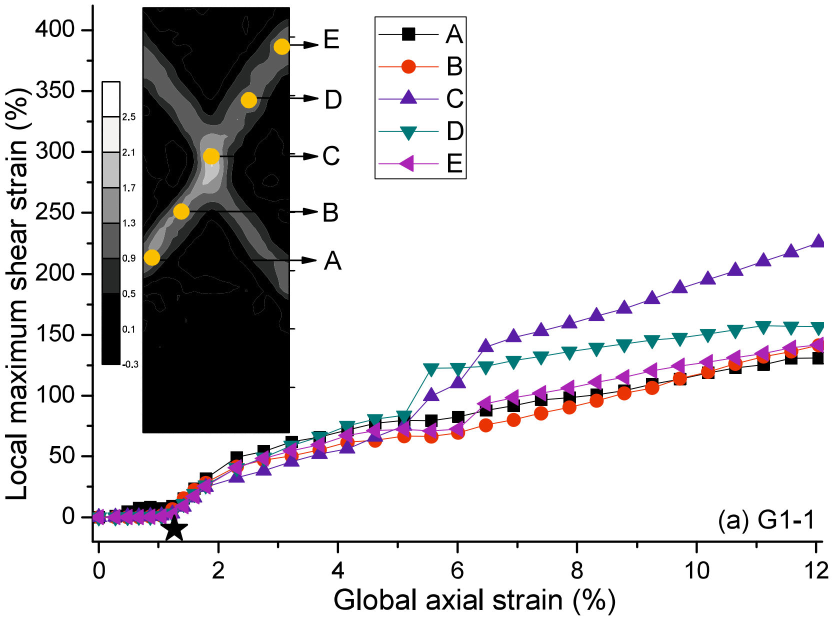

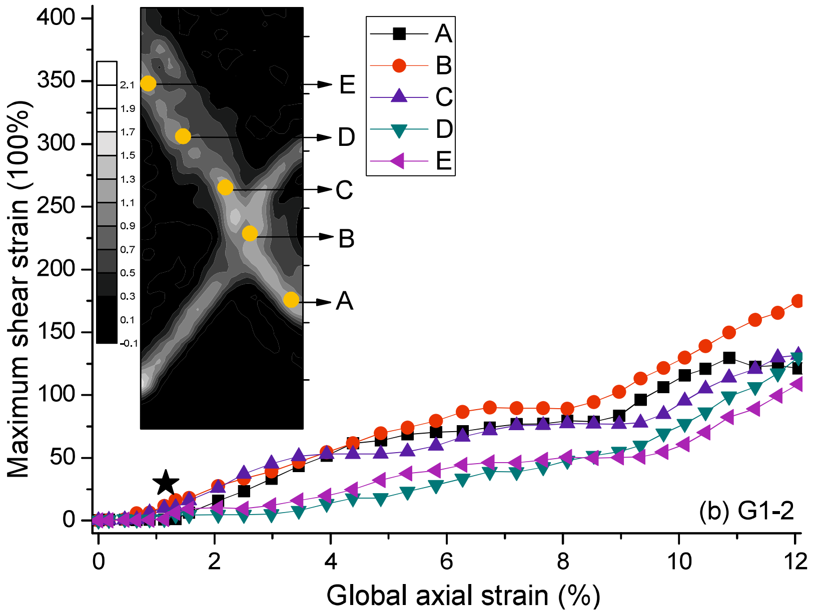
Maximum shear strain (100%)
400
350
300
250
200
150
100
50
0
Global axial strain (%)
0
2
4
6
8
10
12
2.1
1.9
1.7
1.5
1.3
1.1
0.9
0.7
0.5
0.3
0.1
-0.1
E
D
C
B
A
A
B
C
D
E
(b) G1-2

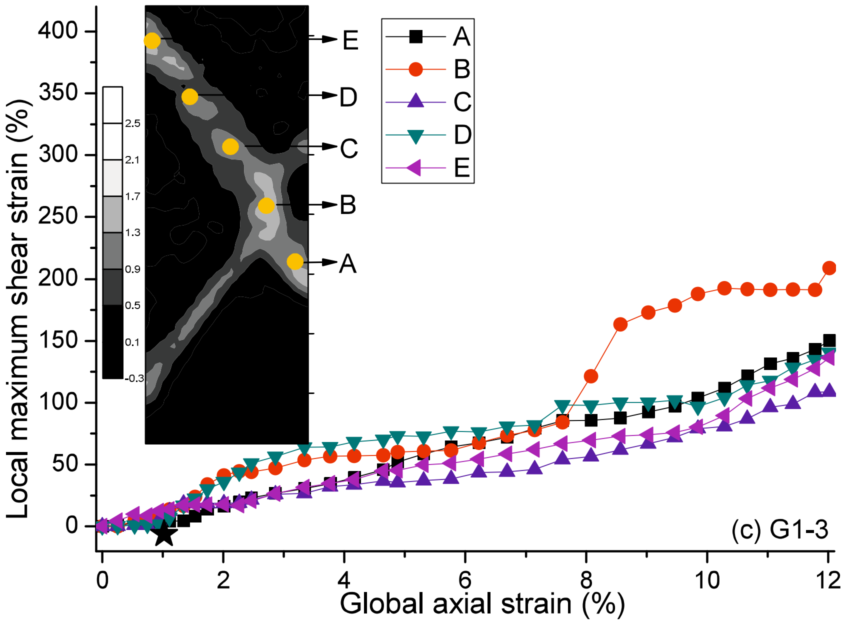
Local maximum shear strain (%)
400
350
300
250
200
150
100
50
0
Global axial strain (%)
0
2
4
6
8
10
12
2.5
2.1
1.7
1.3
0.9
0.5
0.1
-0.3
E
D
C
B
A
A
B
C
D
E
(c) G1-3

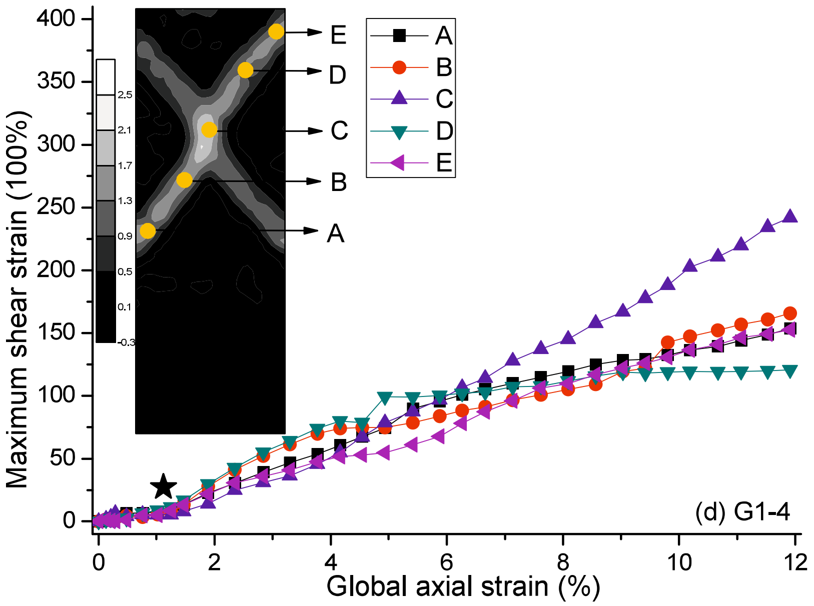
Maximum shear strain (100%)
Global axial strain (%)
0
50
100
150
200
250
300
350
400
0
2
4
6
8
10
12
2.5
2.1
1.7
1.3
0.9
0.5
0.1
-0.3
E
D
C
B
A
A
B
C
D
E
(d) G1-4

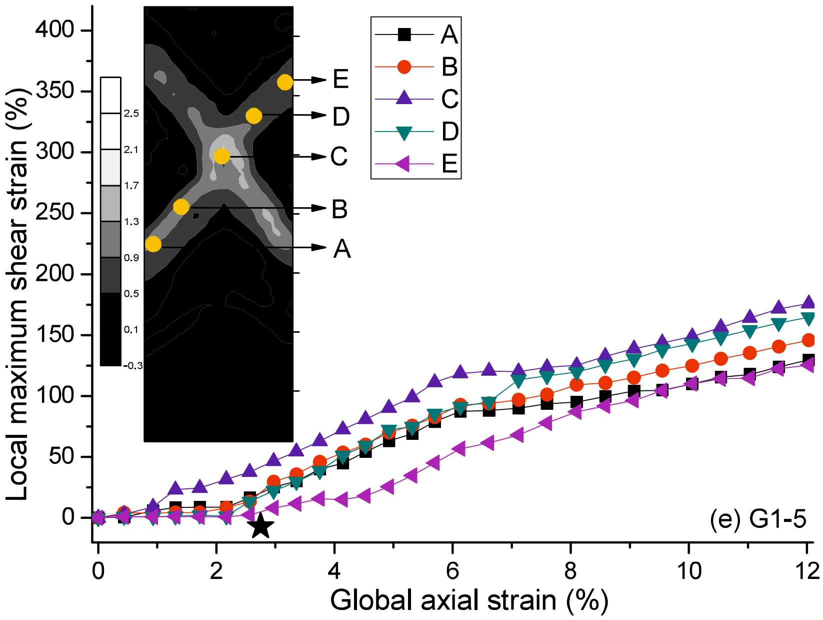
Local maximum shear strain (%)
Global axial strain (%)
0
50
100
150
200
250
300
350
400
0
2
4
6
8
10
12
2.5
2.1
1.7
1.3
0.9
0.5
0.1
-0.3
E
D
C
B
A
A
B
C
D
E
(e) G1-5

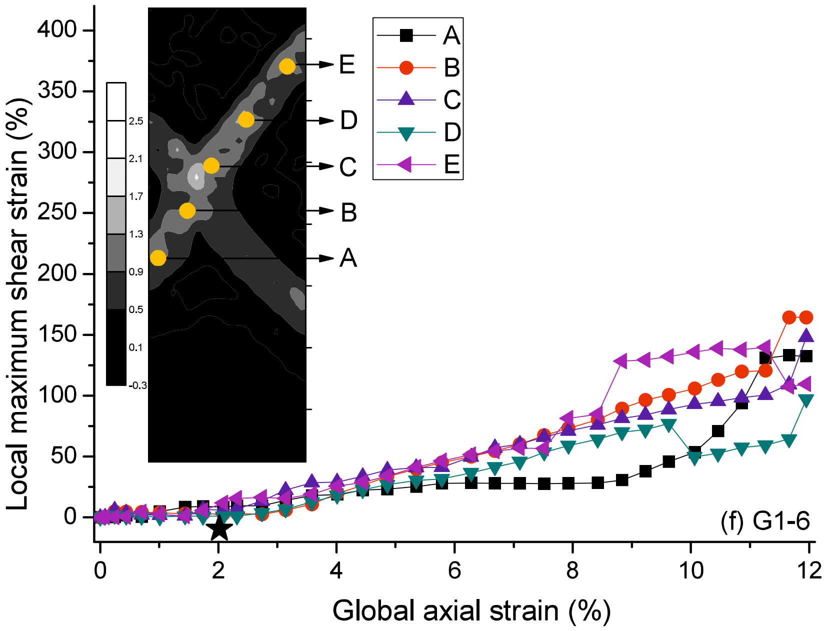

Figure 2.23 Local deformation developments within shear bands in Glassbead1:
(a) dense, PSC, σ'_{c0} = 50 kPa; (b) dense, PSCD, σ'_{c0} = 50 kPa;
(c) dense, PSCD, σ'_{c0} = 100 kPa; (d) dense, PSCD, σ'_{c0} = 200 kPa;
(e) loose, PSC, σ'_{c0} = 50 kPa; (f) loose, PSCD, σ'_{c0} = 100 kPa

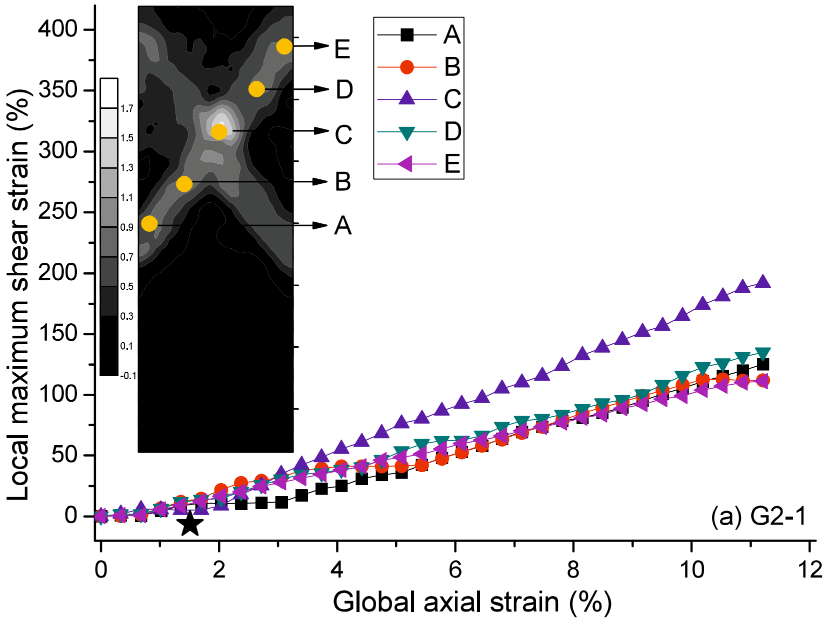

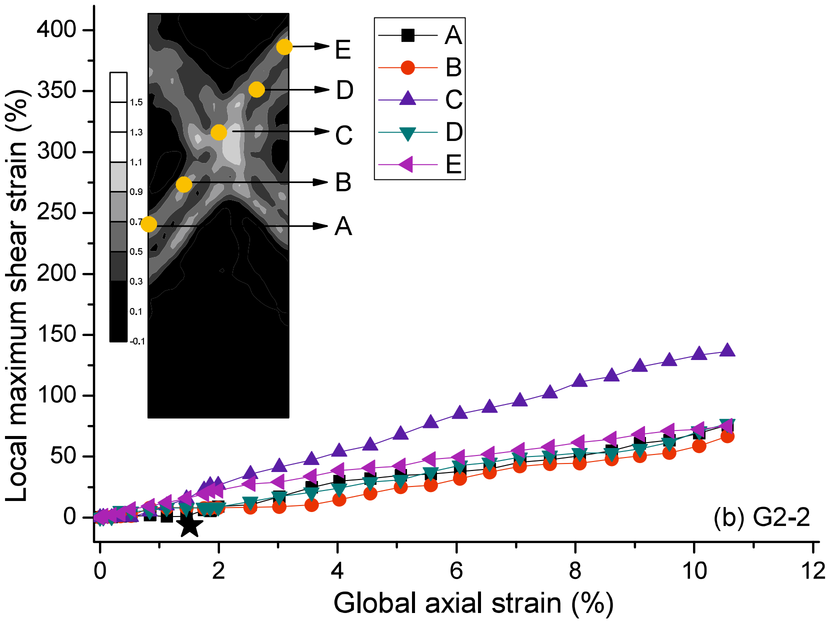
Local maximum shear strain (%)
400
350
300
250
200
150
100
50
0
Global axial strain (%)
0
2
4
6
8
10
12
1.5
1.3
1.1
0.9
0.7
0.5
0.3
0.1
-0.1
E
D
C
B
A
A
B
C
D
E
(b) G2-2

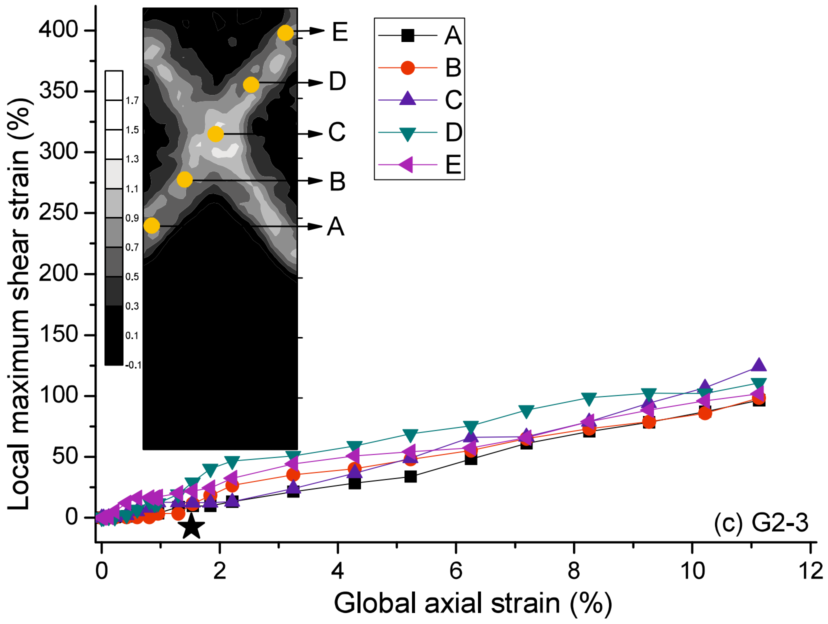
Local maximum shear strain (%)
400
350
300
250
200
150
100
50
0
Global axial strain (%)
0
2
4
6
8
10
12
1.7
1.5
1.3
1.1
0.9
0.7
0.5
0.3
0.1
-0.1
E
D
C
B
A
A
B
C
D
E
(c) G2-3

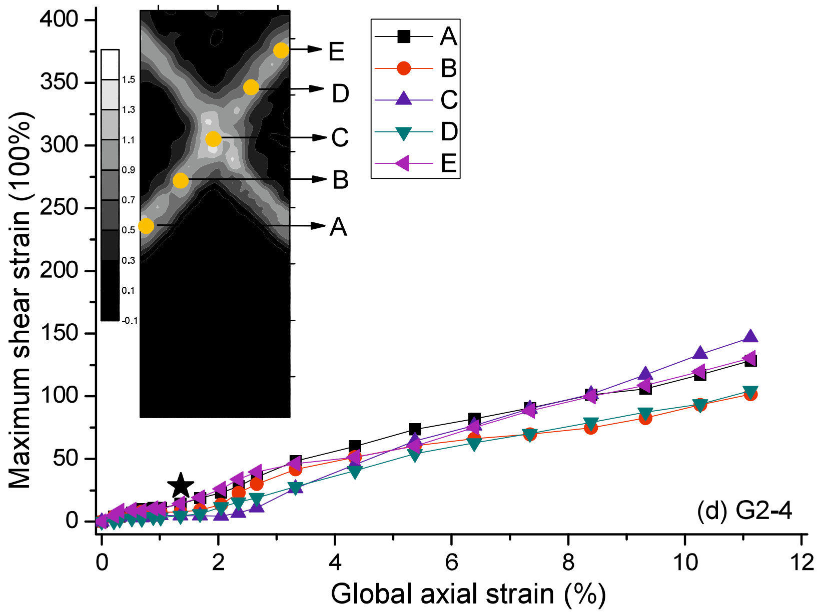
Maximum shear strain (100%)
Global axial strain (%)
0
50
100
150
200
250
300
350
400
0
2
4
6
8
10
12
1.5
1.3
1.1
0.9
0.7
0.5
0.3
0.1
-0.1
E
D
C
B
A
A
B
C
D
E
(d) G2-4

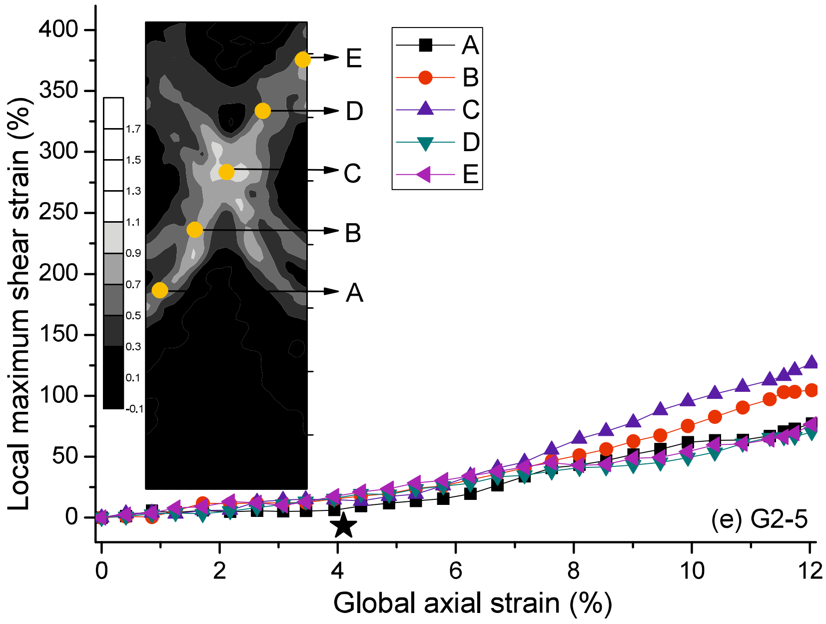
Local maximum shear strain (%)
Global axial strain (%)
0
50
100
150
200
250
300
350
400
0
2
4
6
8
10
12
1.7
1.5
1.3
1.1
0.9
0.7
0.5
0.3
0.1
-0.1
E
D
C
B
A
A
B
C
D
E
(e) G2-5

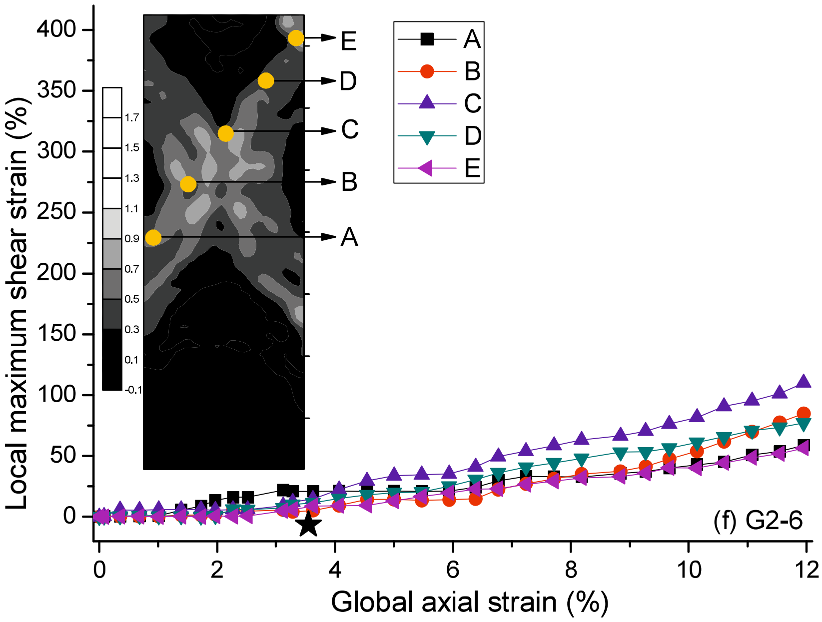

Figure 2.24 Local deformation developments within shear bands in Glassbead2:

(a) dense, PSC, σ'_{c0} = 50 kPa; (b) dense, PSCD, σ'_{c0} = 50 kPa;

(c) dense, PSCD, σ'_{c0} = 100 kPa; (d) dense, PSCD, σ'_{c0} = 200 kPa;

(e) loose, PSC, σ'_{c0} = 50 kPa; (f) loose, PSCD, σ'_{c0} = 100 kPa

Separately from the onset of shear band development, the global axial strains (ε_a) corresponding to the peak strengths were also marked using a symbol '★' in Figs. 2.21-2.24 and summarized in Table 2.4. It is found that ε_a^{sb} is always smaller than or equal to ε_a corresponding to the peak strengths, which means that the onset of shear band occurs prior to the mobilization of peak strength for both dense and loose specimens.

Table 2.4 local deformation characteristics

Material		Test type	Relative density (%)	Number of observed Shear band	ε_a @ peak strength (%)	ε_a^{sb} (%)	Mean growth rate k	Shear band thickness (mm)
Ube No.6A sand	U-1	PSC	73.4	1	2.03	2.0	42.1	4.24
	U-2	PSCD	72.7	2	0.84	0.83	20.8	6.75
	U-3	PSCD	73.6	1	1.22	1.04	21.8	5.75
	U-4	PSCD	73.9	1	1.35	1.17	24.4	5.3
	U-5	PSC	22.8	1	5.00	4.40	19.2	6.67
	U-6	PSCD	21.6	2	3.71	2.97	14.5	7.54
Toyoura sand	T-1	PSC	85.6	1	1.79	1.64	29.6	5.25
	T-2	PSCD	75.1	2	1.13	1.1	15.4	6.67
	T-3	PSCD	79.8	2	1.53	1.19	19.6	6.21
	T-4	PSCD	82.4	1	1.52	1.52	23.6	6.06
	T-5	PSC	24.9	2	4.23	4.00	18.3	7.15
	T-6	PSCD	24	2	4.20	3.07	13.2	7.60
Glass bead1	G1-1	PSC	82.1	2	1.11	1.05	24.5	6.95
	G1-2	PSCD	82.1	2	1.05	0.88	12.7	8.40
	G1-3	PSCD	78	2	0.95	0.94	15.7	8.05
	G1-4	PSCD	76.3	2	1.18	1.16	22.0	5.63
	G1-5	PSC	16.8	2	2.20	2.17	14.9	8.86
	G1-6	PSCD	28.3	2	2.24	2.08	9.8	9.29
Glass bead2	G2-1	PSC	89.8	2	1.59	0.95	13.4	8.14
	G2-2	PSCD	78.8	2	1.55	0.52	8.1	9.73
	G2-3	PSCD	96.6	2	1.43	0.42	9.2	8.78
	G2-4	PSCD	97.5	2	1.47	0.52	12.8	7.62
	G2-5	PSC	11	2	3.38	1.40	9.1	10.51
	G2-6	PSCD	12.7	2	3.43	1.72	8.4	10.59

It is interesting to find that most of the maximum shear strains within the shear band grow approximately linearly with an increasing global axial strain after the onset of shear band. However, the rate of increase in the local maximum shear strain is not always the same at the five locations. As shown in Fig. 2.25, the growth rate k (=$\Delta\gamma_{\mathrm{max}}/\Delta\varepsilon_{\mathrm{a}}$) is defined as the ratio of the change of γ_{max} to that of ε_{a}, and it is obtained from a simple linear regression to the curves in Figs. 2.21-2.24.

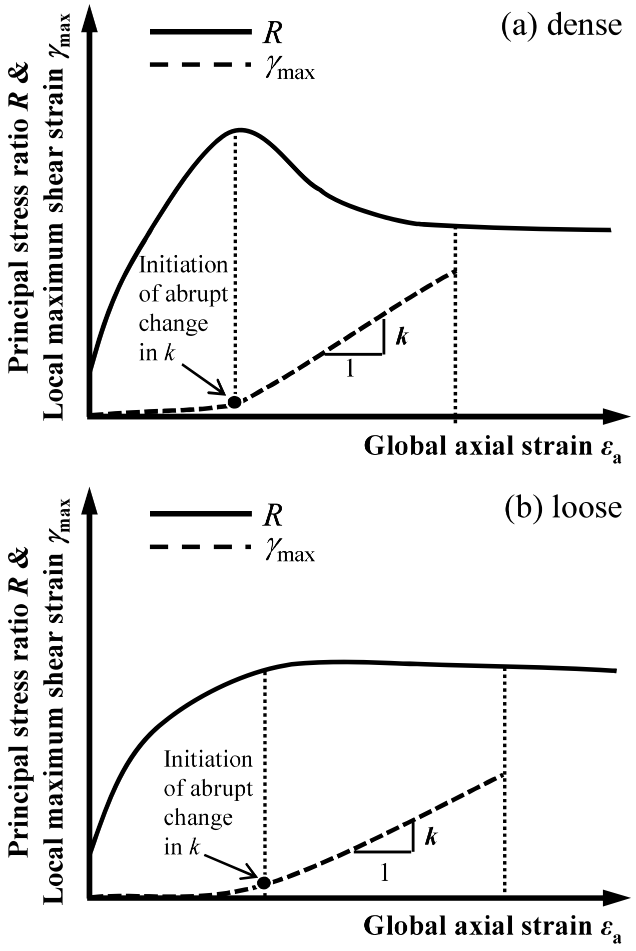

Figure 2.25 Sketch of definition of growth rate k in local maximum shear strain curve for (a) dense and (b) loose specimens

The ε_{a} ranges used for the regression are $\varepsilon_{\mathrm{a}}^{sb} \leq \varepsilon_{\mathrm{a}} \leq$ “ε_{a} corresponding to the end of strain softening” for dense specimens and $\varepsilon_{\mathrm{a}}^{sb} \leq \varepsilon_{\mathrm{a}} \leq$ “ε_{a} at 8%

global axial strain" for loose specimens. The upper bounds of ε_a for dense and loose specimens were chosen as such, because the principal stress ratio variations almost ceased near the specified upper bounds of ε_a.

Fig. 2.26 shows *k* values results in the PSCD tests of dense specimens under different confining pressures. For the same test case, some points overlapped because of the same growth rate of curves at different locations. The mean value of the five locations in each case was also given in the figure. It is found that *k* decreased across Ube No.6A sand, Toyoura sand, Glassbead1 and Glassbead2 under the same test condition. Moreover, for each material, *k* increased with increase of confining pressure.

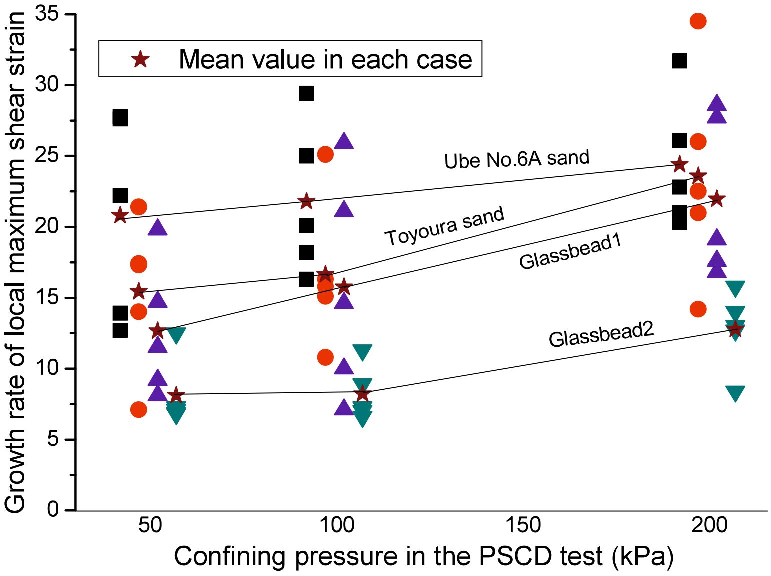

Figure 2.26 Growth rate of maximum shear strain within shear band in the PSCD test for dense specimens

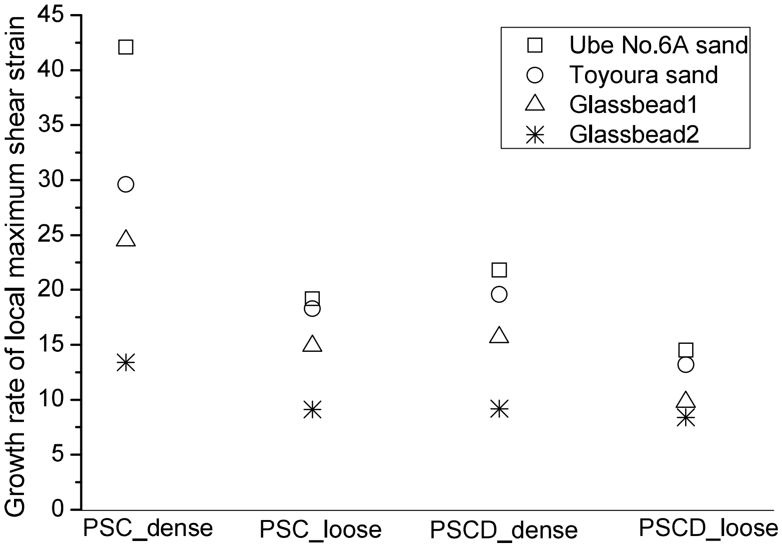

Figure 2.27 Comparisons of growth rate of maximum shear strain *k* within shear band in each case

Figure 2.27 shows comparison results of *k* values in dense and loose specimens. Here, the PSCD test is under σ'_{c0} = 100 kPa. In general, the mean growth rate *k* is higher in dense specimen than that in loose specimen under the same test condition. For both loose and dense specimens of each material, *k* is higher in the PSC tests than that in the PSCD tests.

Referring to Figs. 2.19 and 2.20, the growth rates under different test conditions found to have strong correlation with shear band thickness. The mean growth rates *k* of local maximum shear strain $\gamma_{\max}$ and the shear band thicknesses obtained for all the tests are summarized in Table 2.4. Regardless of the material types, a consistent finding is that the growth rate *k* decreased with an increasing shear band thickness. For example, loose specimen had a wider shear band than that in dense specimen, and the growth rate in loose specimen was lower. When comparing the growth rates in different materials, it is found that Glassbead2 with the largest shear band thickness show the lowest growth rate under each test condition and Ube No.6A with the smallest one shear band thickness shows the highest growth rate. The reason is because that, for specimen with a wider shear band, it generates more displacement to reach a certain extent of maximum shear strain $\gamma_{\max}$ and therefore more global axial strain ε_a is needed to increase γ_{max}. As a result, the growth rate is smaller.

2.4.5 Shear band inclination angles in the PSCD test

Shear band inclination angle has been studied a lot. Two classical formulas proposed by Coulomb and Roscoe were often used for the prediction of shear band inclination angle and their solutions are given in the Table 2.5. For details about these two prediction equations can refer to Alshibli and Sture (2000). Coulomb's and Roscoe's formulas to estimate shear band inclination angles (θ_C and θ_R, respectively) to the horizontal are:

$$\theta_C = 45° + \phi_p / 2 \tag{2.7}$$

$$\theta_R = 45° + \Psi_p / 2 \tag{2.8}$$

where φ_p is the mobilized peak friction angle and Ψ_p is the dilation angle at peak strength (refer to Eq. (2.1) and Eq. (2.3)).

Different comparison results were given by several researchers. Such as, Finno et al. (1997) concluded that the inclination angles in loose sands lied between Coulomb and Arthur solutions; measured results by Alshibli and Sture (2000) were much closer to Roscoe's solution and the result was little influenced by relative density and particle size distribution. In this study, shear band inclination angles θ_p to the horizontal at the peak strength and those θ_r at the maximum global axial strain ($\varepsilon_a \approx 12\%$) in our tests were measured and summarized in Table 2.5.

Table 2.5 Summary of measured and predicted shear band inclination angles

Material		$R_{\max}$	Mobilized angle ϕ_m (°)	Dilation angle Ψ (°)	θ_p (°)	θ_r (°)	Coulomb solution (°)	Roscoe solution (°)
Ube No.6A sand	U-1	9.1	53.3	20.5	70.8	70.8	71.7	55.3
	U-2	11.1	56.6	24.2	72.8	67.8	73.3	57.1
	U-3	10.0	54.9	23.0	72.1	67.7	72.5	56.5
	U-4	9.7	54.4	21.1	68.8	68.1	72.2	55.6
	U-5	5.0	41.8	0.0	64.8	67.4	65.9	45.0
	U-6	6.0	45.6	5.7	60.6	67.4	67.8	47.9
Toyoura sand	T-1	6.8	48	19.2	69.2	69.2	69.0	54.6
	T-2	8.7	52.6	18.1	69.3	69.7	71.3	54.2
	T-3	8.0	51.0	17.7	68.6	68.9	70.5	53.9
	T-4	7.4	49.6	17.7	69.6	70.0	69.8	53.9
	T-5	3.8	35.6	0.0	59.3	68.9	62.8	45.0
	T-6	4.4	39.0	4.0	61.6	62.3	64.5	47.0
Glass bead1	G1-1	4.3	38.6	19.2	56.3	53.8	64.3	54.6
	G1-2	5.2	42.6	18.3	61.6	58.4	66.3	54.1
	G1-3	4.5	39.6	17.8	59.1	56.0	64.8	53.9
	G1-4	4.2	38.0	16.8	54.6	54.3	64.0	53.4
	G1-5	2.9	29.2	4.0	54.6	56.0	59.6	47.0
	G1-6	2.7	27.4	4.0	52.1	51.9	58.7	47.0
Glass bead2	G2-1	4.0	36.8	16.2	54.0	51.8	63.4	53.1
	G2-2	4.5	39.6	15.1	54.5	51.8	64.8	52.6
	G2-3	3.9	36.2	15.1	53.7	51.8	63.1	52.6
	G2-4	3.7	35	15.1	53.7	51.8	62.5	52.6
	G2-5	2.7	27.4	2.2	53.2	51.8	58.7	46.1
	G2-6	3.1	30.8	2.2	48.0	47.3	60.4	46.1

Clearly, θ_p values were much smaller in the loose specimens than in the dense specimens under the same test condition for all the materials. For Ube No.6A sand, measured shear band inclination angle decreased from θ_p to θ_r

for dense specimens while the θ_r was higher than θ_p for loose specimens. For Toyoura sand, almost no change was found between θ_p and θ_r in the dense specimens and only a small decrement (1.8° and 0.7°) from θ_p to θ_r was observed for the loose specimens. However, the measured shear band inclination angles of the two glass beads dropped from θ_p to θ_r for both dense and loose specimens.

Fig. 2.28 shows comparison results on the horizontal axis of maximum principal stress ratio R. The R value was no more than 6 in the two glass beads and it was no less than 6 in the two sands. It is found that measured inclination angles in the two sands are well predicted by Coulomb's formula with errors of $0 - 2°$. For the two glass beads, measured values are quite close to Roscoe solutions in Glassbead2 while they lie between Coulomb solutions and Roscoe solutions in Glassbead1. As a result, Roscoe's formula considering only dilation angle underestimated the shear band inclination angles in the sands, while Coulomb's solution clearly overestimated the angles in the glass beads. The results revealed that the shear band inclination angle calculation method can be different between round and irregular granules. This needs more study in the future.

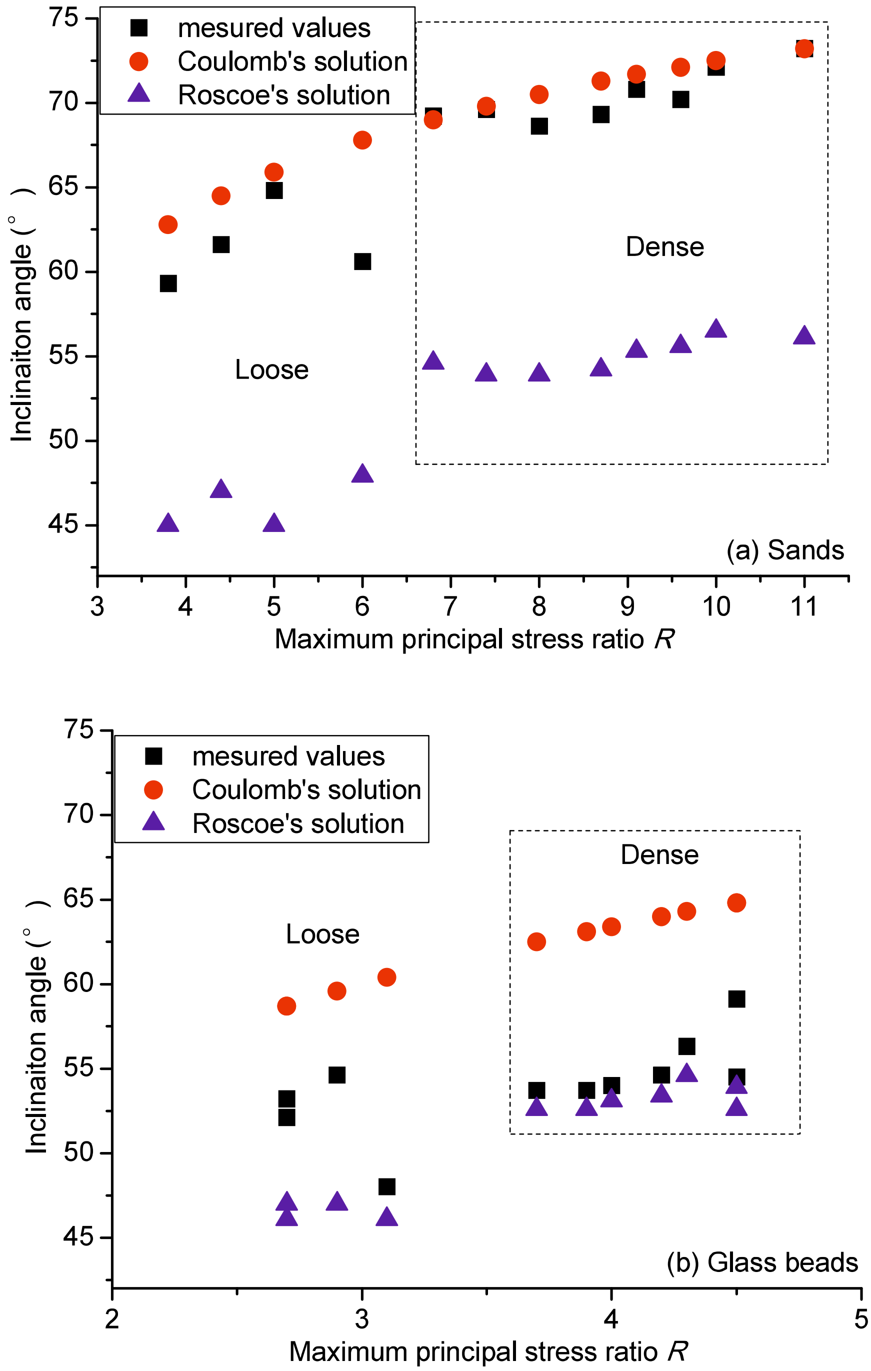

Figure 2.28 Comparison of the measured inclination angles θ_p and the predicted values based on the two classical solutions: (a) Ube No.6A sand and Toyoura sand; (b) Glassbead1 and Glassbead2

2.5 Conclusions

Two types of plane strain compression tests, one with constant and another with decreasing confining pressures, were compared in this study for four kinds of granular materials. Local deformations of specimens were analyzed using the DIC method. It was found that shear compression behavior under the two different stress paths shows different points in several aspects. Some conclusions were drawn as below:

(1) Macro stress – strain behavior is more easily influenced by stress level and stress path in the two sands than that in the two glass beads. The more angular particle shape induced more significant peak strength variations with stress level. For the given stress levels in this study, the peak appeared earlier and initial stiffness was clearly higher in all the PSCD tests than those in the PSC test for the sands.

(2) Local lateral strain showed mainly extension and butterfly shaped distribution near the peak strength. The extension was higher in the PSCD test than that in the PSC test for sands at the same global shear strain. Shear bands already initiated before peak strength and shear band patterns were changing during the whole shearing process.

(3) Under the same test condition, shear band thickness in the two sands was smaller than that in Glassbead1 even if the three types of material have almost the same mean particle size. Shear band thickness also decreased with increase of confining pressure regardless of particle shape or size.

(4) The onset of shear bands is defined at which the growth rate of the local maximum shear strain starts to increase stiffly with an increasing global axial strain. Generally, the onset of shear bands occurs prior to the specimen reaching its maximum principal stress ratio for both dense and loose specimens. Between the peak in shear strength and the end of strain softening, the local maximum shear strain grew approximately linearly with the global axial strain. For the same material, the growth rate of the local maximum shear strain became smaller with wider shear band.

(5) Shear band thicknesses in the two sands were clearly smaller than that in Glassbead1, even with their similar mean particle sizes. Shear band thickness became thinner when particle shape is more angular. Shear band thickness was also much dependent on the particle size. However, shear band thickness was not proportional increased with an increasing mean particle size.

(6) Inclination angles of shear bands corresponding to their peak strengths were in between those estimated values by Coulomb's and Roscoe's formulas for both sands and glass beads. The shear band inclination angles in sands matched well with those estimated by Coulomb's formula, while Roscoe's formula predicted shear band inclination angles relatively close to the corresponding measured values in dense glass beads.

From the experimental study, it is clearly seen that the unloading shear behavior of granular materials in the PSCD test is different from the general loading shear behavior in the PSC test. The differences between the two are influenced by particle shape and relative density in a significant way. In the next chapter, DEM simulation was performed to help understand the mechanism from the viewpoint of the micro mechanics of granular material.

Chapter 3 Unloading shear behavior of granular materials in biaxial DEM simulation

In last chapter, plane strain compression tests on irregularly shaped sands and rounded glass beads were introduced and it is found that particle shape has a great influence on shear behaviors of granular materials under different stress paths. In order to investigate the underlying mechanism of the particle shape effects on the shear behavior under different stress paths, DEM is used to simulate the experiments. Simulations were performed using the *PFC*^{2D} program by the Itasca Company. Simulation results were compared from both macro and micro viewpoints of granular materials.

3.1 DEM Simulation by *PFC*^{2D}

3.1.1 Introduction of *PFC*^{2D}

"PFC" is shorted for "Particle Flow Code", which has two-dimension and three-dimension codes. Two-dimension code of ***PFC***$^{\mathbf{2D}}$ is used in this study.

(1) Fundamental geometric entity and calculation cycle

In PFC, there are only two fundamental geometric entities applied for calculation. One is "ball" and another is "wall". A ***PFC***$^{\mathbf{2D}}$ model consists of a two-dimensional collection of particles. The particles are treated as rigid bodies. Newton's second law is used to determine the motion of each particle arising from the contact and body forces acting upon it, while the force-displacement law is used to update the contact forces arising from the relative motion at each contact, as shown in Fig. 3.1.

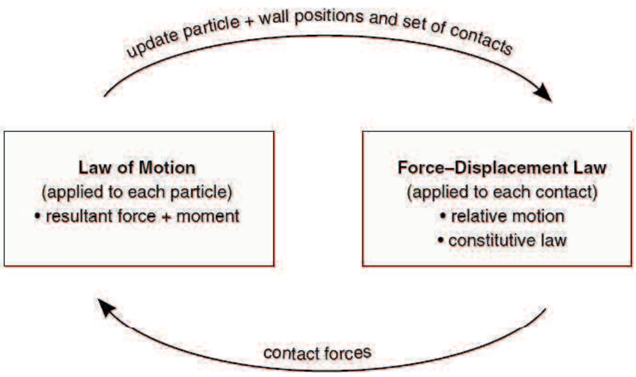

Figure 3.1 Calculation cycle in ***PFC***^{2D} (after "User Manual" 2008)

As shown in Fig. 3.2, the points between two balls signify contacts and lines signify contact forces. The wider of lines, the larger contact forces. For 2D simulation, the out-of-plane force component and the two in-plane moment components are not considered in any way in the equations of motion or in the force-displacement laws.

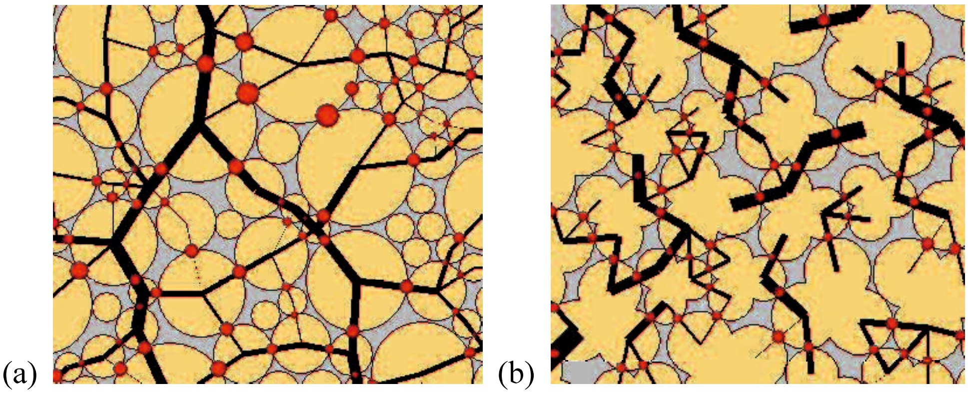

Figure 3.2 Particles used in the DEM calculation: (a) round shape; (b) arbitrary shape

(2) Contact model

There are two frequently-used contact models in the PFC, including the linear model and Hertz model. The linear model provides sliding behavior, constant stiffness and optional bond behavior for particles. For non-cohesive granular materials, bonding is ignored and there is no tension strength between particles. The Hertz model provides sliding behavior and stiffness that varies as a function of the elastic constants of the two contacting entities, overlap and normal force. As the name implies, behavior of contact between particles follows Hertz contact law. There are also several alternative contact models provided by *PFC* to meet different requirements, such as ductile model, smooth-joint model, which can meet user's different requirement.

Hertz contact model is applicable to only spheres. As the maximum pressure applied on the research subject is not big compared to particle's stiffness and referring to past studies, the simplest linear contact model is used in this study. Fig. 3.3 shows contact behaviors of two particles in DEM simulation.

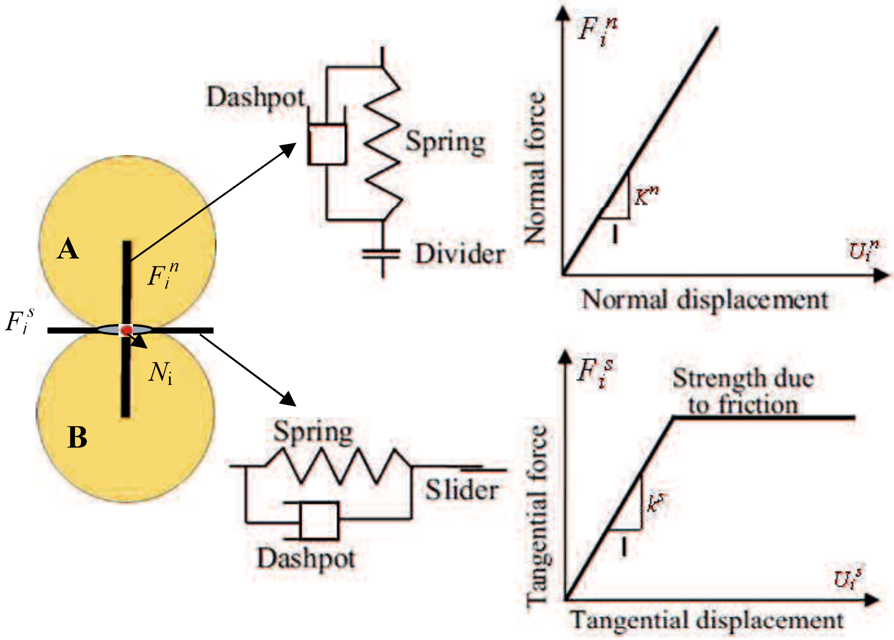

Figure 3.3 Contact behaviors of two balls

The normal force F_i^n and shear force F_i^s at contact N_i are calculated as follows. When Equation (3.3) is satisfied, slip between the two particles occurs.

$$F_i^n = K^n * U_i^n \tag{3.1}$$

$$F_i^s = F_i^s - k^s * \Delta U_i^s \tag{3.2}$$

$$F_i^s > \mu F_i^n \quad \text{(slip)} \tag{3.3}$$

here, K^n and k^s are normal and tangential contact stiffness separately; U_i^n is the normal overlap; μ is friction coefficient, ΔU_i^s is increment of shear displacement.

Contact stiffness is treated as constant in the model. The contact normal secant stiffness and shear tangent stiffness are given by

$$K^n = k_n^A\, k_n^B/(\, k_n^A + k_n^B) \tag{3.4}$$

$$k^s = k_s^A\, k_s^B/(\, k_s^A + k_s^B) \tag{3.5}$$

k_n^A, k_n^B, k_s^A, k_s^B are the normal and shear stiffness of two balls A and B in contact.

The dashpots in Fig. 3.3 are used to dissipate kinetic energy to help the sliding arrive at a steady state solution in a reasonable number of cycles. Local damping and viscous damping are available. Local damping applies a damping force to each ball with magnitude proportional to unbalanced force, while viscous damping adds normal and tangential dashpots at each contact and provides forces that are proportional to a relative velocity difference between the two contacting entities. Since the simulated tests in this study are quasi-static, only local damping is applied and the damping constant is 0.5.

(3) Particle shape

By default, balls are treated as spheres. They can also set to be disks of unit thickness or cylinder with a specified thickness. To simulation plane stain condition, balls are set to be disks of unit thickness. Balls can well simulate round shaped particles such as glass beads. However, natural sands usually have much irregular particle shape. “Clump” model supplied by PFC can help to solve this problem.

Several circular balls can be combined to form a clump, as shown by some examples in Fig. 3.4. The positions of slaved balls in a clump can be adjusted to meet any requirements on the appearance. Clump behaves as a rigid body that will not break apart, regardless of the forces acting upon it. That means the particles comprising the clump remain at a fixed distance from each other only if the clump command is cancelled. Particles within a clump may overlap to any extent and contact forces are not generated between these particles. Therefore, one clump acts as a particle and it can be used to simulate any kind of particle shape by adjusting size and position of particles within a clump. However, to modify real shape of granular particles such as sand, it may need a large number of different balls as shown in Fig. 3.5. This will take long time and require high performance equipment for calculation.

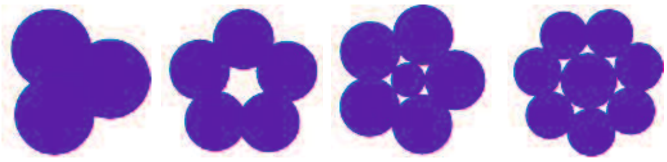

Figure 3.4 Different clumps made by several balls

Figure 3.5 Simulation of real particle shape with overlapping spheres (after Ferellec and McDowell 2010)

(4) Boundary condition

As mentioned above, PFC modeling only contains two elements of ball and wall. Boundaries can be supplied by both ball and wall through applying forces or velocities. For each ball, an applied force or/and moment acting through its center and initial velocity (translational and rotational) can be specified. Balls can also be fixed or fix-released. For each wall, only velocities can be specified. The wall motion is specified and the Newton's second law is not applied to walls. Walls only require that the force-displacement law account for ball-wall contacts. Its motion is specified by the user and remains constant regardless of the contact forces acting on it. Also, contacts may not form between two walls.

(5) Selection of particle size and specimen size

There is no necessary to simulate the real particle sizes of sands used in experiment, because real particle sizes of sands are usually very small and one specimen may contains numerous particles. Also, there is no need to simulate the same size of specimen with that in the experiment. For the same number of particles and same arrangement, the simulation results will be the same. However, for 2D simulation, length-width ratio will have influence when it exceeds a certain range. Particle size effect is not obvious.

The total number of particles and particle size distribution are very important for simulation. If number of particles is too small, the boundary effect is large and simulation result of stress and strain behavior inside specimen maybe unreliable. On the other hand, if you choose too many particles, it will take much time. Generally, particle sizes in simulation can be reduced by the same proportion according to their real sizes.

3.1.2 Test specimens

In this study, after several trials, specimens were set to be 3 cm wide and 6 cm height. A total of 6000 particles with diameters ranging from 0.4 mm to 0.96 mm were generated in specimens, and the size distribution was almost the same as the Toyoura sand often used. In order to consider the particle shape effects on shear behaviors, two types of specimens were generated using round particles (treated as disks of unit thickness) and irregular shaped particles, as being called “disk” and “clump” in Fig. 3.6, separately .

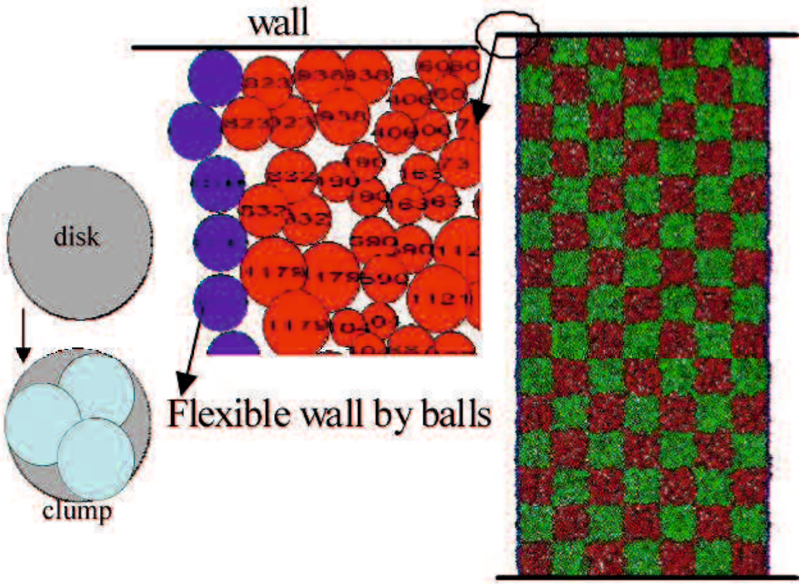

Figure 3.6 Specimens with disks and clumps

The irregular shaped particle “clump” was made by replacing each single particle with a clump consisting of 3 uniform disks, as shown in Fig. 3.6. The center positions of original disks were not changed. Radius and locations of the 3 balls in one clump are decided according to the following equations:

$$r_c=\alpha*r_b*\sin(\mathrm{Pi}/\mathrm{N})/(1+\sin(\mathrm{Pi}/N)) \tag{3.6}$$

$$x_c=x_b+\alpha*(r_b- r_c)*\cos(2*i*\mathrm{Pi}/N) \tag{3.7}$$

$$y_c=y_b+\alpha*(r_b- r_c)*\sin(2*i*\mathrm{Pi}/N) \quad (i=0,1,2) \tag{3.8}$$

where r_c, x_c, y_c are diameter and center coordination of the disks inside each clump; r_b, x_b and y_b are diameter and center coordination of original disk; α is a factor to adjust the overlap between disks and thus the clump shape varies; N is the number of balls compose each clump. In the simulations of this study, α is 1.2 and N is 3.

The selected shape of clump is rather ideal and the aspect ratio is not suitable to judge the shape. As shown in Fig. 3.7, there is only single contact between disks, while single and multiple contacts exist between clumps. Dense clumps have a maximum of 3 contact points and loose clumps have 1 or 2 contact points. This can represent particle roughness to some extent. The particle roughness had been considered in 2D DEM by setting multiple contact points between two disks (Jiang et al. 2009). Moreover, normal contact force between disks always points to the centers of the two disks, and thus rolling resistance is 0. The rolling resistance in real sands can be considered using clump model.

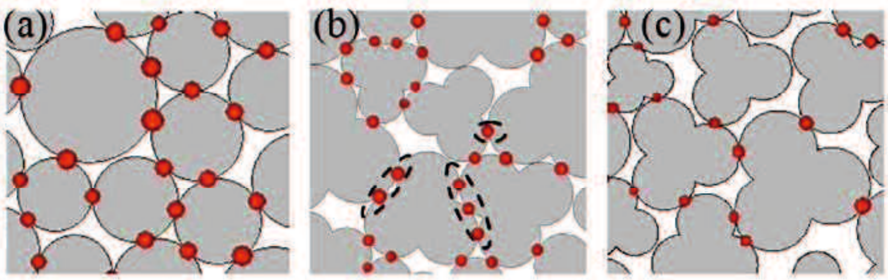

Figure 3.7 Contacts between particles: (a) dense disks; (b) dense clumps and (c) loose clumps

3.1.3 Boundaries and simulation parameters

The top and bottom of the model were confined by rigid wall boundaries, while the lateral sides were confined by flexible boundaries made of disks to simulate the membrane in the real test. The disks used for the membrane were uniform and had the same diameter with the smallest particles in specimens. No friction was supposed and a very high bonding strength was set among these membrane disks to prevent stripping. Single forces were applied to the membrane disks to supply the confining pressure.

Two dense specimens and two loose specimens were generated by giving different initial void ratios for both disk and clump models. All the specimens were consolidated at the same isotropic confining pressure of 100 kPa. The void ratio after consolidation is about 0.16 and 0.18 for dense clump and disk specimens, and 0.25, 0.24 for loose clump and disk specimens respectively. The main calculating parameters are listed in Table 3.1.

Table 3.1 Main parameters in the simulation

Parameter		**value**
Inter particle friction coefficient μ		0.5
contact stiffness	normal kn	3e8 N/m
	tangential ks	2e8 N/m
Density of disks or clumps ρ		2600 kg/m^3
Total number of disks or clumps N		6000
Particle-Wall friction		0.2
Flexible boundary friction		0
Contact model		Linear
Consolidation pressure		100 kPa
Initial void ratio e_0	dense	0.16, 0.18
	loose	0.24, 0.25

After consolidation, each specimen was sheared under two stress paths, as described in Fig. 2.1. The PSC test is simulated by biaxial compression, where the top and bottom plates are given a constant speed to compress the specimen while the confining pressure is kept constant. The PSCD test is simulated by biaxial decompression. Servo-control was set to the top and bottom walls to keep the vertical boundary stress constant. The confining pressure was reduced by decreasing the forces on the membrane disks at an interval (starts from 10 kPa), which was set to be smaller and smaller as peak or failure approaches. After that the forces on the membrane disks were kept constant and the specimen continued to be sheared until 10% axial strain.

3.1.4 Calculation method of local shear deformation

Past studies of both FEM and DEM simulations have shown that shear bands are not only related to the properties of materials but also much dependent on boundary conditions, especially for the positions and shapes of shear bands (Masuda et al. 1999, Rechenmacher 2006, Cheung and Sullivan

2008, Wang et al. 2007). In order to investigate local shear deformations, positions of some particles were traced during the shear. A strain calculation method presented by Wang et al. (2007) is referred. As shown in Fig. 3.8, several grid points were set at a fixed spacing in the specimen, and the disk or clump which is the closest to each grid point was chosen. This is judged by the equation (3.9). The displacements of grid points are thus thought as the same to the selected disks or clumps. The spacing was set to be about $3D_{50}$ in the simulation. It is found that positions of grid points and selected disks or clumps almost coincide with each other, as seen in Fig. 3.9.

$$\frac{d_j}{r_j} \le \frac{d_i}{r_i} (i = 1, 2 \ldots N_p, i \ne j) \tag{3.9}$$

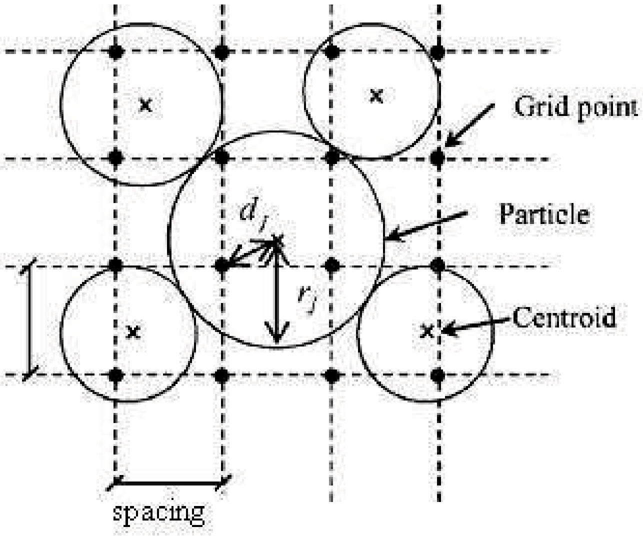

Figure 3.8 Grid points setting and particles selection (After Wang et al. 2007)

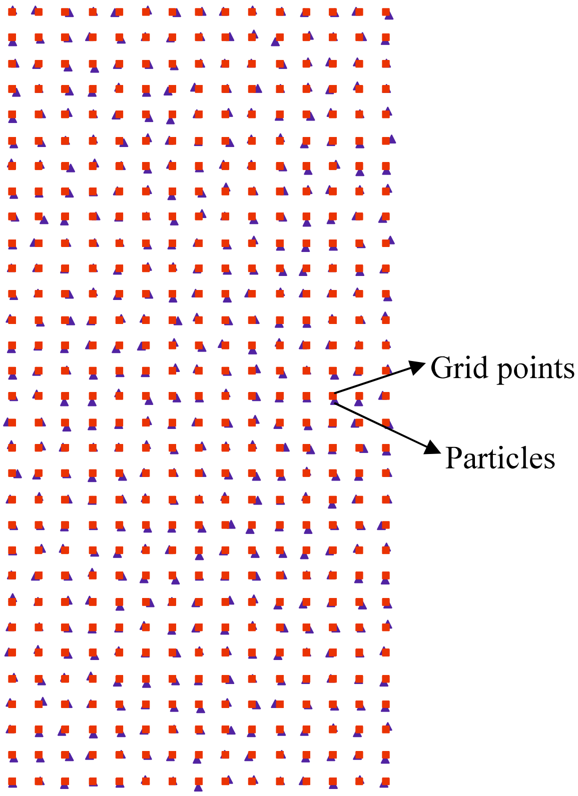

Figure 3.9 Locations of Grid points and selected particles

The value of the selected spacing will influence results of local deformation analysis. Taking the compression test of dense disk specimen as an example, influence of the spacing was investigated by comparing results under spacing of $1.5D_{50}$, $3D_{50}$ and $6D_{50}$, as shown in Fig. 3.10. It is found that different spacing results in the same shear band pattern, but very different values of local strain. Local strain decreases with increase of spacing. Some particles with large displacements will be missed if using too large spacing. On the other hand, if the spacing is too small, some tracing grids will locate at voids. Their displacements are still thought as the same as the nearest particles, and the local deformation will be amplified. Therefore, it is important to select an appropriate spacing according to the particle size distribution.

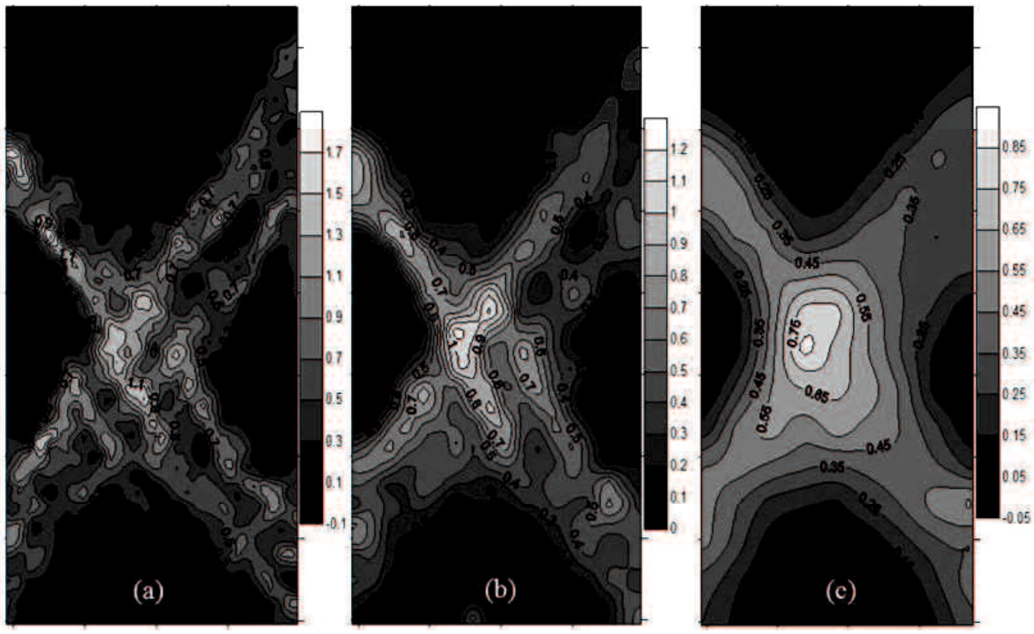

Figure 3.10 Comparison of local maximum shear strain distributions at different spacing in dense disk specimen in compression test: (a) $1.5D_{50}$; (b) $3D_{50}$; (c) $6D_{50}$

3.2 Simulation results

3.2.1 Macro stress-strain relationship

Figures 3.11(a) and (b) show the principal stress ratio-axial strain relationships in the two types of tests for disk specimens and clump specimens. It is clearly seen that the clump specimens show much higher peak and residual stress ratios. For dense clump specimens in Fig. 3.11(a), it is found that the initial stiffness and residual stress ratio are both higher in the PSCD test than in the PSC test, while for dense disk specimens in Fig. 3.11(b), only the initial stiffness is seen a little higher in the PSCD test.

Higher initial stiffness in the PSCD test was also found in laboratory test results for dense sands and glass beads, which is more obvious in sands.

Moreover, it is also found that the principal stress ratios at peak and residual state are both higher in the PSCD test than in the PSC test for irregularly shaped sands (Zhuang et al. 2013). However, only higher residual stress ratio is found for clump specimens in the simulation.

For both loose clump and disk specimens, there is almost no difference between the principal stress-strain relationships in the PSC and PSCD tests. This is the same with observed results of glass beads in the experiments.

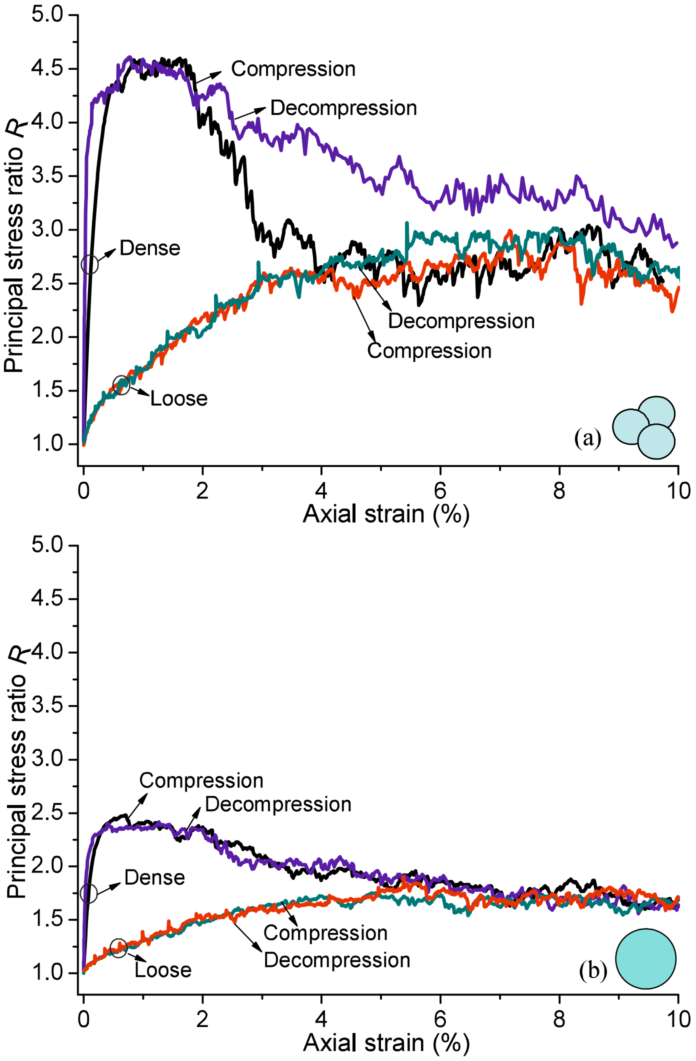

Figure 3.11 Principal stress ratio-axial strain relationships in the two kinds of test: (a) clump specimens; (b) disk specimens

3.2.2 Volume deformation

The total volume strain ε_v is calculated as

$$\varepsilon_v = \varepsilon_x + \varepsilon_y \tag{3.10}$$

ε_x, ε_y is the mean lateral and vertical strain respectively. ε_x was measured according to the mean width of specimen through calculating position of each ball in the flexible boundaries. Volume strain changes are compared in Figs. 3.12(a) and (b) for dense and loose specimens.

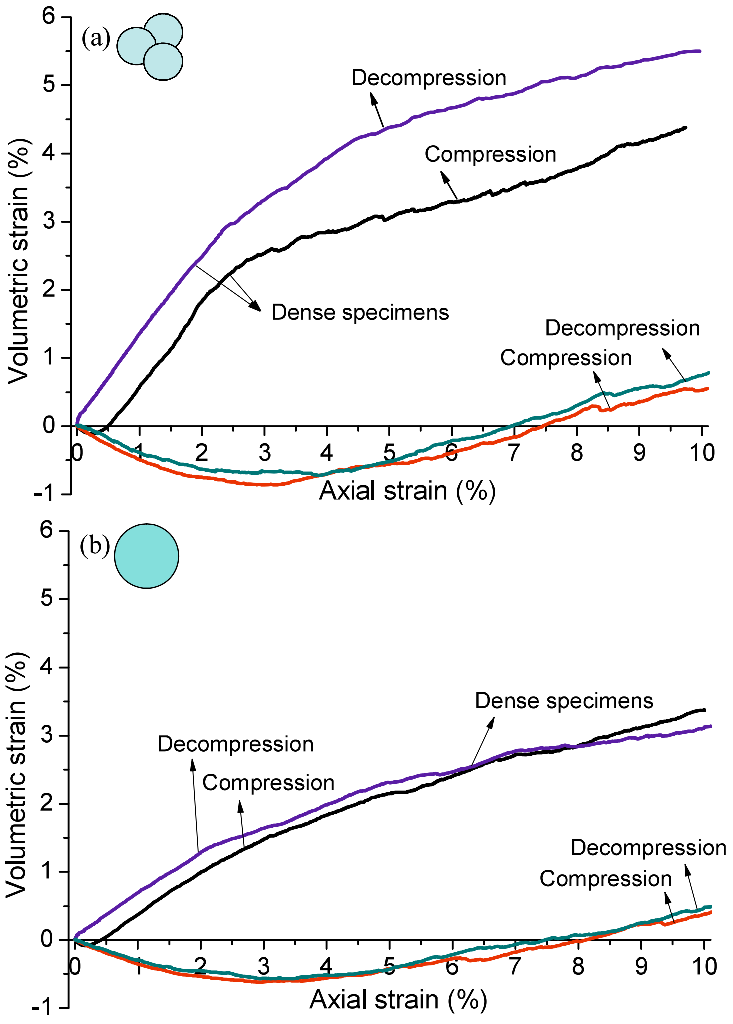

Figure 3.12 Volume change in the two types of test: (a) clump specimens; (b) disk specimens

In both dense disk and clump specimens results shown in Fig. 3.12(a) and (b), it shows contraction first and then dilation in the compression test, while it shows volume expansion first due to unloading and then dilation in the decompression test. Moreover, as the clump specimen behaves more volumetric strain in the decompression test than in the compression test at the same axial strain, more lateral extension (ε_x) happened in the decompression test according to Eq. (3.10). This indicates a higher anisotropy in the decompression test for dense clump specimen, which is proved by the fabric anisotropy in the later section.

For loose specimens, volume behaviors are very similar in the two types of test, regardless of disk or clump. All the loose specimens contract until 3–4% axial strain and then dilate. Compared with dense specimens, little difference between the compression and decompression tests is found in both loose clump and disk specimens.

3.2.3 Local shear deformation

Figures 3.13 and 3.14 show local displacement loci of clump specimens and disk specimens within 10% axial strain in different cases. Comparing the particles inside shear bands and those outside the shear bands, it is seen that translation of particles is smaller while rotation is larger inside shear bands.

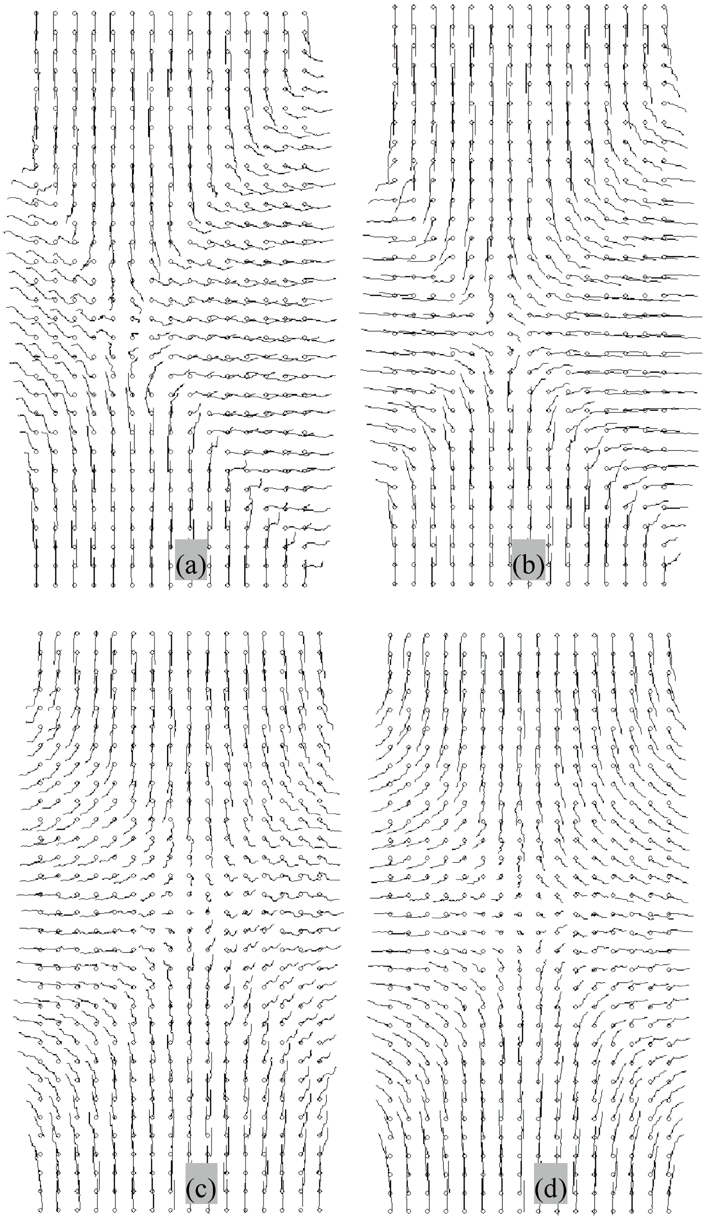

Figure 3.13 Local displacement vectors of clump specimens: (a) dense, compression; (b) dense, decompression; (c) loose, compression; (d) loose, decompression

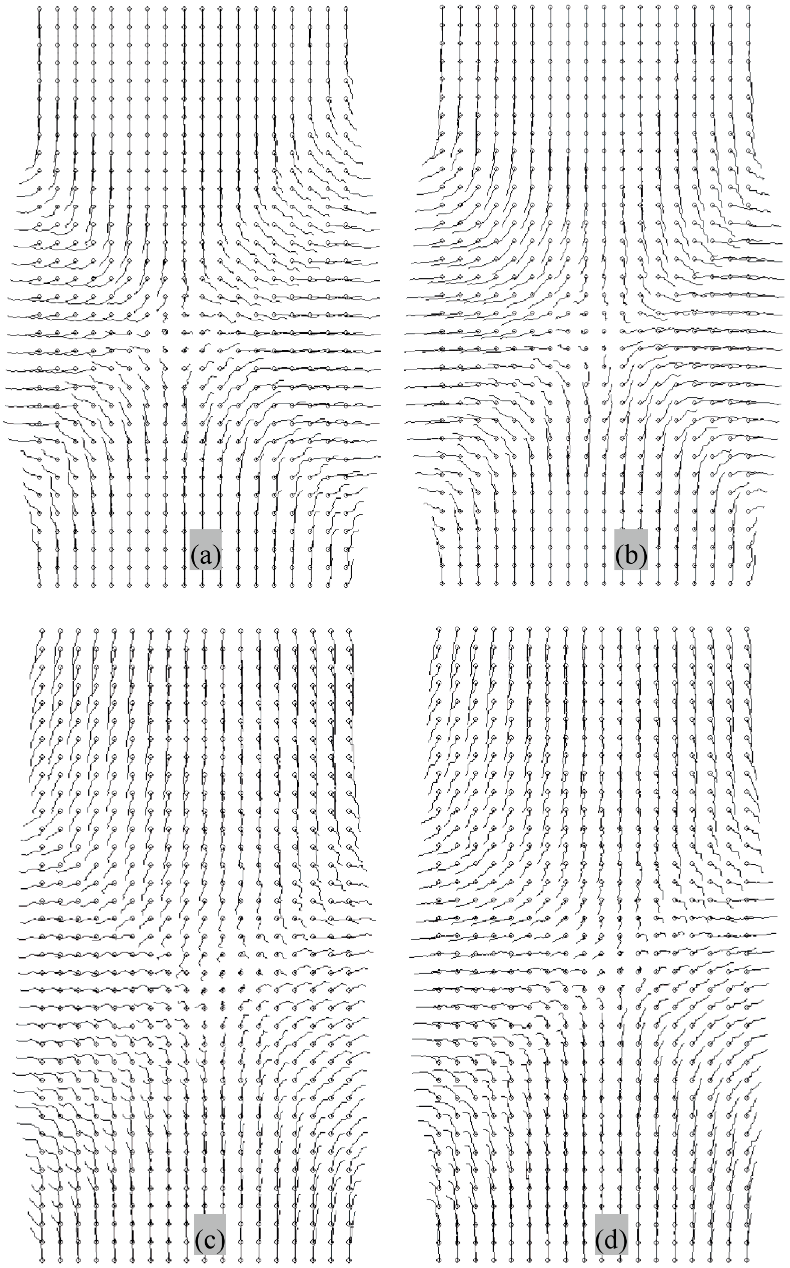

Figure 3.14 Local displacement vectors of disk specimens: (a) dense, compression; (b) dense, decompression; (c) loose, compression; (d) loose, decompression

Figures 3.15 and 3.16 show evolutions of local maximum shear stain in dense clump specimens in compression and decompression tests. Four states including the onset of dilation in compression test (ε_a=0.25%), the peak

(ε_a=1%), the softening (ε_a=2%) and the residual state (ε_a=10%) are chose. It can be seen that shear bands were formed between 0.25–1% axial strain, and similar conjugate shear bands were observed in both compression and decompression tests. Despite the similar shape and inclination angle, the shear bands are relatively narrower in the compression test than in the decompression test.

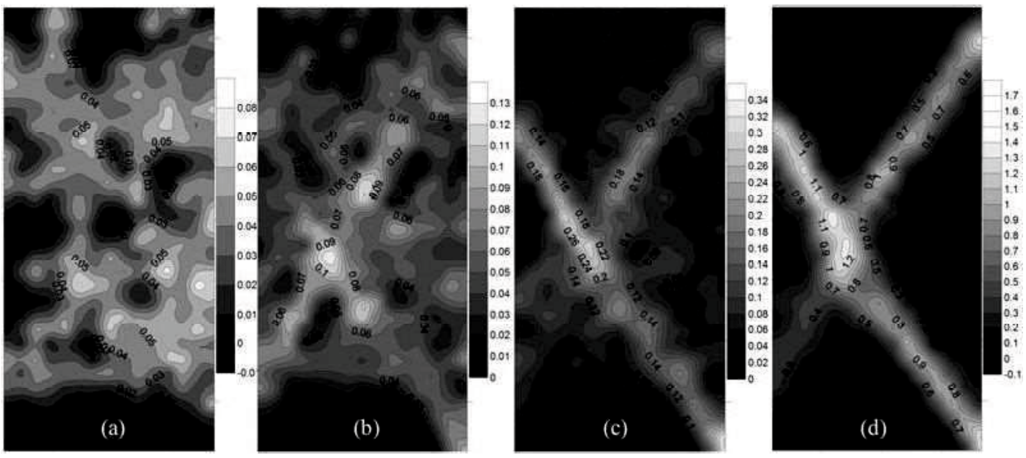

Figure 3.15 Evolutions of local maximum shear strain in compression test of dense clump specimen: (a) ε_a=0.25%; (b) ε_a=1%; (c) ε_a=2%; (d) ε_a=10%

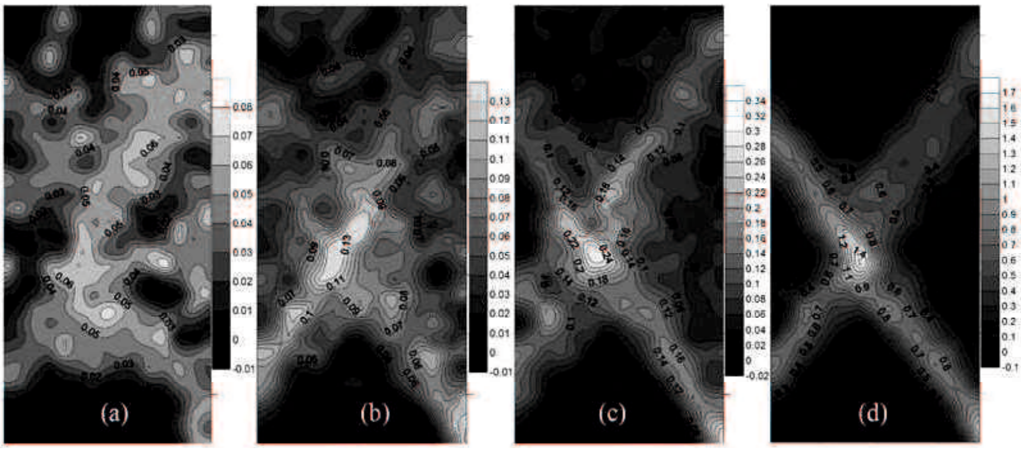

Figure 3.16 Evolutions of local maximum shear strain in decompression test of dense clump specimen: (a) ε_a=0.25%; (b) ε_a=1%; (c) ε_a=2%; (d) ε_a=10%

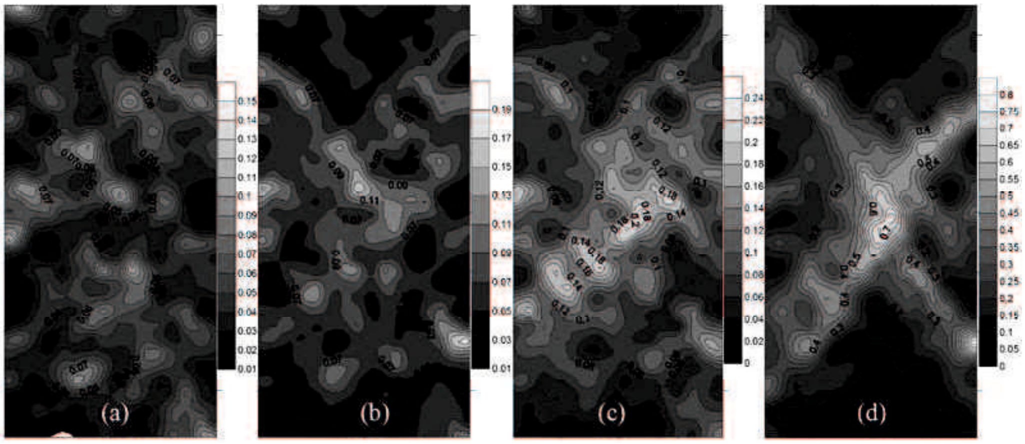

Figure 3.17 Evolutions of local maximum shear strain in compression test of loose clump specimen: (a) ε_a=2%; (b) ε_a=3%; (c) ε_a=4%; (d) ε_a=10%

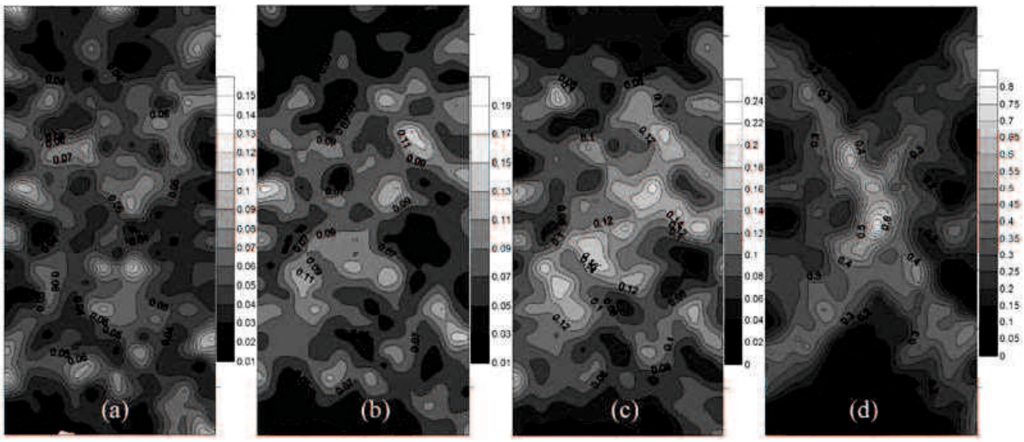

Figure 3.18 Evolutions of local maximum shear strain in decompression test of loose clump specimen: (a) ε_a=2%; (b) ε_a=3%; (c) ε_a=4%; (d) ε_a=10%

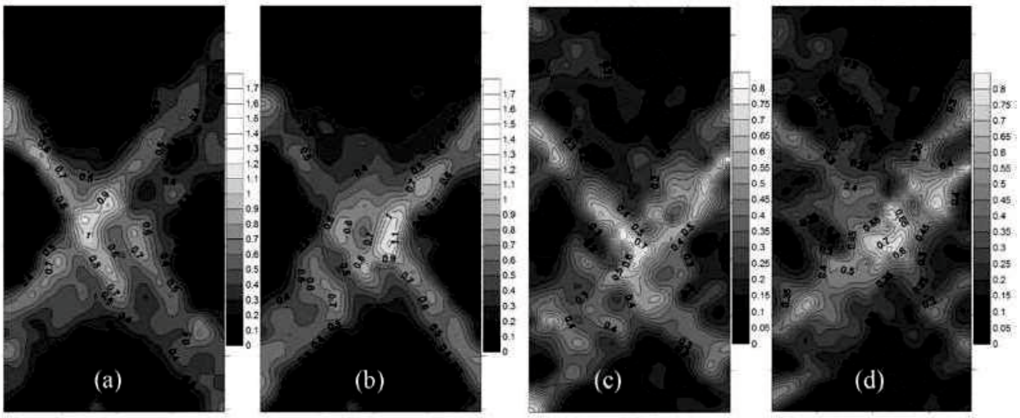

Figure 3.19 Local maximum shear strain distributions at ε_a=10% for disk specimens: (a) dense, compression; (b) dense, decompression; (c) loose, compression; (d) loose, decompression

3.2.4 Coordination number

Coordination number C_N is defined as the mean contact number for all the particles inside the specimen. In the PFC2D, it is calculated by

$$C_N = \frac{\sum_{N_p} n_c^{(p)} + \sum_{N_{cl}} n_c^{(cl)}}{N_p + N_{cl}} \tag{3.11}$$

here, $n_c^{(p)}, n_c^{(cl)}$ are the number of active contacts of disks and clumps respectively; N_p, N_{cl} are the numbers of disks and clumps respectively.

Variations of C_N with axial strain in different cases are shown in Fig. 3.20. It is clearly seen that coordination numbers in clump specimens are much higher than in disk specimens. For dense specimens in Fig. 3.20(a), in all the four cases, C_N decreased first and then kept constant. However, it decreased faster in the decompression test than in the compression test before approximately 1% axial strain, where shear band was clearly generated as noted by the dash line in Fig. 3.20(a). The value of C_N at residual state is different for clump specimens under the two stress paths, which is 4.0 in the compression test and 3.6 in the decompression test; while for the disk specimens, little difference is seen and the residual value of C_N is approximately 3.0 in the two types of test.

For loose specimens in Fig. 3.20(b), the initial value of C_N is approximately 3.5 for clump specimens and 3.0 for disk specimens. Little variation was seen except some small fluctuations in the decompression test. C_N is a little higher in the compression test than in the decompression test for clump specimens while always shows the same value for disk specimens.

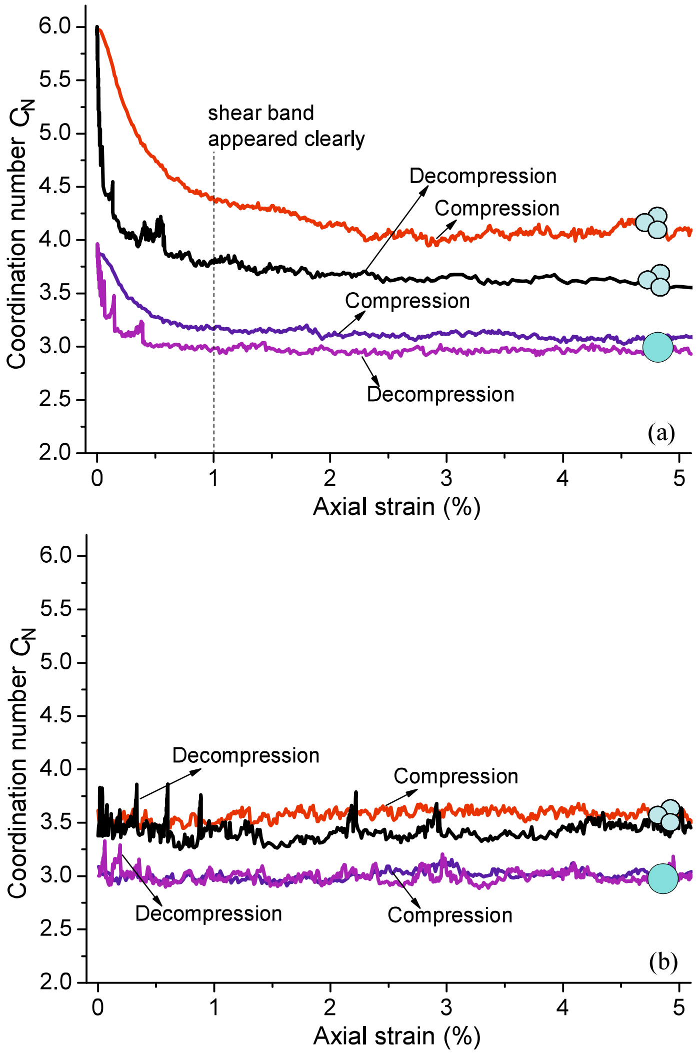

Figure 3.20 Variations of coordination number during the shear: (a) dense specimens; (b) loose specimens

Comparing Figs. 3.20(a) with (b), difference between variations of coordination number in the compression and decompression tests is much obvious in dense clump specimens, and is relative small in dense disk specimens and loose clump specimens. No difference is seen in loose disk specimens. It is possible that particle shape effects on the variation of coordination number under different stress paths are much more significant in dense state than in loose state.

3.2.5 Contact number distribution

Contact numbers at different directions are also counted inside specimens. The plane is divided evenly into 36 parts, and the right horizontal central axis of specimens is set as the initial direction (0°). Because of diagonally symmetric, only values ranging from 0~180° are given. The values are compared for different cases in Fig. 3.21 and Fig. 3.22 for dense and loose specimens respectively.

For all the four cases in Figs. 3.21(a)~(d), contact numbers near the vertical axis (90°) increase a little before the peak and then decrease, while they always decrease in other directions. Variations of contact numbers become larger and larger from the vertical axis to the horizontal axis (0°, 180°). Comparing the contact number distributions between Figs. 3.21 (a) and (b), Figs. 3.21(c) and (d) at the same axial strain, it is found that contact numbers decrease much quicker in the PSCD test than in the PSC test, especially for the pre-peak. Contact numbers lost a lot at very small strain (e.g., 0.01%) in the PSCD test, as can be seen from Figs. 3.21(b) and (d). At the residual state of 10% axial strain for all the four cases, contact numbers in all directions decreased compared to the initial state. However, the residual values of contact numbers in the PSCD test are lower than in the PSC test for both clump and disk specimens. This has already been proved by the coordination numbers in Fig. 3.20(a).

In loose specimens, contact number distribution during shear shows much different behaviors from that in dense specimens. For clump specimens in Figs. 3.22(a) and (b), contact numbers in the directions ranging from 50° to 130° increase gradually during shear, while decrease in other directions. At the residual state, contact numbers in the vertical direction is a little higher in the PSC test than in the PSCD test. For disk specimens in Figs. 3.22(c) and (d), similar behaviors are shown for both the PSC and PSCD tests. Contact number increased in both clump and disk specimens, but was considerable in clump specimens.

In general, despite the particle shape, contact number distributions in loose specimens show little difference between the PSC and PSCD tests compared to that in dense specimens. Therefore, it is also indicated that stress path effects are more significant in dense granular materials.

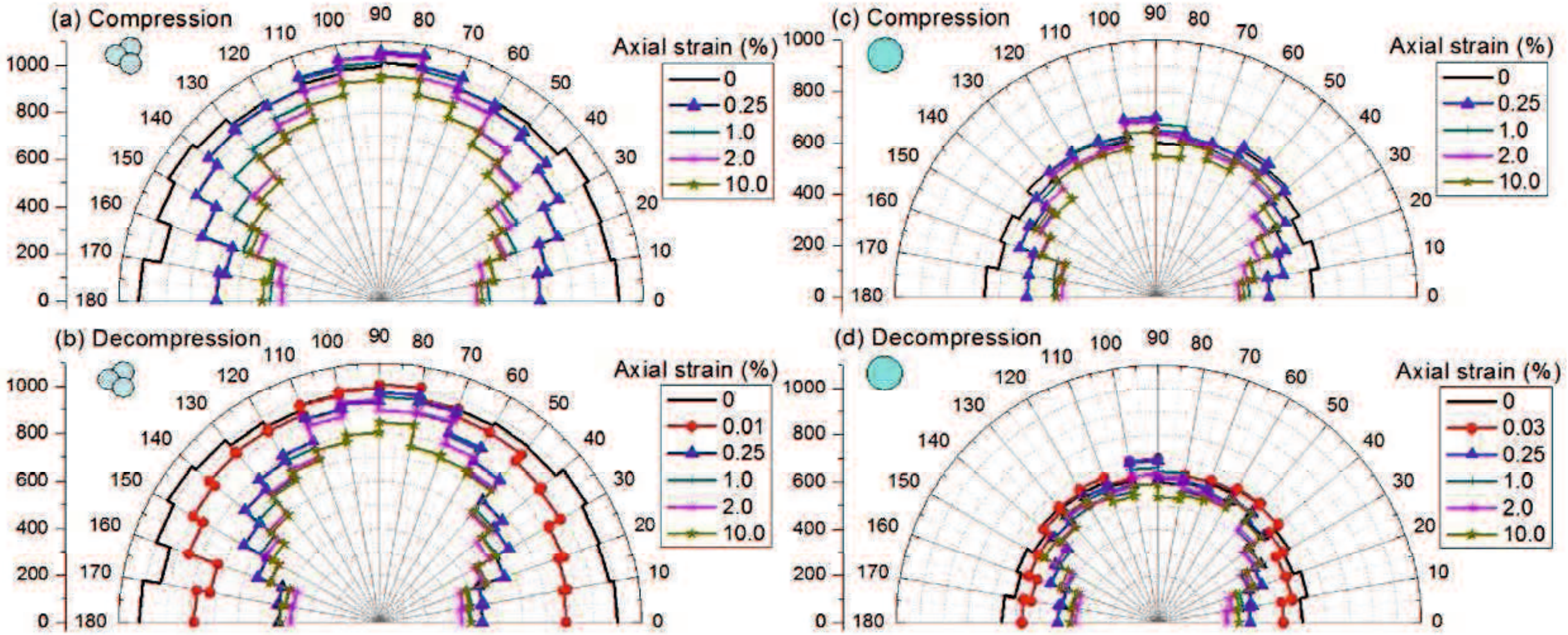

Figure 3.21 Contact number variations in different directions inside dense specimens during shear: (a) clump, PSC; (b) clump, PSCD; (c) disk, PSC; (d) disk, PSCD

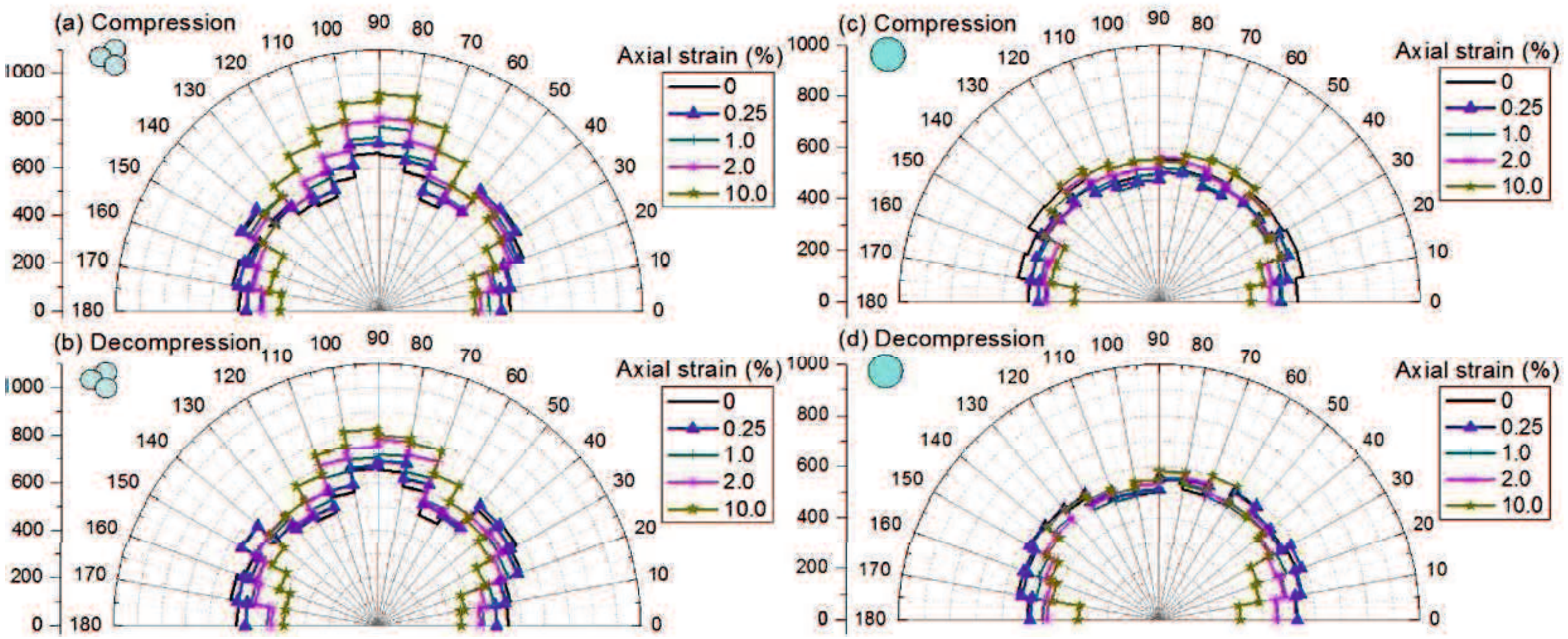

Figure 3.22 Contact number variations in different directions inside loose specimens during shear: (a) clump, PSC; (b) clump, PSCD; (c) disk, PSC; (d) disk, PSCD

3.2.6 Deviator fabric

Satake (1982) first presented the notion of fabric to define the structural anisotropy of granular material, which is defined by

$$\phi_{ij} = \frac{1}{C}\sum_{1}^{C} n_i n_j = < n_i n_j > \qquad (3.11)$$

n_{i}, n_{j} are contact vectors in *i* and *j* directions; *C* is the total contacts.

The degree of structural anisotropy can be evaluated by a deviator fabric

$$a = (\phi_1 - \phi_3) \qquad (3.12)$$

where ϕ_1 and ϕ_3 are the vertical and horizontal fabric in 2D case.

Figures 3.23(a) and (b) show variations of deviator fabric during shear in clump and disk specimens separately. For both dense clump and dense disk specimens, deviator fabric increases before peak then decreases after peak, and finally reaches the same value at the residual state. However, deviator fabric increases faster in the PSCD test than in the PSC test. For loose specimens, deviator fabric always increases until the residual state, and there is almost no difference between the PSCD and PSC tests. It is inferred that the critical deviator fabric is dependent on the particle shape, while is not dependent on initial void ratio and stress path. This is consistent with the study by Maeda *et al.* (2010) that the critical value of deviator fabric is only seen to be dependent on grain shape.

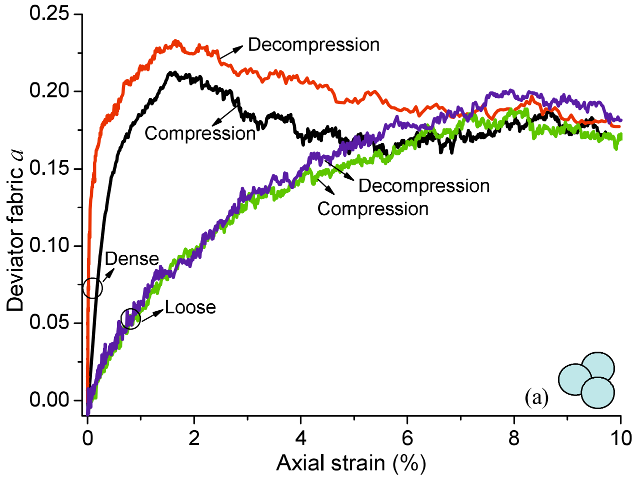

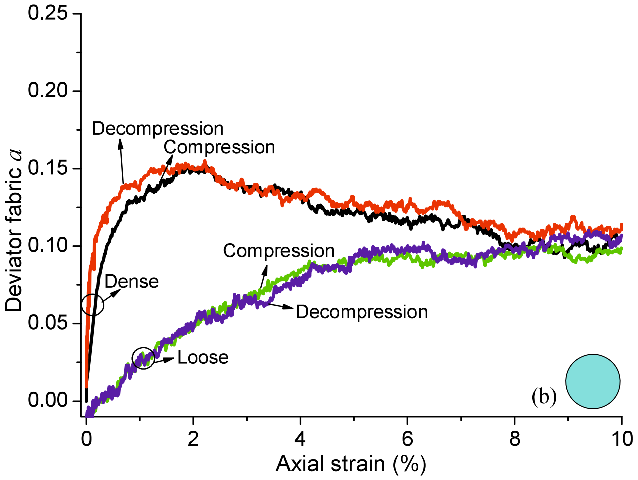

Figure 3.23 Variations of deviator fabric: (a) clump specimens; (b) disk specimens

Compared to the disk specimens, deviator fabric is much higher in the clump specimens. The peak value is 0.23 and 0.21 in dense clump specimens in the decompression and compression tests, while is 0.16 for disk specimens independent of stress path. The residual value is approximately 0.18 for clump specimens and 0.1 for disk specimens. Therefore, it is known that high anisotropy is easier to be formed in irregularly shaped particles, and contributes to higher shear strength of granular materials.

To summarize the simulation results, it is likely that particle shape effect on different shear behaviors under compression test and decompression test are significant for dense specimens, while it is insignificant for loose specimens. Further comparisons are made below from the viewpoint of energy variation to investigate the underlying mechanism.

3.3 Energy variations

PFC program allows us to trace energies and works during the calculation. For the non-cohesive particles, the main items include strain energy E_s, frictional work E_f, body work E_b, boundary work E_w and kinetic energy E_k (almost 0 for quasi-static calculation) (Itasca, 2008). Strain energy E_s is elastic and directly lies on normal and tangential contact forces at all contacts, while frictional work E_f is dissipated plastic energy due to sliding at contacts. Body energy is accumulated work done by body forces including gravity force on the assembly, and boundary work is accumulated work done by all walls on the assembly. Since membrane disks are used in the calculation, the total external work W should be calculated by the body energy and boundary work. The internal work includes the strain energy and dissipated energies. According to the energy balance rule, there should have

$$\varDelta W = \varDelta E_b + \varDelta E_w = \varDelta E_s + \varDelta E_f + \varDelta E_k \qquad (3.13)$$

The strain energy and frictional energy are calculated as

$$E_s = \frac{1}{2}\sum_{N_c}\left(\frac{\left|F_i^n\right|^2}{k^n} + \frac{\left|F_i^s\right|^2}{k^s}\right) \qquad (3.14)$$

$$E_f = \sum_{N_c}\left(\left\langle F_i^s\right\rangle \left\langle \Delta U_i^s\right\rangle^{slip}\right) \qquad (3.15)$$

where, k_n, k_s, F_i^n, F_i^s are the normal and tangential contact stiffness and the normal and tangential contact force respectively; N_c is the total contact number; $\varDelta U_i^s$ is the relative tangential displacement.

Matsushima and Chang (2011) noted that the external work due to boundary load is equal to the internally stored energy at contacts plus the dissipated energy. The dissipation due to damping was found to be much smaller than the dissipation by the interparticle friction.

3.3.1 Global energy variations

After isotropic consolidation to 100kPa, the initial strain energy is 0.27J, 0.31J, 0.44J and 0.42J for dense clump, dense disk, loose clump and loose disk specimen separately. Figs. 3.24 and 3.25 show incremental variations of the W, E_f and E_s (initial values before shearing are set to be 0) with the deviator stress q in dense clump specimens and dense disk specimens separately. The curves before and around the peak are shown in a larger scale to be seen clearly. It is seen that clump and disk specimens show similar rules. Moreover, the external work is almost equal to the sum of the three items of ΔE_{s}, ΔE_{f} and ΔE_{k}, and the Equation (3.13) is verified.

In the compression test in Figs. 3.24(a) and 3.25(a), strain energy increased before peak and then decreased, while the dissipated frictional work increased monotonically. In the decompression test in Figs. 3.24(b) and 3.25(b), strain energy decreased (elastic energy released due to unloading) until the peak, after that it almost keeps constant. The frictional work dissipated as the same as in the compression test. As a result, the external work was minus before the peak, which means the specimen does work to the boundary walls.

It is also found that variation of strain energy is different in the two types of test. As mentioned above, strain energy is the total elastic energy at all the contacts. This energy has been noted from macro viewpoint in past studies. Cucoovillo and Coop (1997) thought that the total work W done by the stresses at the boundary of the soil element was partly dissipated in friction and partly spent in disrupting the structure of the soil. This idea was followed and further explained by Guo and Su (2007), who noted that the soil structure refers to inter-particle locking associated with particle angularity. For a unit volume, the energy relation was expressed by

$$\Delta W = \Delta W_{fric} + \Delta W_{struc} = q'\delta\varepsilon_{\mathrm{s}}^{\mathrm{p}} + p'\delta\varepsilon_{\mathrm{v}}^{\mathrm{p}} \tag{3.16}$$

where q' and p' are effective shear stress and mean stress; $\varepsilon_{\mathrm{s}}^{\mathrm{p}}$ and $\varepsilon_{\mathrm{v}}^{\mathrm{p}}$ are the plastic components of the volumetric and shear strains.

Moreover, Collins (2003, 2005) described the contact energy stored in soil elements as the free energy Ψ, and the total work increment of a representative volume element

$$\delta W = \mathrm{d}\Psi + \delta\Phi = p\mathrm{d}e_{\mathrm{v}}^{\mathrm{e}} + p_c\mathrm{d}e_{\mathrm{v}}^{\mathrm{p}}/2 + \delta\Phi \tag{3.17}$$

where $\delta\Phi$ is increment in dissipation, p and p_c are effective and consolidation pressures, and $e_{\mathrm{v}}^{\mathrm{e}}$ and $e_{\mathrm{v}}^{\mathrm{p}}$ are elastic and plastic volume strains.

Therefore it is thought that the strain energy is related to the mean stress and plastic volume deformation from the macro viewpoint.

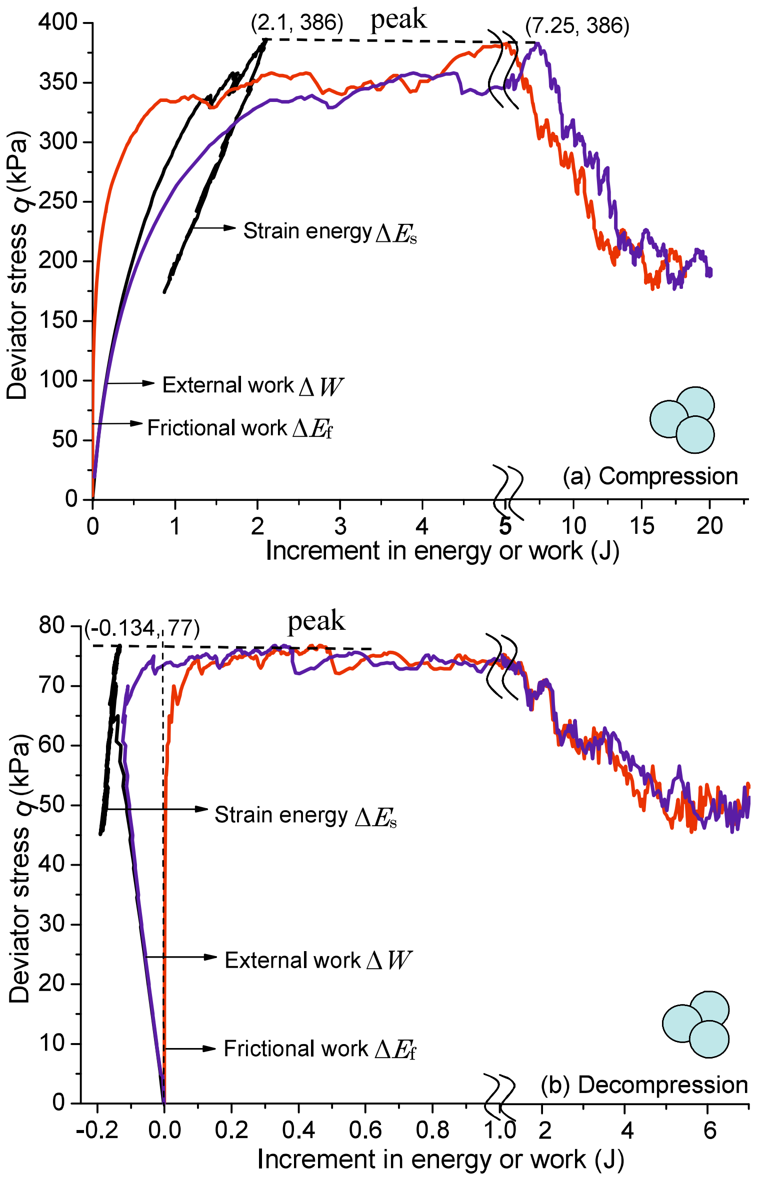

Figure 3.24 Variations of three main works (energies) with the deviator stress q in dense clump specimens: (a) compression, (b) decompression

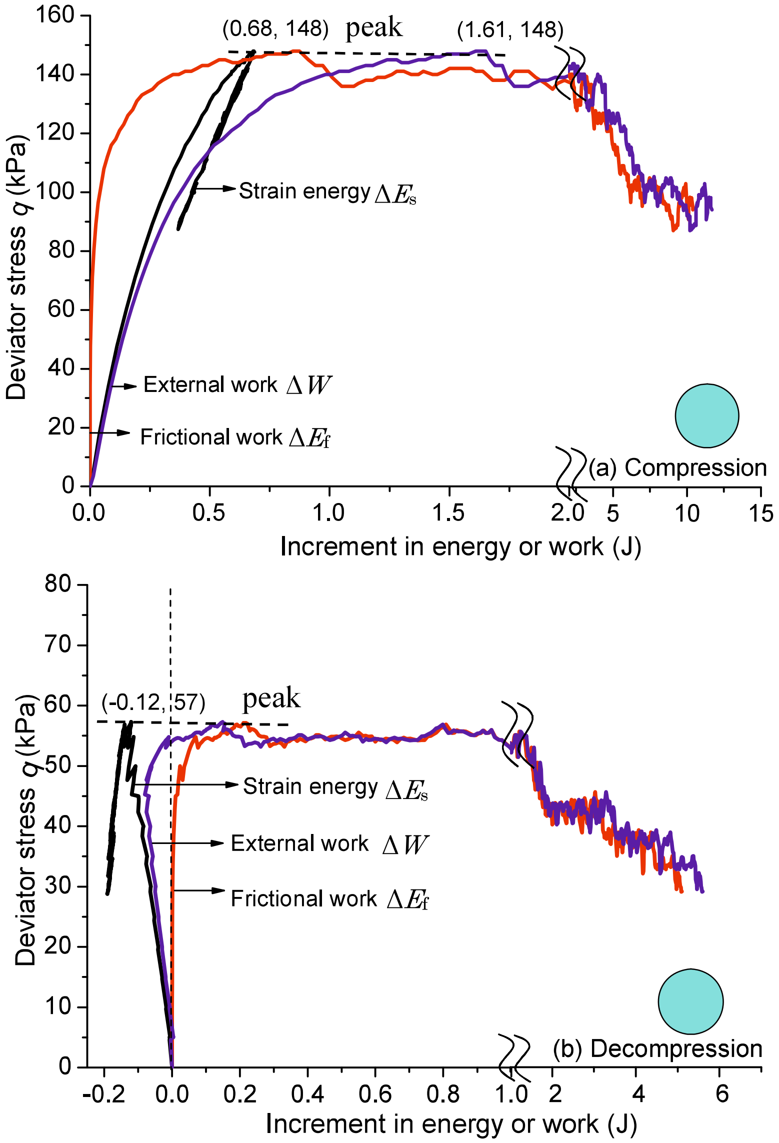

Figure 3.25 Variations of three main works (energies) with the deviator stress q in dense disk specimens: (a) compression; (b) decompression

3.3.2 Strain energy variation with mean stress

Figure 3.26 shows variations of strain energy ΔE_s (increase '+', decrease '-') with mean stress $p = (\sigma_1+\sigma_3)/2$ in the isotropic compression and decompression tests ($\sigma_1=\sigma_3$) for different specimens. Here, the slope of the $p - \Delta E_s$ curve is noted by

$$k = \Delta E_s / \Delta p \tag{3. 18}$$

It can be seen that in both of isotropic compression and decompression tests, the slope increased across the dense clump, dense disk, loose clump and loose disk specimens. The difference between the dense clump and disk specimens, loose clump and disk specimens is only due to the particle shape effect. The difference between the dense and loose clump specimens or the disk specimens is due to the initial void ratio effect. The effect of the initial void ratio is higher than the particle shape effect for the four types of specimens in this study. The variation pattern of strain energy in isotropic compression and decompression test seems independent of particle shape and initial state.

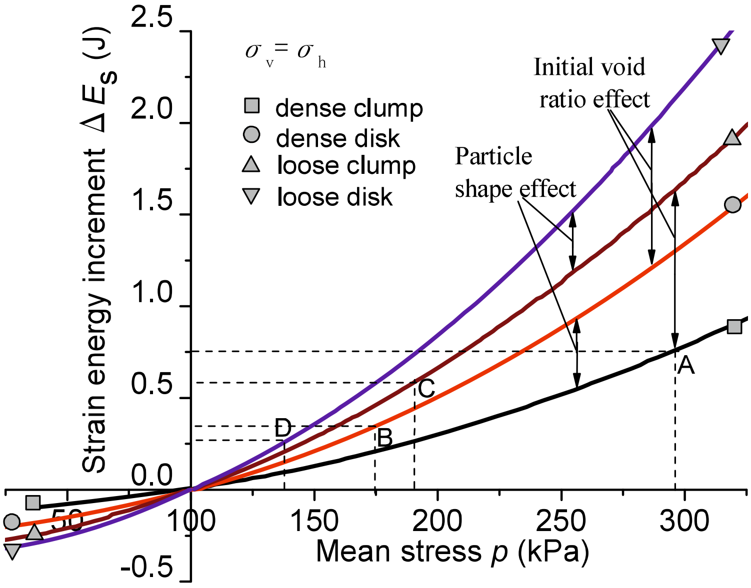

Figure 3.26 Variations of strain energy in isotropic compression and decompression tests

Figure 3.27 shows p–ΔE_s curves in compression tests and decompression tests. According to the compression test results in Fig. 3.27(a), the two dense specimens have the same variation pattern while the two loose specimens have a different variation pattern. The clump specimen gained more strain energy than the disk specimen and also dense specimen gained more than loose specimen. In the decompression test, strain energy decreased monotonically (Fig. 3.27(b)). It can also be seen that the strain energy variation pattern during shearing is determined by the stress path and initial packing density while independent of the particle shape. When comparing points A~D in Fig. 3.26 with points A'~D' in Fig. 3.27(a) at the same mean stress in each case, it is found that more strain energy is stored in the compression test than in the isotropic compression test.

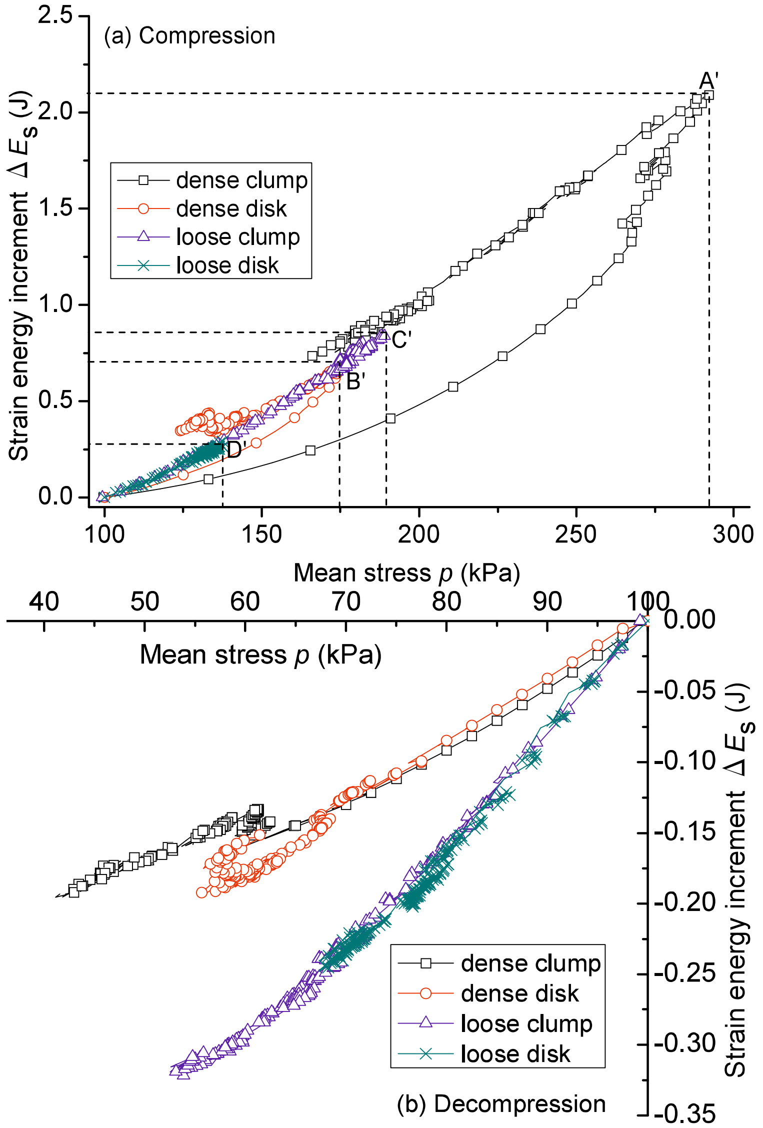

Figure 3.27 Variations of strain energy: (a) compression; (b) decompression

3.3.3 Strain energy variation rate with mean stress

Although the $\Delta E_s - p$ curves in Figs. 3.26 and 3.27 didn't follow the same variation pattern, they can be well fitted by polynomials of degree no more than 3:

$$\Delta E_s = \mathrm{A}p^3 + \mathrm{B}p^2 + \mathrm{C}p + \mathrm{D} \qquad (3.19)$$

A, B, C and D are parameters for the fitted curves. When $p = p_c = 100$ kPa, $\Delta E_s = 0$. For dense specimens, $\Delta E_s - p$ curves before and after the peak are treated separately.

As the net strain energy is much dependent on mean stress, to compare strain energy variation rates with mean stress increment under different stress paths, slope of $\Delta E_s - p$ curve is proposed and it is calculated by differentiation of the equation (3.19):

$$k = \partial(\Delta \mathrm{E}_s) / \partial \mathrm{p} \qquad (3.20)$$

Then k value at each mean stress level can be obtained according to equation (12). Figs. 3.28(a) ~ (d) show the k values being plotted with mean stress p under the different stress paths for different specimens, separately.

Generally, k increases with increase of mean stress in loading tests and decreases with decrease of mean stress in unloading tests. For the isotropic compression and decompression tests, the curves in Fig. 3.26 can be well fitted by second degree polynomials and therefore k displays a linear relationship with mean stress. The variation patterns in compression and decompression tests are different in dense specimens while they are very similar in loose specimens. As shown in Fig. 3.28(a) and (b), in the compression test, k shows a quadratic relationship with mean stress only before the peak in dense specimens, after the peak it has a sudden large decrease and keeps constant. In the decompression test, k decreases linearly with decrease of mean stress until the peak and then keeps constant. For loose specimens in Fig. 3.28(c) and (d), k always varies linearly with mean stress regardless of stress path.

In all the figures, it can be seen clearly that lines under the two shearing stress paths locate above those under isotropic compression and decompression stress paths. This means strain energy variation rate is higher under shearing than that under isotropic consolidation, as discussed in the previous sub-section. When comparing at the same stress level, *k* value is much higher for dense disk specimen than that of dense clump specimen especially in loading tests. However, *k* values are almost the same for loose clump and disk specimens in both compression and decompression tests. Moreover, when comparing Figs. 3.28(a) with (c), and Figs. 3.28(b) with (d), it is found that *k* values in loose specimens are much higher than those in dense specimens at the same stress level under each stress path.

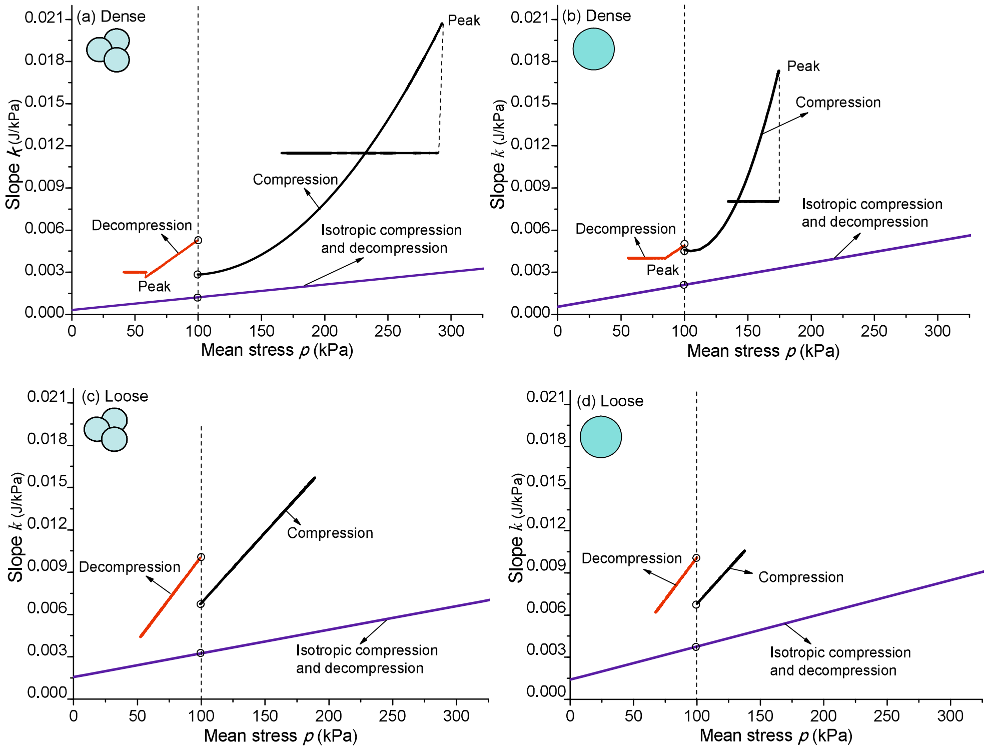

Figure 3.28 Comparisons of slopes of strain energy variation with mean stress: (a) dense clump; (b) dense disk; (c) loose clump; (d) loose disk

The behavior was considered to be influenced by the interlocking among particles. The interlocking is stronger in angular particles than that in round particles, and also stronger in dense specimens than that in loose specimens. When particles are interlocked, the relative displacements between particles shall become difficult and thus strain energy varies little. As a result, the stiffness of specimens behaves strong. In the loading shear test with mean stress increased, the interlocking developed until the peak strength and then failed. Instead, for the shear test with decreasing confining pressure, variation of interlocking gets smaller from the beginning. Thereby, the particle shape effect is different on the different stress path and the difference is more significant in dense specimens.

3.3.4 Discussion on strain energy variation from micro-viewpoint

From micro viewpoint, variation of strain energy only depends on the contact force at all the contacts in specimens (the contact stiffness is constant in the linear contact model). If the contacts distribution is different, the force chains at contacts will certainly be different. Different variation of particle contacts is thought to be the basic reason to explain why strain energy variations are different. Figs. 3.20–3.22 have shown that for dense specimens, average coordination number and contacts distribution both varied differently between the compression test and decompression test, while showed almost the same variations for loose specimens. This is the reason why strain energy behaved much different in the two types of test for dense specimens but not for loose specimens.

However, there are so many contacts in the specimen and their variations are unpredictable currently. As explained in Fig. 3.7, the disks have only single contact, while the clumps have 1~3 multiple contacts, which will produce interlocking. Besides, the total contact number in clump specimen is larger in clump specimen than in disk specimen in despite of dense or loose condition. As a result, particle shape effect is reflected on both the total contacts in the specimen and local contacts between particles.

An interesting finding is about the contact forces at 3-point contacts in dense clump specimen. Local specimens including such typical contacts before and during shearing are shown in Fig. 3.29. The particles in Figs. 3.29 (a) and (b) are not the same ones, particles in (b) are near the shear band. Width of the force chain is proportional to the contact force. Before shearing, contact forces at the 3-point contacts (A, B, C) are very small comparing their force chains with the main force chain. During shearing, contact forces at the 3-point contacts (D, E, F, G) are still found to be very small. Therefore, it is thought that stain energy at these contacts has little contribution to the total strain energy. Moreover, in the whole specimen, locations of 3-point contacts changed and the number of such multiple points contact increased during shearing. Particle shape effect on the variation of individual contact and force chain distribution is beyond this study. However, it is believed that this will help linking stain energy variation with macro behavior of granular materials.

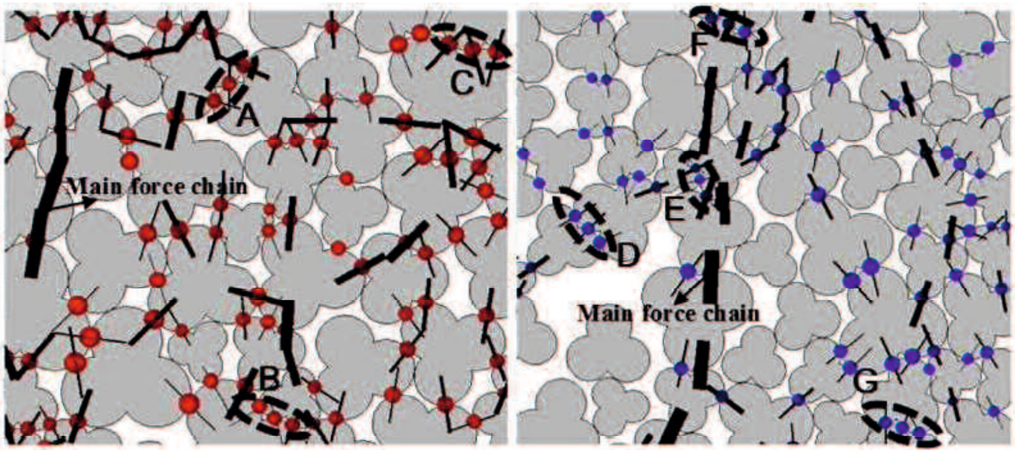

Figure 3.29 Multiple contacts and force chains in dense clump specimen: (a) before shearing; (b) during shearing.

3.4 Conclusions

Shear behaviors of granular materials under biaxial compression and decompression were analyzed using DEM simulation. Particle shape effects were considered for both dense and loose specimens. It is found that particle shape effects on shear behaviors under the two stress paths are much obvious in dense specimens. Some detailed conclusions are drawn as follows:

(1) Principal stress ratio – axial strain relationship was different in the compression and decompression tests for dense clump specimens. Initial stiffness was higher in decompression test. There was little difference for loose clump specimen, both dense and loose disk specimens.

(2) The decompression test showed only dilation for dense specimens, and the dilation was clearly higher than in the compression test for clump specimens. Similar volume behavior was shown for loose specimens in the two types of test despite the particle shape.

(3) Similar conjugate shear bands were found in the two types of test for both clump and disk specimens. Shear bands start before the peak in dense specimens, and before the onset of dilation in loose specimens.

(4) Coordination number decreased quicker and more in the decompression test than in the compression test for dense specimens, while had little change in loose specimens despite the particle shape. Critical coordination number is influenced by both stress path and particle shape, especially in dense specimens.

(5) Deviator fabric before the peak was higher in the decompression test than in the compression test for dense specimens. There was almost no difference in both loose clump and disk specimens. Critical deviator fabric is only dependent on particle shape.

(6) Total external work on the specimen is mostly converted into dissipated frictional energy and elastic strain energy stored at particle contacts. For dense specimens at the peak, more work is dissipated and therefore less work is converted into strain energy in the clump specimen than those in disk specimen in the biaxial compression test; in the decompression test, more strain energy is released in the clump specimen than that in the disk specimen.

(7) Other things being equal, strain energy variation rate with the mean stress is higher in the loose specimens than in the dense specimens, and is also higher in disks than in clumps. Furthermore, strain energy storage or

dissipation is much related to the particle interlocking, which is dependent on the particle shape as well as relative density.

According to the simulation results and referring to the former experimental results, it is thought that irregularly shaped particles can be well simulated by clump model in the DEM simulation. Further study is expected in the future aiming on the particle interlocking.

Chapter 4 Unloading shear behavior of granular materials with different particle shapes in retaining wall model tests

The previous two chapters have shown shear behaviors of granular material specimens under specified stress paths. The specimens suffered load controlled or deformation controlled loading. In practical engineering, boundary conditions are much complex. They maybe load controlled or displacement controlled or the mix of them. Chu and Wanatowski (2009) noted that loading mode has influence on strain softening and instability behavior of sand in plane-strain tests. Past study on model tests of retaining wall has shown that movement of retaining wall has large influence on the earth pressure and deformation of soils behind the wall (Tejchman 2004, Niedostatkiewicz et al. 2010, Widuliński et al. 2011), as well as mean particle size.

In this chapter, a series of retaining wall model tests under 1-g condition were performed to investigate unloading behavior in open cut excavations considering different wall boundaries. The same Ube sand NO.6A, Toyoura sand and Glassbead2 were used. The DIC method is used again to investigate progressive deformation in granular materials.

4.1 Test setup

Model tests were performed using a metal box with thick plastic confining plates at front and back sides. The plates are designed transparent to take photos for image analysis. The retaining wall is a piece of aluminum plate with about 40cm long and 20cm wide, and is supported by two upper wheels and two lower wheels connected to a motor apparatus. The four wheels can move forward or backward in a speed of 0~1.4 mm/min. The retaining wall is set to cling to the four wheels and sit on the foundation at the beginning, and can moves as a rigid body based on the wheels. Translation or rotation of the wall is controlled by embedding depth of the wall. The embedding depth is 0 in case of wall translation, and is about 5~10 cm in case of wall rotation. The foundation is 50cm long, 5~10cm high and 20cm wide. The space behind the retaining wall is 30cm long, 50cm high and 20cm wide. Two soil cells with a diameter of 3.4cm are embedded on the wall to measure pressures generated by the granular materials. Detail designs are shown in Fig. 4.1(a).

The two sands and glassbead2 introduced in Chapter 2 were used again. Dense and loose dry samples were made. For dense sand samples, air pluviation sampling method is used; for dense glassbead2 samples, tamping method is used. Loose samples are made by pouring method with almost no falling height from the sample surface. As a result, final relative density for dense samples is larger than 75%, and for loose samples it is no more than 30%. A case of Toyoura sand is shown as an example in Fig. 4.1(b).

The main test order is as follows:

(1) Preparation of foundation;
(2) Setting the retaining wall;
(3) Sample preparation of materials behind the wall;
(4) Setting camera and lights;
(5) Choose the speed of wall, turn on the switch and unloading starts.

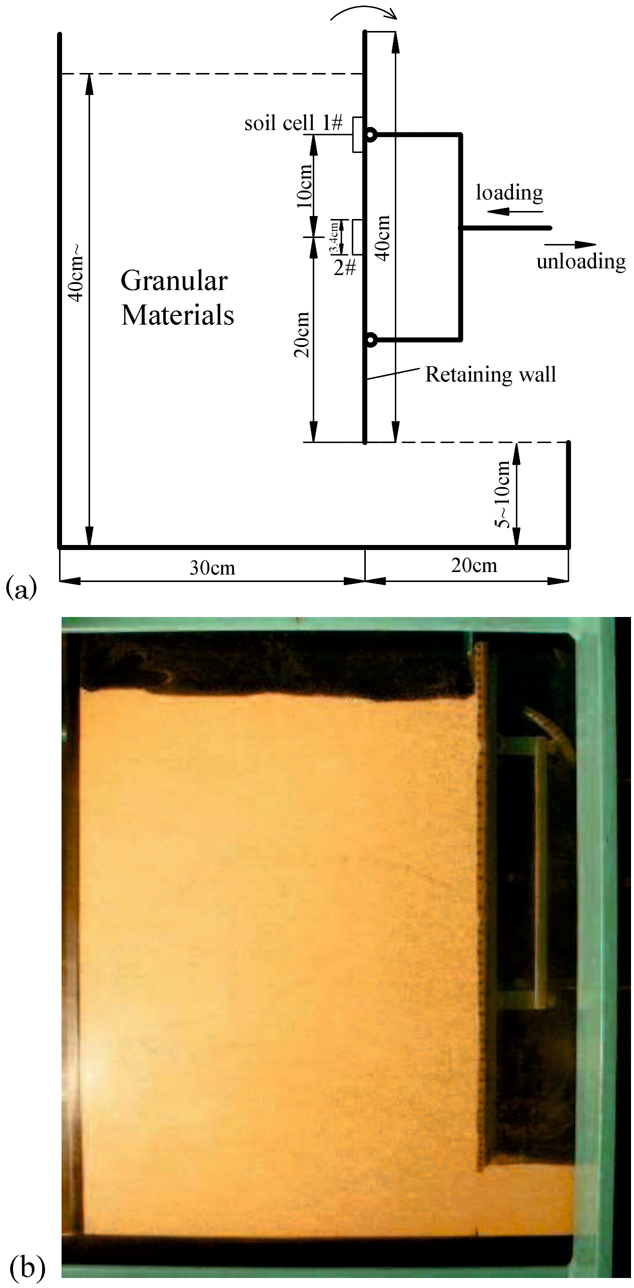

Figure 4.1 Sketch of model box and test photo: (a) sketch; (b) test photo

In this study, the unloading speed was fixed at 0.42 mm/min for investigation of shear band patterns and it is low enough for generating stable deformation. Speeds of 0.84 mm/min, 1.26 mm/min were also compared to investigate influence of unloading speed of wall. Two pieces of sponge strip were pasted to the front and back side of wall plate, therefore the wall did not touch the glass window of the model box. The sponge was greased to minimize friction between sponge and glass window. The frictional force between the two was tested under condition of moving wall before sample preparation. It is found that the frictional force is no more than 1N and therefore it has no influence to the measured wall force during the following experiments.

4.2 Test results and analysis

4.2.1 Cases of active wall translation

Taking the case of loose Toyoura sand as an example, loci of the retaining wall is shown in Fig. 4.2. In the figure, the initial horizontal coordinates of the two points are set to 0, and rightward unloading displacement is noted as positive. The vertical coordinate of the sample surface is set to 0, and the depth in the vertical axis means vertical distance away from the sample surface. It can be seen that the wall underwent translation for about 15 mm total horizontal displacement, and penetration of 12 mm happened during this period. The wall then moved with both translation and rotation but without penetration.

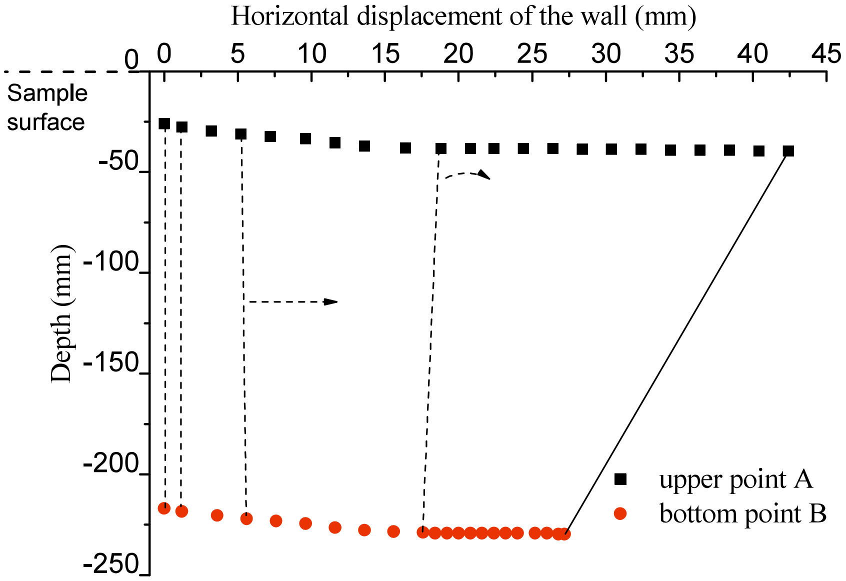

Figure 4.2 Trace of the retaining wall movement

(1) Variation of active force on the retaining wall

Figure 4.3 shows the variation in the resultant active force on the wall with the mean horizontal displacement of the wall *u*. In each case, the resultant force decreased quickly within a small displacement (smaller than 2 mm). We found that the resultant force decreased more quickly in dense samples than in loose samples for all three materials. After the quick decrease, the force increased a little with dense sands and then decreased gradually to zero while it only decreased gradually to zero in loose sands. This also means that sands can finally reach a self-standing state. Loose and dense Glassbead2 samples showed similar behavior, but with some differences from the two sands. After the quick decrease, the resultant wall force increased slightly until about 10 mm wall displacement and then decreased again. The glass beads did not reach a stable state; even at a large displacement of the retaining wall, the resultant force was around 20 N.

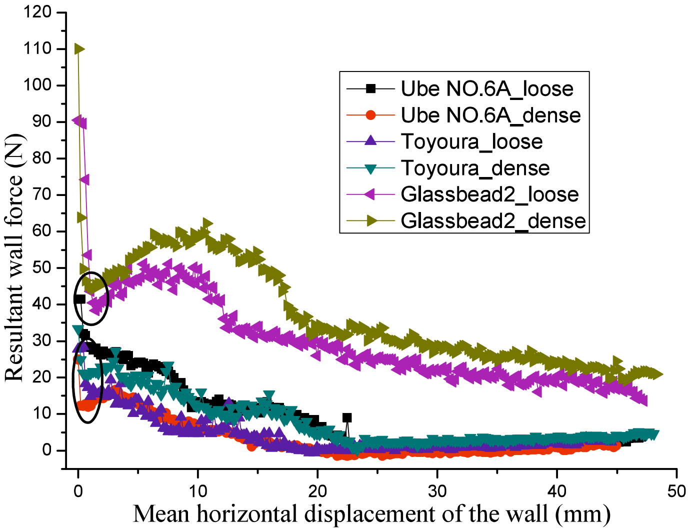

Figure 4.3 Variation of counterforce of the wall in each case

(2) Local deformation development

Developments of local deformation in the three materials are compared at 0.42mm displacement of wall. Figs. 4.4(a)~(f) show the maximum shear strain distribution at the beginning, middle and the residual state of the unloading for loose and dense samples of Ube sand NO.6A, Toyoura sand and Glassbead2, separately. For each group of figures, the same scale was used for the strain distributions at different stages.

It can be seen from the figure that for all the three materials, Shear band formed at the beginning of the unloading, and developed gradually with the movement of the wall. Local deformation started around the toe of the wall, and then extended to the surface of sample.

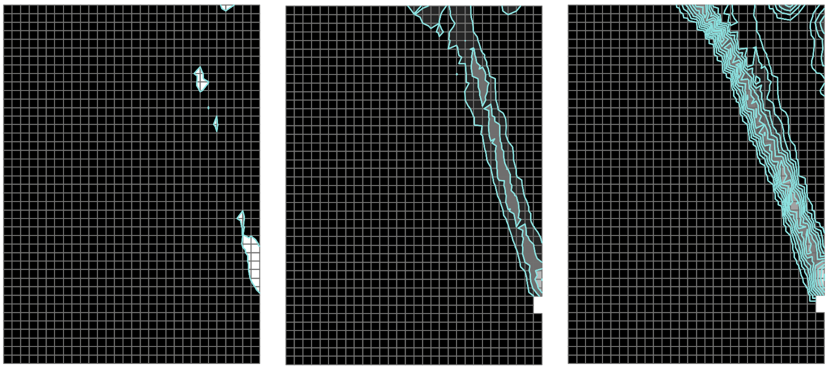

(a) Ube NO.6A sand, loose sample

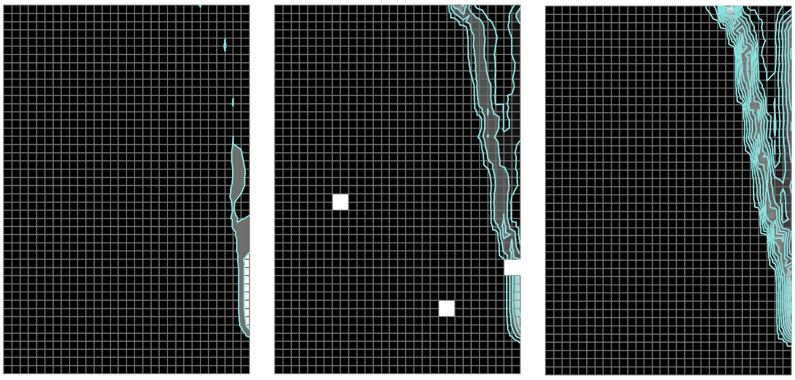

(b) Ube NO.6A sand, dense sample

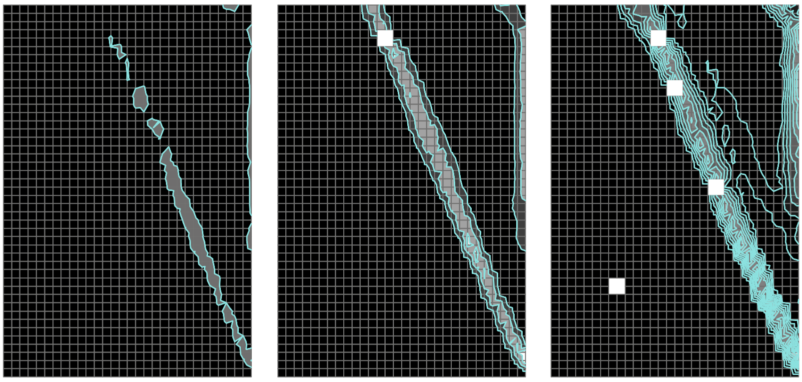

(c) Toyoura sand, loose sample

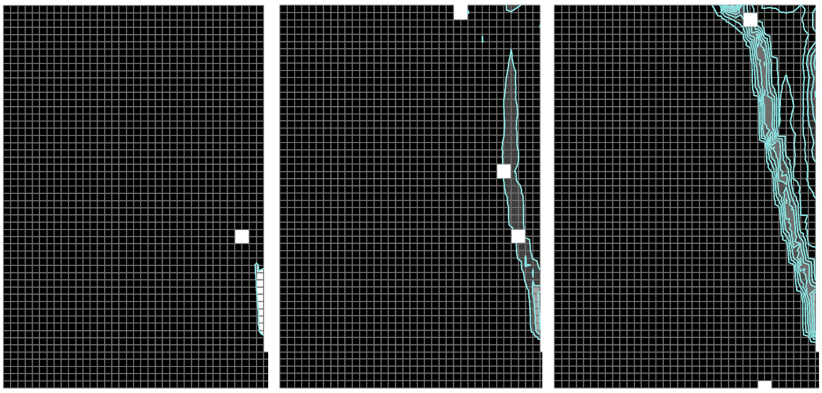

(d) Toyoura sand, dense sample

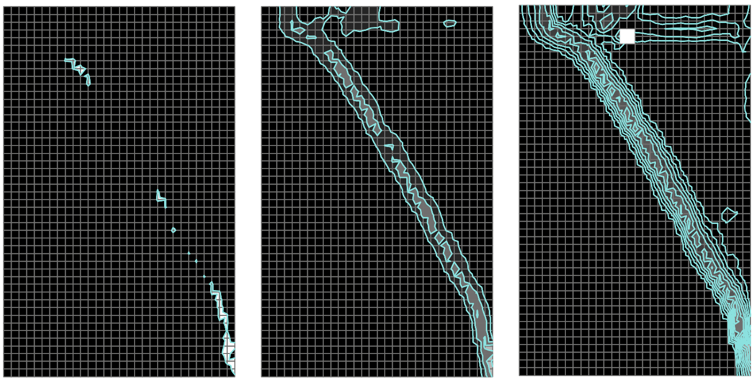

(e) Glassbead2, loose sample

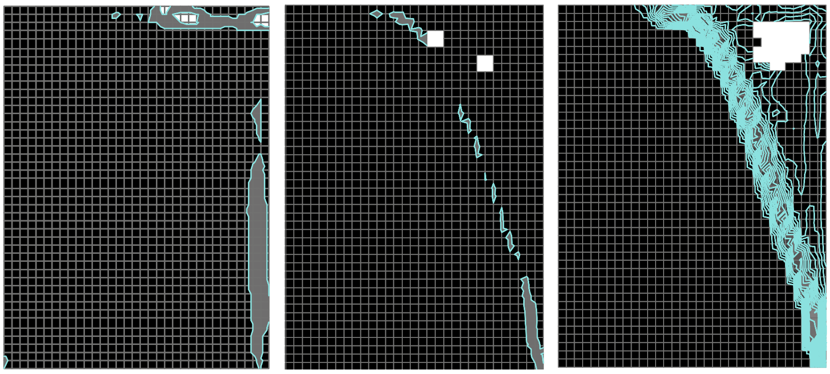

(f) Glassbead2, dense sample

Figure 4.4 Developments of local deformation under wall translation

(3) Maximum shear strain and shear band pattern

Developments of maximum shear strain distribution are compared for the three kinds of materials at u = 4.2 mm (10 min after the unloading). The definition of maximum shear strain has been introduced in Chapter 2 (refer to Eq. (2.6)). Figs. 4.5(a) and (b), (c) and (d), and (e) and (f) show the results in loose and dense samples for the Ube No.6A sand, Toyoura sand and Glassbead2 respectively, under a wall displacement of 2.1 mm. Fig. 4.6 shows similar results under a wall displacement of 4.2 mm.

Table 4.1 lists the initial conditions and finally resulted shear band information in each case. Here, D_r is relative density. θ is the inclination angle of the main shear band. w is the thickness of the main shear band at u = 4.2 mm, and d_{50} is the mean particle size. The thickness was measured based on the 2-order derivative of displacement vector obtained from DIC analysis.

Table 4.1 Comparisons of initial conditions and shear band information

Sample			D_r	θ (°)	w (mm)	w/d_{50}
Ube NO.6A sand	(a)	Loose	26%	73.6	4.8	21.8
	(b)	Dense	78%	79.7	3.73	17
Toyoura sand	(c)	Loose	18%	72.8	4.88	24.4
	(d)	Dense	80%	78.6	3.96	19.8
Glassbead2	(e)	Loose	3%	56.5	9.97	8.9
	(f)	Dense	75%	67.0	4.68	4.2

For all three materials, the shear band shows a higher inclination angle but a smaller thickness in the dense state than that in the loose state. The Ube No.6A sand with more angular particle shape showed a little higher inclination angles than Toyoura sand. The shear band thicknesses in the two sands are quite close. The shear bands in Glassbead2 showed smaller inclination angles than the two sands but much larger thickness. However, w/D_{50} is smaller for the Glassbead2 because of its larger mean particle size. This result is consistent with the findings of elemental test in Chapter 2.

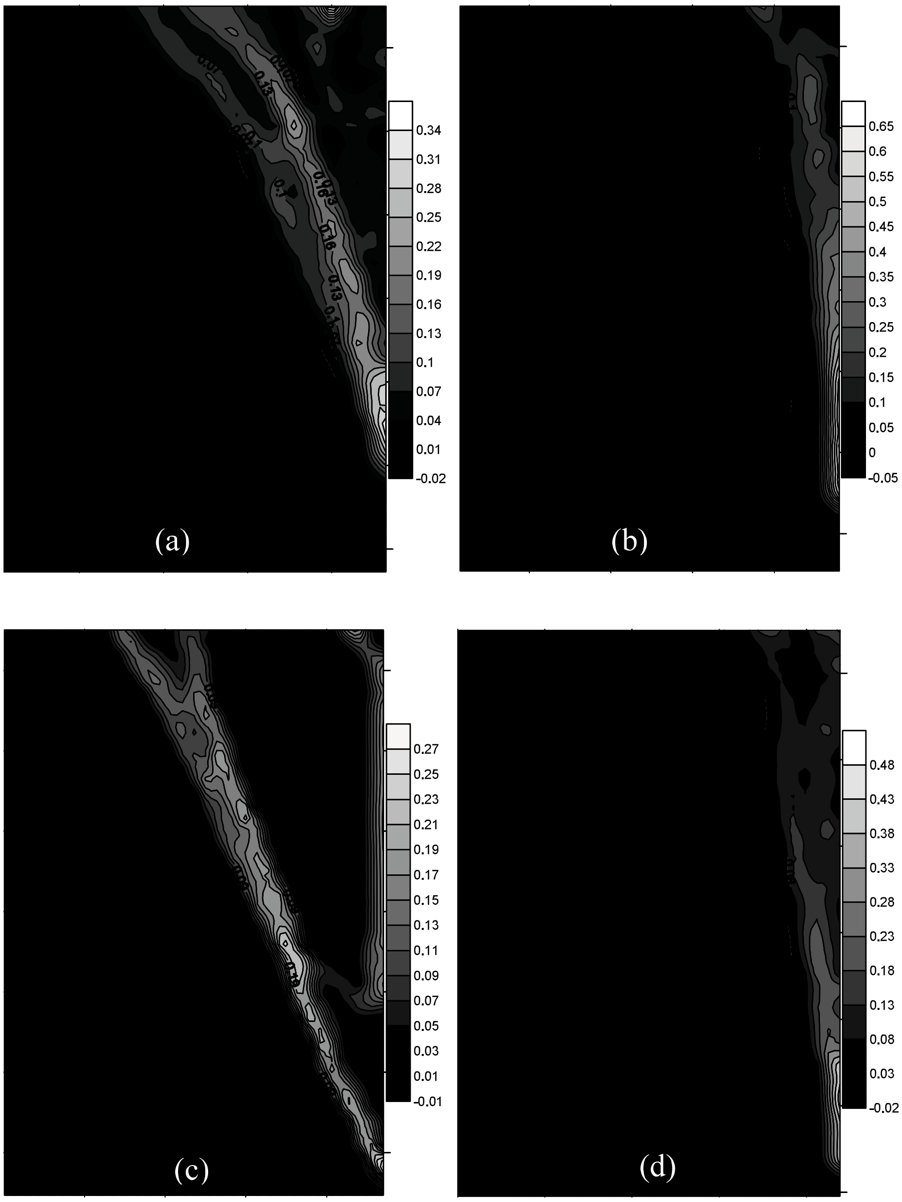
0.34
0.31
0.28
0.25
0.22
0.19
0.16
0.13
0.1
0.07
0.04
0.01
-0.02
(a)
0.65
0.6
0.55
0.5
0.45
0.4
0.35
0.3
0.25
0.2
0.15
0.1
0.05
0
-0.05
(b)
0.27
0.25
0.23
0.21
0.19
0.17
0.15
0.13
0.11
0.09
0.07
0.05
0.03
0.01
-0.01
(c)
0.48
0.43
0.38
0.33
0.28
0.23
0.18
0.13
0.08
0.03
-0.02
(d)

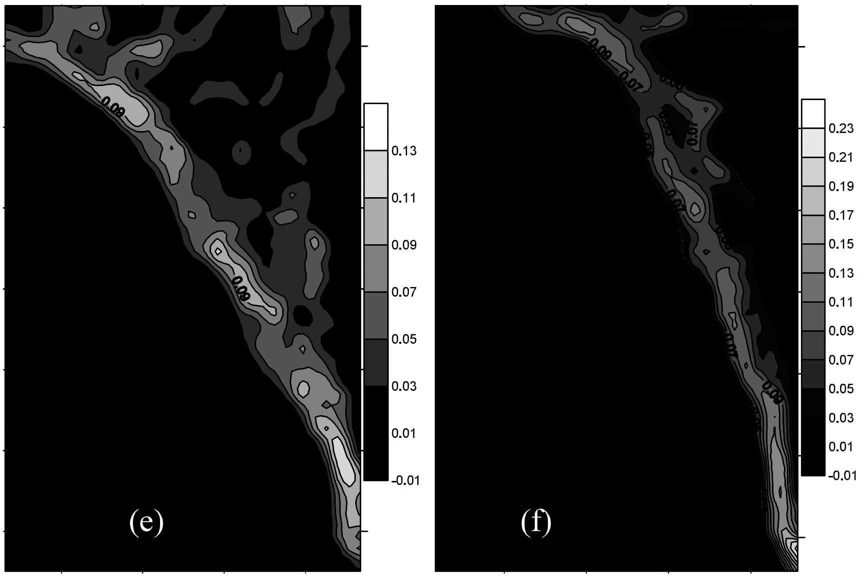

Figure 4.5 Shear bands in different cases at a wall translation, $u = 2.1$mm

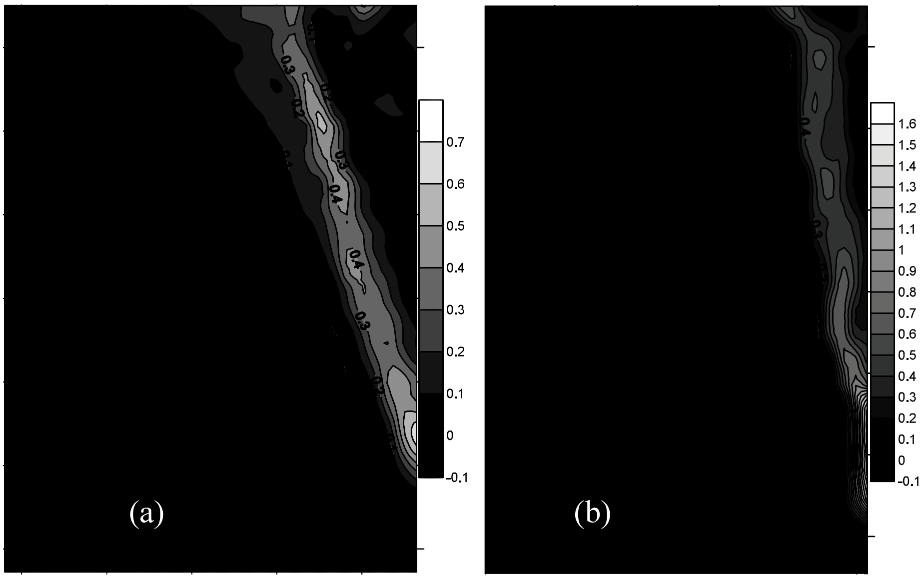

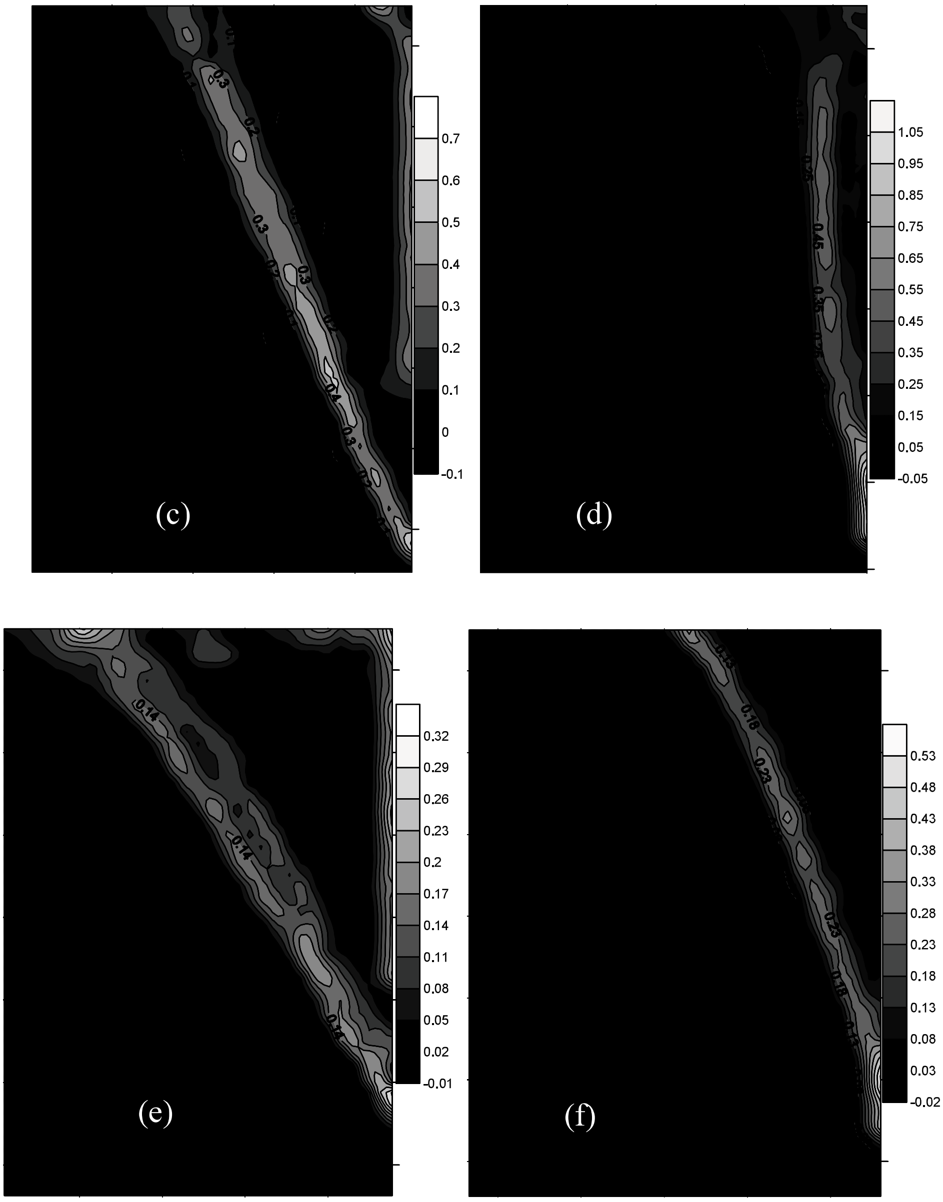

Figure 4.6 Maximum shear strain in different samples for wall translation, $u = 4.2$ mm

(4) Local shear stress and shear strain

An element inside the center of the shear band was chosen to analyze local stress–strain behavior and results for the loose and dense samples of each material were compared. We found that the three materials gave similar results for dense or loose samples, while the behavior was quite different between the loose and dense samples. For instance, developments of local shear stress and local strain in the loose and dense Toyoura sand samples are compared in Fig. 4.7 and Fig. 4.8.

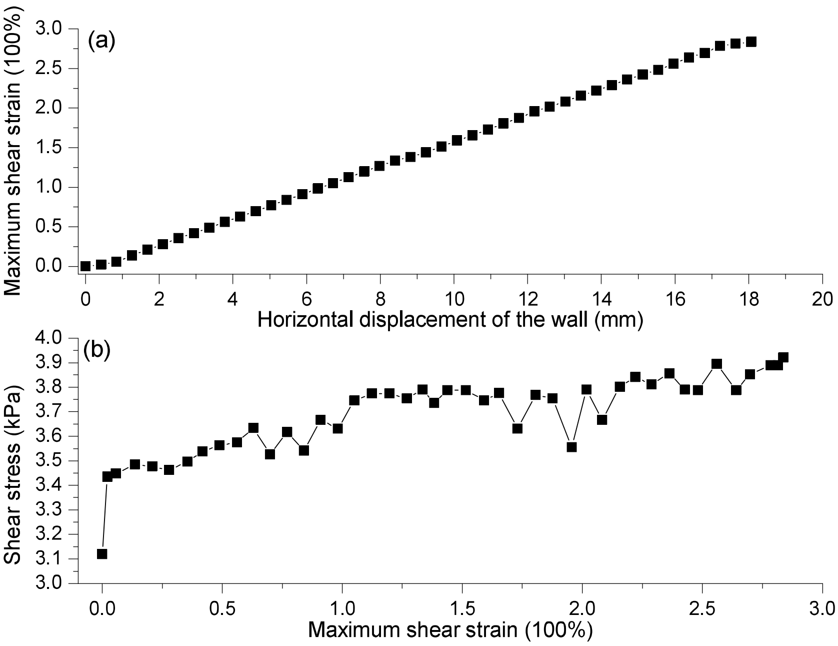

Figure 4.7 Developments of local shear stress and maximum shear strain in loose Toyoura sand

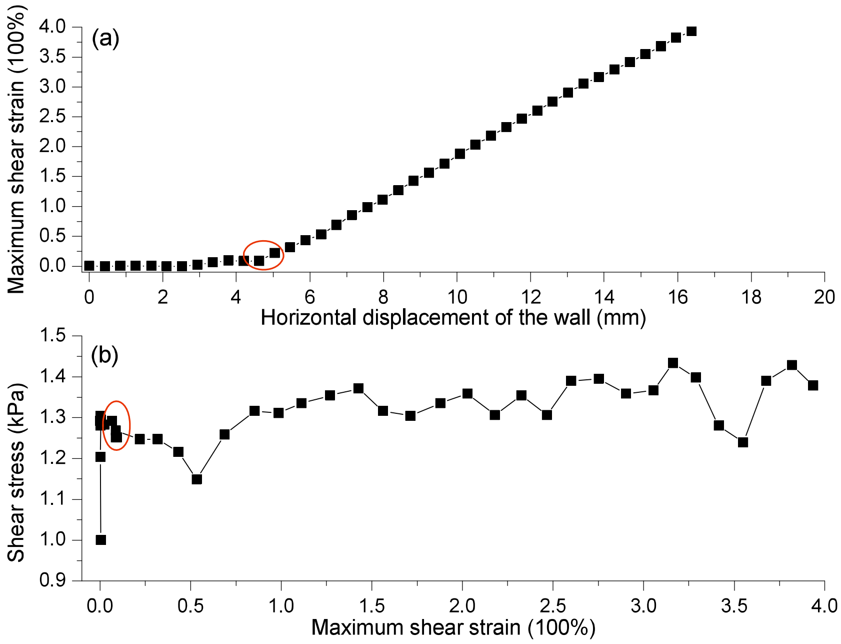

Figure 4.8 Developments of local shear stress and maximum shear strain in dense Toyoura sand

As has been shown in Fig. 4.3, the resultant force decreased quickly at the very beginning of the unloading, while the vertical pressure is thought to remain unchanged, and thus the shear stress increased, as can be seen in Figs. 4.7(b) and 4.8(b). The shear stress became relatively stable after 6 mm wall displacement. In the loose samples, the maximum shear strain increased gradually with the wall displacement and always showed a linear relationship, as shown in Fig. 4.7(a). However, in the dense samples, despite the quick increase of shear stress at the beginning, the maximum shear strain increased very slowly, and was only 0.22 at 5 mm wall displacement. The reason for this is that, at the beginning of unloading, the dense particles supported each other in a stable state and thus little deformation occurred. As the unloading continued, the stable structure was destroyed and local deformation developed quickly. The maximum shear strain was found to be higher in the dense sample than in the loose sample at the same wall displacement.

4.2.2 Cases of active wall rotation around the toe

Taking the case of loose Toyoura sand as an example, loci of the retaining wall is shown in Fig. 4.9. Compared with Fig. 4.2, it can be seen that the wall rotated around the toe at the beginning and no penetration happened.

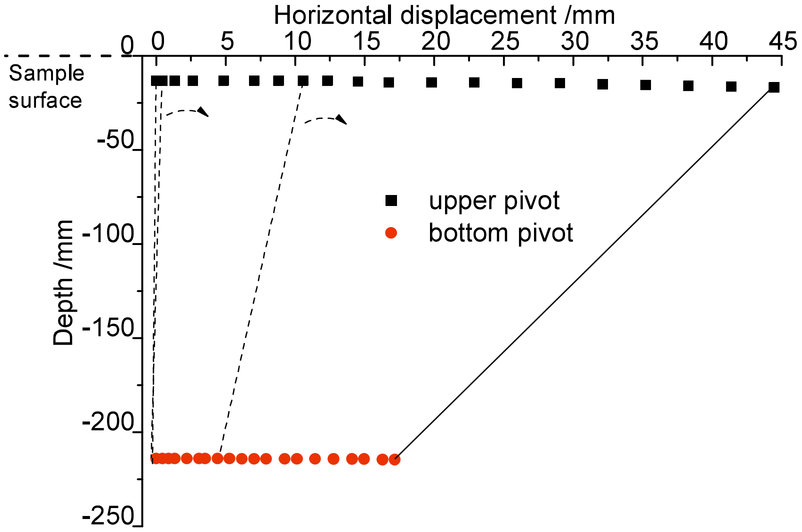

Figure 4.9 Trace of the retaining wall movement

(1) Variation of active force on the retaining wall

Figure 4.10 shows the variation in the resultant active force on the wall with the mean horizontal displacement of the wall. Similarly to Fig. 4.3, the resultant force decreased quickly at the very beginning of the unloading. However, the resultant force arrived at the residual value much earlier compared to that in the case of wall translation.

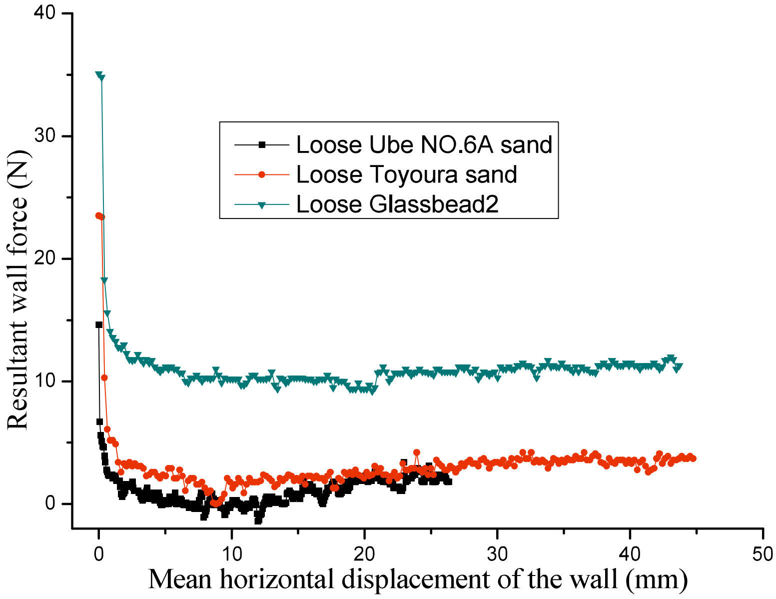

Figure 4.10 Variation of resultant wall forces under wall rotation

(2) Local deformation development

Figures 4.11(a) ~(c) show local deformation development in the three loose samples. Compared with Figure 4.4, it is clearly seen that shear band pattern is much different for the same material. Multiple shear bands generated at the same time under wall rotation and shear bands are shorter and have smaller inclination angles. The shear bands are seen curvilinear in both the Ube No.6A sand and the Toyoura sand but straight and parallel in Glassbead2. Moreover, the shear bands were not generated at the same time and two shear bands combined into one with the development of deformation.

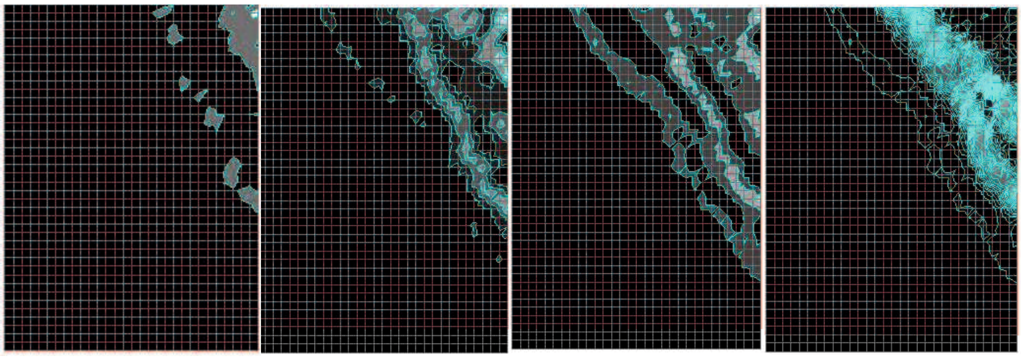

(a) Loose Ube NO.6A sand

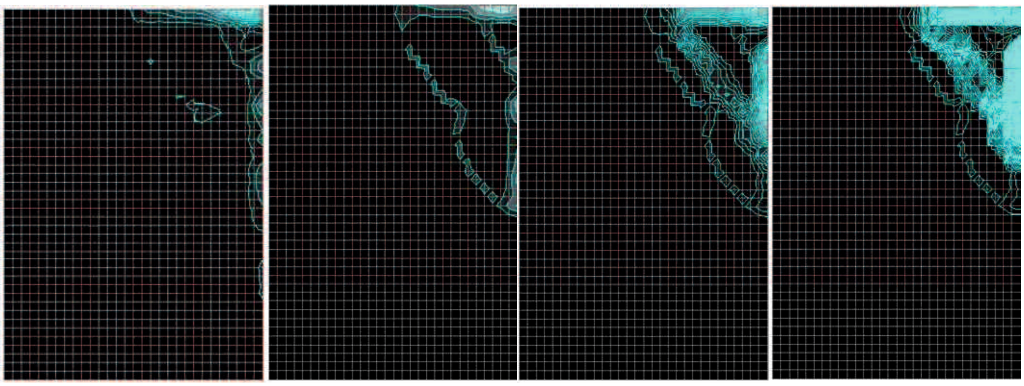

(b) Loose Toyoura sand

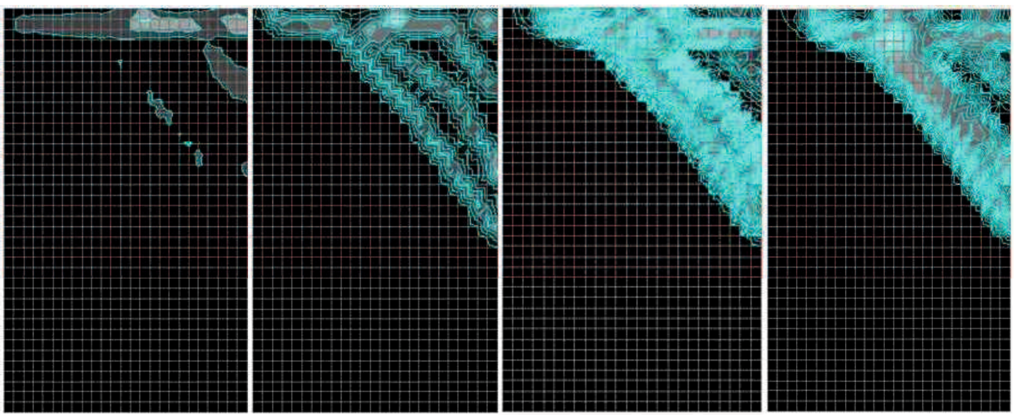

(c) Loose Glassbead2

Figure 4.11 Developments of maximum shear strain under wall rotation

(3) Maximum shear strain and shear band pattern

Figures 4.12(a)–(c) show the maximum shear strain distributions in the three loose samples at the beginning of rotation ($\theta \approx 0.2°$). Compared with Figs. 4.5 and 4.6, it is clear that the shear band pattern is quite different. Multiple shear bands are generated behind the wall and shear bands are shorter and have smaller inclination angles. The shear bands are curvilinear in both the Ube No. 6A sand and Toyoura sand, but approximately straight and parallel in the glass beads. Moreover, the shear bands were not developed synchronously. Fig. 4.13 shows the maximum shear strain distributions at $\theta \approx 4°$. When comparing Fig. 4.12 and Fig. 4.13, it can be seen that only one or two initial shear bands developed into the single main shear band, and the other shear bands disappeared.

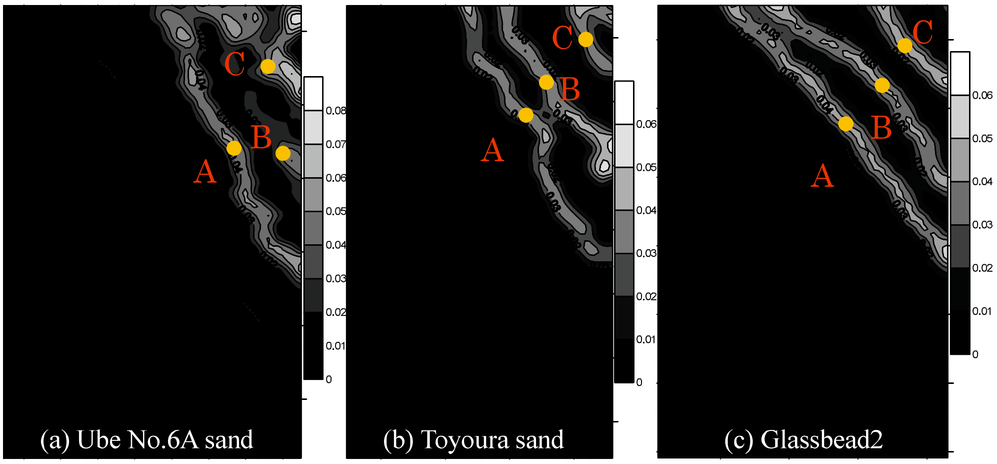

(a) Ube No.6A sand (b) Toyoura sand (c) Glassbead2

Figure 4.12 Maximum shear strain distributions under wall rotation ($\theta \approx 0.2°$)

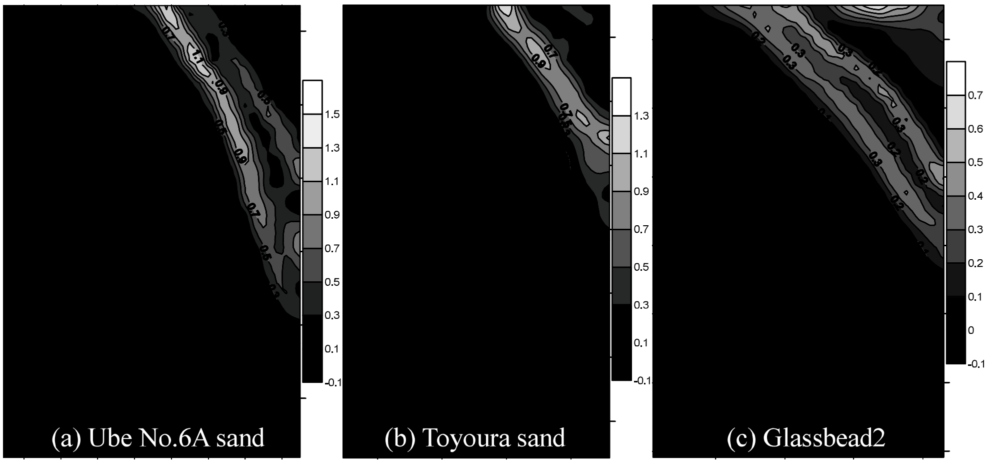

(a) Ube No.6A sand (b) Toyoura sand (c) Glassbead2

Figure 4.13 Maximum shear strain distributions under wall rotation ($\theta \approx 4.0°$)

(4) Local strain development

Developments of local deformations inside the initial shear bands were investigated at three locations, as noted by points A, B, and C in Fig. 4.12, and the results are compared in Fig. 4.14. It can be seen that the local deformation at the three locations varied quite differently in all the materials. The three materials showed very different results: the local strain at location C in Ube No. 6A sand, location B in the Toyoura sand and location A in the glass beads developed much more than at other locations. It is speculated that the initial shear band with a long length and without obvious curvature is easier to develop into the main shear band.

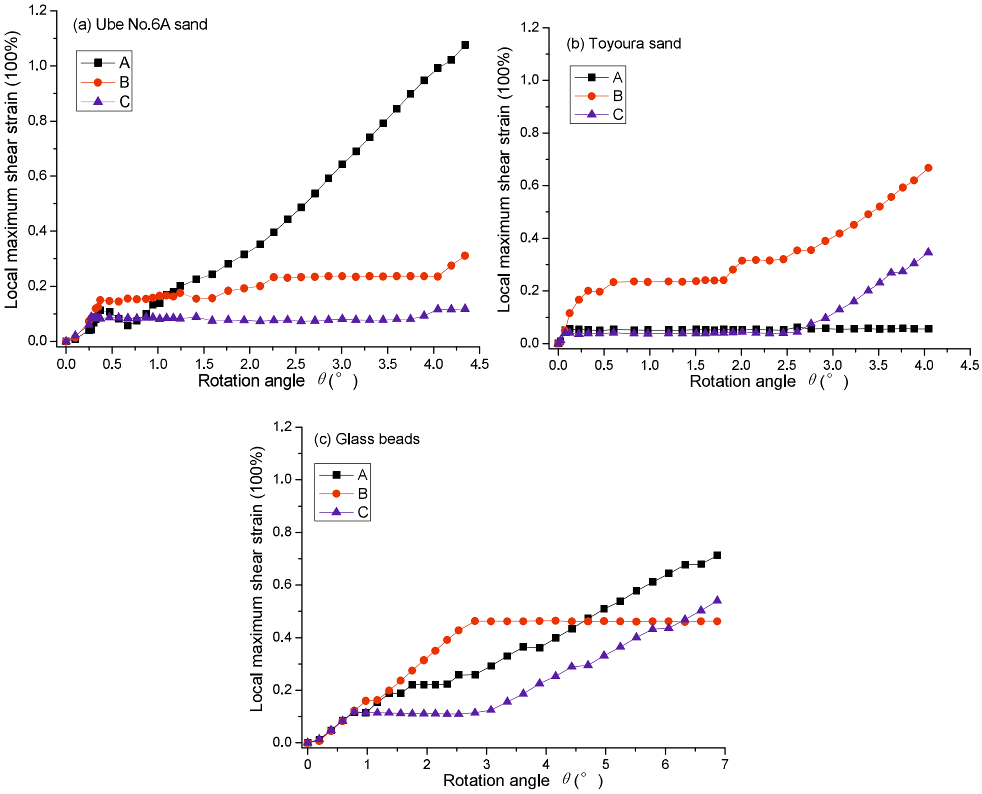

Figure 4.14 Development of local deformations with the rotation angle of the wall for each material

4.2.3 Influence of wall movement mode

From the above two sections it can be seen that shear band pattern is much influenced by the wall movement mode. This section mainly focused on the influences.

(1) Comparison of resultant wall forces

Figure 4.15 shows comparison of the wall force under three different conditions. When comparing the same loose Toyoura sand sample under translation and rotation of the wall, it is found that for the same loose samples, the resultant wall force deceased much more quickly under wall rotation. The residual force on the wall is the same in the three cases.

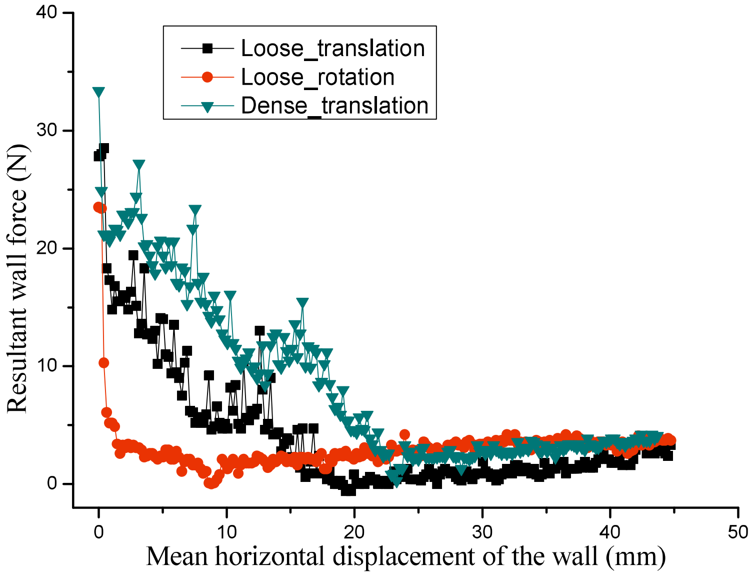

Figure 4.15 Comparison of the resultant wall forces in Toyoura sand

(2) Formation process of shear band

It has been known from Fig. 4.6 that under the wall translation, only one shear band generated in the materials. However, the wall was not under exactly translation due to the self weight and friction at the bottom of the wall. In this case, local deformation is much complex. Figs. 4.16 and 4.17 show local deformations inside loose Ube NO.6A sand and loose Glassbead2 at the beginning of the unloading in different scales.

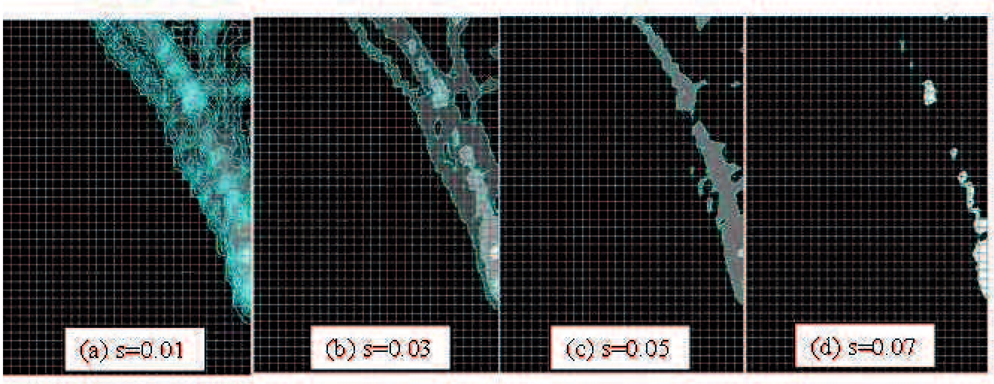

Figure 4.16 Local deformation of loose Ube NO.6A sand at the beginning of unloading in different scales

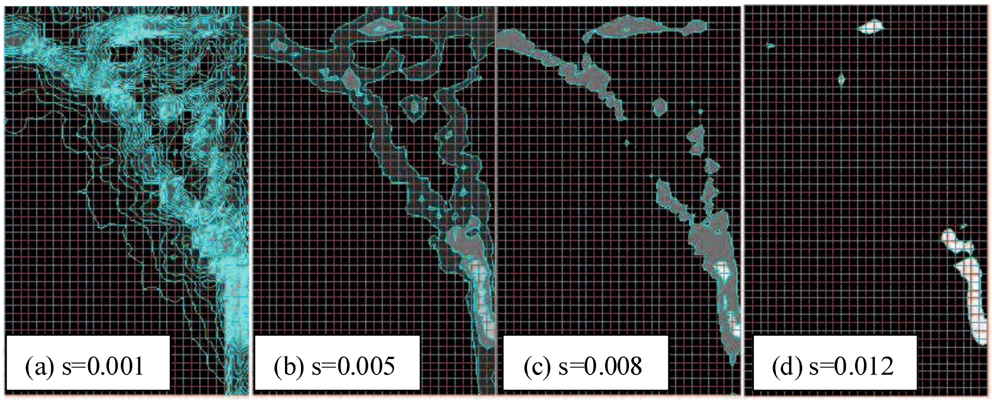

Figure 4.17 Local deformation of loose Glassbead2 at the beginning of unloading in different scales

It can be seen that, at a small scale, multiple shear bands generated inside the samples. However, only one shear band can be seen if plotted at a large scale. This means, although multiple shear bands generated at the beginning of the unloading, but only one is the main shear band. The main shear band continued and others disappeared with the increase of the wall displacement. This is different from the result under wall rotation. Multiple shear bands generated at the same time and they are all main shear bands despite that two main shear bands merge into one main shear band afterward.

(3) Shear band patterns

Figure 4.18 shows the sketches of shear band patterns under the two types of wall movement.

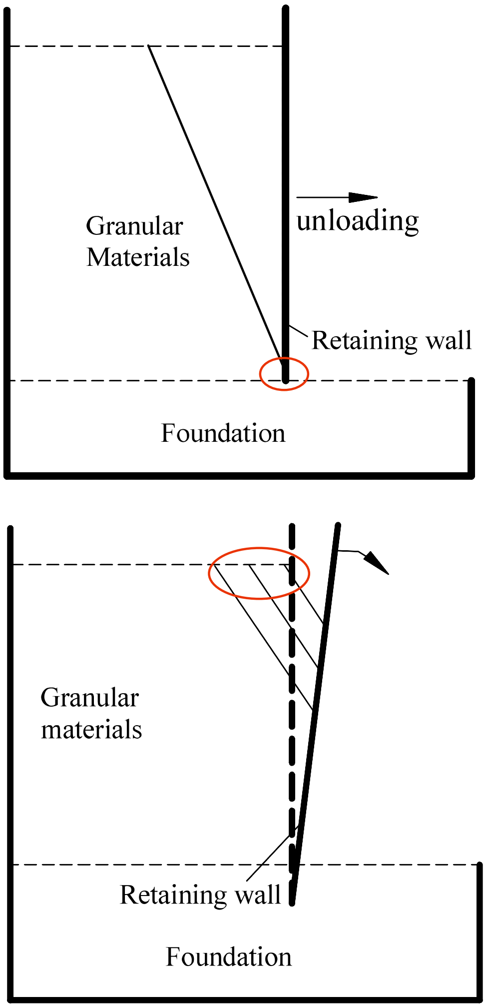

Figure 4.18 Boundary influence on the local deformation

Shear band pattern much depends on boundary condition. Under the active wall translation, local deformation starts from the toe of the retaining wall and only single shear band generates; under active wall rotation, local deformation started from the surface of the sample close to the retaining wall and multiple shear bands generated. The findings have nothing related to particle shape. According to the study by Niedostatkiewicz et al. (2010), in the case of active wall movement, the thickness of the interior shear zone is larger under wall translation than under wall rotation while the inclination is smaller.

The phenomenon of multiple shear bands in granular materials was discussed by Lesniewska (2001). He noted that shear bands may have different roles. For two families of shear bands, one is responsible for a basic soil movement, and the other not always appears and seems to be responsible for adjusting failure mechanism to changing boundary conditions. The investigation results of this study are in accordance with his statement.

4.2.4 Influence of unloading speed of retaining wall

To investigate the influence of wall unloading speed, Three types of wall speed were chose, which are noted as *V*, 2*V*, 3*V* with *V* = 0.42 mm/min. All the tests were performed on loose samples under wall translation.

Figure 4.19 shows variations of resultant wall force with the horizontal displacement of the wall under different unloading speed. It is thought that there is no clear difference among the three cases for the same material.

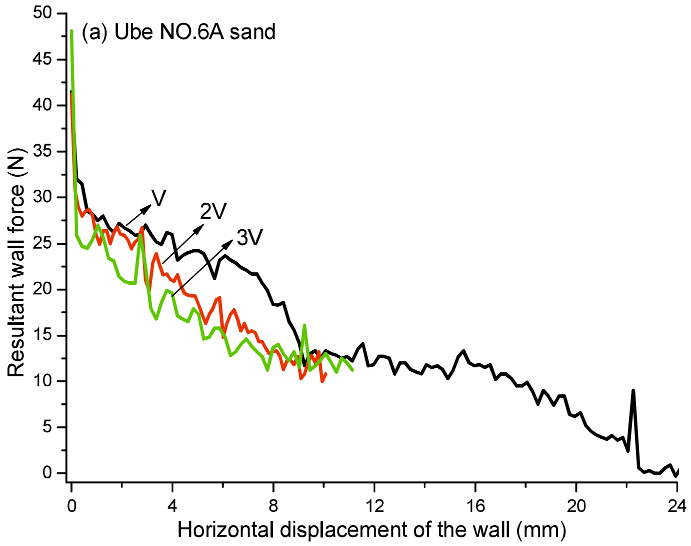

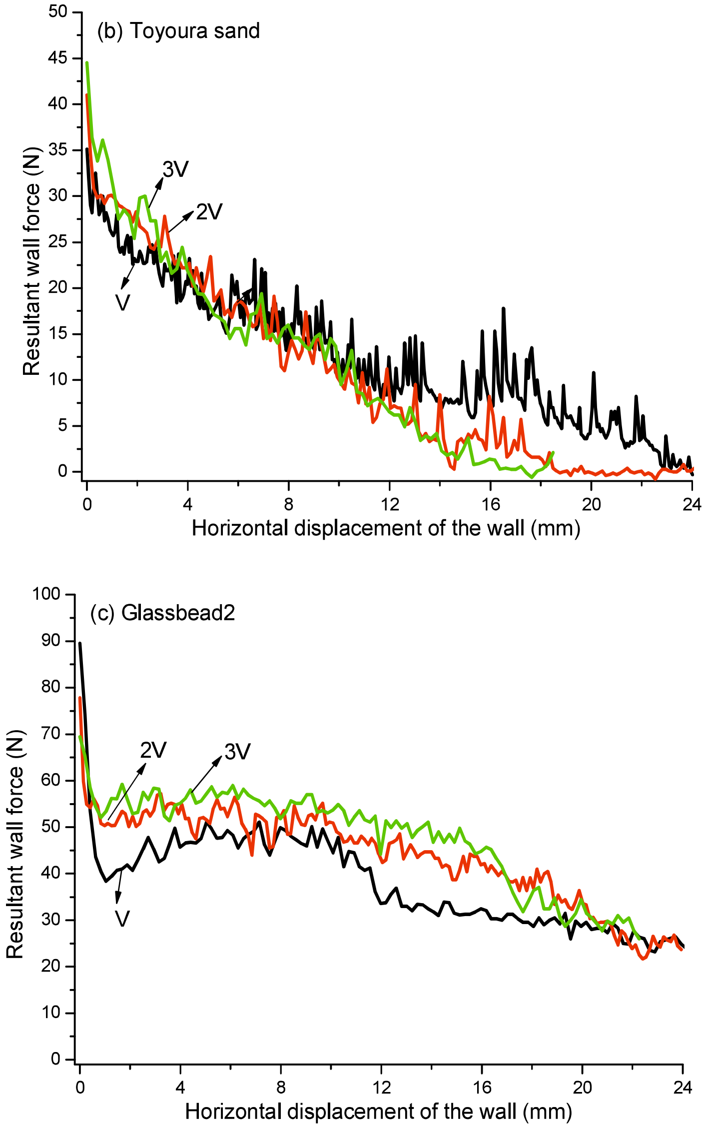

Figure 4.19 Resultant forces on the wall under different wall speeds

Figures 4.20 - 4.22 show comparisons of maximum shear strain distribution at different unloading speed for the three materials. The comparisons were made under three stages with the wall displacement d = 0.42 mm, 0.84 mm and 2.1mm. It is shown that, with increase of unloading speed of the wall, local deformation inside the material became larger. Moreover, distribution of local deformation also became wider.

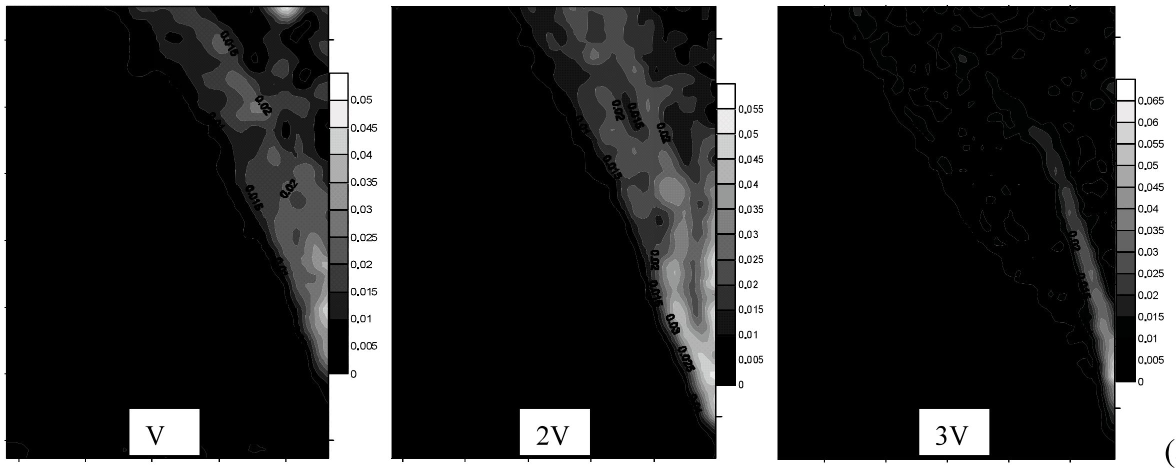

(a) *d* = 0.42 mm

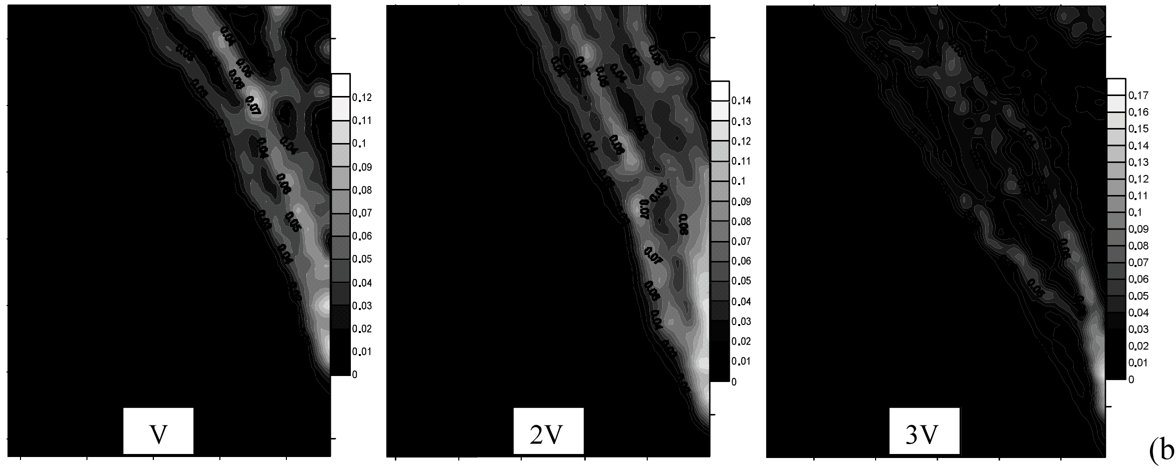

(b) *d* = 0.84 mm

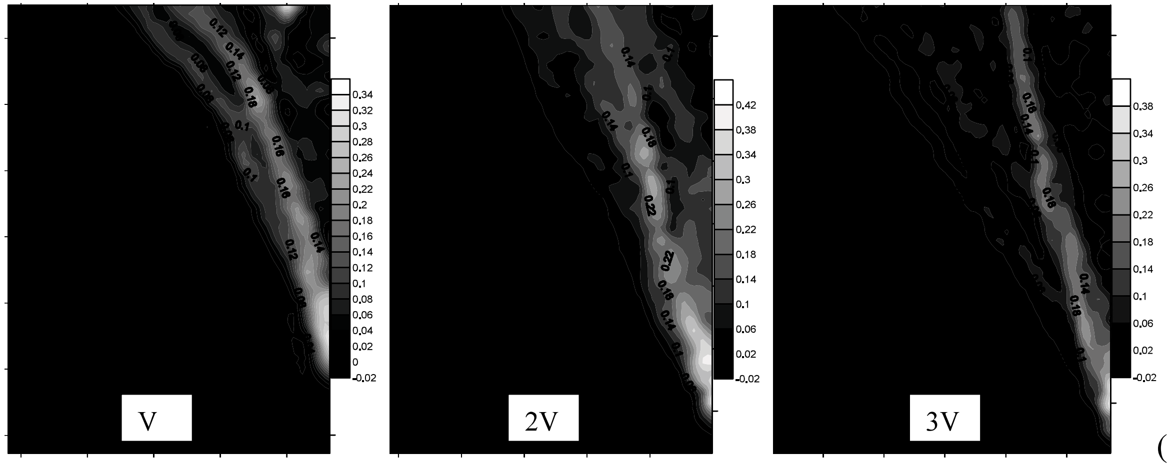

(c) *d*=2.1mm

Figure 4.20 Local deformations in Ube NO.6A sand under different unloading speed

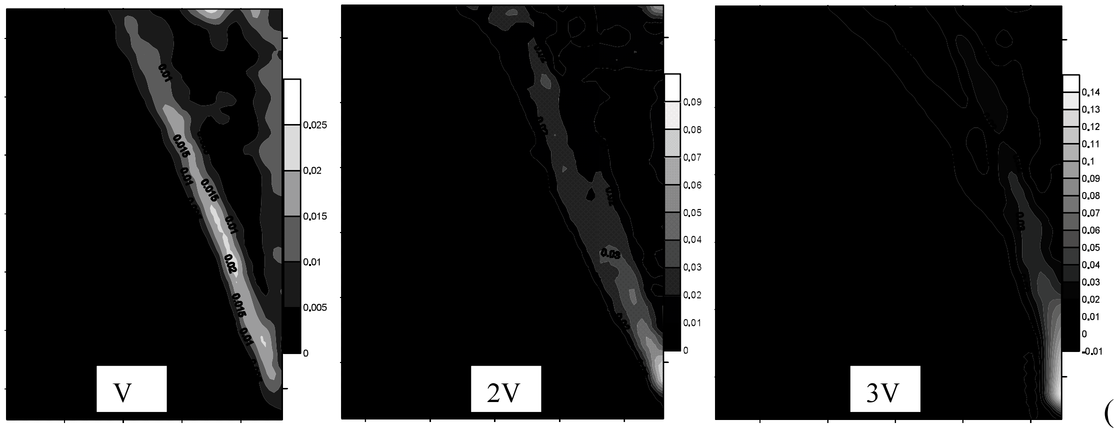

(a) *d*=0.42 mm

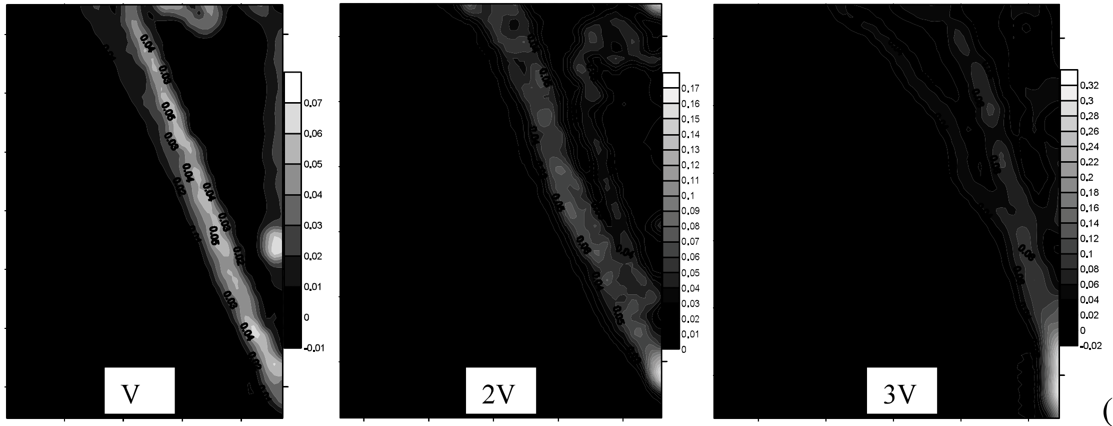

(b) *d*=0.84 mm

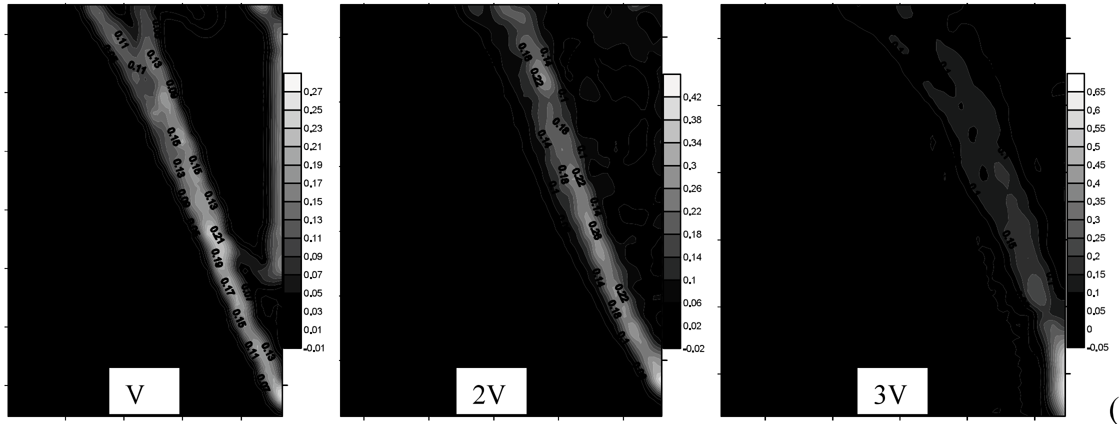

(c) *d*=2.1mm

Figure 4.21 Local deformations in Toyoura sand under different unloading speed

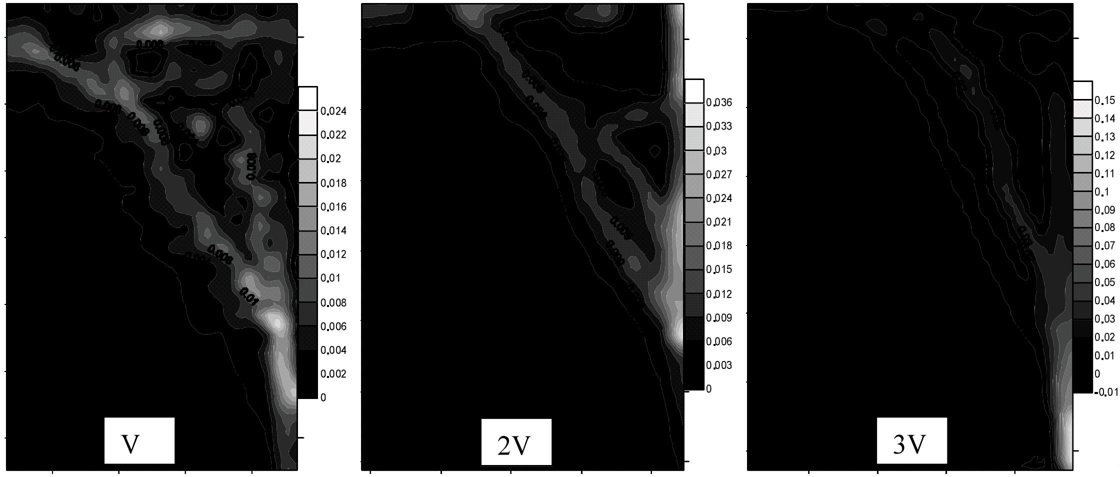

(a) *d*=0.42 mm

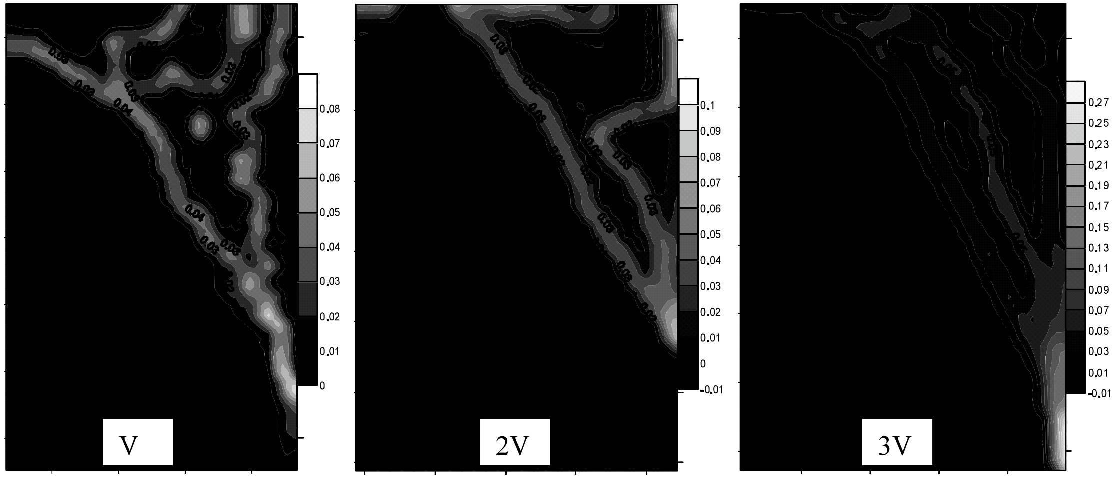

(b) *d*=0.84 mm

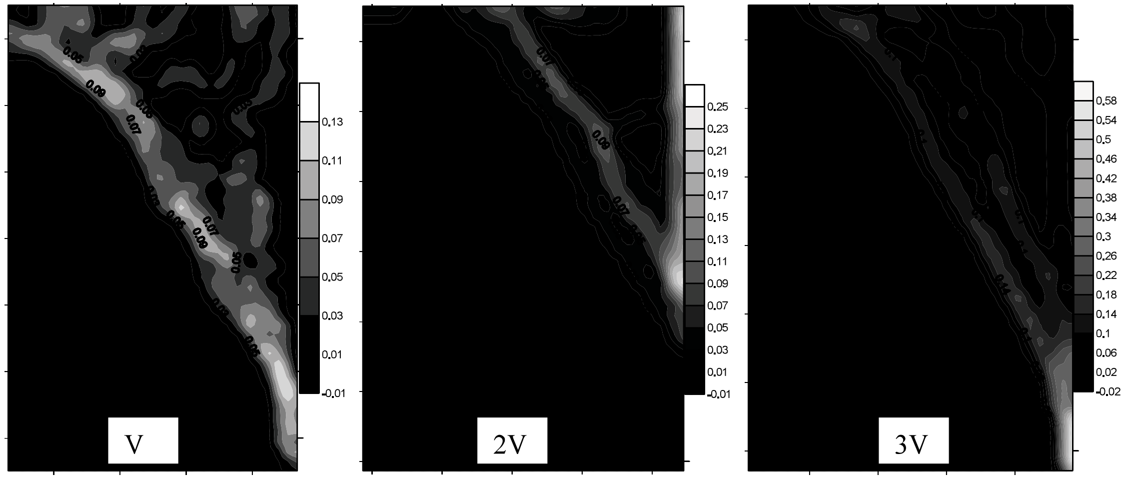

(c) *d*=2.1mm

Figure 4.22 Local deformations in Glassbead2 under different unloading speed

4.3 Conclusions

Based on the above test results and analysis, main findings obtained from the model test are summarized as below:

(1) Wall movement mode has a big influence on the development of local deformation behind the wall. Local deformation started from the toe of the retaining wall and only one shear band generated in case of active wall translation, while it started from the surface adjacent to the wall and multiple shear bands generated in case of wall rotation to the toe. Moreover, the resultant force on the wall under its active rotation arrived at the residual value much earlier compared to that in the case of wall translation.

(2) The influence of retaining wall on the local deformation behavior has found nothing related to particle shape. Particle shape does not influence shear pattern behind wall. It influences the inclination angle of shear band as well as initial density. Particle shape also influences the resultant force on the wall. The more angular particle shape of sand, the resultant force was smaller.

(3) Unloading speed of wall translation has little influence on the resultant force of the retaining wall. However, shear band became wider and local deformation became larger under a higher unloading speed.

Chapter 5 Summary and conclusions

Unloading shear behavior of granular materials with different particle shape was investigated through plane strain compression test, DEM simulation and retaining wall model test. Local deformation developments and shear band properties were analyzed specifically by image analysis. Main conclusions in Chapters 2, 3 and 4 are summarized below:

Chapter 2 Plane strain compression test

Plane strain compression tests under two different stress paths (PSCD and PSC) were performed on two sands and two glass beads with different particle shape. Image analysis was done to investigate local deformation inside specimens.

(1) Macro stress – strain behavior is more easily influenced by stress level and stress path in the two sands than that in the two glass beads. The more angular particle shape induced more significant peak strength variations with stress level. For the given stress levels in this study, the peak appeared earlier and initial stiffness was clearly higher in all the PSCD tests than those in the PSC test for both the sands. The above differences were not found for the two glass beads.

(2) Local lateral strain showed mainly extension and butterfly shaped distribution near the peak strength. The extension was higher in the PSCD test than that in the PSC test for sands at the same global shear strain. Shear bands already initiated before peak strength and shear band patterns were changing during the whole shearing process.

(3) Under the same test condition, shear band thickness in the two sands was smaller than that in Glassbead1 even if the three types of material have almost the same mean particle size. Shear band thickness also decreased with increase of confining pressure regardless of particle shape or size.

(4) The onset of shear bands is defined at which the growth rate of the local maximum shear strain starts to increase stiffly with an increasing global axial strain. Generally, the onset of shear bands occurs prior to the specimen reaching its maximum principal stress ratio for both dense and loose specimens. Between the peak in shear strength and the end of strain softening, the local maximum shear strain grew approximately linearly with the global axial strain. For the same material, the growth rate of the local maximum shear strain became smaller with wider shear band.

(5) Shear band thicknesses in the two sands were clearly smaller than that in Glassbead1, even with their similar mean particle sizes. Shear band thickness became thinner when particle shape is more angular. Shear band thickness was also much dependent on the particle size. However, shear band thickness was not proportional increased with an increasing mean particle size.

(6) Inclination angles of shear bands corresponding to their peak strengths were in between those estimated values by Coulomb's and Roscoe's formulas for both sands and glass beads. The shear band inclination angles in sands matched well with those estimated by Coulomb's formula, while Roscoe's formula predicted shear band inclination angles relatively close to the corresponding measured values in dense glass beads.

Chapter 3 Biaxial DEM simulation

Two-dimensional DEM simulation results qualitatively reflected the differences between shear behaviors under the two different stress paths as in plane strain compression tests.

(1) Principal stress ratio – axial strain relationship was different in the compression and decompression tests for dense clump samples. Initial stiffness was higher in decompression test. There was little difference for loose clump sample, both dense and loose disk samples.

(2) The decompression test showed only dilation for dense samples, and

the dilation was clearly higher than in the compression test for clump samples. Similar volume behavior was shown for loose samples in the two types of test despite the particle shape.

(3) Similar conjugate shear bands were found in the two types of test for both clump and disk samples. Shear bands start before the peak in dense samples, and before the onset of dilation in loose samples.

(4) Coordination number decreased quicker and more in the decompression test than in the compression test for dense samples, while had little change in loose samples despite the particle shape. Critical coordination number is influenced by both stress path and particle shape, especially in dense samples.

(5) Deviator fabric before the peak was higher in the decompression test than in the compression test for dense samples. There was almost no difference in both loose clump and disk samples. Critical deviator fabric is only dependent on particle shape.

(6) Total external work on the specimen is mostly converted into dissipated frictional energy and elastic strain energy stored at particle contacts. For dense specimens at the peak, more work is dissipated and therefore less work is converted into strain energy in the clump specimen than those in disk specimen in the biaxial compression test; in the decompression test, more strain energy is released in the clump specimen than that in the disk specimen.

(7) Other things being equal, strain energy variation rate with the mean stress is higher in the loose specimens than in the dense specimens, and is also higher in disks than in clumps. Furthermore, strain energy storage or dissipation is much related to the particle interlocking, which is dependent on the particle shape as well as relative density.

Chapter 4 Retaining wall model test

Retaining wall model tests on the two sands and one glass beads were performed under boundary conditions of active translation and active rotation. Some findings are as below:

(1) Wall movement mode has a big influence on the development of local deformation behind the wall. Local deformation started from the toe of the retaining wall and only one shear band generated in case of active wall translation, while it started from the surface adjacent to the wall and multiple shear bands generated in case of wall rotation to the toe. Moreover, the resultant force on the wall under its active rotation arrived at the residual value much earlier compared to that in the case of wall translation.

(2) The influenced of retaining wall on the local deformation behavior has found nothing related to particle shape. Particle shape does not influence shear pattern behind wall. It influences the inclination angle of shear band as well as initial density. Particle shape also influences the resultant force on the wall. The more angular particle shape of sand, the resultant force was smaller.

(3) Unloading speed of wall translation has little influence on the resultant force of the retaining wall. However, shear band became wider and local deformation is larger under a higher unloading speed.

The research findings in this study can be used as a reference for excavation problem calculation especially in coheisonless granular materials. There are still several problems not solved well in this study:

(1) Shear band thickness measurement.

In this study, shear band thickness was measured according to maximum shear strain distributions in the middle of shear band. While the shear bands are not uniform in most cases, the measurements have limited accuracy. As mentioned by Niedostatkiewicz et al. (2010), there is no unified way of determination of shear band thickness agreed between researchers.

Measuring shear band thickness accurately is still a challenging problem, especially for those nonuniform shear bands.

(2) Particle interlocking.

Although interlocking of granular materials has been presented since a long time ago, there was no way or standard to evaluate the level of interlocking. Even the physical meaning is not clear enough. The interlocking was found to be related to particle shape, relative density and maybe other more factors. It is suggested to relate the interlocking to the strain energy mentioned in this study. This topic still need further study.

(3) Shear band simulation in retaining wall model test.

The model test simulation was failed in this study. The key reason is considered to be the contact model of particles. It is expected to modify the current linear contact model to simulate the model test.

References

A

Alshibli K, Sture S. (2000) Shear band formation in plane strain experiments of sand. *Journal of Geotechnical and Geoenvironmental Engineering, ASCE*, 126(6), 495–503.

Alshibli K, Batiste S, Sture S. (2003) Strain Localization in Sand: Plane Strain versus Triaxial Compression. *Journal of Geotechnical and Geoenvironmental Engineering*, 129(6), 483–494.

Asaoka A, Adachi T, Oka F. (1997) *Deformation and Progressive Failure in Geomechanics*, IS-Nagoya'97.

Asmar BN, Langston PA, Matechett AJ, Walters, JK. (2003) Energy monitoring in distinct element models of particle systems. *Advanced Powder Technology*, 14(1), 43–69.

B

Bardet JP, Proubet J. (1992) Shear-band analysis in idealized granular material. *Journal of Engineering Mechanics, ASCE*, 118(2), 397–415.

Batiste SN, Alshibli KA, Sture S, Lankton M. (2004) Shear band characterization of triaxial sand specimens using computed tomography. *ASTM Geotechnical Testing Journal*, 27(6), 568–579.

Belheine N, Plassiard JP, Donzé FV, Darve F, Seridi A. (2009) Numerical simulation of drained triaxial test using 3D discrete element modeling. *Computers and Geotechnics*, 36, 320–331.

Bi ZW, Sun QC, Jin F, Zhuang M. (2011) Numerical study on energy transformation in granular matter under biaxial compression. *Granular Matter*, 13, 503–510.

Borja RI, Song XY, Rechenmacher AL, Abedi S, Wu W. (2013) Shear band in sand with spatially varying density. *Journal of the Mechanics and Physics of Solids*, 61(1), 219–234.

Bruck, H.A., McNeill, S.R., Sutton, M.A., Peters, W.H. (1989) Digital image correlation using Newton-Raphson method of partial differential corrections. *Experimental Mechanics*, 29 (3), 261–268.

C

Clinton H. Characterization of Geomaterials with X-ray Computed Tomography (X-ray CT).

Cavarretta I, Coop M, O'Sullivan C. (2010) The influence of particle characteristics on the behaviour of coarse grained soils. *Géotechnique*, 60(6), 413–423.

Chang CS, Yin ZY. (2010) Modeling stress-dilatancy for sand under compression and extension loading conditions. *Journal of Engineering Mechanics*, *ASCE*, 136(6), 777–786.

Cheung G, O'Sullivan C. (2008). Effective simulation of flexible lateral boundaries in two- and three-dimensional DEM simulations. *Particuology*, 6, 483–500.

Cho GC, Dodds J, Santamarina JC. (2006) Particle Shape Effects on Packing Density, Stiffness, and Strength: Natural and Crushed Sands. *Journal of Geotechnical and Geoenvironmental Engineering*, *ASCE*, 132(5), 591–602.

Chu J, Wanatowski D. (2009) Effect of loading mode on strain softening and instability behavior of sand in plane-strain test. *Journal of Geotechnical and Geoenvironmental Engineering, ASCE*, 135(1), 108–120.

Chu J, Leong WK, Loke WL, Wanatowski D. (2012) Instability of loose sand under drained conditions. *Journal of Geotechnical and Geoenvironmental Engineering, ASCE*, 138(2), 207–5216.

Cleary PW. (2008) The effect of particle shape on simple shear flows. *Powder Technology*, 179, 144–163.

Collins IF. (2002) A thermomechanical analysis of a family of soil models. *Géotechnique*, 52(7), 611–618.

Collins IF. (2005) Elastic/plastic model for soils and sands. *International Journal of Mechanical Sciences*. 47, 493–508.

Collins IF. (2005) The concept of stored plastic work or frozen elastic energy in soil mechanics. *Géotechnique*, 55(5), 373–382.

Cundall PA, Strack ODL. (1979) A discrete numerical model for granular assemblies. *Géotechnique*, 29, 47–65.

Cuccovillo T, Coop MR. (1999) On the mechanics of structured sands. *Géotechnique*, 49(6), 741–760.

D

Darve F, Laouafa F. (2000) Instabilities in granular materials and application to landslides. *Mechanics of cohesive-frictional materials*, 5, 627–652.

Darve F, Sibille L, Daouadji A, Nicot F. (2007). Bifurcations in granular media: macro- and micro-mechanics approaches. *C. R. Mecanique*, 335, 496–515.

Desrues J, Chambon, R., Mokni, M., Mazerolle, F. (1996). Void ratio evolution inside shear bands in triaxial sand specimens studied by computed tomography. *Géotechnique*, 46(3), 529–546.

Desrues J, Viggiani G. (2004) Strain localization in sand: an overview of the experimental results obtained in Grenoble using stereophotogrammetry. *International Journal for Numerical and Analytical Methods in Geomechanics*, 28, 279–321

Desrues J, Viggiani G, Bésuelle P. (2006) *Advances in X-ray Tomography for Geomaterials*, ISTE

F

Ferellec JF, McDowell GR. (2010) A method to model realistic particle shape and inertia in DEM. *Granular Matter*, 12, 459–467.

Finno RJ, Harris WW, Mooney MA, Viggiani G. (1997) Shear bands in plane strain compression of loose sand. *Géotechnique*, 47(1), 149–165.

Fu PC, Dafalias YF. (2011) Fabric evolution within shear band of granular materials and its relation to critical state theory. *International Journal for Numerical and Analytical Methods in Geomechanics*, 35(18), 1918–1948

G

Gao JH, Zhao WB, Li XW. (1999) Simulation of Unloading due to Excavation in FEM Analysis—modified mana method based on comparison of three methods. *Journal of Hohai University (Natural Sciences)*, 7(1), 47–52.

Guo PJ, Su XB. (2007) Shear strength, interparticle locking, and dilatancy of granular materials. *Canadian Geotechnical Journal*, 44, 579–591.

Guo PJ. (2012) Critical length of force chains and shear band thickness in dense granular materials. *Acta Geotechnica*, 7, 41–55

H

Handy RL. (1985) The arch in soil arching. *Journal of Geotechnical Engineering*, 111(3), 302–318.

Hall SA, Bornert M, Desrues J, Pannier Y, Lenoir N, Viggiani G, Bésuelle P. (2010) Discrete and continuum analysis of localised deformation in sand using X-ray μCT and volumetric digital image correlation. *Géotechnique*, 60(5), 315–322.

Head KH. (1992) *Manual of Soil Laboratory Testing*. Second Edition, Volume 3, *Effective Stress Tests*. Pentech Press, London.

http://en.wikipedia.org/wiki/Digital_image_correlation

Huang WX, Sun DA, Sloan SW. (2007) Analysis of the failure mode and softening behavior of sands in true triaxial tests. *International Journal of Solids and Structures*, 44, 1423–1437

I

Iwashita K, Oda M. (1998) Rolling resistance at contacts in the simulation of shear band development by DEM. *Journal of Engineering Mechanics, ASCE*, 124, 285–292.

Iwashita K, Oda M. (2000) Micro-deformation mechanism of shear banding process based on modified distinct element method. *Powder Technology*, 109, 192–205.

J

Jefferies M. (1997) Plastic work and isotropic softening in unloading. *Géotechnique*, 47(5), 1037–1042.

Jiang MJ, Leroueil S, Zhu HH, Yu HS, Konrad JM. (2009) Two-dimensional discrete element theory for rough particles. *International Journal of Geomechanics*, 9(1), 20–33.

K

Katagiri J, Matsushima T, Yamada Y. (2010) Simple shear simulation of 3D irregularly -shaped particles by image-based DEM. *Granular Matter*, 12, 491–497.

Kato Y, Nakata Y, Hyodo M, Murata, H. (2002) Grains characteristic and one - dimensional compression properties of crushable soils. *Journal of geotechnical engineering, JSCE*, 701/III-58, 343–355.

Khan HA. (2009). *Shear induced relative permeability change in uncemented sands*. Master thesis, The University of Texas at Austin.

Kiyota T, Tatsuoka F. (2006) Viscous property of loose sand in triaxial compression, extension and cyclic loading. *Soils and Foundations*, 46(5), 665–684.

Kock I, Huhn K. (2007) Influence of particle shape on the frictional strength of sediments — A numerical case study. *Sedimentary Geology*, 196, 217–233.

L

Lade PV, Yamamuro JA, Skyers BD. (1996) Effects of Shear Band Formation in Triaxial Extension Tests, *Geotechnical Testing Journal,* 19, 398–410.

Leśniewska D, Mróz Z. (2001) Study of evolution of shear band systems in sand retained by flexible wall. *International Journal for Numerical and Analytical Methods in Geomechanics*, 25, 909–932.

Lin CL, Miller JD. (2005) 3D characterization and analysis of particle shape using X-ray micro tomography (XMT). *Powder Technology*, 154, 61–69.

M

Maeda K, Sakai H, Kondo A, Yamaguchi T, Fukuma M, Nukudani E. (2010) Stress-chain based micromechanics of sand with grain shape effect. *Granular Matter*, 12, 499–505.

Mana AI, Clough GW. (1981) Prediction of movements for braced cuts in clay. *Journal of Geotechnical Engineering Division*, 107, 759–778.

Masuda T, Tatsuoka F, Yamada S, Sato T. (1999) Stress-strain behavior of sand in plane strain compression, extension and cyclic loading tests. *Soil and Foundation*, 39(5), 31–45.

Matsushima T, Chang CS. (2011) Quantitative evaluation of the effect of irregularly shaped particles in sheared granular assemblies. *Granular Matter*, 13(3), 269–276.

Mitchell JK, Soga K. (2005) *Fundamentals of soil behavior*. Thrid Edition, Johy Wiley & Sons, Inc.

Murakami H. (2007) *Slope failure of embankment due to seepage*. Master thesis, Yamaguchi University.

N

Nakai T, Xu LM, Yamazaki H. (1997) 3D and 2D model tests and numerical analyses of settlements and earth pressures due to tunnel excavation. *Soils and Foundations*, 37(3), 31–42.

Nicolini E, Nova R. (2000) Modelling of a tunnel excavation in a non-cohesive soil improved with cement mix injections. *Computers and Geotechnics*, 27, 249-272

Nicot F, Darve F. (2007) A micro-mechanical investigation of bifurcation in granular materials. *International Journal of Solids and Structures*, 44, 6630–6652.

Niedostatkiewicz M, Leśniewska D, Tejchman J. (2010) Experimental analysis of shear zone patterns in sand for earth pressure problems using Particle Image Velocimetry. *Strain*, 1–14.

Ng CWW, Lee GTK. (2002) A three-dimensional parametric study of the use of soil nails for stabilizing tunnel faces. *Computers and Geotechnics*, 29, 673–697.

Ng TT. (2004) Macro- and micro-behaviors of granular materials under different sample preparation methods and stress paths. *International Journal of Solids and Structures*, 41, 5871–5884.

O

Oda M, Nemat-Nasser S, Konishi J. (1985) Stress-induced anisotropy in granular masses. *Soils and Foundations*, 25(3), 85–97.

Oda M, Kazama H, Konishi J. (1998) Effects of induced anisotropy on the development of shear bands in granular materials. *Mechanics of Materials*, 28, 103–111.

Oda M, Iwashita K. (2000) Study on couple stress and shear band development in granular media based on numerical simulation analyses. *International Journal of Engineering Science*, 38, 1713–1740.

P

Peters JF, Lade PV, Bro, A. (1988) “Shear band formation in triaxial and plane strain tests.” In: Donaghe, R.T. et al. (Eds.), Advanced Triaxial Testing of Soil and Rock, ASTM STP 977, Philadelphia.

PFC2D. Particle Flow Code in 2 Dimensions, Version 4.0, User Manual. (2008) *Minneapolis,* Minnesota, Itasca Consulting Group Inc.

Powrie W, Ni Q, Harkness RM, Zhang X. (2005) Numerical modelling of plane strain tests on sands using a particulate approach. *Géotechnique*, 55(4), 297–306.

Pradhan TBS. (1997) Characteristics of shear band in plane strain compression tests of sands. *Deformation and progressive failure in geomechanics*, IS-Nagoya

R

Rechenmacher, A. L., Saab, N. A. (2002) Digital image correlation (DIC) to evaluate progression and uniformity of shear bands in dilative sands. *15th ASCE Engineering mechanics conference*, June 2-5, New York

Rechenmacher, A. L., Finno, R. J. (2004) Digital image correlation to evaluate shear banding in dilative sands. *Geotechnical Testing Journal*, 27, 13–22.

Rechenmacher AL. (2006) Grain-scale processes governing shear band initiation and evolution in sands. *Journal of the Mechanics and Physics of Solids*, 54, 22–45.

Rechenmacher AL, Abedi S, Chupin O, Andrés DO. (2011) Characterization of mesoscale instabilities in localized granular shear using digital image correlation. *Acta Geotechnica*, 6(4), 205–217

Ren G, Smith JV, Tang JW, Xie YM. (2005) Underground excavation shape optimization using an evolutionary procedure. *Computers and Geotechnics*, 32, 122–132.

Röchter L, König D, Schanz T, Triantafyllidis T. (2010) Shear banding and strain softening in plane strain extension, physical modeling. *Granular Matter*, 12, 287–301.

Röchter L, König D, Schanz T, Niemunis A, Triantafyllidis T. (2011) Shear band systems in plane strain extension: analytical solution and comparison with experimental results. *Granular Matter*, 13, 553–563.

Rowe PW. (1969) The relation between the shear strength of sands in triaxial compression, plane strain and direct shear. *Géotechnique*, 19(1), 75–86.

S

Sadek S, Iskander MG, Liu JY. (2003) Accuracy of digital image correlation for measuring deformations in transparent media. *Journal of Computing in Civil Engineering*, 2003, 17(2), 88–96.

Salot C, Gotteland P, Villard P. (2009) Influence of relative density on granular materials behavior: DEM simulations of triaxial tests. *Granular Matter*, 11, 221–236

Satake M. (1982) *Deformation and failure of granular materials*, 63–68, Rotterdam, Balkema.

Sezer A, Altun S, Göktepe BA. (2011) Relationships between shape characteristics and shear strength of sands. *Soils and Foundations*, 51(5), 857–871.

Shinohara K, Oida M, Golman B. (2000) Effect of particle shape on angle of internal friction by triaxial compression test. *Powder Technology*, 107, 131–136.

Slominski C, Niedostatkiewicz M, Tejchman J. (2007) Application of particle image velocimetry (PIV) for deformation measurement during granular silo flow. *Powder Technology*, 173, 1–18

Stegmann T, Török J, Brendel L, Wolf DE. (2011) Minimal dissipation theory and shear bands in biaxial tests. *Granular Matter*, 13(5), 565–572.

Sun QC, Song SX, Jin F, Bi ZW. (2011) Elastic energy and relaxation in triaxial compressions. *Granul. Matter*, 13, 743–750.

T

Tagliaferri F, Waller J, Andò E, Hall SA, Viggiani G, Bésuelle P, DeJong JT. (2011) Observing strain localisation processes in bio-cemented sand using x-ray imaging. *Granular Matter*, 13, 247–250

Talesnick M, Horany H, Dancygier AN, Karinski YS. (2008) Measuring soil pressure on a buried model structure for the validation of quantitative framewoks. *Journal of Geotechnical and Geoenvironmental Engineering*, 134(6), 855–8658

Tatsuoka F. (1980) Stress-strain behavior of an idealized anisotropic granular material. *Soil and Foundations*, 20(3), 75–90.

Thomas PA, Bray JD. (1999) Capturing nonspherical shape of granular media with disk clusters. *Journal of Geotechnical and Geoenvironmental Engineering*, 125(3), 169–178.

Thornton C, Antony SJ. (2000) Quasi-static shear deformation of a soft particle system. *Powder Technology*, 109, 179–191.

Ting JM, Corkum BT, Kauffman CR, Greco C. (1989) Discrete numerical model for soil mechanics. *Journal of Geotechnical Engineering*, 115(3), 379–398.

U

Unland G, Al-Khasawneh Y. (2009) The influence of particle shape on parameters of impact crushing. *Minerals Engineering*, 22, 220–228.

V

Vardoulakis I. (1981) Constitutive properties of dry sand observable in the triaxial test. *Acta Mechanica*, 38(3-4), 219–239.

W

Wanatowski D, Chu J. (2006) Stress-strain behavior of a granular fill measured by a new plane-strain apparatus. *Geotechnical Testing Journal*, 29(2), 149–157.

Wanatowski D, Chu J, Loke WL. (2010) Drained instability of sand in plane strain. *Canadian Geotechnical Journal*, 47(4), 400–412.

Wang J, Dove JE, Gutierrez MS. (2007) Discrete-continuum analysis of shear banding in the direct shear test. *Géotechnique*, 57(6), 513–526.

Wang J, Gutierrez MS, Dove JE. (2007) Numerical studies of shear banding in interface shear tests using a new strain calculation method. *International Journal for Numerical and Analytical Methods in Geomechanics*, 31, 1349–1366.

Wang J, Yu HS, Langston P, Fraige F. (2011) Particle shape effects in discrete element modelling of cohesive angular particles. *Granular Matter*, 13, 1–12.

White DJ, Take WA, Bolton MD. (2003) Soil deformation measurement using particle image velocimetry (PIV) and photogrammetry. *Géotechnique*, 53(7), 619–631.

Wichtmann T, Niemunis A, Triantafyllidis T. (2007) Strain accumulation in sand due to cyclic loading: Drained cyclic tests with triaxial extension. *Soil Dynamics and Earthquake Engineering*, 27, 42–48.

Widuliński Ł, Tejchman J, Kozicki J, Leśniewska D. (2011) Discrete simulations of shear zone patterning in sand in earth pressure problems of a retaining wall. *International Journal of Solids and Structures*, 48, 1191–1209.

Wolf H, König D, Triantafyllidis T. (2006) The influence of the stress–strain behavior of non-cohesive soils on the geometry of shear band systems under extensional strain. *Engineering Structures*, 28, 1760–1773.

X

Xu LM, Wang XR. (2004) Numerical simulation of shear band in clayey soils using finite deformation theory. *Chinese journal of Geotechnical Engineering*, 26(2), 225–228. (in Chinese)

Xu LM. (2005) Effects of boundary condition and loading speed on shear band localization. *Chinese journal of hydraulic engineering,* 36(1), 9–15. (in Chinese)

Y

Yan WM. (2009) Fabric evolution in a numerical direct shear test. *Computer and Geotechnics*, 36, 597–603.

Yasufuku N, Murata H, Hyodo M. (1991) Yield characteristics of anisotropically consolidated sand under low and high stresses. *Soil and Foundations*, 31(1), 95–101.

Yimsiri S, Soga K. (2010) DEM analysis of soil fabric effects on behaviour of sand. *Géotechnique*, 60(6): 483–495.

Yoshimine M, Kataoka M. (2007) Steady state of sand in triaxial extension test. *Proceeding of International Workshop on Earthquake Hazards and Mitigation,* 431–438, Guwahati, Indian.

Z

Zeghal M. (2001) Effect of particle shapes on the resilient behaviour of aggregate materials. *Canadian Society for Civil Engineering Annual Conference*, 1–5, Victoria.

Zhou SH. (2005) Principles of pipe roof applied to shallow-buried tunnels in soft ground. *Chinese Journal of Rock Mechanics and Engineering*, 24 (14), 2565–2570. (in Chinese)

Zhuang L. (2009) *Loading-unloading behavior and stress release of granular materials*. Doctoral thesis of Tongji University, Shanghai.

Zhuang L, Nakata Y, Kim UG, Kim D. (2013) Influence of relative density, particle shape, and stress path on the plane strain compression behavior of granular materials. *Acta Geotechnica.* **DOI**: 10.1007/s11440-013-0253-4.

Appendixes Main DEM codes for the simulation

A. Sampling, consolidation and shearing process for a disk sample

Step 1: Sampling

```
; Undercompaction method for biaxial sample

new
set random 20000
SET disk on
set dt max 5e-7
set gravity 0 -9.8
damp default local 0.7 viscous normal 0.1
   shear 0.1 notension on
; -----------------------------------------
def sample_parameters
   ball_num = 6000
   N=10; clump is composed of N balls
   id_s=0
   id_cl=1
   rad_num = 13
   layer_num = 5
   min_rad = 0.0002
   ep = 0.1
   ep_ini = 1.0
   compres_vel = -10.0
   ball_kn = 3.0e8 ; initial stiffnesses
   ball_ks = 2.0e8
   b_fric_ini = 0.01
   ball_dens = 2600
   w_nstiff = 3.0e8
   w_sstiff = 2.0e8
   array ep_layers(5)
   ep_layers(1) = ep+0.000
   ep_layers(2) = ep+0.000
   ep_layers(3) = ep+0.000
   ep_layers(4) = ep+0.000
   ep_layers(5) = ep+0.000

 array ball_rad(13) weight_percent(13)
   ball_rad(1) = 0.00048
   weight_percent(1) = 0.033
   ball_rad(2) = 0.00044
   weight_percent(2) = 0.033
   ball_rad(3) = 0.00042
   weight_percent(3) = 0.0815
   ball_rad(4) = 0.0004
   weight_percent(4) = 0.0815
   ball_rad(5) = 0.00038
   weight_percent(5) = 0.0815
   ball_rad(6) = 0.00036
   weight_percent(6) = 0.0815
   ball_rad(7) = 0.00034
   weight_percent(7)= 0.124
   ball_rad(8) = 0.00032
   weight_percent(8)= 0.124
   ball_rad(9) = 0.0003
   weight_percent(9)= 0.124
   ball_rad(10) = 0.00028
   weight_percent(10)= 0.095
   ball_rad(11) = 0.00026
   weight_percent(11)= 0.095
   ball_rad(12) = 0.00024
   weight_percent(12)= 0.0337
   ball_rad(13) = 0.0002
   weight_percent(13)= 0.0123
 end
; -----------------------------------------
def get_size
   p_avre=0.0
   loop counter (1,rad_num)
      pp = weight_percent(counter)
      rr = ball_rad(counter)
      p_avre = p_avre + pp/rr^2
   end_loop
   sum = 0.0
   loop counter (1,rad_num)
      pp = weight_percent(counter)
      sum = sum + pi * pp * ball_num / p_avre
   end_loop
   width = sqrt((ep+1)*sum/2)
   height = (ep_ini+1)*sum/(width*layer_num)
end
; -----------------------------------------
def make_walls ; create walls with
```

```
overhang of extend
   extend = 0.3
   _x0 = -extend*width
   _y0 = 0.0
   _x1 = width*(1.0 + extend)
   _y1 = 0.0
   Command
   wall id=1 kn=w_nstiff ks=w_sstiff
fric=0 nodes (_x0,_y0) (_x1,_y1)
   end_command
   _x0 = width
   _y0 = -layer_num*extend*height/2
   _x1 = width
   _y1 = height*layer_num
   command
      wall id=2 kn=w_nstiff ks=w_sstiff
fric=0 nodes (_x0,_y0) (_x1,_y1)
   end_command
   _x0 = 0.0
   _y0 = height*layer_num
   _x1 = 0.0
   _y1 = -layer_num*extend*height/2
   command
      wall id=3 kn=w_nstiff ks=w_sstiff
fric=0 nodes (_x0,_y0) (_x1,_y1)
   end_command
   _x0 = width*(1.0 + extend)
   _y0 = 0
   _x1 = -extend*width
   _y1 = 0
   command
      wall id=4 kn=w_nstiff ks=w_sstiff
fric=0 nodes (_x0,_y0) (_x1,_y1)
   end_command
end
; -----------------------------------------
def assemble    ; assemble sample
   make_walls
   id_1 = 1
   y_0 = 0.0
   loop m (1,layer_num)
      command
         del wall 4
      end_command
      _x0 = width*(1.0 + extend)
      _y0 = y_0 + height
      _x1 = -extend*width
      _y1 = y_0 + height
      command
         wall id=4 kn=w_nstiff ks=w_sstiff
fric=0 nodes (_x0,_y0) (_x1,_y1)
      end_command
      ball_1=id_1
      loop counter (1,rad_num)
         pp = weight_percent(counter)
         rr = ball_rad(counter)
         id_2 = id_1 + pp * ball_num /
(rr^2*p_avre*layer_num)-1
         y_1 = y_0- min_rad
         y_2 = y_0 + height
         command
            gen id=id_1,id_2 rad=rr,rr
x=0,width y=y_1,y_2 tries 100000000
         end_command
         id_1 = id_2+1
      end_loop
      color_id = m-1
      command
         prop dens=ball_dens kn=ball_kn
ks=ball_ks fric=b_fric_ini
         prop color color_id range id
ball_1,id_2
      end_command

      bp = ball_head
      sum = 0.0
      loop while bp # null
         sum = sum + pi * b_rad(bp)^2
         bp = b_next(bp)
      end_loop
      ep_need = ep_layers(m)
      command
         wall id=4 yvel=compres_vel
      end_command
      wp = find_wall(4)
      i=1.0
      loop while i>0.00001
         command
            cycle 100
         end_command
         ep_meas =
(width*(y_2+w_y(wp)))/sum-1
         i=(ep_meas-ep_need)/ep_need
      end_loop
      y_0 = y_2+w_y(wp)
      command
         wall id=4 yvel=0
         cycle 3000
```

```
         ini xvel=0 yvel=0 spin=0
      end_command
   end_loop
   height = y_0
   command
      wall prop x=0 y=0
   end_command
end
; -----------------------------------------
sample_parameters
get_size
plot create assembly
plot add ball lorange wall black
plot show
assemble
save UCM_0.1_6000.SAV
; -----------------------------------------
```

Step 2: Isotropic consolidation with rigid boundary wall

```
; Servo-control and initial stress state for biax sample
prop dens ball_dens ks ball_ks kn ball_kn fric 0.01
; -------------------------------------------------
def get_ss ; determine average stress and strain at walls
   xdif    = w_x(wadd2) - w_x(wadd3)
   ydif    = w_y(wadd4) - w_y(wadd1)
   new_xwidth = width + xdif
   new_height = height + ydif
   wsxx    = 0.5*(w_xfob(wadd2)-w_xfob(wadd3))/new_height
   wsyy    = 0.5*(w_yfob(wadd4)-w_yfob(wadd1))/new_xwidth
   wexx = xdif / width
   weyy = ydif / height
   wevol=wexx + weyy
end
; -----------------------------------------
def get_gain    ; determine servo gain parameters for x and y
   alpha = 0.5 ; relaxation factor
   count = 0
   avg_stiff = 0
   cp = contact_head    ; find avg. number of contacts on x-walls
   loop while cp # null
      if c_ball1(cp) = wadd2
         count = count + 1
         avg_stiff = avg_stiff + c_kn(cp)
      end_if
      if c_ball1(cp) = wadd3
         count = count + 1
         avg_stiff = avg_stiff + c_kn(cp)
      end_if
      if c_ball2(cp) = wadd2
         count = count + 1
         avg_stiff = avg_stiff + c_kn(cp)
      end_if
      if c_ball2(cp) = wadd3
         count = count + 1
         avg_stiff = avg_stiff + c_kn(cp)
      end_if
      cp = c_next(cp)
   end_loop
   nxcount = count / 2.0
   avg_stiff = avg_stiff / count
   gx = alpha * (height * 1.0) / (avg_stiff * nxcount * tdel)

   count = 0
   avg_stiff = 0
   cp = contact_head           ; find avg. number of contacts on y-walls
   loop while cp # null
      if c_ball1(cp) = wadd1
         count = count + 1
         avg_stiff = avg_stiff + c_kn(cp)
      end_if
      if c_ball1(cp) = wadd4
         count = count + 1
         avg_stiff = avg_stiff + c_kn(cp)
      end_if
      if c_ball2(cp) = wadd1
         count = count + 1
         avg_stiff = avg_stiff + c_kn(cp)
      end_if
      if c_ball2(cp) = wadd4
         count = count + 1
         avg_stiff = avg_stiff + c_kn(cp)
      end_if
      cp = c_next(cp)
   end_loop
   nycount = count / 2.0
   avg_stiff = avg_stiff / count
   gy = alpha * (width * 1.0)/ (avg_stiff *
```

```
nycount * tdel)
end
; -----------------------------------------
def servo_xy
   while_stepping
   get_ss                         ; compute
stresses & strains
   if x_servo=1
      udx = gx*(wsxx-sxxreq)
      w_xvel(wadd3) = -udx
      w_xvel(wadd2) = udx
   end_if
   if y_servo=1
      udy = gy*(wsyy-syyreq)
      w_yvel(wadd1) = -udy
      w_yvel(wadd4) = udy
   end_if
end
; -----------------------------------------
def iterate_xy
   loop while 1 # 0
      get_gain
      if abs((wsxx-sxxreq)/sxxreq)<sig_tol
then
         if abs((wsyy-
syyreq)/syyreq)<sig_tol then
            exit
         end_if
      end_if
      command
         cycle 100
      end_command
   end_loop
end
; -----------------------------------------
def iterate_y
   loop while 1 # 0
      get_gain
         if abs((wsyy-
syyreq)/syyreq)<sig_tol then
            exit
         end_if
      command
         cycle 100
      end_command
   end_loop
end
; -----------------------------------------
def wall_addr
   wadd1 = find_wall(1)
   wadd2 = find_wall(2)
   wadd3 = find_wall(3)
   wadd4 = find_wall(4)
end
; -----------------------------------------
wall_addr
ini xvel 0 yvel 0 spin 0
set sxxreq=1.0e5 syyreq=1.0e5
sig_tol=0.005 x_servo=1 y_servo=1
iterate_xy
save RigCon_100.sav
; -----------------------------------------
```

Step 3: Isotropic Consolidation with flexible boundary wall

```
;define a membrane and re-consolidation
set ydif=0
; -----------------------------------------
def wall_addr
   wadd1 = find_wall(1)
   wadd2 = find_wall(2)
   wadd3 = find_wall(3)
   wadd4 = find_wall(4)
   rc = 0.4*width
   xc1 = 0.5*width
   yc1 = 0.25*height
   xc2 = 0.5*width
   yc2 = 0.5*height
   xc3 = 0.5*width
   yc3 = 0.75*height
   command
      measure id 10001 x xc1 y yc1 rad rc
      measure id 10002 x xc2 y yc2 rad rc
      measure id 10003 x xc3 y yc3 rad rc
   end_command
   madd1 = find_meas(10001)
   madd2 = find_meas(10002)
   madd3 = find_meas(10003)
end
; -----------------------------------------
def membrane
   height_0=new_height
   width_0=new_xwidth
   x_l=w_x(wadd2)
   x_r=w_x(wadd3)
   start_NO=ball_num
command
```

```
 del wall 2 3
end_command
  mb_rad = min_rad
  mb_num =
int(new_height/(2.0*mb_rad))+1
  mb_kn = ball_kn/10.0
  mb_ks = ball_ks/10.0
  mb_dens = 1000.0
  loop count (1,mb_num)
    _x = x_r-0.95*mb_rad
    _y = w_y(wadd1)+(2.0*count-
1)*mb_rad
    _id = start_NO+count
    if count = mb_num
      _y = height+w_y(wadd4)-mb_rad
    end_if
    command
      ball rad=mb_rad id=_id x=_x y=_y
      group membrane1 range id _id
    end_command
  end_loop

  loop count (1,mb_num)
    _x = x_l+0.95*mb_rad+width
    _y = w_y(wadd1)+(2.0*count-
1)*mb_rad
    _id = start_NO+mb_num+count
    if count = mb_num
      _y = height+w_y(wadd4)-mb_rad
    end_if
    command
      ball rad=mb_rad id=_id x=_x y=_y
      group membrane2 range id _id
    end_command
  end_loop

  mb_id1 = start_NO+1
  mb_id2 = _id
  command
    prop kn=mb_kn ks=mb_ks
dens=mb_dens range id mb_id1 mb_id2
    prop n_bond=1e100 s_bond=1e100
color 4 range id mb_id1 mb_id2
  end_command
  badd1 = find_ball(mb_id1)
  badd2 = find_ball(start_NO+mb_num)
  badd3 = find_ball(mb_id1+mb_num)
  badd4 = find_ball(mb_id2)
  b_yfix(badd1) = 1
  b_yfix(badd2) = 1
  b_yfix(badd3) = 1
  b_yfix(badd4) = 1
  b_yvel(badd1) = w_yvel(wadd1)
  b_yvel(badd3) = w_yvel(wadd1)
  b_yvel(badd2) = w_yvel(wadd4)
  b_yvel(badd4) = w_yvel(wadd4)
end
; -----------------------------------------
def get_ss ; determine average stress and
strain at walls
   LXcoord=0
   RXcoord=0
   LXforce=0
   RXforce=0
loop count (1,mb_num)
  baddi = find_ball(start_NO+count)
  LXcoord = LXcoord + b_x(baddi)
  LXforce = LXforce + b_xfap(baddi)
  end_loop
loop count(1,mb_num)
  baddi =
find_ball(start_NO+mb_num+count)
  RXcoord = RXcoord + b_x(baddi)
  RXforce = RXforce + b_xfap(baddi)
  end_loop
 aver_LXcoord =    LXcoord/mb_num
 aver_RXcoord =    RXcoord/mb_num
 new_width = aver_RXcoord -
aver_LXcoord
 ydif = w_y(wadd4) - w_y(wadd1)
 new_height = height + ydif
 wsxx = 0.5*(LXforce -
RXforce)/new_height
 wsyy = 0.5 * (w_yfob(wadd4) -
w_yfob(wadd1)) / (new_width * 1.0)
 wexx = (new_width - width_0) / width_0
 weyy = ydif / height_0
 wevol = wexx + weyy
 mean_stress_w    = (wsxx+wsyy)/2

 _flag = measure(madd1,1)
  msxx1 = -m_s11(madd1)
  msyy1 = -m_s22(madd1)
  mporos1 = m_poros(madd1)
  _flag = measure(madd2,1)
  msxx2 = -m_s11(madd2)
  msyy2 = -m_s22(madd2)
  mporos2 = m_poros(madd2)
```

```
  _flag = measure(madd3,1)
  msxx3 = -m_s11(madd3)
  msyy3 = -m_s22(madd3)
  mporos3 = m_poros(madd3)
  msxx = (msxx1+msxx2+msxx3)/3.0
  msyy = (msyy1+msyy2+msyy3)/3.0
  msxy = msyy-msxx
  mean_stress_m    = (msxx+msyy)/2
  mporos = (mporos1+mporos2+mporos3)/3.0
  void_ratio = mporos/(1-mporos)
end
; ----------------------------------------
def get_gain    ; determine servo gain parameters for y
  count = 0
  avg_stiff = 0
  cp = contact_head            ; find avg. number of contacts on y-walls
  loop while cp # null
    if c_ball1(cp) = wadd1
      count = count + 1
      avg_stiff = avg_stiff + c_kn(cp)
    end_if
    if c_ball1(cp) = wadd4
      count = count + 1
      avg_stiff = avg_stiff + c_kn(cp)
    end_if
    if c_ball2(cp) = wadd1
      count = count + 1
      avg_stiff = avg_stiff + c_kn(cp)
    end_if
    if c_ball2(cp) = wadd4
      count = count + 1
      avg_stiff = avg_stiff + c_kn(cp)
    end_if
    cp = c_next(cp)
  end_loop
  nycount = count / 2.0
  avg_stiff = avg_stiff / count
    gy = alpha * width / (avg_stiff * nycount* tdel)
end
; ----------------------------------------
def servo_xy
 while_stepping
 get_ss ; compute stresses & strains
  if y_servo=1
    udy = gy*(wsyy-syyreq)
    if abs(udy) > 0.1
       udy = sgn(udy)*0.1
    end_if
    w_yvel(wadd1) = -udy
    w_yvel(wadd4) = udy
    b_yvel(badd1) = w_yvel(wadd1)
    b_yvel(badd3) = w_yvel(wadd1)
    b_yvel(badd2) = w_yvel(wadd4)
    b_yvel(badd4) = w_yvel(wadd4)
  end_if

  if x_servo=1
    fx0 = -sxxreq*mb_rad
    fy0 = 0.0
   bp = ball_head
    loop while b_id(bp)>ball_num+mb_num+1
      bp_next = b_next(bp)
      fx = fx0-0.5*sxxreq*abs(b_y(bp)-b_y(bp_next))
      fy = fy0+0.5*sxxreq*(b_x(bp)-b_x(bp_next))
      fx0 = -0.5*sxxreq*abs(b_y(bp)-b_y(bp_next))
      fy0 = 0.5*sxxreq*(b_x(bp)-b_x(bp_next))
      b_xfap(bp) = fx
      b_yfap(bp) = fy
      bp = b_next(bp)
      b_color(bp)=2
    end_loop
      if b_y(bp)<w_y(wadd4)+height_0
      if b_y(bp)>w_y(wadd1)
        b_xfap(bp) = fx0-sxxreq*mb_rad
        b_yfap(bp) = fy0
        b_color(bp)=3
    end_if
    end_if
    ;b_xfap(find_ball(ball_num+mb_num*2)) = fx
    ;b_color(find_ball(ball_num+mb_num*2))=2

    fx0 = sxxreq*mb_rad
    fy0 = 0.0
    bp = b_next(bp)
    loop while b_id(bp)>ball_num+1
      bp_next = b_next(bp)
```

```
      fx = fx0+0.5*sxxreq*abs(b_y(bp)-
b_y(bp_next))
      fy = fy0-0.5*sxxreq*(b_x(bp)-
b_x(bp_next))
      fx0 = 0.5*sxxreq*abs(b_y(bp)-
b_y(bp_next))
      fy0 = -0.5*sxxreq*(b_x(bp)-
b_x(bp_next))
      b_xfap(bp) = fx
      b_yfap(bp) = fy
      bp = b_next(bp)
      b_color(bp)=4
    end_loop
      if b_y(bp)<w_y(wadd4)+height_0
      if b_y(bp)>w_y(wadd1)
        b_xfap(bp) =
fx0+sxxreq*mb_rad
        b_yfap(bp) = fy0
        b_color(bp)=5
    end_if
    end_if
    ;b_xfap(find_ball(ball_num+mb_num
)) = fx
    ;b_color(find_ball(ball_num+mb_nu
m))=3

 end_if
end
; -----------------------------------------
def iterate_xy
  loop while 1 # 0
    get_gain
      if abs((wsxx-
sxxreq)/sxxreq)<sig_tol then
        if abs((wsyy-
syyreq)/syyreq)<sig_tol then
          exit
        end_if
      end_if
    command
      cycle 100
    end_command
  end_loop
end
; -----------------------------------------
wall_addr
membrane
set sxxreq=1e5 syyreq=1e5
set sig_tol=0.001 alpha = 0.1 x_servo=1
   y_servo=1
iterate_xy
save flexCon_100_new.sav
; -----------------------------------------
```

Step 4: Shearing and data recording (an example of PSCD test)

```
prop fric 0.5 range id 1 6000
set dt max 1.0e-5 hist_rep=2000
   x_servo=0 y_servo=1
ini xvel=0 yvel=0 xdis=0 ydis=0 spin=0
wall id 1 fric 0.2
wall id 4 fric 0.2
; -----------------------------------------
def set_numbers
  band_num = 11
  column_num = 5
  strain_rate = 1000.0 ;1.0%/s
  grid_num = band_num*column_num
end
set_numbers
; -----------------------------------------
def make_arrays
  array ball_x0(ball_num)
ball_y0(ball_num) ball_r0(ball_num)
  array ball_xvel(ball_num)
ball_yvel(ball_num) ball_vel(ball_num)
  array stress_1(grid_num)
stress_2(grid_num) stress_drct(grid_num)
  array f_big(grid_num)
f_small(grid_num) f_drct(grid_num)
  array grid_apr(grid_num)
grid_fdev(grid_num) grid_ep(grid_num)
  array cont_fabric(18) _fabrics(72)
  array max_1(2) max_2(2) max_i1(2)
max_i2(2) max_j1(2) max_j2(2)
  array min_1(2) min_2(2) min_i1(2)
min_i2(2) min_j1(2) min_j2(2)
end
; -----------------------------------------
def set_ini
  height_ini = new_height
  width_ini = new_width
  weyy_0 = weyy
  wevol_0 = wevol
  bp = ball_head
  loop while bp # null
    if b_id(bp) <= ball_num
```

```
         ball_id = b_id(bp)
         b_rot(bp) = 0.0
         b_xdisp(bp) = 0.0
         b_ydisp(bp) = 0.0
         ball_r0(ball_id) = b_rot(bp)
         ball_x0(ball_id) = b_x(bp)
         ball_y0(ball_id) = b_y(bp)
      end_if
      bp = b_next(bp)
   end_loop
end
; ------------------------------------------------
def y_strain
   y_strain = weyy - weyy_0
   vol_strain = wevol- wevol_0
end
; -----------------------------------------
def paint_ball
   a0 = aver_LXcoord
   color_n = -1
   loop _column (1,column_num)
      loop _band (1,band_num)
         xc = (_column-0.5)*new_width/column_num + a0
         yc = w_y(wadd1)+(_band-0.5)*new_height/band_num
         color_n = color_n+1
         if color_n = 4
            color_n = 0
         end_if
         bp = ball_head
         loop while bp # null
            if b_id(bp) <= ball_num
               if b_y(bp) >= yc-0.5*new_height/band_num
                  if b_y(bp) < yc+0.5*new_height/band_num
                     if b_x(bp) >= xc-0.5*new_width/column_num
                        if b_x(bp) < xc+0.5*new_width/column_num
                           b_color(bp) = color_n
                        else
                           if _column = column_num
                              b_color(bp) = color_n
                           end_if
                        end_if
                     else
                        if _column = 1
                           b_color(bp) = color_n
                        end_if
                     end_if
                  end_if
               end_if
            end_if
            bp = b_next(bp)
         end_loop
      end_loop
   end_loop
end
; -----------------------------------------
def measure_circle
   a0 = aver_LXcoord
   array x_m(grid_num) y_m(grid_num) ball_num_m(grid_num)
   command
      set extra ball 1
   end_command
   circle_num = 0
   loop _column (1,column_num)
      loop _band (1,band_num)
         xc = (_column-0.5)*new_width/column_num + a0
         yc = w_y(wadd1)+(_band-0.5)*new_height/band_num
         circle_num = circle_num+1
         x_m(circle_num) = 0.0
         y_m(circle_num) = 0.0
         ball_num_m(circle_num) = 0.0
         bp = ball_head
         loop while bp # null
            if b_id(bp) <= ball_num
               if b_y(bp) >= yc-0.5*new_height/band_num
                  if b_y(bp) < yc+0.5*new_height/band_num
                     if b_x(bp) >= xc-0.5*new_width/column_num
                        if b_x(bp) < xc+0.5*new_width/column_num
                           b_extra(bp,1) = circle_num
                           x_m(circle_num) = x_m(circle_num)+b_x(bp)
```

```
                  y_m(circle_num) =
y_m(circle_num)+b_y(bp)

ball_num_m(circle_num) =
ball_num_m(circle_num)+1
                end_if
              end_if
            end_if
          end_if
        end_if
        bp = b_next(bp)
      end_loop
      xc =
x_m(circle_num)/ball_num_m(circle_num)
      yc =
y_m(circle_num)/ball_num_m(circle_num)
   rc = 0.5*min(new_width/column_num,
new_height/band_num)
      if _band = 1
        rc =
0.45*min(new_width/column_num,
new_height/band_num)
      end_if
      if _band = band_num
        rc =
0.45*min(new_width/column_num,
new_height/band_num)
        yc = yc-0.5*rc
      end_if
      if _column = 1
        rc =
0.45*min(new_width/column_num,
new_height/band_num)
      end_if
      if _column = column_num
        rc =
0.45*min(new_width/column_num,new_h
eight/band_num)
      end_if
      command
        measure id circle_num x xc y yc
rad rc
      end_command
    end_loop
  end_loop
end
; -----------------------------------------
def stress_field
  stress_max = 0.0
  loop id_m (1,circle_num)
      mp = find_meas(id_m)
      xc = m_x(mp)
      yc = m_y(mp)
      _flag = measure(mp,1)
      ms_mean =
abs((m_s11(mp)+m_s22(mp))/2)
      ms_shear = sqrt((m_s11(mp)-
m_s22(mp))^2/4.0+m_s12(mp)^2)
      if ms_shear = 0.0
         ms_shear = 1.0e-5
      end_if
      stress_1(id_m) =
ms_mean+ms_shear
      stress_2(id_m) = ms_mean-
ms_shear
      stress_max =
max(stress_max,stress_1(id_m))
      _angle =
atan2(2*m_s12(mp),m_s11(mp)-
m_s22(mp))/2.0
      if round(100*cos(2*_angle)) #
round(50*(m_s22(mp)-
m_s11(mp))/ms_shear)
          _angle = _angle+pi/2.0
      else
        if round(100*sin(2*_angle)) #
round(100*m_s12(mp)/ms_shear)
          _angle = _angle+pi/2.0
        end_if
      end_if
      stress_drct(id_m) = _angle
      mporos = m_poros(mp)
      void_r = mporos/(1.0-mporos)
      grid_ep(id_m) = string(xc)+'
'+string(yc)+'      '+string(void_r)
  end_loop
  poros_name =
'grid_ep_'+stringfmt(y_strain,1,1)+'.txt'
  _flag_ = open(poros_name,1,1)
  _flag_ = write(grid_ep,circle_num)
  _flag_ = close
end
; -----------------------------------------
def draw_stress
  rc = 0.5*min(new_width/column_num,
new_height/band_num)
  loop id_m (1,circle_num)
      section
```

```
         if stress_1(id_m) = 0.0
            exit_section
         end_if
         mp = find_meas(id_m)
         xc = m_x(mp)
         yc = m_y(mp)
         _r1 = rc*stress_1(id_m)/stress_max
         _r2 = rc*stress_2(id_m)/stress_max
         angle = stress_drct(id_m)
         _angle = angle+pi/2
         if _angle > pi
              _angle = _angle-pi
         end_if
            xi = xc+_r1*cos(angle)
            yi = yc+_r1*sin(angle)
            xi1 = xc+_r1*cos(angle-pi/9)/3
            yi1 = yc+_r1*sin(angle-pi/9)/3
            xi2 = xc+_r1*cos(angle+pi/9)/3
            yi2 = yc+_r1*sin(angle+pi/9)/3
            xj = xc-_r1*cos(angle)
            yj = yc-_r1*sin(angle)
            xj1 = xc-_r1*cos(angle-pi/9)/3
            yj1 = yc-_r1*sin(angle-pi/9)/3
            xj2 = xc-_r1*cos(angle+pi/9)/3
            yj2 = yc-_r1*sin(angle+pi/9)/3
            _xi = xc+_r2*cos(_angle)
            _yi = yc+_r2*sin(_angle)
            _xi1 = xc+_r2*cos(_angle-pi/9)/3
            _yi1 = yc+_r2*sin(_angle-pi/9)/3
            _xi2 = xc+_r2*cos(_angle+pi/9)/3
            _yi2 = yc+_r2*sin(_angle+pi/9)/3
            _xj = xc-_r2*cos(_angle)
            _yj = yc-_r2*sin(_angle)
            _xj1 = xc-_r2*cos(_angle-pi/9)/3
            _yj1 = yc-_r2*sin(_angle-pi/9)/3
            _xj2 = xc-_r2*cos(_angle+pi/9)/3
            _yj2 = yc-_r2*sin(_angle+pi/9)/3
            command
               wall nodes (xc,yc) (xi,yi)
               wall nodes (xc,yc) (xi1,yi1)
               wall nodes (xc,yc) (xi2,yi2)
               wall nodes (xc,yc) (xj,yj)
               wall nodes (xc,yc) (xj1,yj1)
               wall nodes (xc,yc) (xj2,yj2)
               wall nodes (xc,yc) (_xi,_yi)
               wall nodes (xc,yc) (_xi1,_yi1)
               wall nodes (xc,yc) (_xi2,_yi2)
               wall nodes (xc,yc) (_xj,_yj)
               wall nodes (xc,yc) (_xj1,_yj1)
               wall nodes (xc,yc) (_xj2,_yj2)
            end_command
            end_section
      end_loop
   stress_name = 'stress_'+stringfmt(y_strain,1,1)+'.emf'
   command
      set plot emf size 4096 3072
      plot create stressfield
      plot set background white
      plot add ball lcyan lcyan lcyan lcyan outline off wall
      plot hardcopy stressfield file stress_name
      plot show
   end_command
end
; -----------------------------------------
def stress_item
   plot_item
   rc = 0.5*min(new_width/column_num,new_height/band_num)
   loop id_m (1,circle_num)
      section
      if stress_1(id_m) = 0.0
         exit_section
      end_if
      mp = find_meas(id_m)
      xc = m_x(mp)
      yc = m_y(mp)
      _r1 = rc*stress_1(id_m)/stress_max
      _r2 = rc*stress_2(id_m)/stress_max
      angle = stress_drct(id_m)
      _angle = angle+pi/2
      if _angle > pi
         _angle = _angle-pi
      end_if
            max_1(1) = xc+_r1*cos(angle)
            max_1(2) = yc+_r1*sin(angle)
            max_2(1) = xc-_r1*cos(angle)
            max_2(2) = yc-_r1*sin(angle)
            _flag = draw_line(max_1,max_2)
```

```
        max_i1(1) = xc+_r1*cos(angle-pi/9)/3
        max_i1(2) = yc+_r1*sin(angle-pi/9)/3
        max_i2(1) = xc-_r1*cos(angle-pi/9)/3
        max_i2(2) = yc-_r1*sin(angle-pi/9)/3
        _flag = draw_line(max_i1,max_i2)
        max_j1(1) = xc+_r1*cos(angle+pi/9)/3
        max_j1(2) = yc+_r1*sin(angle+pi/9)/3
        max_j2(1) = xc-_r1*cos(angle+pi/9)/3
        max_j2(2) = yc-_r1*sin(angle+pi/9)/3
        _flag = draw_line(max_j1,max_j2)
        min_1(1) = xc+_r2*cos(_angle)
        min_1(2) = yc+_r2*sin(_angle)
        min_2(1) = xc-_r2*cos(_angle)
        min_2(2) = yc-_r2*sin(_angle)
        _flag = draw_line(min_1,min_2)
        min_i1(1) = xc+_r2*cos(_angle-pi/9)/3
        min_i1(2) = yc+_r2*sin(_angle-pi/9)/3
        min_i2(1) = xc-_r2*cos(_angle-pi/9)/3
        min_i2(2) = yc-_r2*sin(_angle-pi/9)/3
        _flag = draw_line(min_i1,min_i2)
        min_j1(1) = xc+_r2*cos(_angle+pi/9)/3
        min_j1(2) = yc+_r2*sin(_angle+pi/9)/3
        min_j2(1) = xc-_r2*cos(_angle+pi/9)/3
        min_j2(2) = yc-_r2*sin(_angle+pi/9)/3
        _flag = draw_line(min_j1,min_j2)
    end_section
  end_loop
end
; -----------------------------------------
def fabric_field
  loop _count (1,18)
    cont_fabric(_count)=0
  end_loop
  cp = contact_head
  loop while cp # null
    section
    if c_nforce(cp)=0
       if c_bflag(cp)=0
          exit section
       end_if
    else
       if pointer_type(c_ball2(cp)) = 101
          exit section
       end_if
    end_if
    if b_id(c_ball1(cp)) > ball_num
       exit section
    else
      if b_id(c_ball2(cp)) > ball_num
        exit section
      end_if
    end_if
    if c_xun(cp) # 0.0
      cont_drt = 18*atan(c_yun(cp)/c_xun(cp))/pi
    else
      cont_drt = 9
    end_if
    if cont_drt < 0.0
       cont_drt = cont_drt+18
    end_if
    case_of int(cont_drt)
      case 0
           cont_fabric(1) = cont_fabric(1)+1
      case 1
           cont_fabric(2) = cont_fabric(2)+1
      case 2
           cont_fabric(3) = cont_fabric(3)+1
      case 3
           cont_fabric(4) = cont_fabric(4)+1
      case 4
           cont_fabric(5) = cont_fabric(5)+1
      case 5
```

```
          cont_fabric(6) =
cont_fabric(6)+1
      case 6
          cont_fabric(7) =
cont_fabric(7)+1
      case 7
          cont_fabric(8) =
cont_fabric(8)+1
      case 8
          cont_fabric(9) =
cont_fabric(9)+1
      case 9
          cont_fabric(10) =
cont_fabric(10)+1
      case 10
          cont_fabric(11) =
cont_fabric(11)+1
      case 11
          cont_fabric(12) =
cont_fabric(12)+1
      case 12
          cont_fabric(13) =
cont_fabric(13)+1
      case 13
          cont_fabric(14) =
cont_fabric(14)+1
      case 14
          cont_fabric(15) =
cont_fabric(15)+1
      case 15
          cont_fabric(16) =
cont_fabric(16)+1
      case 16
          cont_fabric(17) =
cont_fabric(17)+1
      case 17
          cont_fabric(18) =
cont_fabric(18)+1
    end_case
    end_section
    cp = c_next(cp)
  end_loop
  loop _n (1,18)
    _n1 = 2*_n-1
    _n2 = 2*_n
    _n3 = _n1+36
    _n4 = _n2+36
    _fabrics(_n1)=string(cont_fabric(_n))
    _fabrics(_n2)=_fabrics(_n1)
```

```
    _fabrics(_n3)=_fabrics(_n1)
    _fabrics(_n4)=_fabrics(_n1)
  end_loop
  _fname =
'fabric_'+stringfmt(y_strain,1,1)+'.txt'
  _flag_=open(_fname,1,1)
  _flag_=write(_fabrics,72)
  _flag_=close

  rc = min(new_width/column_num,
new_height/band_num)
  incrm_time = time-time_0
  apr_max=0.0
  f_big_max = 0.0
  loop id_m (1,circle_num)
    mp = find_meas(id_m)
    xc = m_x(mp)
    yc = m_y(mp)
    pr_sum = 0.0
    c_count = 0.0
    f_11 = 0.0
    f_22 = 0.0
    f_12 = 0.0
    cp = contact_head
    loop while cp # null
      section
      if c_nforce(cp)=0
        if c_bflag(cp)=0
          exit section
        end_if
      else
        if pointer_type(c_ball2(cp)) =
101
          exit section
        end_if
      end_if
      if b_id(c_ball1(cp)) > ball_num
        exit section
      else
        if b_id(c_ball2(cp)) > ball_num
          exit section
        end_if
      end_if
      if (c_x(cp)-xc)^2+(c_y(cp)-yc)^2
<= rc^2
        c_count = c_count+1
        bp_1 = c_ball1(cp)
        bp_2 = c_ball2(cp)
        r_1 = b_rad(bp_1)
```

```
        r_2 = b_rad(bp_2)
        r_avg = 2*r_1*r_2/(r_1+r_2)
        ball_id = b_id(bp_1)
        sp_1 = (b_rot(bp_1)-
ball_r0(ball_id))/(incrm_time)
        ball_id = b_id(bp_2)
        sp_2 = (b_rot(bp_2)-
ball_r0(ball_id))/(incrm_time)
        pr_sum = pr_sum +
(sp_1*r_1+sp_2*r_2)/r_avg
        f_11 = f_11+c_xun(cp)^2
        f_22 = f_22+c_yun(cp)^2
        f_12 =
f_12+c_xun(cp)*c_yun(cp)
      end_if
      end_section
      cp = c_next(cp)
    end_loop
    apr = pr_sum/c_count
    grid_apr(id_m) = string(xc)+'
'+string(yc)+'     '+string(apr)
    f_11 = f_11/c_count
    f_22 = f_22/c_count
    f_12 = f_12/c_count
    f_dev0 = sqrt((f_11-
f_22)^2/4+f_12^2)
    if f_dev0 = 0.0
       f_dev0 = 1.0e-5
    end_if
    f_big(id_m) = 0.5+f_dev0
    f_small(id_m) = 0.5-f_dev0
    f_big_max =
max(f_big_max,f_big(id_m))
    _angle = atan2(2*f_12,f_11-f_22)/2
    if round(100*cos(2*_angle)) #
round(50*(f_11-f_22)/f_dev0)
       _angle = _angle+pi/2
    else
      if round(100*sin(2*_angle)) #
round(100*f_12/f_dev0)
        _angle = _angle+pi/2
      end_if
    end_if
    f_drct(id_m) = _angle
    grid_fdev(id_m) = string(xc)+'
'+string(yc)+'       '+string(f_dev0)
  end_loop
  _fname = 'grid-
apr_'+stringfmt(y_strain,1,1)+'.txt'
  _flag_ = open(_fname,1,1)
  _flag_ = write(grid_apr,circle_num)
  _flag_ = close
  _fname = 'grid-fabric-
dev_'+stringfmt(y_strain,1,1)+'.txt'
  _flag_ = open(_fname,1,1)
  _flag_ = write(grid_fdev,circle_num)
  _flag_ = close
end
; ------------------------------------------
def draw_fabric
  rc = 0.5*min(new_width/column_num,
new_height/band_num)
  loop id_m (1,circle_num)
      section
      if f_big(id_m) = 0.0
        exit_section
      end_if
      mp = find_meas(id_m)
      xc = m_x(mp)
      yc = m_y(mp)
      _r1 = rc*f_big(id_m)/f_big_max
      _r2 = rc*f_small(id_m)/f_big_max
      angle = f_drct(id_m)
      _angle = angle+pi/2
      if _angle > pi
         _angle = _angle-pi
      end_if
        xi = xc+_r1*cos(angle)
        yi = yc+_r1*sin(angle)
        xj = xc-_r1*cos(angle)
        yj = yc-_r1*sin(angle)
        _xi = xc+_r2*cos(_angle)
        _yi = yc+_r2*sin(_angle)
        _xj = xc-_r2*cos(_angle)
        _yj = yc-_r2*sin(_angle)
        command
          wall nodes (xc,yc) (xi,yi)
          wall nodes (xc,yc) (xj,yj)
          wall nodes (xc,yc) (_xi,_yi)
          wall nodes (xc,yc) (_xj,_yj)
        end_command
        end_section
    end_loop
  fabric_name =
'fabric_'+stringfmt(y_strain,1,1)+'.emf'
  command
    set plot emf size 4096 3072
    plot create fabricfield
```

```
    plot set background white
    plot add ball lcyan lcyan lcyan lcyan outline off wall
    plot hardcopy fabricfield file fabric_name
    plot show
  end_command
end
; ------------------------------------------
def fabric_item
  plot_item
  rc = 0.5*min(new_width/column_num, new_height/band_num)
  loop id_m (1,circle_num)
    section
    if f_big(id_m) = 0.0
      exit_section
    end_if
    mp = find_meas(id_m)
    xc = m_x(mp)
    yc = m_y(mp)
    _r1 = rc*f_big(id_m)/f_big_max
    _r2 = rc*f_small(id_m)/f_big_max
    angle = f_drct(id_m)
    _angle = angle+pi/2
    if _angle > pi
      _angle = _angle-pi
    end_if
        max_1(1) = xc+_r1*cos(angle)
        max_1(2) = yc+_r1*sin(angle)
        max_2(1) = xc-_r1*cos(angle)
        max_2(2) = yc-_r1*sin(angle)
        _flag = draw_line(max_1,max_2)
        min_1(1) = xc+_r2*cos(_angle)
        min_1(2) = yc+_r2*sin(_angle)
        min_2(1) = xc-_r2*cos(_angle)
        min_2(2) = yc-_r2*sin(_angle)
        _flag = draw_line(min_1,min_2)
    end_section
  end_loop
end
; ------------------------------------------
def cf_range
  range_element
  cf_range = 1.0
  cp = fc_arg(0)
  if b_id(c_ball1(cp))>ball_num
     cf_range = 0
  end_if
  if pointer_type(c_ball2(cp)) = 101
     cf_range = 0
  end_if
  if pointer_type(c_ball2(cp)) = 100
    if b_id(c_ball2(cp))>ball_num
      cf_range = 0
    end_if
  end_if
  if c_nforce(cp)<av_cforce
     cf_range = 0
  end_if
end
; ------------------------------------------
def plot_cforce
  cf_fname = 'cforce_'+stringfmt(y_strain,1,1)+'.emf'
  b_fname = 'balls_'+stringfmt(y_strain,1,1)+'.emf'
  command
    plot close cforce
    plot destroy cforce
    plot create cforce
    plot set background white
    plot add cforce black range fish cf_range
    plot hardcopy cforce file cf_fname
    plot hardcopy balls file b_fname
  end_command
end
; ------------------------------------------
def plot_stress
  stress_name = 'stress_'+stringfmt(y_strain,1,1)+'.emf'
  command
    plot close stressfield
    plot destroy stressfield
    plot create stressfield
    plot set background white
    plot add ball lcyan lcyan lcyan lcyan outline off
    plot add fish stress_item black
    plot hardcopy stressfield file stress_name
  end_command
end
; ------------------------------------------
def plot_fabric
  fabric_name = 'fabric_'+stringfmt(y_strain,1,1)+'.emf'
```

```
  command
    plot close fabricfield
    plot destroy fabricfield
    plot create fabricfield
    plot set background white
    plot add ball lcyan lcyan lcyan lcyan outline off
    plot add fish fabric_item black
    plot hardcopy fabricfield file fabric_name
  end_command
end
; ------------------------------------------
def fabric_trace
    f11 = 0.0
    f22 = 0.0
    f12 = 0.0
    c_count = 0.0
    cp = contact_head
    loop while cp # null
      section
      if c_nforce(cp)=0
        if c_bflag(cp)=0
          exit section
        end_if
      else
        if pointer_type(c_ball2(cp)) = 101
          exit section
        end_if
      end_if

      if b_id(c_ball1(cp)) > ball_num
        exit section
      else
        if b_id(c_ball2(cp)) > ball_num
          exit section
        end_if
      end_if
        c_count = c_count+1
        f11 = f11+c_xun(cp)^2
        f22 = f22+c_yun(cp)^2
        f12 = f12+c_xun(cp)*c_yun(cp)
      end_section
      cp = c_next(cp)
    end_loop

    f11 = f11/c_count
    f22 = f22/c_count
    f12 = f12/c_count
end
 ; ----------------------------------------
def servo_xy
 while_stepping
 get_ss ; compute stresses & strains
 fabric_trace
  if y_servo=1
    udy = gy*(wsyy-syyreq)
    if abs(udy) > 0.005
       udy = sgn(udy)*0.005
    end_if
    w_yvel(wadd1) = -udy
    w_yvel(wadd4) = udy
  b_yfix(badd1) = 1
  b_yfix(badd2) = 1
  b_yfix(badd3) = 1
  b_yfix(badd4) = 1
    b_yvel(badd1) = w_yvel(wadd1)
    b_yvel(badd3) = w_yvel(wadd1)
    b_yvel(badd2) = w_yvel(wadd4)
    b_yvel(badd4) = w_yvel(wadd4)
  end_if

  if x_servo=1
    fx0 = -sxxreq*mb_rad
    fy0 = 0.0
    bp = ball_head
    loop while b_id(bp)>ball_num+mb_num+1
      bp_next = b_next(bp)
      fx = fx0-0.5*sxxreq*abs(b_y(bp)-b_y(bp_next))
      fy = fy0+0.5*sxxreq*(b_x(bp)-b_x(bp_next))
      fx0 = -0.5*sxxreq*abs(b_y(bp)-b_y(bp_next))
      fy0 = 0.5*sxxreq*(b_x(bp)-b_x(bp_next))
      b_xfap(bp) = fx
      b_yfap(bp) = fy
      bp = b_next(bp)
    end_loop
      if b_y(bp)<w_y(wadd4)+height_0
      if b_y(bp)>w_y(wadd1)
        b_color(baddi)=5
        b_xfap(bp) = fx0-sxxreq*mb_rad
        b_yfap(bp) = fy0
```

```
        end_if
        end_if

        fx0 = sxxreq*mb_rad
        fy0 = 0.0
        bp = b_next(bp)
        loop while b_id(bp)>ball_num+1
           bp_next = b_next(bp)
           fx = fx0+0.5*sxxreq*abs(b_y(bp)-b_y(bp_next))
           fy = fy0-0.5*sxxreq*(b_x(bp)-b_x(bp_next))
           fx0 = 0.5*sxxreq*abs(b_y(bp)-b_y(bp_next))
           fy0 = -0.5*sxxreq*(b_x(bp)-b_x(bp_next))
           b_xfap(bp) = fx
           b_yfap(bp) = fy
           bp = b_next(bp)
        end_loop
           if b_y(bp)<w_y(wadd4)+height_0
           if b_y(bp)>w_y(wadd1)
              b_color(baddi)=5
              b_xfap(bp) = fx0+sxxreq*mb_rad
              b_yfap(bp) = fy0
        end_if
        end_if
    end_if
end
; -------------------------------------------
def cellpressure
        bp=ball_head
        fx = sxxreq*new_height/mb_num
        loop while b_id(bp)>start_NO
           b_xfap(bp)= -fx*sgn(b_x(bp)-0.5*width)
           bp=b_next(bp)
        end_loop
end
; -------------------------------------------
set_ini
paint_ball
trace energy on
        history id=1 measure coord id 10001
        history id=2 measure coord id 10002
        history id=3 measure coord id 10003
        history id=4 wexx
        history id=5 wevol
        history id=6 measure poro id 10001
        history id=7 measure poro id 10002
        history id=8 wsxx
        history id=9 wsyy
        history id=10 msxx
        history id=11 msyy
        history id=12 y_strain
        history id=13 void_ratio
        history id=14 f11
        history id=15 f22
        history id=16 f12
        history id=17 energy body
        history id=18 energy boundary
        history id=19 energy fric
        history id=20 energy kinetic
        history id=21 energy strain

        plot create stress-strain
        plot add hist 8,9,10,11 vs 12
        plot create volstrain
        plot add hist 5 vs 12
        plot create cforce
        plot create fabricfield
        plot create stressfield
        plot create balls
        plot add ball blue lred
        plot set background white
        set plot emf size 4096 3072
; -------------------------------------------
def save_state
    loop _num (1,circle_num)
        x_m(_num) = 0.0
        y_m(_num) = 0.0
    end_loop
    bp = ball_head
    loop while bp # null
        if b_id(bp)<= ball_num
            if b_extra(bp,1) # 0
                _num = b_extra(bp,1)
                x_m(_num) = x_m(_num)+b_x(bp)
                y_m(_num) = y_m(_num)+b_y(bp)
            end_if
        end_if
        bp = b_next(bp)
    end_loop
    loop _num (1,circle_num)
        mp = find_meas(_num)
```

```
      m_x(mp) = x_m(_num)/ball_num_m(_num)
      m_y(mp) = y_m(_num)/ball_num_m(_num)
    end_loop

    stress_field
    fabric_field
    plot_stress
    plot_fabric
    plot_cforce

    bp = ball_head
    loop while bp # null
      if b_id(bp)<= ball_num
        _num = b_id(bp)
        ball_x0(_num) = b_x(bp)
        ball_y0(_num) = b_y(bp)
        ball_r0(_num) = b_rot(bp)
      end_if
      bp = b_next(bp)
    end_loop
    time_0 = time
end
; ------------------------------------------
def set_space
    grid_space=0.002
    x_grid = int(new_width/grid_space) + 1
    y_grid = int(new_height/grid_space) + 1
    grid_num = x_grid * y_grid
    array x0_grid(10000) y0_grid(10000) z0_grid(10000)
    array x1_grid(10000) y1_grid(10000) z1_grid(10000)
    array x2_grid(10000) y2_grid(10000) z2_grid(10000)
    array grid_No(10000) grid_zahyou(10000); NO of balls attached to grids
    array loci_1(2) loci_2(2) xdisp(10000,30) ydisp(10000,30)
end
set_space
; ------------------------------------------
def grid_search ;get initial coordinations of grids
  id_grid=1
loop j(1,y_grid)
  loop i(1,x_grid)
    x0_grid(id_grid) = -0.012 * width + (i-1) * grid_space
    y0_grid(id_grid) = (j-1) * grid_space
    id_grid = id_grid + 1
    end_loop
end_loop
end
; ------------------------------------------
def zahyou_judge ;search the balls nearest to the grids
array grid_id(grid_num) ball_pos(grid_num)
array gg(grid_num)
  loop i(1,grid_num)
    xi = x0_grid(i)
    yi = y0_grid(i)
    grid_zahyou(i) = string(xi)+' '+string(yi)
    dri = 10.0
    bp = ball_head
    loop while bp # null
      xp = b_x(bp)
      yp = b_y(bp)
      rp = b_rad(bp)
        di = sqrt((xp-xi)^2+(yp-yi)^2)
        dri = min(di/rp,dri)
          if dri = di/rp
          grid_No(i) = bp
          grid_id(i) = b_id(grid_No(i))
          gg(i) = string(grid_id(i))
          ball_pos(i) = string(b_x(bp))+' '+string(b_y(bp))
      end_if
      bp = b_next(bp)
  end_loop
end_loop
    _fname = 'grid_zahyou'+'.txt'
    _flag_=open(_fname,1,1)
    _flag_=write(grid_zahyou,grid_num)
    _flag_=close

    _fname = 'ball_pos'+'.txt'
    _flag_ = open(_fname,1,1)
    _flag_ = write(ball_pos,grid_num)
    _flag_ = close

; Data output to txt file -----------------------
status = open('file1.fio', 1, 0)
status = write(grid_id,grid_num)
```

```
status = close

status = open('file2.txt', 1, 1)
status = write(gg,grid_num)
status = close
end
; ------------------------------------------
def grid_disp_out
        command
                table 1 erase
        end_command

array bb(grid_num)
status = open('file2.txt', 0, 1)
status = read(bb, grid_num)
status = close

      loop i (1,grid_num)
                  ball_add = int(bb(i))
                ii=out('bb_id=' + string(l)+'
'+string(n)+' '+string(ball_add))
                  x_value =
b_x(find_ball(ball_add)) * 1000
                  y_value =
b_y(find_ball(ball_add)) * 1000
                  r_value =
b_rot(find_ball(ball_add))
                  ii=out('x=' + string(x_value)+'
y='+string(y_value)+' r='+string(r_value))

      command
                table 1 x_value y_value ;
      end_command
      end_loop

file_name_log = file_name+
sub_name+'disp.log'
command
        set logfile file_name_log
        set echo on
        set log on
            print table 1
        set log off
        set echo off
        set logfile pfc.log
end_command
end
; ------------------------------------------
def grid_kiroku
```

```
    plot_item
    load_grad = load_grad + 1
    loop i(1, grid_num)
            xdisp(i,load_grad) =
b_xdisp(grid_No(i))
            ydisp(i,load_grad) =
b_ydisp(grid_No(i))
    end_loop
end
; ------------------------------------------
def grid_draw
  loop j(1,load_grad-1)
  plot_item
      loop i(1,grid_num)
        x1_grid(i) = xdisp(i,j) + x0_grid(i)
        y1_grid(i) = ydisp(i,j) + y0_grid(i)

        x2_grid(i) = xdisp(i,j+1) + x0_grid(i)
        y2_grid(i) = ydisp(i,j+1) + y0_grid(i)
            loci_1(1) = x1_grid(i)
            loci_1(2) = y1_grid(i)
            loci_2(1) = x2_grid(i)
            loci_2(2) = y2_grid(i)

             _flag = set_color(2)
            _flag = draw_line(loci_1,loci_2)
  end_loop
end_loop

loop i(1,grid_num)
            loci_1(1) = x0_grid(i)
            loci_1(2) = y0_grid(i)
            _flag = draw_circle(loci_1,0.0002)
end_loop
end
; ------------------------------------------
def plot_dis
    command
        plot create disfield
        plot set background white
        plot add fish grid_draw lblue ;orange
red blue brown
    end_command
end
; ------------------------------------------
grid_search
zahyou_judge
grid_kiroku
```

```
measure_circle
save_state

set sxxreq=0.95e5
cellpressure
cyc 10000
grid_kiroku
save de5.sav

set sxxreq=0.9e5
cellpressure
cyc 10000
grid_kiroku
save de10.sav

set sxxreq=0.85e5
cellpressure
cyc 20000
grid_kiroku
save de15.sav

set sxxreq=0.8e5
cellpressure
cyc 20000
grid_kiroku
save de20.sav

set sxxreq=0.75e5
cellpressure
cyc 30000
grid_kiroku
save de25.sav

set sxxreq=0.7e5
cellpressure
cyc 30000
grid_kiroku
save de30.sav

set sxxreq=0.65e5
cellpressure
cyc 40000
grid_kiroku
save de35.sav

set sxxreq=0.6e5
cellpressure
cyc 40000
grid_kiroku
save de40.sav

set sxxreq=0.55e5
cellpressure
cyc 50000
grid_kiroku
save de45.sav

set sxxreq=0.5e5
cellpressure
cyc 50000
grid_kiroku
save de50.sav

set sxxreq=0.45e5
cellpressure
cyc 50000
grid_kiroku
save de55.sav

set sxxreq=0.42e5
cellpressure
cyc 100000
grid_kiroku
save de58.sav

set sxxreq=0.4e5
cellpressure
cyc 100000
grid_kiroku
save de60.sav

set sxxreq=0.4e5
cellpressure
cyc 100000
grid_kiroku
save de60_1.sav

…… ; shearing until the peak state
; -----------------------------------------
```

B. Sampling and consolidation for a clump sample with three disks

Step 1: Sampling

```
; based on the disk sample ------------
def clump_gen; generate N small particles along the boundary to make a clump
bp=ball_head
ball_NO=ball_num+1
N=3
id_cl=1
loop while bp # null
    bpn = b_next(bp)
    x0=b_x(bp)
    y0=b_y(bp)
    r0=b_rad(bp)
    ball_id=b_id(bp)
    rc=1.2*r0*sin(pi/N)/(1+sin(pi/N))
    dis=r0-rc
    r_m=r0-2*rc

    _a_=b_delete(bp)
    bp=bpn

  rad=r_m
      ball_NO=ball_NO+1
  loop i(0,N-1)
    xc=x0+1.2*dis*cos(2*i*pi/N)
    yc=y0+1.2*dis*sin(2*i*pi/N)
     command
        ball id=ball_NO x=xc y=yc rad=rc
     end_command
     ball_NO=ball_NO+1
  end_loop
end_loop

loop j(1,ball_num)
    id_start=ball_num+(j-1)*(N+1)+1
    id_end=id_start+N
  command
    clump id=id_cl perm range id=id_start,id_end
  end_command
id_cl=id_cl+1
end_loop
end
; -----------------------------------------
clump_gen
prop dens ball_dens ks ball_ks kn ball_kn fric 0.5
plot creat clump
plot add clump lcyan
save sample_C3.sav
; -----------------------------------------
```

Step 2: Rigid consoildation
Similar to the Step 2 in Appendix A

```
; -----------------------------------------
```

Step 3: Flexible consoildation

```
;define a membrane and re-consolidation
def wall_addr
  wadd1 = find_wall(1)
  wadd2 = find_wall(2)
  wadd3 = find_wall(3)
  wadd4 = find_wall(4)
  rc = 0.4*width
  xc1 = 0.5*width
  yc1 = 0.25*height
  xc2 = 0.5*width
  yc2 = 0.5*height
  xc3 = 0.5*width
  yc3 = 0.75*height
  command
    measure id 10001 x xc1 y yc1 rad rc
    measure id 10002 x xc2 y yc2 rad rc
    measure id 10003 x xc3 y yc3 rad rc
  end_command
  madd1 = find_meas(10001)
  madd2 = find_meas(10002)
  madd3 = find_meas(10003)
end
; -----------------------------------------
def membrane
  height_0=new_height
  width_0=new_xwidth
  x_l=w_x(wadd2)
  x_r=w_x(wadd3)
  start_NO=id_end
command
```

```
 del wall 2 3
end_command
  mb_rad = min_rad
  mb_num =
int(new_height/(2.0*mb_rad))+1
  mb_kn = ball_kn/100.0
  mb_ks = ball_ks/100.0
  mb_dens = 1000.0

  loop count (1,mb_num)
    _x = x_r
    _y = w_y(wadd1)+(2.0*count-
1)*mb_rad
    _id = start_NO+count
    if count = mb_num
      _y = height+w_y(wadd4)-mb_rad
    end_if
    command
      ball rad=mb_rad id=_id x=_x y=_y
     group membrane1 range id _id
    end_command
  end_loop

  loop count (1,mb_num)
    _x = x_l+width
    _y = w_y(wadd1)+(2.0*count-
1)*mb_rad
    _id = start_NO+mb_num+count
    if count = mb_num
      _y = height+w_y(wadd4)-mb_rad
    end_if
    command
      ball rad=mb_rad id=_id x=_x y=_y
      group membrane2 range id _id
    end_command
  end_loop

  mb_id1 = start_NO+1
  mb_id2 = _id
  command
    prop kn=mb_kn ks=mb_ks
dens=mb_dens range id mb_id1 mb_id2
    prop n_bond=1e100 s_bond=1e100
color 4 range id mb_id1 mb_id2
  end_command
  badd1 = find_ball(mb_id1)
  badd2 = find_ball(start_NO+mb_num)
  badd3 = find_ball(mb_id1+mb_num)
  badd4 = find_ball(mb_id2)
```

```
    b_xfix(badd1) = 1
    b_xfix(badd2) = 1
    b_xfix(badd3) = 1
    b_xfix(badd4) = 1
    b_yvel(badd1) = w_yvel(wadd1)
    b_yvel(badd3) = w_yvel(wadd1)
    b_yvel(badd2) = w_yvel(wadd4)
    b_yvel(badd4) = w_yvel(wadd4)
end
; -------------------------------------------------
--
def get_ss ; determine average stress and
strain at walls
      LXcoord=0
      RXcoord=0
      LXforce=0
      RXforce=0
loop count (1,mb_num)
    baddi = find_ball(start_NO+count)
    LXcoord = LXcoord + b_x(baddi)
    LXforce = LXforce + b_xfap(baddi)
    end_loop
loop count(1,mb_num)
    baddi =
find_ball(start_NO+mb_num+count)
    RXcoord = RXcoord + b_x(baddi)
    RXforce = RXforce + b_xfap(baddi)
    end_loop
  aver_LXcoord =    LXcoord/mb_num
  aver_RXcoord =    RXcoord/mb_num
  new_width = aver_RXcoord -
      aver_LXcoord
  ydif = w_y(wadd4) - w_y(wadd1)
  new_height = height_0 + ydif
  wsxx = 0.5*(LXforce -
RXforce)/new_height
  wsyy = 0.5 * (w_yfob(wadd4) -
      w_yfob(wadd1)) / (new_width * 1.0)
  wexx = (new_width - width_0) / width_0
  weyy = ydif / height_0
  wevol = wexx + weyy
  mean_stress_w = (wsxx+wsyy)/2

  _flag = measure(madd1,1)
    msxx1 = -m_s11(madd1)
    msyy1 = -m_s22(madd1)
    mporos1 = m_poros(madd1)
   _flag = measure(madd2,1)
    msxx2 = -m_s11(madd2)
```

```
    msyy2 = -m_s22(madd2)
    mporos2 = m_poros(madd2)
    _flag = measure(madd3,1)
    msxx3 = -m_s11(madd3)
    msyy3 = -m_s22(madd3)
    mporos3 = m_poros(madd3)
    msxx = (msxx1+msxx2+msxx3)/3.0
    msyy = (msyy1+msyy2+msyy3)/3.0
    msxy = msyy-msxx
    mean_stress_m    = (msxx+msyy)/2
    mporos =
(mporos1+mporos2+mporos3)/3.0
    void_ratio = mporos/(1-mporos)
end
; -------------------------------------------------
def get_gain    ; determine servo gain
parameters for y
    count = 0
    avg_stiff = 0
    cp = contact_head ; find avg. number of
contacts on y-walls
    loop while cp # null
        if c_ball1(cp) = wadd1
            count = count + 1
            avg_stiff = avg_stiff + c_kn(cp)
        end_if
        if c_ball1(cp) = wadd4
            count = count + 1
            avg_stiff = avg_stiff + c_kn(cp)
        end_if
        if c_ball2(cp) = wadd1
            count = count + 1
            avg_stiff = avg_stiff + c_kn(cp)
        end_if
        if c_ball2(cp) = wadd4
            count = count + 1
            avg_stiff = avg_stiff + c_kn(cp)
        end_if
        cp = c_next(cp)
    end_loop
    nycount = count / 2.0
    avg_stiff = avg_stiff / count
        gy = alpha * width / (avg_stiff *
nycount* tdel)
end
; ------------------------------------------
def servo_xy
  while_stepping
  get_ss ; compute stresses & strains
```

```
    if y_servo=1
        udy = gy*(wsyy-syyreq)
        if abs(udy) > 0.1
              udy = sgn(udy)*0.1
        end_if
        w_yvel(wadd1) = -udy
        w_yvel(wadd4) = udy
        b_yvel(badd1) = w_yvel(wadd1)
        b_yvel(badd3) = w_yvel(wadd1)
        b_yvel(badd2) = w_yvel(wadd4)
        b_yvel(badd4) = w_yvel(wadd4)
    end_if

    if x_servo=1
        fx0 = -sxxreq*mb_rad
        fy0 = 0.0
      bp = ball_head
        loop while
b_id(bp)>start_NO+mb_num+1
            bp_next = b_next(bp)
            fx = fx0-0.5*sxxreq*abs(b_y(bp)-
b_y(bp_next))
            fy = fy0+0.5*sxxreq*(b_x(bp)-
b_x(bp_next))
            fx0 = -0.5*sxxreq*abs(b_y(bp)-
b_y(bp_next))
            fy0 = 0.5*sxxreq*(b_x(bp)-
b_x(bp_next))
            b_xfap(bp) = fx
            b_yfap(bp) = fy
            bp = b_next(bp)
            b_color(bp)=2
        end_loop
            if b_y(bp)<w_y(wadd4)+height_0
            if b_y(bp)>w_y(wadd1)
                b_xfap(bp) = fx0-
sxxreq*mb_rad
                b_yfap(bp) = fy0
                b_color(bp)=3
        end_if
        end_if

b_xfap(find_ball(start_NO+mb_num*2)) =
fx
b_color(find_ball(start_NO+mb_num*2))=
2
        fx0 = sxxreq*mb_rad
        fy0 = 0.0
        bp = b_next(bp)
```

```
    loop while b_id(bp)>start_NO+1
      bp_next = b_next(bp)
      fx = fx0+0.5*sxxreq*abs(b_y(bp)-
b_y(bp_next))
      fy = fy0-0.5*sxxreq*(b_x(bp)-
b_x(bp_next))
      fx0 = 0.5*sxxreq*abs(b_y(bp)-
b_y(bp_next))
      fy0 = -0.5*sxxreq*(b_x(bp)-
b_x(bp_next))
      b_xfap(bp) = fx
      b_yfap(bp) = fy
      bp = b_next(bp)
      b_color(bp)=4
    end_loop
      if b_y(bp)<w_y(wadd4)+height_0
      if b_y(bp)>w_y(wadd1)
        b_xfap(bp) =
fx0+sxxreq*mb_rad
        b_yfap(bp) = fy0
        b_color(bp)=5
    end_if
    end_if

 end_if
end
; ------------------------------------------
def iterate_xy
  loop while 1 # 0
    get_gain
      if abs((msxx-
sxxreq)/sxxreq)<sig_tol then
        if abs((wsyy-
syyreq)/syyreq)<sig_tol then
          exit
        end_if
      end_if
    command
      cycle 100
    end_command
  end_loop
end
; ------------------------------------------
wall_addr
membrane
set sxxreq=1.0e5 syyreq=1.0e5
set sig_tol=0.01 alpha = 0.1 x_servo=1
y_servo=1
iterate_xy
save FlexiCon_C3.sav
```